



HUNGARIAN UNIVERSITY OF  
AGRICULTURE AND LIFE SCIENCES  
(SZENT ISTVÁN UNIVERSITY formerly)

The effect of 3D printing structures and surfaces on the  
tribological behaviour of polymer and polymer composites

PhD Dissertation

by

Muammel M. Hanon Sharba

DOI: 10.54598/002100

Gödöllő  
2022

**Doctoral school**

**Denomination:** Doctoral School of Mechanical Engineering

**Science:** Mechanical Engineering

**Leader:** Prof. Dr. Gábor Kalácska, DSc  
Institute of Technology  
Hungarian University of Agriculture and Life Sciences,  
Szent István Campus, Gödöllő, Hungary

**Supervisor:** Dr. László Zsidai, PhD  
Institute of Technology  
Hungarian University of Agriculture and Life Sciences,  
Szent István Campus, Gödöllő, Hungary

.....

Affirmation of supervisor

.....

Affirmation of head of school

## CONTENTS

NOMENCLATURE AND ABBREVIATIONS .....	6
1. INTRODUCTION, OBJECTIVES .....	8
<b>1.1. Introduction</b> .....	<b>8</b>
<b>1.2. Objectives</b> .....	<b>9</b>
2. LITERATURE REVIEW .....	10
<b>2.1. Manufacturing techniques classification</b> .....	<b>10</b>
<b>2.2. Additive manufacturing (3D printing)</b> .....	<b>11</b>
2.2.1. <i>3D printing methods</i> .....	11
2.2.2. <i>Materials for 3D printing</i> .....	18
2.2.3. <i>Applications of 3D printing</i> .....	21
<b>2.3. Polymers for 3D printing</b> .....	<b>23</b>
2.3.1. <i>The chemical structure of polymer</i> .....	23
2.3.2. <i>The classifications of engineering plastics</i> .....	25
<b>2.4. Tribology of polymers</b> .....	<b>26</b>
2.4.1. <i>Friction of polymers</i> .....	27
2.4.2. <i>Wear of polymers</i> .....	32
<b>2.5. Tribology of 3D-printed polymers</b> .....	<b>34</b>
<b>2.6. Summary of literature review</b> .....	<b>35</b>
3. MATERIALS AND METHODS .....	37
<b>3.1. Design of experiment</b> .....	<b>37</b>
<b>3.2. The 3D printing technologies</b> .....	<b>38</b>
<b>3.3. Manufacturing of 3D-printed specimens</b> .....	<b>38</b>
3.3.1. <i>PLA filaments printed by FDM technique</i> .....	38
3.3.2. <i>Bronze/PLA composite filament printed by FDM technique</i> .....	42
3.3.3. <i>WANHAO neat resin printed by DLP technique</i> .....	43
3.3.4. <i>Graphene/resin composite printed by DLP technique</i> .....	45
<b>3.4. Post-processing</b> .....	<b>48</b>
<b>3.5. Determination of tribological properties</b> .....	<b>49</b>
3.5.1. <i>Tribometer system and procedure of experiments</i> .....	49
3.5.2. <i>Tribology test data analysis</i> .....	51
<b>3.6. Tensile testing</b> .....	<b>54</b>
<b>3.7. Microstructure, hardness, roughness, and surface energy characterizations</b> .....	<b>55</b>
4. RESULTS AND DISCUSSION .....	58
<b>4.1. Investigation of tribological properties</b> .....	<b>58</b>
4.1.1. <i>Tribology of neat PLA material FDM 3D-printed</i> .....	58

4.1.1.1. Influence of process parameters and filament colour on friction.....	58
4.1.1.2. Influence of process parameters and filament colour on wear.....	61
4.1.1.3. Effect of different colours on thermal conductivity.....	63
4.1.2. Tribology of bronze/PLA composite material FDM 3D-printed.....	65
4.1.3. Tribology of neat resin material DLP 3D-printed.....	67
4.1.4. Tribology of graphene/resin composite material DLP 3D-printed.....	67
4.1.4.1. Friction coefficient behaviour profile.....	68
4.1.4.2. Static and dynamic friction coefficient.....	70
4.1.4.3. Wear depth and specific wear rate.....	72
4.1.5. Theoretical sliding surfaces as a function of measured wear.....	75
4.1.5.1. Overview.....	75
4.1.5.2. Approximate definition of cross-section and creation of basic models.....	76
4.1.5.3. Results of the approximate determination of wear surfaces.....	76
4.1.6. Summary and conclusions on the investigation of tribological properties.....	79
<b>4.2. Investigation of mechanical characteristics.....</b>	<b>80</b>
4.2.1. Tensile of neat PLA material FDM 3D-printed.....	80
4.2.2. Tensile of bronze/PLA composite FDM 3D-printed.....	83
4.2.3. Tensile of neat resin DLP 3D-printed.....	85
4.2.4. Tensile of graphene/resin composite DLP 3D-printed.....	86
4.2.4.1. Impact of layer thickness.....	86
4.2.4.2. Influence of graphene existence.....	87
4.2.5. Summary and conclusions on the investigation of mechanical characteristics.....	89
<b>4.3. Hardness test observation.....</b>	<b>90</b>
4.3.1. Hardness of neat PLA material FDM 3D-printed.....	91
4.3.2. Hardness of bronze/PLA composite FDM 3D-printed.....	92
4.3.3. Hardness of neat resin material DLP 3D-printed.....	93
4.3.4. Hardness of graphene/resin composite DLP 3D-printed.....	93
4.3.5. Summary and conclusions on the investigation of hardness.....	94
<b>4.4. Determination of surface roughness.....</b>	<b>95</b>
4.4.1. Surface roughness of neat PLA material FDM 3D-printed.....	95
4.4.2. Surface roughness of bronze/PLA composite FDM 3D-printed.....	97
4.4.3. Surface roughness of neat resin material DLP 3D-printed.....	98
4.4.4. Surface roughness of graphene/resin composite DLP 3D-printed.....	99
4.4.4.1. Surface roughness of the test specimens.....	99
4.4.4.2. Surface roughness of the counterpart.....	102
4.4.5. Summary and conclusions on the investigation of surface roughness.....	102
<b>4.5. Surface structure observation.....</b>	<b>103</b>

4.5.1. Surface structure of neat PLA material FDM 3D-printed.....	103
4.5.2. Surface structure analysis of bronze/PLA composite FDM 3D-printed.....	106
4.5.3. Surface morphology analysis of neat resin material DLP 3D-printed.....	109
4.5.4. SEM of graphene/resin composites prepared with different relaxation times.....	110
4.5.5. Summary and conclusions on the investigation of surface morphology.....	113
<b>4.6. Determination of surface energy .....</b>	<b>114</b>
4.6.1. FDM 3D-printed PLA - single-liquid measurement results .....	114
4.6.2. DLP 3D-printed Resin - single-liquid measurement results.....	114
4.6.3. DLP 3D-printed Resin - two-liquid measurement results.....	115
<b>4.7. New scientific results .....</b>	<b>116</b>
5. CONCLUSION AND SUGGESTIONS .....	118
6. SUMMARY .....	119
7. ÖSSZEFOGLALÁS (SUMMARY IN HUNGARIAN) .....	120
8. APPENDICES.....	121
<b>A1: Bibliography.....</b>	<b>121</b>
<b>A2: Publications related to the dissertation .....</b>	<b>138</b>
<b>A3: Technical specifications of the used printers .....</b>	<b>140</b>
<b>A4: Chemical composition of the used photopolymer resin materials .....</b>	<b>140</b>
<b>A5: Tensile stress-strain curves of various layer thickness specimens .....</b>	<b>141</b>
<b>A6: Mechanical behaviour under different graphene concentrations.....</b>	<b>142</b>
<b>A7: Variance in values of tensile test results .....</b>	<b>143</b>
<b>A8: Illustration of hardness testing along with the specimen length.....</b>	<b>144</b>
<b>A9: Correlation between the tribological and mechanical/physical properties.....</b>	<b>145</b>
9. ACKNOWLEDGEMENT .....	148

## NOMENCLATURE AND ABBREVIATIONS

### *Symbols*

$A$	Cross-sectional area	$\text{mm}^2$
$A_a$	Area of contact	$\text{mm}^2$
$A_r$	Real area of contact	$\text{mm}^2$
$d$	Total sliding distance	m
$F$	Tensile force	N
$f$	Alternating motion frequency	Hz
$F_f$	Frictional force	N
$F_n$	Applied normal load	N
$K$	Specific wear rate	$\text{mm}^3/\text{Nm}$
$L$	Initial length before tensile test	mm
$p_v$	Contact pressure multiplied by the sliding speed	$\text{MPa} \cdot \text{m/s}$
$R_a$	Surface average roughness	$\mu\text{m}$
Rh	Relative humidity	%
T	Ambient temperature	$^{\circ}\text{C}$
$T$	Temperature of sliding surfaces	$^{\circ}\text{C}$
$t$	Test duration	min
$T_g$	Glass-transition temperature	$^{\circ}\text{C}$
$\Delta L$	Change in length after tensile test	Mm
$\Delta V$	Wear volume loss	$\text{mm}^3$
$E$	Modulus of elasticity	GPa
$v$	Sliding velocity	m/s

### *Greek symbols*

$\gamma^D$	Dispersive component of surface energy	mN/m
$\gamma^P$	Polar component of surface energy	mN/m
$\gamma^{lv}$	Liquid-vapor interfacial	mN/m
$\gamma^{sl}$	Solid-liquid interfacial	mN/m
$\gamma^{sv}$	Solid-vapor interfacial	mN/m
$\mu$	Coefficient of friction	-
$\varepsilon$	Tensile strain	%
$\theta$	Droplet contact angle	degree ( $^{\circ}$ )
$\sigma$	Tensile stress	MPa
$\gamma$	Total surface energy	mN/m

### *Abbreviations*

3D printing	Three-Dimensional Printing
ABS	Acrylonitrile Butadiene Styrene
AM	Additive Manufacturing
ASTM	American Society for Testing and Materials
CAD	Computer-Aided Design
CF	Carbon Fibre Reinforced
CNC	Computer Numerical Control
CNT	Carbon Nanotube Reinforced
cws	CreationWorkshop
DED	Directed Energy Deposition

## Nomenclature and abbreviations

---

DLP	Digital Light Processing
DMD	Direct Metal Deposition
DOD	Drop On Demand
EBAM	Electron Beam Additive Manufacturing
EBM	Electron Beam Machining
FDM	Fused Deposition Modelling
FFF	Fused Filament Fabrication
GNP	Graphene Nanoplatelets
GO	Graphene Oxide
HDPE	High Density Polyethylene
HIPS	High Impact Polystyrene
ISO	International Organization for Standardization
LCD	Liquid Crystal Display
LENS	Laser Engineered Net Shaping
LMD	Laser Metal Deposition
LOM	Laminated Objective Manufacturing
MFAF	Magnetic Field Assisted Finishing
MWCNT	Multi-Walled Carbon Nanotube
PA	Polyamide
PBF	Powder Bed Fusion
PC	Polycarbonate
PE	Polyethylene
PEEK	Polyetheretherkeytone
PEI	Polyetherimide
PETG	Polyethylene Terephthalate Glycol
PEVA	Polyethylene Vinyl Acetate
PLA	Polylactic Acid
PMMA	Polymethyl Methacrylate
PP	Polypropylene
PS	Polystyrene
PTFCE	Polytrifluorochloroethylene
PTFE	Polytetrafluoroethylene
PUA	Polyurethane Acrylate
PVA	PolyVinyl Alcohol
PVC	Polyvinylchloride
PVDC	Polyvinylidene Chloride
SD	Standard Deviation
SE	Secondary Electron
SEM	Scanning Electron Microscopy
SLA	Stereolithography
SLM	Selective Laser Melting
SLS	Selective Laser Sintering
STL	Surface Tessellation Language
SWCNT	Single-Wall Carbon Nanotube
UHDPE	Ultra High Density Polyethylene
UTS	Ultimate Tensile Strength
UV	Ultraviolet
WAAM	Wire + Arc Additive Manufacturing
WD	Working Distance

# 1. INTRODUCTION, OBJECTIVES

This chapter describes the background and objectives of the current research.

## 1.1. Introduction

Additive manufacturing (AM), often known as 3D printing, has drew the interests of industry, academics and research societies, and hobbyists alike. The application of additive manufacturing technologies in several sectors has risen dramatically in recent years (Attaran, 2017). This can be explained by the decrease in the price of printers and the widening of their use (machine parts, manufacturing aids, medical applications prostheses, light industry, tools, etc.) (Rayna and Striukova, 2016). 3D printing has evolved into a versatile tool for making custom-needed products that may cut production costs, shorten lead times, and diminish waste material created during the manufacturing process. Therefore, it may serve as an alternative processing technique for production of small machine elements, including bearings, gears, fittings and other elements. The capability to construct functional end components with integrated electronic and mechanical elements is one of the most recent 3D printing developments (Tofail et al., 2017).

Tribology is the branch of knowledge and technology of surfaces in contact and at a relative motion, in addition to supporting activities aimed at lowering friction and wear-related expenses. Polymer components have been popular in tribological applications for decades, owing to their favourable qualities such as vibration damping capabilities, self-lubrication, and corrosion resistance. In parallel with that, the transition from traditional fossil-oil based polymers towards bio-based polymers have been stimulated and can further enhance the sustainability of dry sliding polymer elements. Furthermore, polymer composites are an excellent selection for various implementations due to their abrasion resistance, high durability, and fracture toughness properties. Consequently, polymers and polymer composites are becoming more widely used as bearing and sliding materials with each year of their availability (Briscoe and Sinha, 2013).

Many process parameters can be controlled when producing 3D-printed part structures. Since then, the influence of process parameter settings on the mechanical qualities (e.g., tensile, flexural impact, compressive, and fatigue strength) has been described in thorough for various production scenarios. These parameters were exhaustively investigated for different categories of materials. The 3D printing of ABS (acrylonitrile butadiene styrene) and bio-based polymers such as PLA (polylactic acid) are largely used for AM technologies. Researches that investigated PLA have been mostly dealing with the mechanical characteristics of this polymeric material (Cifuentes et al., 2017; Revati et al., 2017). Analysing the mechanical-material structure of 3D-printed PLAs can also be found (Ferreira et al., 2017). However, the tribological studies on 3D-printed structures are still limited today, as few literature explored the tribological characteristics (Bustillos et al., 2017). For this, researchers have begun in recent years to investigate further the effect of 3D printing on tribological features. This indicates the timeliness of the topic.

In the present study, 3D-printed polymer specimens will be produced by different printing technologies (FDM-fused deposition modelling and DLP-digital light processing). The mechanical characteristics (under static conditions) and surface properties of 3D-printed polymer parts, which are important for eventual further correlations with the tribological properties, will be determined. Therefore, tribological, tensile, hardness, surface energy, and surface roughness tests, as well as scanning electron microscopy (SEM) and optical microscopic examination, will be performed. During mechanical testing, the anisotropy of the parts owing to the layer-by-layer printing will be taken into account.



A specifically developed tribological testing equipment for reciprocating sliding under adhesive conditions will be used. As experimental test conditions for the sliding testing, various normal loads will be applied leading to normal wear conditions and overload conditions, to determine the operating range and failure modes of 3D-printed polymer specimens. Four different polymer materials will be examined (neat PLA and bronze/PLA composite for FDM, and neat resin and graphene/resin composite for DLP). The effect of various print settings and material colours used during the specimens' manufacture will be investigated. DLP specimens will be inspected with and without post-processing (heating and UV post-curing).

This research will lead to better control and optimization of the 3D printing parameters of polymers and will provide a better understanding of the tribological properties of these polymeric elements. This is a novel cross-over research area that will allow the collection of a unique set of testing data with combined tribological, mechanical and chemical characteristics. Based on the results, suggestions will be formulated for mechanical and/or tribological applications. These findings will be helpful for the industrial producers, who now started to use the up-to-date additive manufacturing technologies not just for rapid prototyping but also for any products of sliding elements (e.g., guideway, bushings and bearings, and green (self-lubricating) machine components).

### 1.2. Objectives

FDM and DLP 3D printing techniques will be employed to print specimens using various materials and different manufacturing process parameters. The produced samples, with this variety of conditions, will be subject to tribological, microstructure, surface roughness and energy, tensile, and hardness tests. The main objectives of the present work are to investigate the following:

- a) What is the influence of 3D printing conditions on the intrinsic mechanical, physical, and chemical polymer properties and polymer structure?
- b) Comparison of friction and wear behaviour of the different printed polymers in connection with printing options, methods and mechanical properties.
- c) Determination of optimal operating conditions of the selected polymers and printing methods.
- d) What are the tribo-physical reactions taking place within the sliding interface?
- e) Evaluation of the effect of filler/additives attendance in the case of composites.

## 2. LITERATURE REVIEW

This chapter seeks to provide a thorough overview of 3D printing processes, including the major methods used, materials employed (with a concentration on polymers), and applications in different sectors. The chapter will furthermore present the tribology of polymers focusing on the 3D-printed polymer composites and the effect of its structures and surfaces on the tribological behaviour as one of the main objectives of this research. In addition, identifying the gaps and challenges that were encountered in literature which is considered the reason of initiating this research.

### 2.1. Manufacturing techniques classification

The majority of manufacturing techniques may be divided into three categories. At the most basic level, these categories are: formative manufacturing (forging, injection moulding, stamping, and casting), subtractive manufacturing (drilling, CNC, and turning), and additive manufacturing (3D printing). A schematic comparison illustrated in Fig. 2.1 to clarify how the additive, formative, and subtractive manufacturing produce parts.

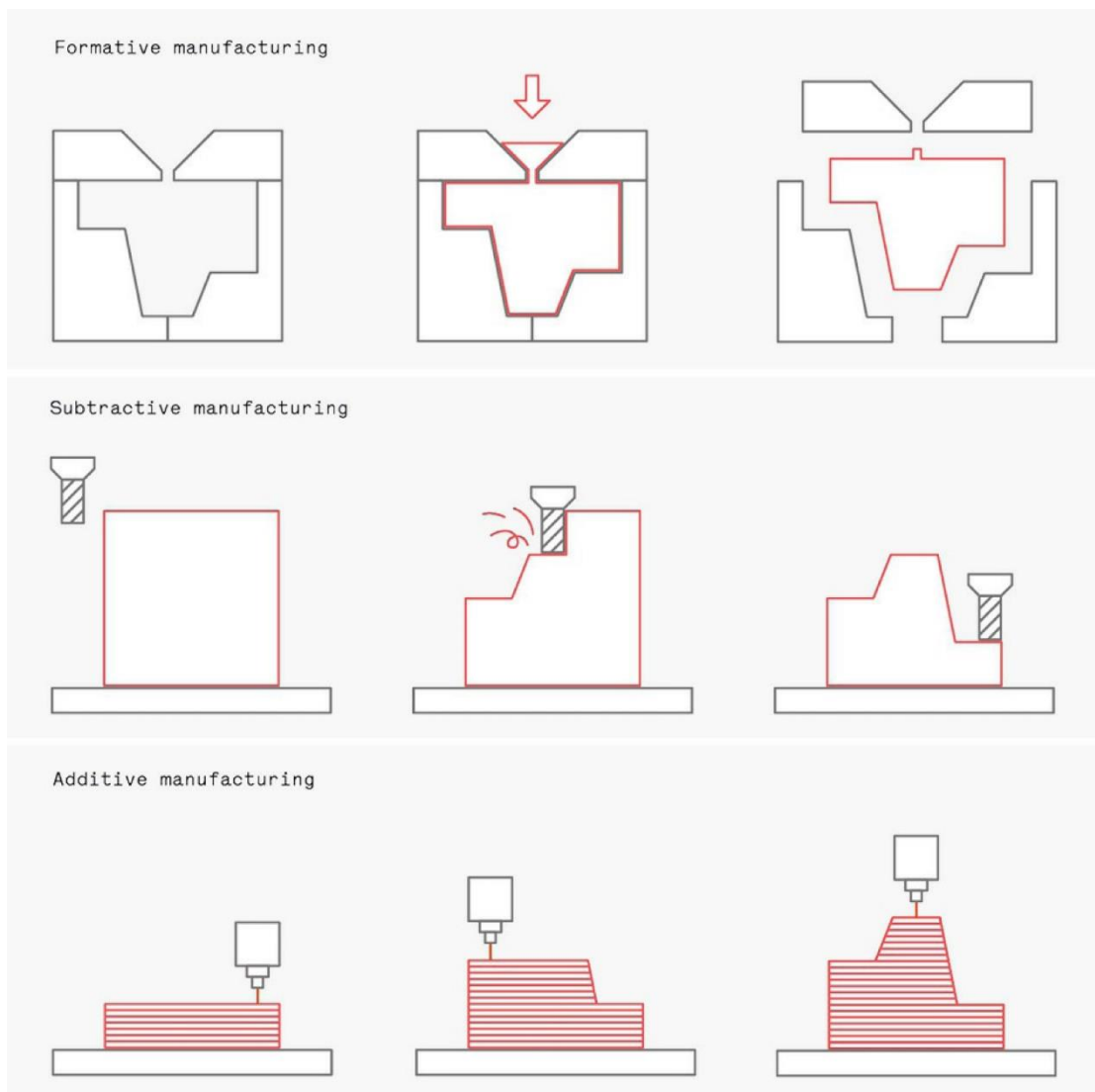


Fig. 2.1. A schematic diagram illustrating how formative manufacturing (top), subtractive manufacturing (centre) and additive manufacturing (bottom) processes produce parts (Redwood et al., 2017)

Additive manufacturing is less wasteful (concerning both replacement machine tools and construction material) than subtractive manufacturing methods. In addition, it allows for the integration of more complicated internal undercuts and substructures. AM is not only much more flexible compared to traditional casting or formative moulding processes, but it may also be more cost-effective in cases where the time expenditure and high financial required for the creation of tools and moulds for formative manufacturing outweigh the relatively higher production expenses per part in additive manufacturing.

### **2.2. Additive manufacturing (3D printing)**

Three-dimensional printing (3D printing) is an additive manufacturing technique that enables the manufacture of products, without the necessity for moulds, by layering materials (adding successive layers) on top of each other using computer-aided design (CAD) (Zhang and Xiao, 2018). It is also recognised as additive processes, additive fabrication, direct digital manufacturing, solid freeform fabrication, layer manufacturing, rapid manufacturing, and rapid prototyping (ASTM International, 2013). This technology was first invented in 1986 by Charles Hull in a technique famed as SLA (stereolithography) (Jacobs, 1992). That was followed by numerous novel AM processes development over the span of more than 20 years include, among others, LOM (laminated objective manufacturing) (Feygin and Hsieh, 1991), FDM (fused deposition modelling) (Comb et al., 1994), SLS (selective laser sintering) (Beaman et al., 1997), and LMD (laser metal deposition) (Mazumder et al., 1999). These AM technologies were applied in various fields such as construction, automotive, aerospace, dentistry, biomedical, surgery, drug delivery, tissue engineering, digital art, consumer products (e.g., jewellery and electrical components) and food industry, etc. Mass-customized items, prototypes, and replacement components are just a few of the small production run uses of 3D printing. These are usually high-value products customized or manufactured in tiny numbers (Berman, 2012).

Freedom of design, ability to fabricate complex structures, waste (chips) minimisation, and the fast prototyping, in addition to the mass customisation, are the main advantages of 3D printing (Ngo et al., 2018). However, time consumption and high costs of the additive manufacturing process remain primary obstacles that impede mass production. Void formation results in porosity which can reduce the mechanical performance of the printed products (Bourell et al., 2017).

A large number of polymers, metals, ceramics, and composites are among the materials that can be utilized for 3D printing in the form of powder, filaments, wire, inks, paste, and sheets. The major polymers used in composites' 3D printing are PLA (polylactic acid) and ABS (acrylonitrile butadiene styrene). Advanced alloys and metals are often used in the aerospace industry because conventional processes are time-consuming, costly, and demanding. Ceramics are usually used in scaffolds' 3D printing, while concrete is the most common material used in buildings' additive manufacturing (Guo and Leu, 2013).

#### *2.2.1. 3D printing methods*

ASTM International has defined seven categories for additive manufacturing technologies in their standard terminology of additive manufacturing processes (ASTM International, 2013). These categories are, material extrusion, directed energy deposition, binder jetting, material jetting, sheet lamination, vat photopolymerization, and powder bed fusion. The first step in 3D printing is to create a meshed 3D computer model, which may be produced using obtained image data or structures designed in CAD software. Typically, a file in STL format (surface tessellation language) is prepared. The mesh data will then be sliced into a 2D layer build file and transmitted

to the 3D printer (Wang et al., 2017). Although a coffee cup is not very sophisticated, it is a useful object for demonstrating the fundamentals of the 3D printing process (Fig. 2.2).

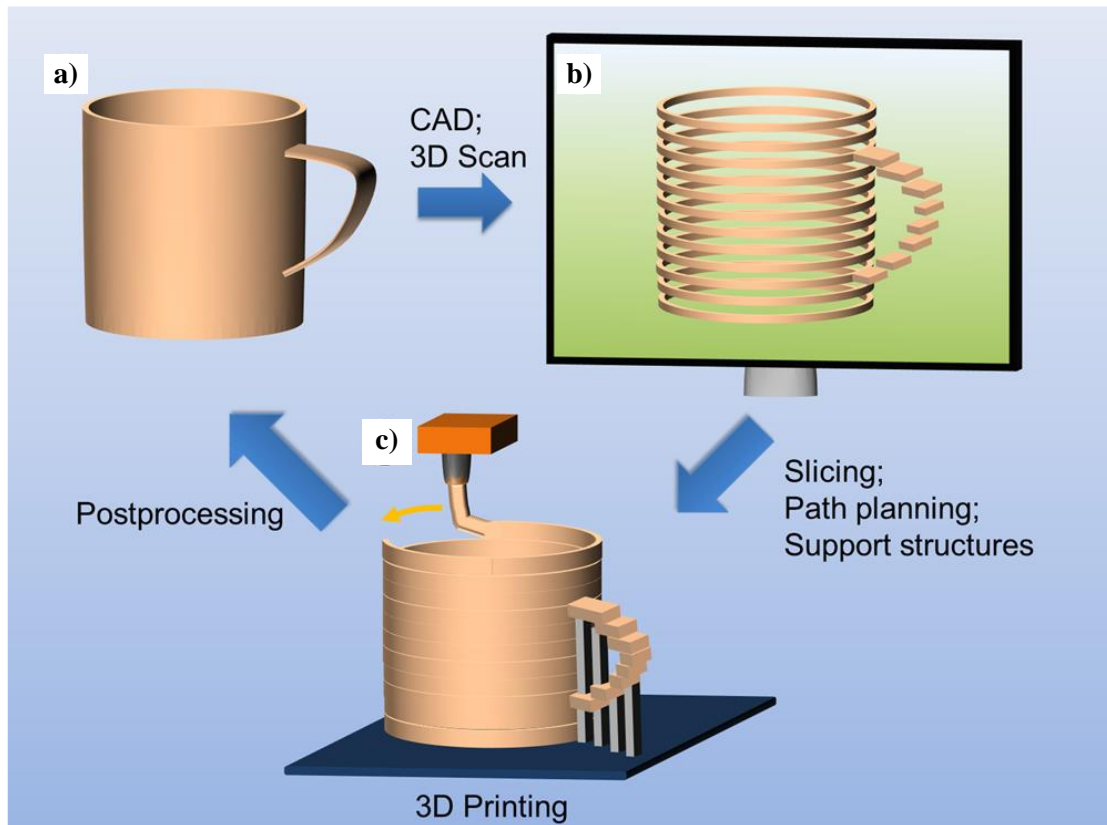


Fig. 2.2. Basic additive manufacturing principles: a) creation of a product idea that is converted into digital data using CAD, b) slicing the virtual model into 2D layers data, and c) the additive manufacturing of product or model (Ligon et al., 2017)

### *Material extrusion*

The material is delivered selectively via a moveable nozzle or aperture with this AM method. This includes FDM (fused deposition modelling), also known as FFF (fused filament fabrication), and 3D dispensing (alias 3D micro extrusion and 3D plotting). The most widely used AM technique is FDM. Its printers utilise thermoplastic polymer filaments' controlled extrusion to 3D construct layers (as a layer by layer) of materials that subsequently solidify into finished components (N. Turner et al., 2014), as displayed in Fig. 2.3. Because of their low melting temperatures, thermoplastics such as ABS (acrylonitrile butadiene styrene) (Sun et al., 2008; Tran et al., 2017), PLA (polylactic acid) (Tymrak et al., 2014), and PC (polycarbonate) (Garcia et al., 2012) are widely utilized. In literature, among other FDM 3D printing process parameters; building orientation (Keleş et al., 2017), raster direction angle (Cantrell et al., 2017), layer thickness (Ayrimis et al., 2019), infill percentage (Aw et al., 2018), raster pattern (Akhoundi and Behraves, 2019), air gaps (Rezayat et al., 2015), number of perimeters (contour width) (Lanzotti et al., 2015), extrusion temperature (Guessasma et al., 2019), and deposition speed (Laureto and Pearce, 2018) were the most examined ones.

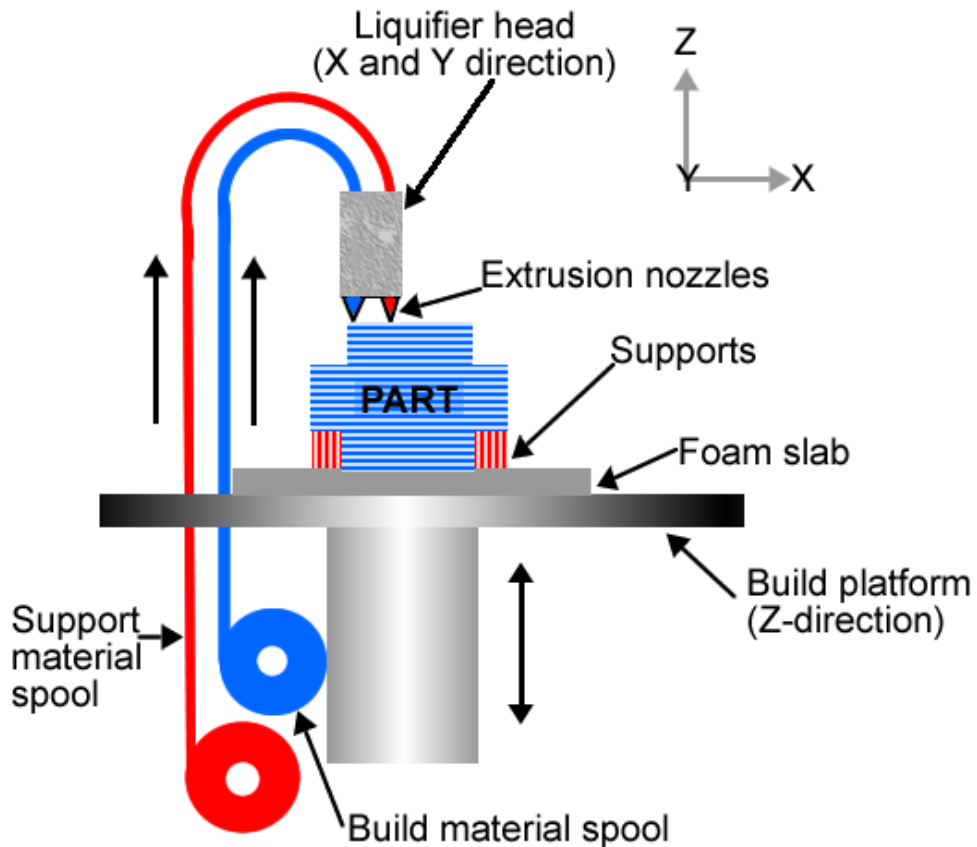


Fig. 2.3. Schematic representation of fused deposition modelling (Sidambe, 2014)

### *Powder bed fusion*

PBF (powder bed fusion) is an AM method that uses thin layers of ultra-fine powders which need to be spread and packed tightly on a platform. An electron beam or a laser provides the thermal energy required in this method, which selectively fuses portions of a powder bed. SLS (selective laser sintering), EBM (electron beam machining), and SLM (selective laser melting) fall into this category (Lee et al., 2017). In all PBF processes, powders are rolled over a build chamber, and a binder or laser is directed into the powder to produce the component layer. The next layer is created by rolling new powder over the previous layer's top, and the procedure is repeated until the component is finished. The loose powder that is not built into the element stays in the chamber to help support the part while being manufactured (Cao et al., 2015). In the SLS process (Fig. 2.4), the sintering refers to the deposited powder layer's irradiation by scanning of a selective laser beam which sinters the powder locally in corresponding to the predefined component slice geometry (Shahzad et al., 2014). SLS can be used with a wide range of polymers, alloy powders, and metals, but SLM can only be employed with particular metals like aluminium and steel (Yap et al., 2015). EBM techniques need a vacuum, yet they may be utilized to make functional items out of metals and alloys.

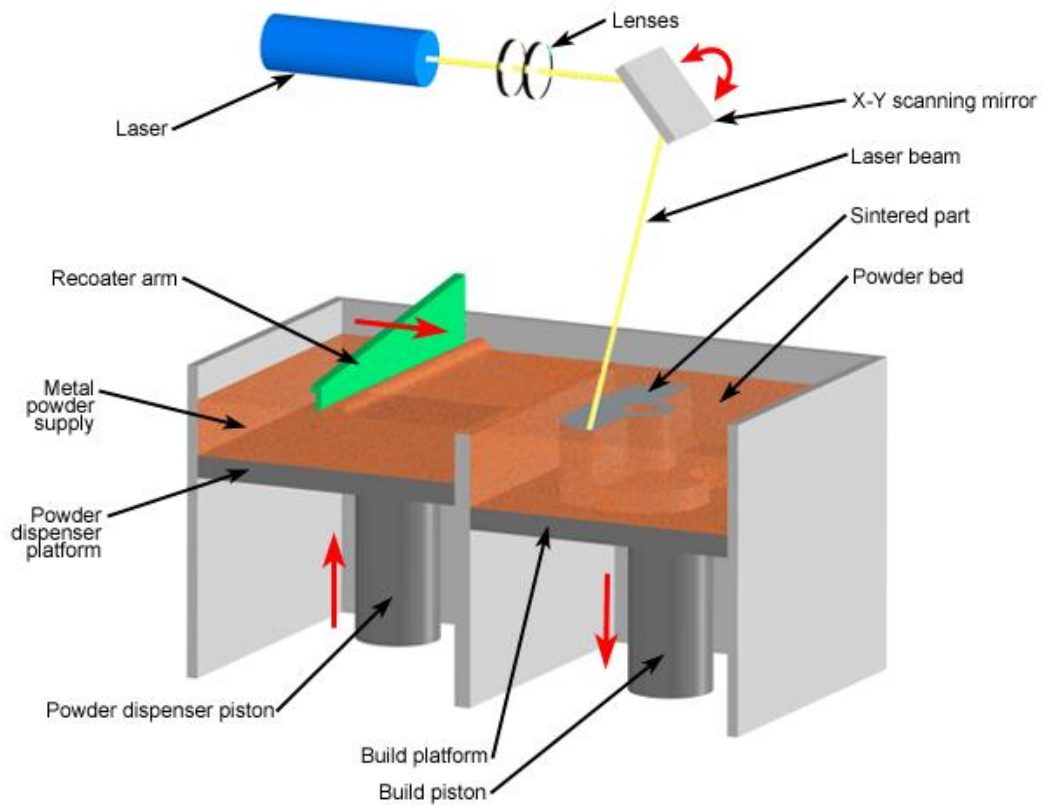


Fig. 2.4. Schematic of SLS (selective laser sintering) (Singh et al., 2017)

*Vat photopolymerization*

In this additive manufacturing process, the liquid photopolymer is put in a vat and cured selectively by polymerization that is light-activated. This category encompasses lithography-based AM techniques such as DLP (digital light processing) and SLA (stereolithography). Photopolymers that are able to be cured using a UV laser are used in SLA. A UV laser is directed into the resin reservoir in a specific path, and the photocurable resin polymerizes, forming a 2D patterned layer. The platform lowers after each layer is treated, and another uncured resin's layer will be available to be patterned (Melchels et al., 2010), as shown in Fig. 2.5.

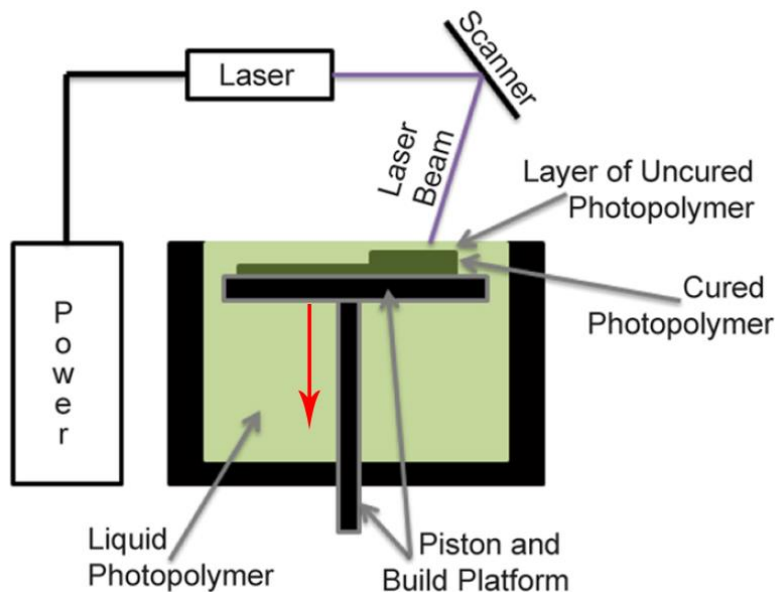


Fig. 2.5. Schematic illustration of a typical SLA setup (Bhushan and Caspers, 2017)

SLA produces high-quality items with a precise resolution of 10  $\mu\text{m}$ . The primary factors governing the height of each layer are the light source's energy and exposure (Cho et al., 2005). SLA may be effectively utilized for the AM of complicated nanocomposites (Manapat et al., 2017).

When compared to SLA, DLP uses a nearly identical way of creating components. The key distinction is that DLP employs a screen for a digital light projector that simultaneously flashes a single image, at once, for each layer (for larger parts, it can be multiple flashes). DLP can perform quicker prints than SLA since a complete layer is exposed to the light at once instead of tracing the area of the cross-section with a point of the laser (Redwood et al., 2017), as illustrated in Fig. 2.6.

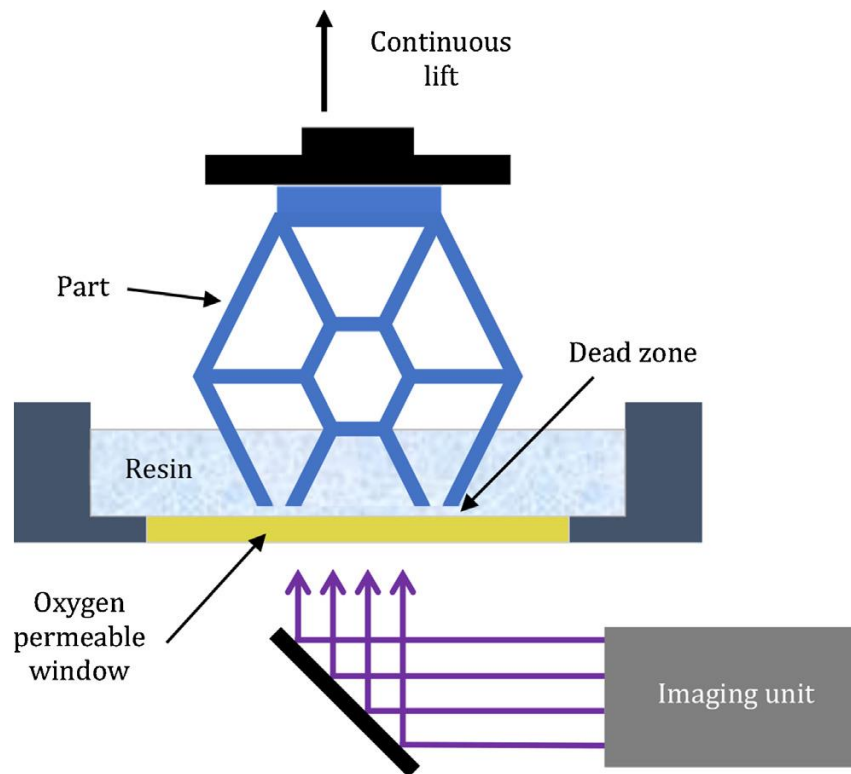


Fig. 2.6. Schematic of a DLP device that dramatically increases component manufacturing speed by using a continuous instead of a step-by-step construction procedure (Stansbury and Idacavage, 2016)

### *Sheet lamination*

Sheet lamination, also known as LOM (laminated object manufacturing), is an additive manufacturing technique in which material sheets are bonded together to make an object. To construct an item, thin sheets consisting of paper or synthetic polymers are progressively laminated, sliced, and glued together layer by layer.

The adhesive coated material's sheets are supplied with rollers to the construction platform and laminated utilising a heated roller in the first phase of the LOM process (Fig. 2.7). Contours are carved in the second stage as per predefined in the two-dimensional slices obtained from a 3D CAD file. A carbon dioxide laser, or knives, connected to a print head may be used to accomplish cutting. Excess materials are left for support after cutting and may be removed and repurposed when the process is completed (Gibson et al., 2015b). LOM can be employed for a wide range of materials such as metal-filled tapes, polymer composites, paper and ceramics (Sun et al., 2010).

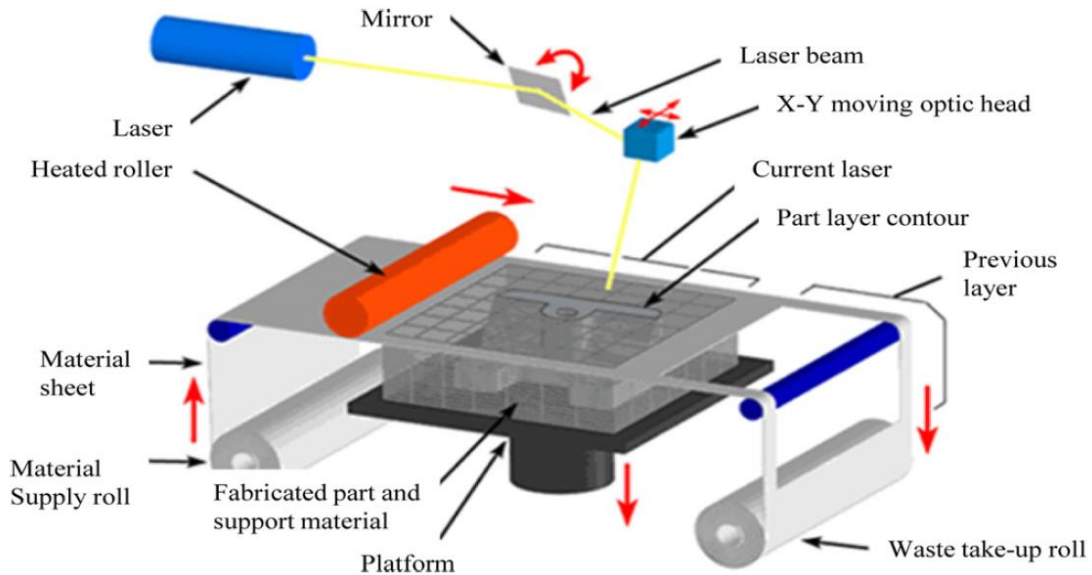


Fig. 2.7. Schematic representation of laminated object manufacturing (Ahn et al., 2012)

### *Binder jetting*

3DP is a term used to describe the binder jetting process. It utilises two materials: a powder and a binder. Between the powder layers, the binder functions as an adhesive. The binder is normally liquid, whereas the construction material is usually a powder. A print head locomotes horizontally along the machine's x and y axes, depositing alternating layers of construction and binding materials. The build platform with the item being printed on it is lowered after each layer (Fig. 2.8). The item being printed is self-supported inside the powder bed due to the binding mechanism and is removed from the powder that is unbound after being done (Srinivas and Babu, 2017). The quantity of deposited binder may be changed to control the interior structure. Binder viscosity, powder size, binder-powder interaction, and binder deposition speed are all factors that influence the quality of finished products (Utela et al., 2008).

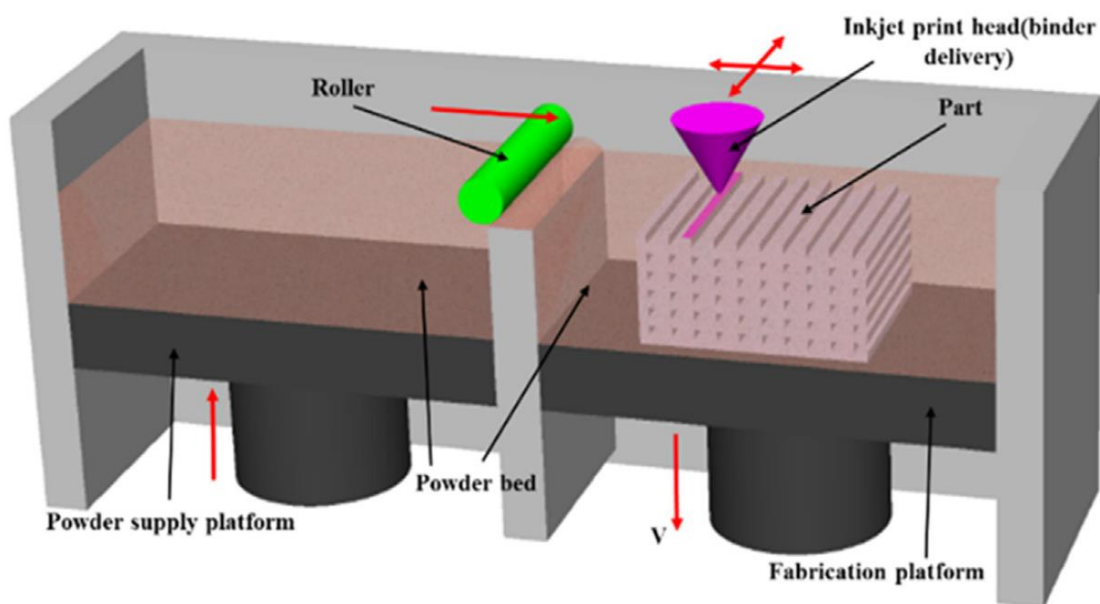


Fig. 2.8. Schematic diagram of binder jetting (3DP) setup (Wang et al., 2017)



### *Directed energy deposition*

DED (directed energy deposition) can have other names such as DMD (direct metal deposition), LMD (laser metal deposition), DLD (direct laser deposition), LENS (laser engineered net shaping), EBAM (electron beam AM), WAAM (wire + arc AM), laser cladding, and laser deposition welding (Kumar et al., 2013). DED is accomplished by focusing a laser beam on a workpiece, resulting in a melt pool. Metallic powder is introduced into the melt pool at the same time. To make a single layer, single weld tracks are put adjacent to each other. By stacking numerous layers on top of each other, a near net form geometry may be created (Schmidt et al., 2017). As an illustration of the DED method, Fig. 2.9 depicts the work principle. Depending on the process settings (powder feed rate, velocity, and laser power), layer thickness might range from 0.1 mm to some millimetres (Ocylok et al., 2014). DED is generally characterized by high speeds (for WAAM, reach up to 10 kg/h) and extremely large work envelopes (for commercial printers, as much as 6 m × 1.4 m × 1.4 m) (Williams et al., 2016). However, when compared to SLM or SLS, it has lower surface quality, lower accuracy (0.25 mm), and can produce less complex parts (Gibson et al., 2015a).

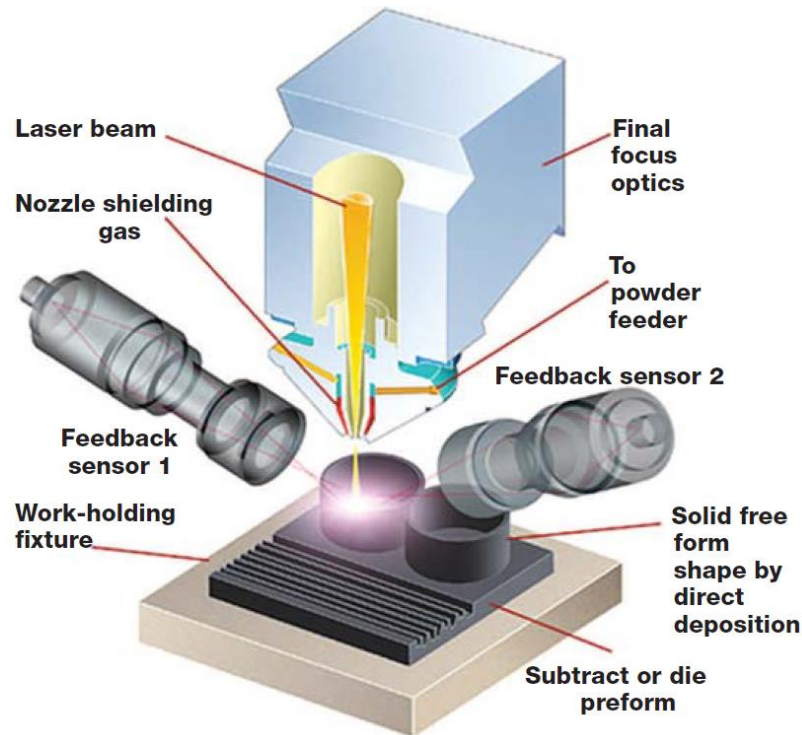


Fig. 2.9. Exemplary sketch of the laser energy deposition process (Dutta et al., 2011)

### *Material jetting*

Poly-jet is a name used to describe this process (Bhushan and Caspers, 2017). Material jetting works in a similar way as a two-dimensional ink jet printer to build items (Fig. 2.10). In this technique, droplets of liquid photopolymer (build material) are deposited selectively from a nozzle moving horizontally over the construct platform, activated by UV lamps to harden or cure the layer. Then subsequent layers are added in the same way. In case of DOD (drop on demand) method, the printer head contains two inkjets and deposits two kinds of materials: the construction material and the support material (Fahad et al., 2013). There are a restricted number of materials that may be used. Because of their viscous nature and propensity to produce droplets, polymers and waxes are ideal and often employed. Inks may incorporate nano-fillers such as clay or silica that are small enough to fit inside a jetted ink droplet and give both viscosity control (while

deposition) and strengthened mechanical qualities in the finished product (Sugavaneswaran and Arumaikkannu, 2015). The parts produced are high resolution, have moderate surface quality (Srinivas and Babu, 2017), and have mechanical qualities that are reliable. The build orientation, on the other hand, may have a substantial impact on elastic modulus and fracture stress. However, tensile strength is relatively unaffected by print direction (Cazón et al., 2014). Material jetting is one of few technologies that can print in both multi-materials and full colour.

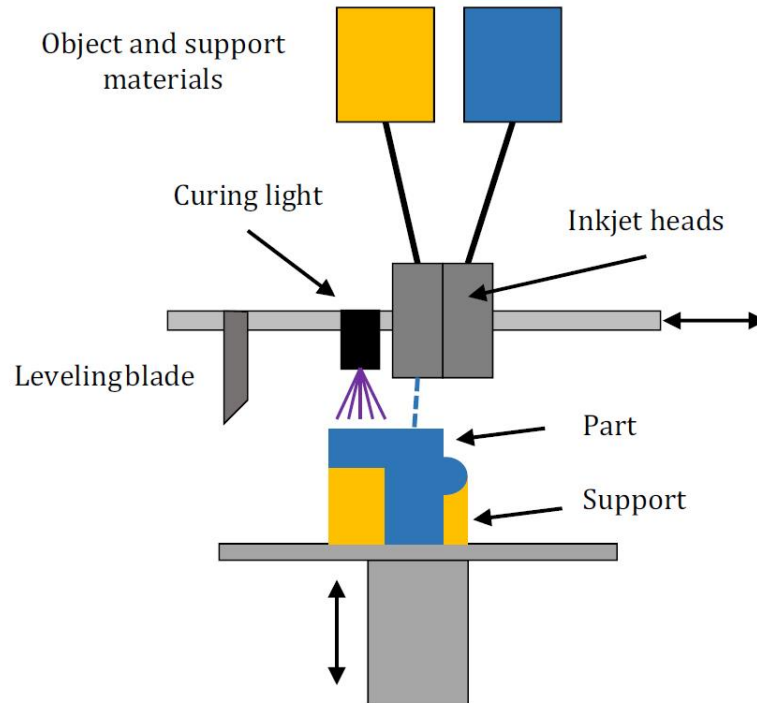


Fig. 2.10. Schematic illustration of material jetting printer (Stansbury and Idacavage, 2016)

### 2.2.2. Materials for 3D printing

Many additive manufacturing technologies (e.g., SLA, FDM, 3DP, SLS) have been developed to create components from a variety of materials (any material where the melting temperature lower than 300-400 °C, even for those unexpected materials to be printed like: wax, sugar, chocolate and so on). AM was applied in its early development to produce plastic prototypes. However, following years of research and development, AM technology has advanced to the point where it can now produce sophisticated net-shaped or almost net-shaped components in materials that may be utilized directly as functional parts, such as ceramics, composites, and metals. The various types of materials are discussed in the following sections, with more details for polymers and its composites as the main materials for this research.

#### *Metals and alloys*

PBF (powder bed fusion) and DED (direct energy deposition) are the two most used methods for printing metals. Numerous metallic materials such as titanium and its alloys, stainless and tool steels, nickel-based alloys, and some aluminium alloys can be manufactured employing PBF-based AM methods (Herzog et al., 2016). PBF technologies have the ability to produce components with robust mechanical characteristics and complicated forms with high precision ( $\pm 0.02$  mm). However, because of their modest speed (with four lasers, up to 105 cm<sup>3</sup>/h), these methods are primarily employed for tiny components. Different types of lasers, such as femtosecond lasers, are also being studied (Nie et al., 2015). AM has been optimized for steel alloys, titanium and its alloys, a few aluminium alloys, some cobalt-based, nickel, and magnesium alloys (Herzog et al., 2016). Titanium and its alloys, in particular, are high-performance materials

that are widely employed in a variety of sectors (Wang et al., 2018). They have significant machining costs and a longer lead time due to the use of traditional production processes. As a result, AM may provide considerable financial benefits by constructing more complex structures at cheaper prices and less waste. Ti (Attar et al., 2014) and Ti6Al4V (Vaithilingam et al., 2015) have been carefully investigated and are now being employed in commercial aerospace and healthcare applications.

### *Ceramics*

High accuracy appears in the process of layer-by-layer printing, however the main challenging that still facing the 3D printing of ceramics are the limited selection of materials. AM has become a critical technique for producing improved ceramics for tissue engineering and biomaterials, such as bone and tooth scaffolds (Wen et al., 2017). Inkjet (suspension), paste extrusion, stereolithography, and powder bed fusion are the most common techniques for 3D printing ceramics. Inkjet is considered the most common technology for producing dense ceramic pieces that do not mostly need post-treatment (Travitzky et al., 2014). Furthermore, 3D printing offers the benefit of allowing the porosity of lattices to be controlled (Withell et al., 2011). Various techniques and materials have been researched in order to improve the mechanical qualities of 3D-printed ceramic lattices as compared to conventional methods. Moreover, a honeycomb construction with an elevated specific strength can be generated with better dimensional stability and no cracking by refining the ink-printing process in terms of homogeneity and rheology of the ceramic suspension and optimized sintering (Maurath and Willenbacher, 2017).

### *Composites*

A pre-prepared combination of appropriate materials, such as filaments in mixed materials for FDM, a composite powder bed for SLM, SLS, and 3DP, a mixture of liquid resin (photocurable) with particulates for SLA, or a combined laminate for LOM, are commonly used to produce composites utilizing AM methods. Polymer matrix, metal matrix, ceramic matrix, and particle and fibre reinforced composites are all composite materials that can be made using AM technology. (Kumar and Kruth, 2010).

Fibre-reinforced composites are one of the most significant uniform composite groups for industrial applications. SLS/SLM has been used to process metal-metal composites (such as stainless steel-Cu and Fe-Cu), ceramic-ceramic composites (such as Si-SiC), and metal-ceramic composites (such as WC-Cu, WC-CuFeCo, WC-Co, TiC-Ni/Co/Mo, TiB<sub>2</sub>-Ni, and ZrB<sub>2</sub>-Cu) (Kumar and Kruth, 2010). LENS was used to create porous Ti6Al4V implants with a Co-Cr-Mo coating that is functionally graded (Bandyopadhyay et al., 2009). These implants have a high hardness level and a good interaction among the bone cell and the other components. Further, graded nickel-titanium components have been created from Ti6Al4V to IN 718 utilising LENS (Domack and Baughman, 2005). LENS was also used to create a compositionally graded Ti-TiO<sub>2</sub> structure by utilising various powders transported by non-reactive gases via separate nozzles (Balla et al., 2009). Using a modified FDM method, many ceramic sensors and actuators with unique characteristics have been manufactured (Jafari et al., 2000).

### *Polymers and polymeric composites*

Polymers are the most widely used materials in the 3D printing industry because of their variety and simplicity in adopting various 3D printing techniques. Thermoplastic filaments, resin, powder, and reactive monomers are all forms of polymers used in additive manufacturing (Fig. 2.11). Many industry applications, including architectural, aerospace, toy manufacture, and medical, have been exploring the capacity of using 3D printing of polymers and their composites for several years.

Numerous studies have been conducted in order to resolve the poor mechanical characteristics of 3D-printed polymers, resulting in improved performance of advanced polymer-based composites (Takezawa and Kobashi, 2017).

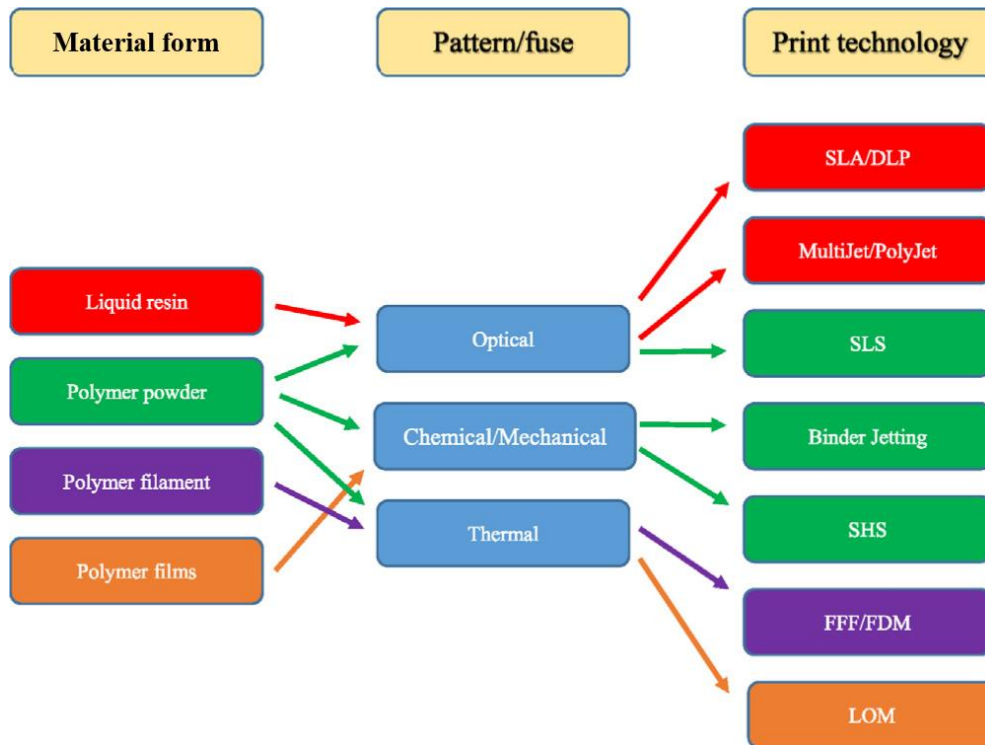


Fig. 2.11. An overview of polymer/monomer materials employed with various layered construction processes in additive manufacturing (Stansbury and Idacavage, 2016)

In stereolithography 3D printing, UV light is used to activate photopolymer resins and thus they are polymerised. Photopolymer-generated prototypes account for roughly half of the 3D printing market in the industry sector. Plastic for SLS (selective laser sintering), on the other hand, is stated to be the second most significant class for 3D printing. Polyamides, polystyrene, and thermoplastic elastomers are examples of SLS polymers (Ligon et al., 2017).

Thermoplastic polymers (e.g. ABS (acrylonitrile-butadiene-styrene copolymers) (Postiglione et al., 2015), PC (polycarbonate) (Yang et al., 2017), and PLA (polylactic acid) (Zhuang et al., 2017)) can be processed by various 3D printing technologies. PLA is ecologically friendly but has low mechanical characteristics, while ABS possesses good mechanical properties but generates a disagreeable odour during manufacturing (Kuo et al., 2016). Although PLA shows some restrictions like low toughness, brittleness, and water sensitivity (Bajpai et al., 2013), however, it has an interesting chemical, mechanical, and physical properties (degradability, high stiffness and tensile strength, and easily processed) (Vidakis et al., 2019). Due to these desirable features, PLA is the most broadly utilized bio-based polymer for numerous applications (such as packaging, automotive, prosthesis fabrication, and electronic industries) since it can effectively substitute petroleum-based polymers (Notta-Cuvier et al., 2014). In addition, it is widely used as a binder for composite materials, here the additive can be bronze, sawdust, ceramic grains, and various metal powders. When compared to injection-moulded PLA, 3D-printed PLA had better mechanical characteristics (Song et al., 2017). Furthermore, the shape memory effect is another spectacular physical property of PLA that several groups recently investigated (Kumar et al., 2020; Ehrmann and Ehrmann, 2021). Besides this, PLA has a comparatively low melting point, between 150-160 °C, hence achieves effortless processability, which also makes it more attractive for the prosumer 3D printer users (Wittbrodt and Pearce, 2015).

## 2. Literature review

The combination of 3D printing with a polymer matrix composite shows considerable potential in terms of industrial production with high functionality and mechanical performance (Alaimo et al., 2017). The limitations of 3D printing fibre reinforced composites were highlighted in a published study (Tekinalp et al., 2014), which also assessed the load-bearing capacity of composite items manufactured from ABS resin feedstock and carbon fibre. 3D-printed scaffolds for the sake of tissue engineering are presently being created using PLA-based composite mixes. By using SEM imaging, researchers were able to demonstrate the existence of interconnected pores inside the PLA-based scaffolds' structure (Senatov et al., 2016). To generate bio-compatible 3D porous scaffolds for diverse tissue engineering implementations, a combination of a bioactive CaP glass and PLA was 3D-printed (Serra et al., 2013). The mechanical characteristics of CNTABS (carbon nanotube reinforced ABS) and short CFABS (carbon fibre reinforced ABS) were further enhanced as well (W. Zhang et al., 2018; Yao et al., 2018).

Table 2.1 lists the many kinds of plastics used in AM, organized by process category and with entries of commercial polymers. Thermosets, amorphous polymers, and semicrystalline polymers are the plastics mentioned. Amorphous polymers are used in material extrusion. The wide viscosity softening temperature range aids in the successful deposit of the plastic bead. Semicrystalline polymers usually soften with a significant change in viscosity over a limited temperature range. While this behaviour is advantageous for plastics' powder bed fusion, material extrusion makes controlling polymer flow properties challenging.

Table 2.1. Popular commercial polymers that are directly processed by AM (Bourell et al., 2017)

	Amorphous	Semi-crystalline	Thermoset	Material extrusion	Vat polymerization	Material jetting	Powder bed fusion
ABS [Acrylonitrile Butadiene Styrene]	X			X			
Polycarbonate	X			X			
PC/ABS Blend	X			X			
PLA [Polylactic Acid]	X			X			
Polyetherimide (PEI)]	X			X			
Acrylics			X		X	X	
Acrylates			X		X	X	
Epoxies			X		X	X	
Polyamide (Nylon) 11 and 12		X					X
Neat		X					X
Glass filled		X					X
Carbon filled		X					X
Metal (Al) filled		X					X
Polymer bound	X	X		X			
Polystyrene	X						X
Polypropylene		X					X
Polyester ("Flex")							X
Polyetheretherkeytone (PEEK)		X		X			X
Thermoplastic polyurethane (Elastomer)				X			X

### 2.2.3. Applications of 3D printing

As AM grew in popularity and the quality of its methods and materials improved, its applications expanded to include prototypes for functional prototyping (functional testing). Parallel to this, the increasing competitiveness of CAD reproduction as well as surface quality has helped the use of additive manufacturing in the rapid tooling (tooling sector), either by direct mould production or combining AM with postprocessing methods (e.g., electro discharge machining or CNC machining) (Chua and Leong, 2014).

Another emerging paradigm of 3D-printed polymer composites use in the bio-medical sector is the bio-fabrication employing live cells for organ and tissue transplantation. Several organs and tissues have already been successfully created (by 3D printing) to satisfy the transplanting functionality requirement, including aortic valves (Duan et al., 2013), vasculatures (Zhao et al., 2012), ears (Kang et al., 2016), constructs of liver tissue (Robbins et al., 2013), and constructs of cartilage (Markstedt et al., 2015).

Ceramic functional components are a burgeoning topic for additive manufacturing since the technology can make complicated parts with feature sizes as small as a millimetre. A researcher developed a set of AM components made of ceramics such as  $ZrO_2$ ,  $Al_2O_3$ , and  $Ca_3(PO_4)_2$ , the latter of which is suitable for the applications of bone tissue engineering (Fisher, 2005).

The majority of aircraft components have complicated geometry that requires a lot of time and money to produce. As a result, 3D printing is an excellent choice for the creation of these components. Most aeronautical components, such as turbine blades and engine exhaust, have been 3D-printed using metal materials up until now (Appleyard, 2015). Aerospace components made of non-metallic materials are also essential. Ceramics, plastics, and composites may be manufactured by stereolithography, FDM methods, and multi-jet printing.

Because AM technology can lower product and manufacturing costs and shorten the cycle of development, the automotive industry has been adopting it as a major tool in designing and developing automotive components. SLM, SLS, and EBM are examples of additive manufacturing processes that have been successfully used to design and build diverse components for car racing.

Attempts to construct 3D structural electronics have recently been made. For example, a DLP printer created a 3D connection for an electrical circuit by using a cross-linked and silver photopolymer (Cooperstein et al., 2015).

In recent years, automated building construction using 3D printing technology has gotten a lot of attention. It has the potential to transform the building sector and make construction on the moon simpler for astronauts (Labeaga-Martínez et al., 2017). It allows for substantial time and personnel savings during construction (Wu et al., 2016).

It is, nevertheless, projected to revolutionize several specialized fields. Therefore, exponential growth is anticipated to be soon. In the literature, cost and speed savings have been expected. Fig. 2.12 shows the production savings (facts and prediction) for AM with metals from 2013 to 2023.

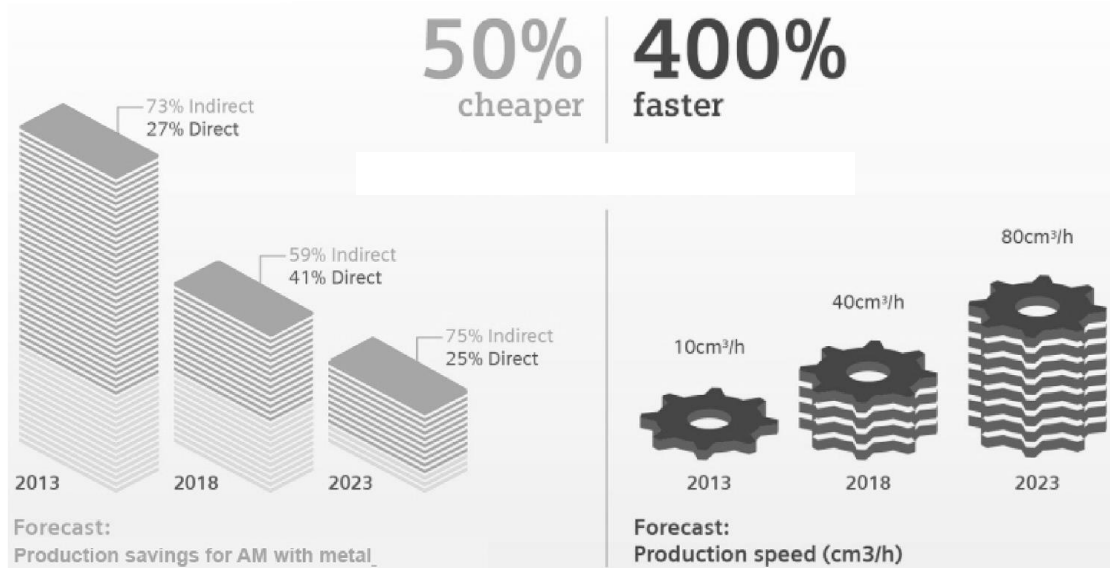


Fig. 2.12. Production savings (facts and forecast) in speed and cost for AM (Attaran, 2017)

### 2.3. Polymers for 3D printing

Polymer is another name for plastic. The term polymer comes from the Greek words *poly*, which means "many", and *meros*, which means "parts" (Ebewele, 2000). The most prevalent kinds of polymers for 3D printing include thermoplastic polymers (e.g., ABS, PC, PA, and PLA), thermosetting powders (e.g., polyamides and polystyrene), and photopolymer resins, as discussed in section (2.2.2.).

The majority of the filaments employed in fused deposition modelling are thermoplastics. Filament manufactured from these thermoplastic polymers can be made in a variety of colours, including glow-in-the-dark and translucent options. The thermoplastics' general rule of thumb states that the better the engineering characteristics, the higher the temperature needed to heat to a malleable condition, and hence the further challenging the material to print. The likelihood of distortion or warping increases when the printing process is performed at higher temperatures, as components cool at a faster pace, creating more severe internal stresses (Hausman and Horne, 2014).

Fig. 2.13 illustrates the most common thermoplastics. The further up the pyramid a thermoplastic is, the higher the printing temperature required, and the engineering properties are even better. ABS and PLA lie near the bottom of the pyramid and are generally considered easy to print with, while thermoplastics like PEEK and PEI offer excellent engineering properties but are generally printed using industrial machines that provide greater control over the print environment.

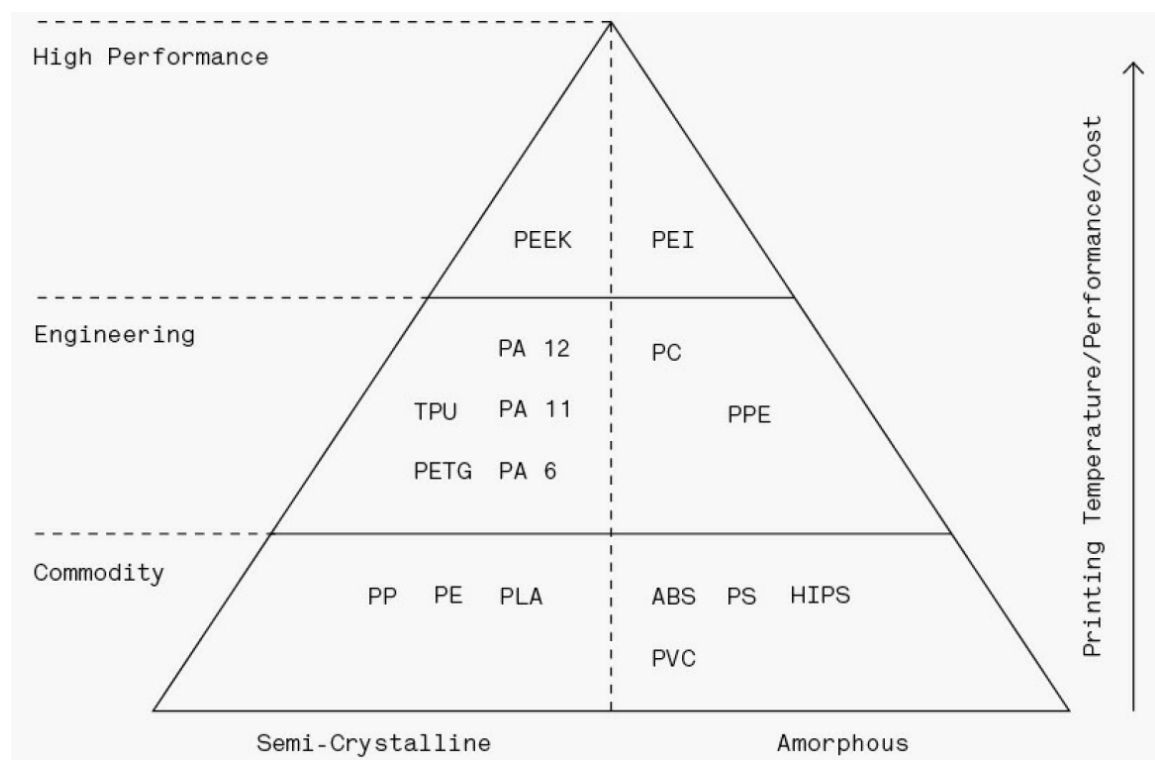


Fig. 2.13. The pyramid of thermoplastic materials (Redwood et al., 2017)

#### 2.3.1. The chemical structure of polymer

Polymers are made up of extremely large molecules (*macromolecules*) that are created by combining tiny molecular substances termed *monomers* in a chemical process. *Polymerization* is the term given to this chemical reaction. Polyethylene, for example, is made from the monomer ethylene (see Fig. 2.14). Ethylene is formed from two carbon atoms connected by a double bond and with the carbon atoms' free valencies saturated by hydrogen. To create polymers, monomers either contain double (or triple) bonds or reactive functional groups whose reaction provides the

essential connections between repeat units (Kumar and Gupta, 2003). The *degree of polymerization* refers to the number of mers (given as  $n$  in Fig. 2.14), or more accurately, the number of mer repeats, in a polymer chain (Ram, 1997). The polymer structure's main feature is that macromolecules are made up of rigid segments that may rotate, allowing molecular chains to be flexible (Myshkin and Kovalev, 2009).

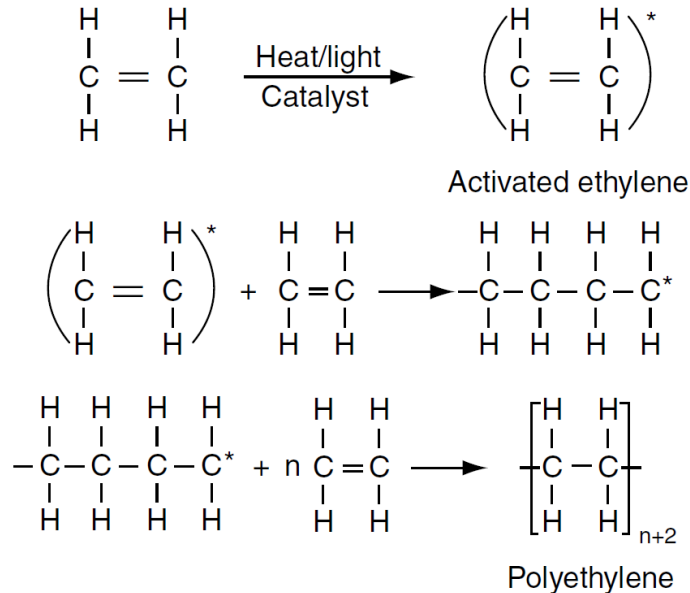


Fig. 2.14. Intermediate steps during the creation of polyethylene (PE) (Chanda and Roy, 2007)

Secondary *Van der Waals* and *ion* bonds link the molecules of a polymer, that are weaker than the covalent bond between molecules (intermolecular covalent connection) (Gustafsson, 2013). As a result, chain molecules may be thought of as the fundamental building blocks of a polymer. Polymers, unlike metals and ceramics, are composed of linear components rather than atoms (point-like particles). Their structure, therefore, is more complex than that of the other materials classes (Roesler et al., 2006). Figure 2.15 depicts an example of a linear polymer chain made up of carbon atoms. Each atom is connected, by a single bond, to two other atoms of carbon along the chain. Hydrogen fills the remaining valencies of the atoms of carbon. To halt the reaction, specific chemicals may be introduced to saturate the radicals' free electrons, thereby stopping the process.

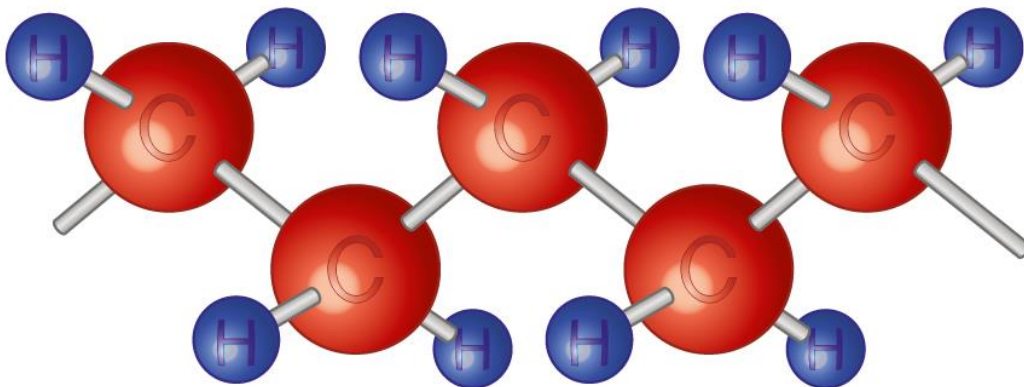


Fig. 2.15. Schematic representation of a polyethylene molecule (Osswald and Menges, 2012)



### 2.3.2. The classifications of engineering plastics

*Thermoplastics*, *thermosets*, and *elastomers* are the three forms of synthetic polymer materials that vary chemically in their molecular arrangement. The primary differences between these three polymers classifications (thermoplastic, thermosetting, and elastomeric) during a cross-linking chain reaction are explained in Fig. 2.16.

#### *Thermoplastics*

They are often referred to as linear polymers since their chains are not cross-linked (they, though, may branch occasionally). This is the reason why they soften when heated while when cooled harden: the secondary bonds that hold the molecules together dissolve, enabling the polymer to flow like a viscous liquid and be created. Some are amorphous, such as polystyrene, while others, such as polyethylene, are somewhat crystalline. As a result, thermoplastics lack a distinct melting point due to their wide variety of packing geometries and molecular weights. The mechanical properties of thermoplastics can retain without degradation even after they are melted and solidified a limited number of times. The colour of thermoplastics, however, can be degraded as the number of recycling increases, impacting their appearance and properties (Crawford, 1998).

#### *Thermosets*

Thermosets are also called thermosetting polymers, duromers, or resins. Epoxy is a thermoset that is often used as an adhesive and as a fibre-glass matrix. Thermosets are formed by combining two materials (a resin and a hardener) that react and solidify at room temperature or when heated. Because the resultant polymer is often intensely cross-linked, thermosets are also known as network polymers. The structure is usually always amorphous because cross-links occur during the polymerization process of the liquid resin with a hardener. The additional secondary bonds are melted when the polymer is reheated, lowering the polymer's modulus. The cross-links, however, prevent viscous flow or true melting; the polymer, therefore, cannot be hot-worked as it turns into rubber. Also, the polymer will degrade if it is heated any longer (Ashby and Jones, 2005).

#### *Elastomers*

Elastomers or rubbers have excellent elastic properties and are nearly linear polymers containing occasional cross-links, the secondary bonds of which have already melted at room temperature. When a force not exceeding their yield strength is released, the cross-links supply the material with the "memory", allowing the polymer to return to its previous form (Meyer and Keurentjes, 2005).

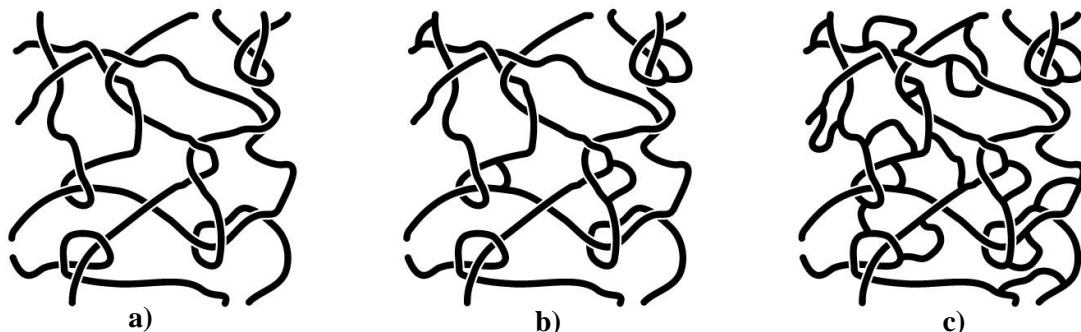


Fig. 2.16. Schematic illustration of the cross-linking of various polymers a) the molecular chains in *thermoplastics* are not cross-linked, b) in *elastomers*, there are a few cross-links between the chains, and c) in *thermosets*, there are numerous cross-links between the chains (Roesler et al., 2006)

## 2.4. Tribology of polymers

The term tribology is derived from the root tribo- (from Greek τρίβος, which means "rubbing") and the suffix -logy (from Greek -λογία, means "the study of"). It was first used in the renowned Jost report of 1966. According to the Jost study, lubrication issues in engineering need an interdisciplinary approach that includes materials and chemistry science, physics, and solid mechanics (Department of Education and Science, 1966).

The science of tribology is concerned with the relative motion of surfaces. Friction, material wear, scraping, and rubbing are all involved. Tribology is defined as the study and technology of surfaces in contact and with a relative motion, in addition to supporting activities that aim to decrease costs associated with friction and wear (Bhushan, 2013a).

Surfaces that look smooth to the naked eye are usually rough when examined under a microscope. When two surfaces are pushed on each other, the actual/real area of contact ( $A_r$ ) differs from the apparent (geometrical) area of contact ( $A_a$ ) since the surfaces are only in touch at tiny areas called junctions, as shown in Fig. 2.17.

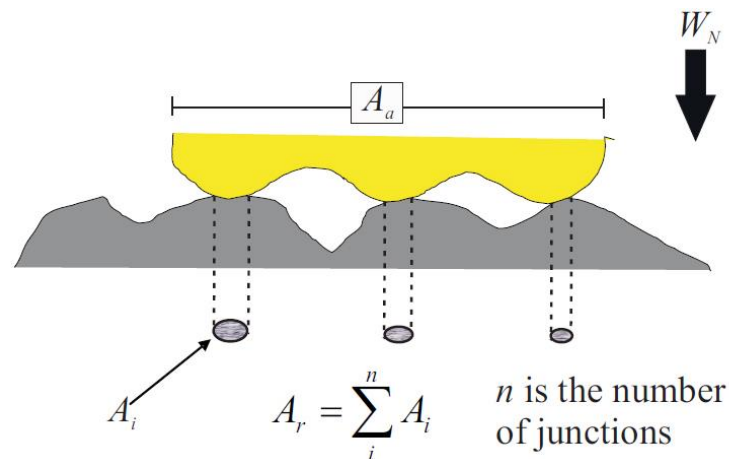


Fig. 2.17. An illustration of the difference between the real ( $A_r$ ) and the apparent area of contact ( $A_a$ ) of two surfaces pushed on each other by a force  $W_N$  (Larsen et al., 2007)

Because most of the effects of wear and friction are unfavourable, such as increased power consumption and causing mechanical failure, it is therefore critical economic relevant. Friction may also generate heat build-up, contributing to component damage owing to thermo-mechanical fatigue. Comprehension of friction is the foremost step toward minimizing it using creative design, low-friction materials, and correct lubricating greases and oils. Friction offers several advantages, including the contact between the tire of a car and the road and also the interaction between the footwear and the floor (Pope, 1996). The tribology study aims to reduce and eliminate losses caused by wear and friction at all levels, including rubbing, polishing, grinding, and cleaning of surfaces.

Polymers are essential in mechanical and materials engineering for a variety of reasons, including their ease of manufacture and cheap unit cost, as well as their potential for outstanding tribological performance in designed forms. Polymers provide several tribological benefits, including a low friction coefficient (relatively), self-lubricating capabilities, chemical resistance to alkalis and acids, and low noise emission (Matthews and Holmberg, 2009). Polymers, on the other hand, have some drawbacks such as visco-elastic and creep behaviour, poor wear resistance, lower ultimate elastic and strength modulus than metals, low limiting temperatures (less than 300 °C, making softening, melting, oxidation, and thermal deterioration easy), and very low thermal conductivities (dissipation of frictional heat is poor). As a result, single-component polymers are often weak

under external strain and fail to fulfil the majority of tribological standards. However, polymers, in composite and hybrid forms, nowadays meet performance requirements for particular applications, frequently outperforming conventional materials like metals and ceramics from a tribological standpoint.

The different chemical structures of polymers, due to polymer's nature (thermoplastic, thermosetting, or elastomer), affect friction and wear. For example, PTFE (polytetrafluoroethylene) is well-known for its ability to produce a transfer film (layer) that lubricates the contact and reduces friction dramatically. Other polymers, e.g., UHDPE (ultra high density polyethylene), on the other hand, do not form a transfer layer while sliding, and as a result, friction is substantially greater (Tabor, 1992).

#### 2.4.1. Friction of polymers

The resistance to motion which happens when one solid body comes into touch with another solid body is known as friction (Brostow et al., 2010). The force of friction is a tangential force that operates in the opposite direction to the motion direction. The friction coefficient is a measurement of how well a surface can resist continuous motion when subjected to normal stress. Thus,  $F/L$  is the coefficient of friction ( $\mu$ ) between two solids, where  $F$  represents the force of friction and  $L$  signifies the load or normal force (normal to the surface). There is a basic law regarding  $\mu$  that is very well followed in this area. According to this law, the coefficient of friction is unaffected by the apparent contact area. This indicates that given the same load ( $L$ ), the friction forces on a small and large block will be the same (Persson, 2000).

Frictional energy is dissipated differently in polymers at the contact region and in the material's bulk (Briscoe and Tabor, 1978). As a result, energy is dissipated in two zones: the interfacial zone and the subsurface (cohesive) zone (shown in Fig. 2.18). As a consequence, the frictional force caused by adhesion equals the resultant of the interfacial zone's "real contact area" (with the counterpart) and the subsurface zone's "shear stress" (Tromborg et al., 2014).

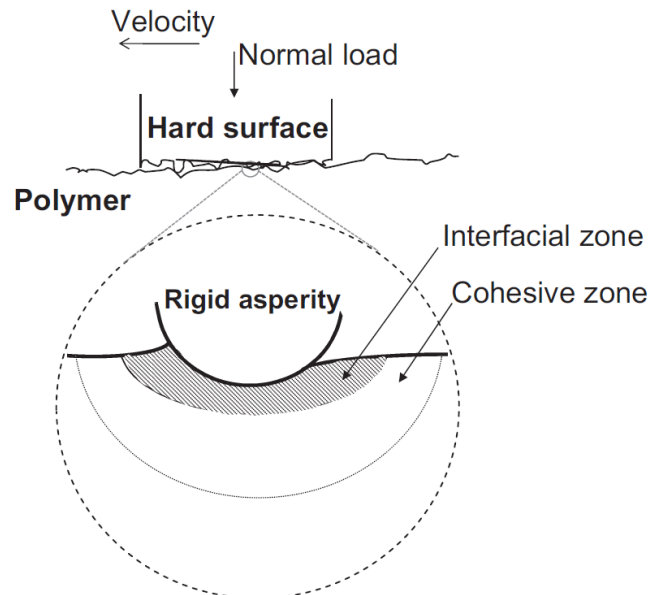


Fig. 2.18. Polymer interface exhibiting cohesive and interfacial zones during the process of friction (Briscoe and Sinha, 2002)

There is another phenomenon that takes place during the friction process which is known as (stick-slip), when jerky motion that can occur while two materials are sliding over each other. The stick-slip motion appears when static friction is considerably greater than dynamic friction and occurs

at extremely low velocities (Biron, 2013). When the contact area expands, the stick process occurs, and the process of slip happens when the frictional force is adequately high to shear the joints (junctions) and plough the material. During the stick, the friction coefficient and contact area are high, but they quickly drop during the slip process. Therefore, increasing the sliding velocity or reducing the normal load leads to a decrease in the stick-slip action (Gustafsson, 2013). Fig. 2.19 depicts the behaviour of typical friction force for the stick-slip motion phenomenon.

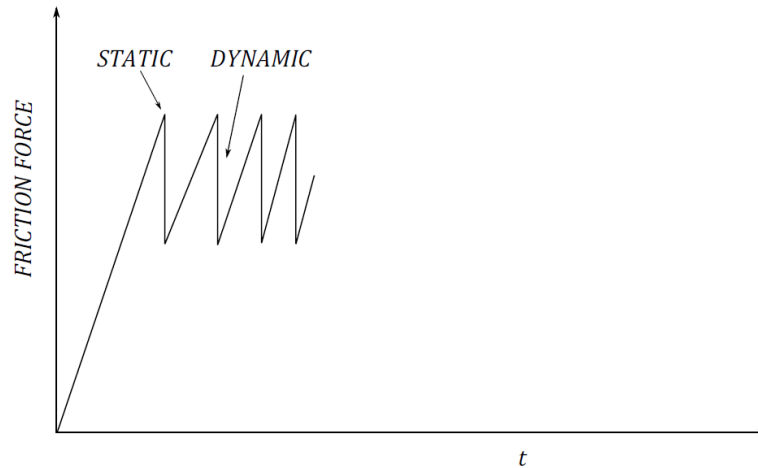


Fig. 2.19. Stick-slip motion phenomenon when friction force as a function of time (Gustafsson, 2013)

The friction force is greatly influenced by the contact load, sliding velocity, as well as temperature. The effects of these factors are not independent; for instance, the contact temperature might change significantly depending on the velocity and contact load, modifying the friction mode. The following sections go through these aspects in detail.

#### *Influence of load on friction*

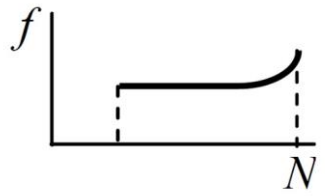
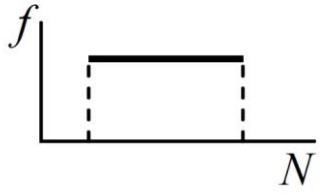
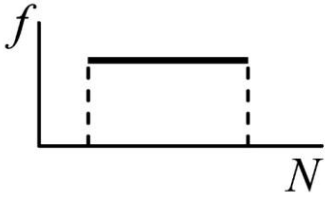
The friction coefficient is in proportion with the normal load, according to the relationship stated in section 2.4.1. However, there has been no consensus on the relationship between normal load and friction until now. Due to the primary challenge faced in comparing research undertaken by various authors, which is the lack of a consistent test procedure, the experimental data available may lead to unpredictable results. This occurs owing to sample dimension variability, the values of sliding velocity and applied load, surface finish, and other factors (Totten and Liang, 2004).

Table 2.2 summarizes some studies' experimental data, which indicates that the first law of friction, which states that frictional force is proportional to the applied load, holds true for particular polymers evaluated under specific circumstances (Myshkin et al., 2005). As an example from these experiments, when a steel ball with a radius of 6.35 mm slides on top of PTFE (polytetrafluoroethylene), PMMA (polymethyl methacrylate), PVC (polyvinylchloride), PE (polyethylene), and Nylon under a load of 10 to 100 N, the coefficient of friction remains almost constant (Shooter and Tabor, 1952). Other authors have obtained similar findings with the same and some further materials, such as PTFE, PMMA, PS (polystyrene), and PE under loads ranging from 10 up to 40 N (Shooter & Thomas, 1949), also PTFE, PTFCE (polytrifluorochloroethylene), PVC, PVDC (polyvinylidene chloride), and PE under loads from 2 up to 15 N (Bowers et al., 1953).

Nevertheless, Kalácska (2013) reported that in the case of pure plastic deformation, the coefficient of friction of the molecular component depends only on the hardness of the softer material and the shear strength of the atomic-molecular bond, it is not affected by load and surface roughness. In the case of elastic deformation, however, the actual contact area increases not linearly but

digressively as the load in the normal direction increases. Therefore, the molecular component decreases with increasing load force. However, the deformation component increases progressively under load due to the rapid increase in the groove cross-section. Together, these two effects cause the phenomenon illustrated in Fig. 2.20: with dry friction, the frictional force first decreases with increasing load and then increases after reaching the minimum.

Table 2.2. The load effect on coefficient of friction

Materials experimented	Applied loads (N)	Graphical illustration
Steel–polymer (PTFE, PMMA, PE, PVC, and nylon) (Shooter and Tabor, 1952)	10 – 100	
Steel–polymer (PTFE, PMMA, PE, and PC) (Shooter & Thomas, 1949)	10 – 40	
Steel–polymer (PTFE, PVC, PVDC, PFCE, and PE) (Bowers et al., 1953)	2 – 15	

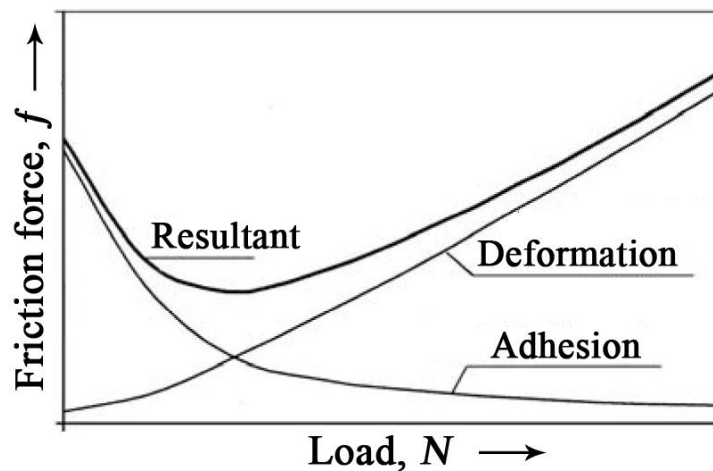


Fig. 2.20. Effect of load on the coefficient of friction (Kalacska, 2013)

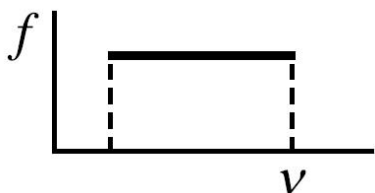
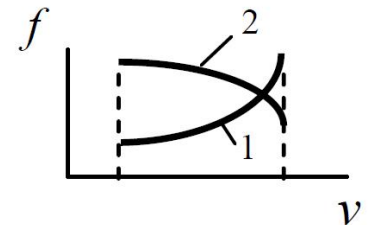
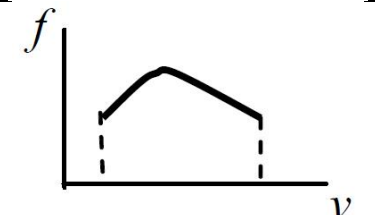
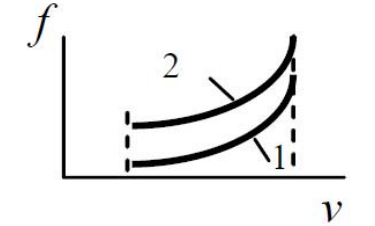
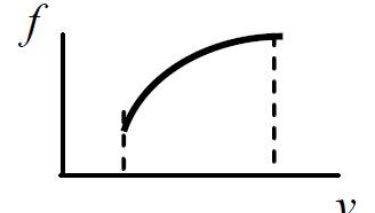
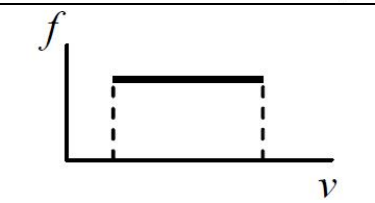
### Sliding velocity effect on friction

The friction force is often assumed to be independent of sliding velocity. However, this claim is only valid for polymers if the temperature at the contact region increases just a little. In addition, variations in the relaxation qualities, as well as physicochemical activity of macromolecules, usually explain a complicated dependency of the friction coefficient on velocity (Myshkin and Kovalev, 2009). It is hard to separate the impacts of temperature and velocity on friction (Totten and Liang, 2004). The only feasible approach for assessing this dependency is to take measurements at various sliding velocities. Table 2.3 shows examples of the influence of sliding

## 2. Literature review

velocity on the coefficient of friction, with a wide range of data produced by the researchers. It may be deduced from the table that the relationship between friction force and sliding velocity is mainly affected by the test temperature. When the polymer sample's test temperature approaches glass transition, the friction coefficient strongly influences velocity. However, at lower temperatures, the coefficient of friction is almost independent of velocity (Vinogradov et al., 1970).

Table 2.3. The impact of sliding velocity on the coefficient of friction (Myshkin et al., 2005)

Materials experimented	Sliding velocities (cm/s)	Graphical illustration
Steel–polymer (PTFE, PMMA, PE, and PC)	0.01 – 1.0	
Polymer–polymer (nylon (1), and PC (2))	4 – 183	
Steel–polymer (PETF)	$10^{-5}$ – 10	
Steel–polymer (PTFE (1), and nylon (2))	0.1 – 10	
Steel–polymer (PTFE)	1.1 – 180	
Polymer–polymer (fibres)	1.5	

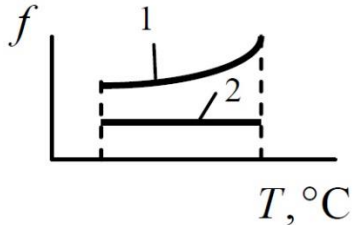
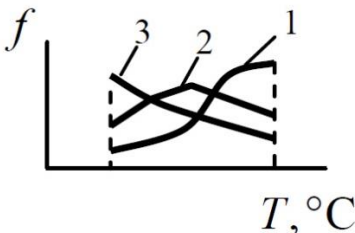
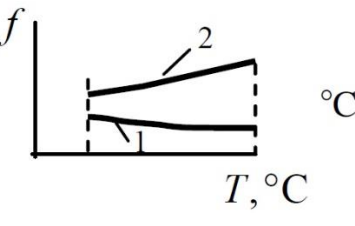
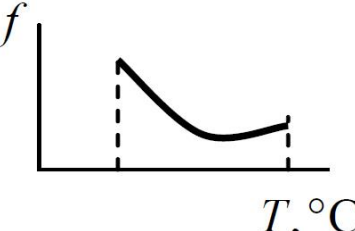
The viscous resistance, in the contact zone, rises with increasing velocity in the low velocities range. The flow becomes abnormally viscous, when high contact pressure, resulting in a rapid increase in viscosity as the velocity increases (Flom & Porile, 1955). As a result, friction force must grow as velocity increases. On the other hand, elastic behaviour dominates in the contact

zone at high velocities. Consequently, the friction force varies very minimally depending on velocity or decreases with velocity (Tanaka, 1984). It is also worth noting that the contact period at high velocity is short, resulting in a further reduction in friction force. All of the foregoing components compete with one another in the velocities' intermediate range, and a maximum arises in the curve of friction force-sliding velocity, the location of which relies on the relaxation characteristics of the polymer (Fort, 1962).

#### *Temperature impact on friction*

The temperature of the sliding process and the material's nature have significant effects (Bartenev and Lavrentev, 1981). Polymers are highly sensitive to frictional heating since they are viscoelastic materials. The material's deformation on real contact sites causes heat generation during friction, as is well known. The creation and disruption of adhesive bonds provide another source of heat. However, these activities are almost certainly energetically incompatible, and the energy difference might result in heat generation or absorption.

Table 2.4. The influence of temperature on the coefficient of friction (Myshkin et al., 2005)

Materials experimented	Test temperature (°C)	Graphical illustration
Steel-polymer (PS (1), and PTFE (2))	20 – 80	
Steel-polymer (PCTFE (1, 2), and PP (3)) $v = 3.5 \times 10^{-5}$ cm/s (1), and $v = 3.5 \times 10^{-2}$ m/s (2, 3)	-50 up to +150	
Steel-polymer (PE (1), and PTFE (2))	-40 up to +20	
Steel-rubber	20 - 200	

It is often thought that the mechanical properties of polymers evaluated at different temperatures may be used to account for the influence of temperature on friction. For certain polymers, a

connection of the friction coefficient with hardness and shear strength has been found, which supports this hypothesis (Ludema and Tabor, 1966). Only when the temperature does not influence adhesion, such a correlation is valid (King and Tabor, 1953). Table 2.4 shows the results of tests for various combinations of materials as a function of temperature. For different materials, the coefficient of friction revealed a tendency to both rise and decrease. The temperature dependency increases, in general, when a polymer is heated nearly to the temperature of glass transition ( $T_g$ ).

#### 2.4.2. Wear of polymers

Wear is defined as the gradual loss of material from a body's operational surface as a consequence of relative motion on the surface (Yamaguchi, 1990). Unlike friction, which results in energy losses, wear results in material losses (Cirino et al., 1988). Mechanical stresses, chemical reactions, and temperature cause changes in the surface layer. Polymers are especially susceptible to these variables owing to their unique structure and mechanical behaviour (Myshkin et al., 2005). Adhesion, abrasion, and fatigue are the three main mechanisms of polymers' wear (Bahadur, 2000). However, there are some other mechanisms of wear, including erosive, transfer, fretting, tribochemical, delamination, etc (Briscoe and Sinha, 2002). The issue stems from the fact that these various mechanisms are often intertwined, making it difficult to distinguish between the harm produced by each.

The capacity of polymers (particularly thermoplastics) to produce transfer films while sliding on steel counterfaces is an important tribological phenomenon (Bahadur, 2000), which is illustrated in Fig. 2.21. Shear occurs between the transfer film (or inside the transfer film) and the polymer rather than between the steel and the bulk polymer when such a transfer layer is present. As a result, the transfer film serves as a protective spacer, between the sliding surfaces, and the film characteristics become the determining factor for wear and friction. Under specific circumstances, PTFE and HDPE are recognized for their capacity to form thin (transfer films), with extremely low friction coefficient values. In addition, an ideal intermediate roughness of counterface is often reported concerning the transfer film development and stability (Wieleba, 2002). A very smooth counterface may lead to poor film stability owing to the lack of mechanical interlocking (i.e., the polymeric material trapped between asperities and in fissures in the steel surface). In contrast, a very rough counterface may be challenging to cover, resulting in an inhomogeneous film.

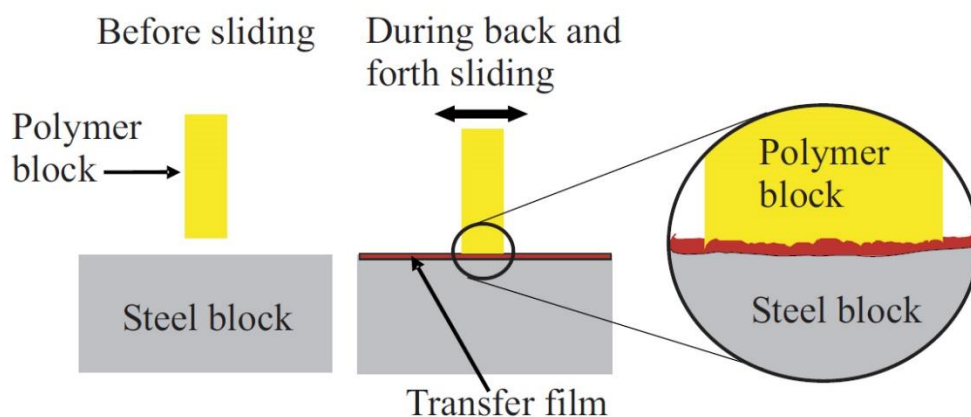


Fig. 2.21. Transfer film appearance when a polymer block slides against a steel counterpart (Larsen et al., 2007)

It should be referred that, similar to friction, the type of polymer (amorphous, semi-crystalline, elastomer) has a significant impact on polymer wear. Properties like tensile strength, elastic modulus, and elongation percentage at failure (toughness) are particularly important since they vary dramatically from one kind of polymer to another (Briscoe and Sinha, 2013). In the following



sections, the primary mechanisms of polymer wear (abrasion, adhesion, and fatigue) are briefly discussed.

### *Abrasive wear*

For polymers, abrasive wear is particularly interesting. When a hard-rough surface (such as a counterface) slip on a substantially softer surface (i.e., polymer), abrasive wear occurs. When roughness is the determining characteristic of friction, this kind of wear takes place. In this situation, harsh asperities partly penetrate the softer surface, causing a groove to form when sliding, resulting in material loss (Myshkin and Kovalev, 2009). Abrasive wear may also happen if hard particles (abrasives) are trapped between two soft surfaces (see Fig. 2.22).

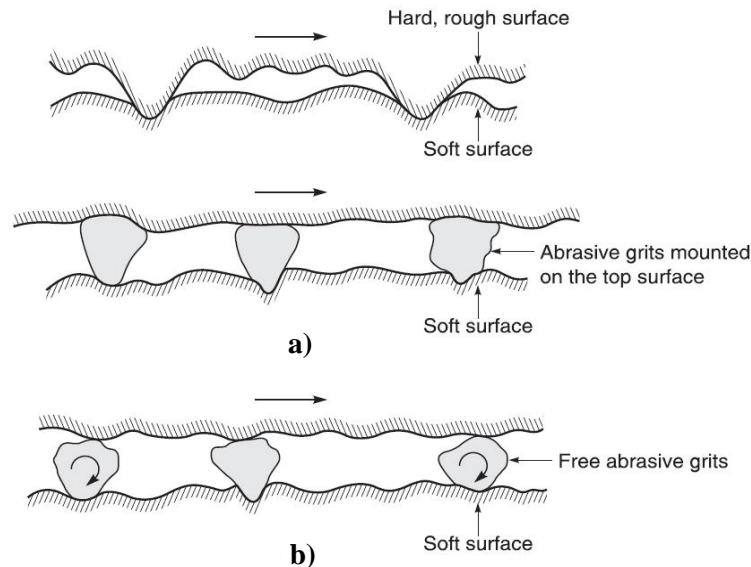


Fig. 2.22. Diagrams depict a) a rough-hard surface or a surface containing abrasive grits moving on another surface (softer), and b) free abrasive grits stuck between two surfaces, at least one of which is softer compared to the abrasive grits (Bhushan, 2013b)

### *Adhesive wear*

Adhesive wear, the most prevalent kind of dry wear, is often experienced by polymers. Adhesive wear occurs when a polymer slides over a dissimilar surface, such as metal, and adhesive bonds develop between the contacting components. High local pressure is applied between the surface of the polymer and the counterface during repeated sliding, inducing plastic deformation and the creation of an adhesive junction. As the motion persists, these junctions continue to form and rupture (as illustrated in Fig. 2.23). The following consequences are often associated with strong adhesion between the sliding surfaces' contacting asperities: frictional force is grown, and the surface's material may be removed to produce transfer layers or wear particles (Myshkin and Kovalev, 2018). As a result, some of the worn material is transferred to the counterface forming a transfer film, while another portion is removed from the zone of friction as wear debris. Also, adhesive wear is affected by the hardness and surface roughness: low-hardness surfaces have more adhesion. Further, Van der Waals forces are thought to have an important influence on polymer adhesion (Stachowiak and Batchelor, 2005).

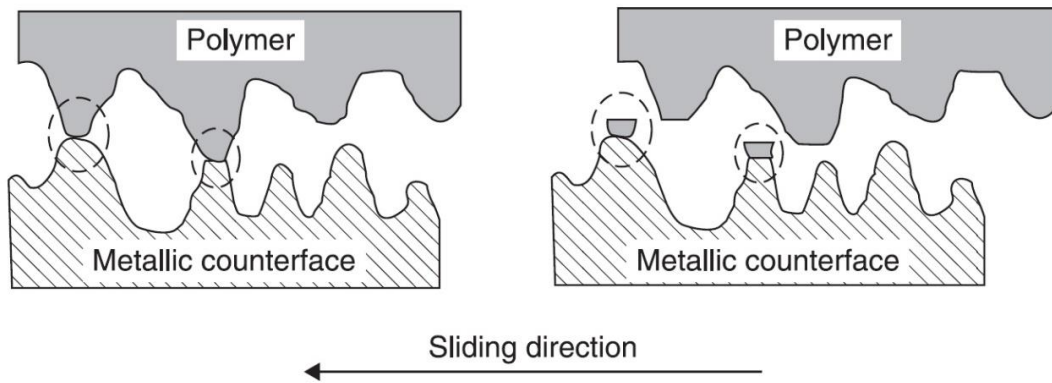


Fig. 2.23. Schematic representation of the adhesive junction (Abdelbary, 2014)

### *Fatigue wear*

When asperities are repeatedly stressed during sliding and rolling motions, fatigue wear may result (as illustrated in Fig. 2.24). This happens during friction, and the process accompanies almost all wear modes. Generation of surface or subsurface cracks, as well as delamination, may result from these fluctuating stresses. The wear debris is created by the formation and junction of microscopic cracks on the surface of polymer that are perpendicular to the direction of sliding. The material's new surface is subjected to the same cyclic stress, resulting in a progressive process and fast flaking off of fragments (P. Suh, 1973). The sort of stress cycle engaged in a fatigue process is determined by the concerned polymer's mechanical characteristics. When a counterface is smooth, fatigue wear develops after prolonged friction, which may be crucial in case of the absence of adhesive wear. The primary source of fatigue cracks initiation, owing to stress concentration, is surface and subsurface defects. Surface markings, scratches, dents, cracks, pits, cavities, impurities, and voids in the subsurface area are examples of defects forms. Surface and subsurface cracks emerge and propagate gradually, link together, and meet on the surface as a result of repeated stress until wear debris is separated after a particular number of stress cycles (Abdelbary, 2014).

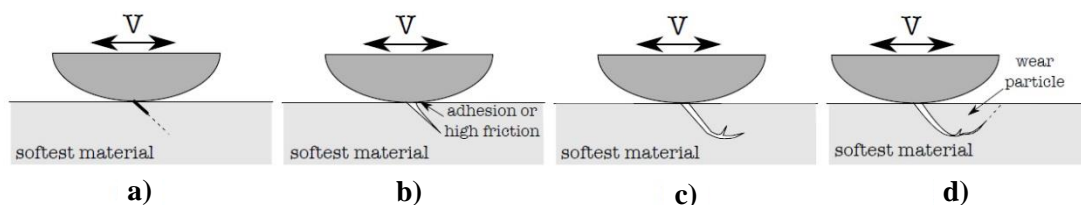


Fig. 2.24. Schematic illustration of fatigue wear initiation and propagation a) crack initiation, b) elementary crack propagation, c) initiation of secondary crack, and d) propagation of secondary crack and wear particle formation (Smerdova, 2012)

## **2.5. Tribology of 3D-printed polymers**

The tribology is essential in enhancing the reliability of materials and any mechanical components (Nirmal et al., 2015). In terms of tribological applications, polymeric products are becoming more favourable due to its unique properties, such as self-lubrication, corrosion resistance, and vibration damping ability (Briscoe and Sinha, 2013). Despite the fact that the mechanical properties of 3D-printed polymers are already studied extensively in the previous researches (as mentioned in section 2.2.2.). However, polymers' tribological properties in 3D-printed mode have not been sufficiently investigated. Sood et al. (2012) determined the relationship between process parameter settings and wear for ABS polymer using FDM printing technology. Five process parameters were considered: layer thickness, raster angle, orientation, air gap, and raster width. They have stated

that the wear of 3D-printed ABS parts is a complex phenomenon that might create cracks within surface regions and remove material because of scratching and fatigue. These consequences occur due to the formation and rupture of interfacial adhesive bonds. The effect of different parameters and their interactions could be described to some extent but challenging to assign specific reasons. Ertane et al. (2018) reviewed the tribological properties of FDM 3D-printed PLA reinforced by biocarbon. Abrasive and fatigue wear mechanisms have been observed during the tribology testing. They revealed that when the total mass volume contains 30% carbon, wear decreases significantly. As the fluctuations reduce in the coefficient of friction values, which settled at approximately 0.5.

Furthermore, numerous studies have shown promising tribological characteristics when graphene is incorporated in polymers as a composite (Min et al., 2020). Bustillos et al. (2017) integrated graphene in polylactic acid (PLA) to develop graphene/PLA composite. The original PLA and the obtained graphene/PLA filaments were then used for the fabricate of specimens by FDM 3D printing to examine the wear-resistant behaviours. The tribological features of PLA and graphene/PLA composites were assessed by a ball-on-disk wear rig tester. It was observed that wear resistance increased by 14% in graphene/PLA than in PLA. However, the microstructure of printed graphene/PLA composite exhibited a higher degree of inherent porosity than PLA because of the porous structure of the received filament. In a recent study (Arif et al., 2020), poly(ether ether ketone) (PEEK) polymer was reinforced with graphene nanoplatelets (GNP) and carbon nanotubes (CNT) to assess the multifunctional performance (including the wear) of the earned composites. The testing samples were produced utilizing the fused filament fabrication (FFF) printing technique. The friction coefficient resultant through fretting wear tests revealed a decrease by 56% and 67% for 3 wt.% GNP and 1 wt.% CNT loaded PEEK nanocomposites, respectively. This reduction is attributed to the decreased hardness and increased porosity. Yang et al. (2020) presented an innovative method to develop functionalized graphene oxide (LFG)/PEEK composites through melt blending to improve the mechanical and tribological performance. LFG amounts of 0.1, 0.3, 0.5, 0.7, and 1.0 wt.% were loaded to the PEEK matrix, and it was found that LFG had substantial interface adhesion. Next, the acquired composites were additively manufactured by fused deposition modelling technology. The results showed that the impact and tensile strength of composite with LFG amount of 0.1 wt.% are 20.5% and 5.7% higher than that of original PEEK, respectively. Moreover, 0.5 wt.% LFG composite offered great wear and friction performance with specific wear rate and coefficient of friction 18.3% and 27.3% lower than that of neat PEEK, respectively.

Although these studies have been published, there is still a big shortage in describing the impact of 3D printing process parameters on the tribological properties (in terms of friction and wear) of polymers, i.e., thermoplastics and thermosets, and their composites. Also, the tribological performance of 3D-printed objects was examined on limited systems/models for tribology testing, and there is no data yet concerning some remaining methods (e.g., cylinder-on-plate tribometer). This suggests that these unexplored concerns should be investigated in order to enrich science by filling in the gaps in this white spot's data.

### 2.6. Summary of literature review

Information about three wide topics which are, additive manufacturing (3D printing), polymers with its classifications, and the tribology science of the plastic materials have been reviewed in this chapter. The main seven categories of 3D printing (*material extrusion, vat photopolymerization, powder bed fusion, sheet lamination, directed energy deposition, binder jetting, and material jetting*) are discussed for a variety of materials (include: *metals, polymers,*

*ceramics*, and *composites*) in diverse states of matter (*filaments*, *powder*, *inks*, *paste*, and *sheets*). Types of polymers with its chemical structure as well as the classifications of engineering plastics (*thermoplastics*, *thermosets*, and *elastomers*) have been highlighted, with illustrating the most common polymers that are suitable to be utilised in the 3D printing technologies. Furthermore, the tribology of polymers involving the genres of wear modes (*abrasive*, *adhesive*, and *fatigue*) and the factors that considerably affect the friction force (*sliding velocity*, *contact load*, and *temperature*) in addition to some other related phenomena (*stick-slip* and *transfer film*) are described. Finally, the latest investigations on the tribology of 3D-printed polymers were briefly reviewed in order to point out the knowledge gap.

According to the literature on the subjects discussed above, plastics sparked extensive attention in the mid-twentieth century because of their structural characteristics, unique mechanical behaviour, and substantial ability to modify the properties of polymer. As a result, extensive scientific research over many years contributed to developing the field of contemporary engineering in which plastics may be used as tribological materials. It is worth mentioning that the number of publications in the field of polymers' 3D printing and its applications have been increased dramatically day by day starting from the year 2010, which indicates the timeliness of the topic. However, it is evident from the literature that there is a gap in the knowledge on the tribological properties of 3D-printed structures. Therefore, the study of 3D printing polymers' tribology seems vital to understanding the impact of 3D-printed surfaces and structures on the tribological behaviour of polymers and polymer composites. It is also essential to find the effect of 3D printing conditions on the intrinsic physical and chemical polymer properties and polymer structure. This will open up a slew of new possibilities for plastics applications. The research, therefore, in their tribological and mechanical behaviour would be a challenging and productive area of science and technology.

### 3. MATERIALS AND METHODS

This chapter presents the materials, equipment, procedures, and processes employed in the current research. It also includes the experimental measurements' scientific methods and the test systems' description to accomplish the set research aims.

#### 3.1. Design of experiment

In the current research, two different 3D printing techniques have been utilized which are FDM and DLP. Thermoplastics in a form of filament are printed by FDM, while DLP uses thermosetting (resin) for producing the parts. For each 3D printing method, two types of materials were examined either neat (pure) or composite polymer. Each individual material was employed to fabricate the required specimens with different print parameters for various tests. These specimens were subjected mainly to tribological and mechanical testing. However, investigating the hardness, surface roughness, surface energy, and morphological characteristics was an inevitable task. The procedure and sequence of experiments carried out in this study are displayed in a flowchart in Fig. 3.1. The experimental work was conducted primarily at Szent Istvan Campus, MATE University, Hungary, in the laboratories of additive manufacturing, mechanical testing, and tribology. The following sections outline the procedure applied concerning the preparation of materials, 3D printing of specimens, post processing, and performing tribological and other tests for each inspected material and method, separately.

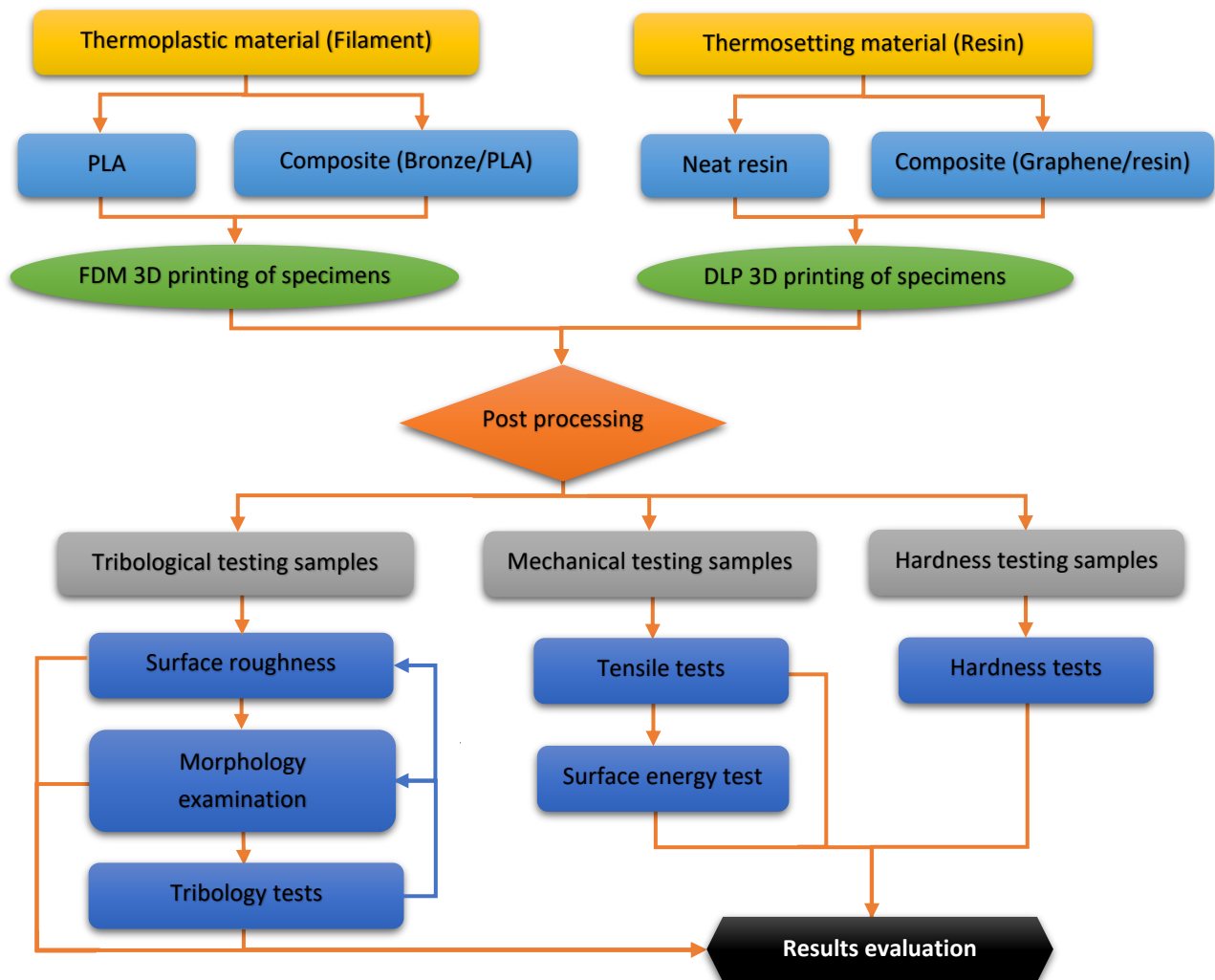


Fig. 3.1. Flowchart for the steps of the experiments

### 3.2. The 3D printing technologies

The printed test pieces were manufactured using two different 3D printers work according to the fused deposition modelling (FDM) and digital light processing (DLP) technologies. The models of the used 3D printers are WANHAO Duplicator 6 for the FDM and WANHAO D7 for the DLP, which are exhibited in Fig. 3.2a and Fig. 3.2b, respectively. Both 3D printing machines were supplied by the WANHAO 3D PRINTER company (WANHAO 3D PRINTER, 2016, 2018).

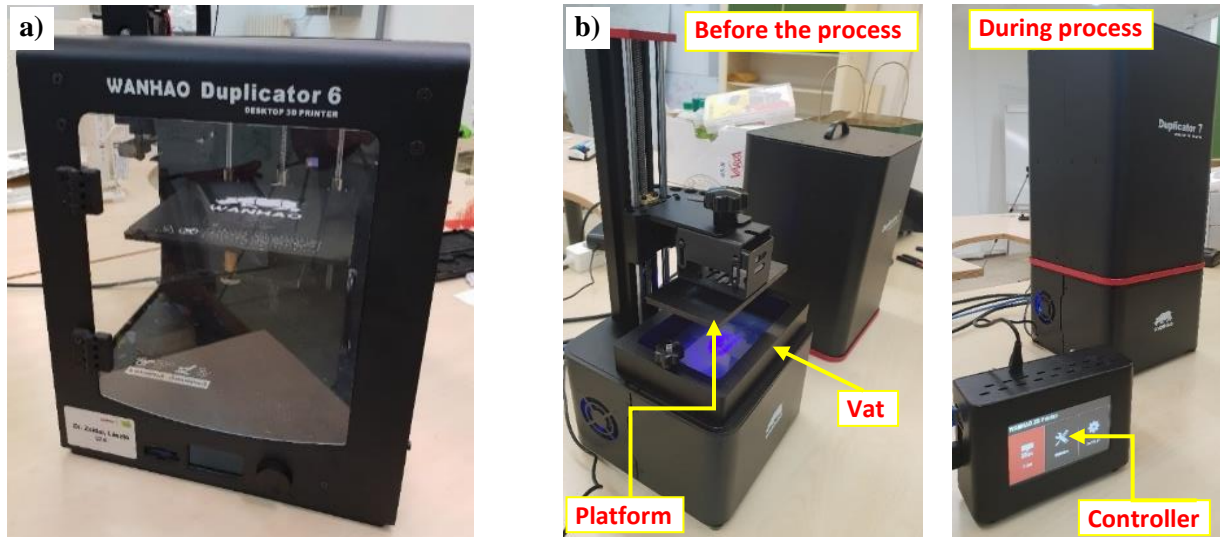


Fig. 3.2. The 3D printers employed, a) FDM 3D printer WANHAO Duplicator 6, and b) DLP 3D printer WANHAO D7

For the FDM 3D printer WANHAO Duplicator 6, the G-Code of the 3D model can be incorporated directly from the SD card. The model can be designed using any CAD software such as Solid work or AutoCAD. The file must be saved as ".stl" format due to its compatibility with most slicing programs. The FDM printing technology utilises the materials in a filament form (thermoplastics). Regarding the DLP 3D printer WANHAO D7, all parameters and commands could be given from a supplement controller supplied with the printer (shown in Fig. 3.2b-right). The format ".cws" is the file extension that can be recognisable by the controller. The model file can be uploaded to the controller using a pen drive. The material that employed for the DLP printing is the so-called resin (thermosetting) which is a chemical liquid curable by light. The technical specifications of both 3D printers (FDM WANHAO Duplicator 6 and DLP WANHAO D7) are listed in Appendix A3.

### 3.3. Manufacturing of 3D-printed specimens

As mentioned in section 3.1., two types of polymer materials were examined, neat and composite, for each 3D printing method. The following sections describe the details of producing the 3D-printed specimens for each material and technique used. Illustrations of all 3D printing parameters examined throughout the experiments versus the tests carried out and materials used are presented in Table 3.1.

#### 3.3.1. PLA filaments printed by FDM technique

PLA filaments with a diameter of 1.75 mm were provided from a commercial 3D printing filament manufacturer. The test specimens were printed on a commercial WANHAO Duplicator 6 desktop using the PLA filaments in the following colours: white, grey, and black. These filaments were employed to fabricate samples for the tribological and mechanical tests with different printing conditions. A printer nozzle diameter of 0.4 mm was utilized. The printing temperature and build

### 3. Materials and methods

platform temperature during the process were maintained at 195 °C and 60 °C, respectively. The print speed, fill percentage, and the number of perimeters were set as 60 mm/s, 100%, and 2 outlines, consecutively. Ultimaker Cura 4.3 software was utilized to slice the 3D model (STL file), control the 3D printing process parameters, and export the G-code file, which is compatible with the 3D printer.

The tribological test pieces were produced at three print orientations, which were Horizontal, 45° angle, and Vertical (see the illustration in Table 3.1a, and the real printed samples in Fig. 3.3a) with a layer thickness of 0.2 mm and 45/135° raster direction angle. The PLA filament colour exhibited an influence on the mechanical properties according to a published study (Wittbrodt and Pearce, 2015). Therefore, the reason for the use of filaments with different colours in the current work was to simulate the assessment of the anisotropic tribological characteristics of PLA material for 3D printing.

During the fabrication of the tensile test specimens, the filament used is only white coloured PLA material. Three different 3D printing factors were examined (print orientation, layer thickness, and raster direction angle). The print orientations were performed at three levels which were Flat, On-edge, and Upright (see Table 3.1b), where the layer thickness and raster direction angle fixed at 0.2 mm and 45/135°, respectively. Whereas these values were considered (0.1 mm, 0.2 mm, and 0.3 mm) and (0/45°, 45/135°, and 45/90°) when the specimens were produced with varying layer thickness and raster direction angle, consecutively, at Flat print orientation, as illustrated in Table 3.1c. The direction angle of the rasters for each new layer generated as alternated, and the angle (0°) counted towards the transverse (cross-section) of the specimen (see Table 3.1c-middle). Thus, when the chosen settings of the raster direction angle are 45/90°, this resulting in rasters of the odd layers printed with 90° angle (parallel to the axis of the applied tensile force) and even layers printed with 45° (see Table 3.1c-top right). A typical photo of the 3D-printed test pieces after production is presented in Fig. 3.3b. The numbers of all printed PLA samples, with different colours and parameters, examined on each test are listed in Table 3.2 (upper part of the table).

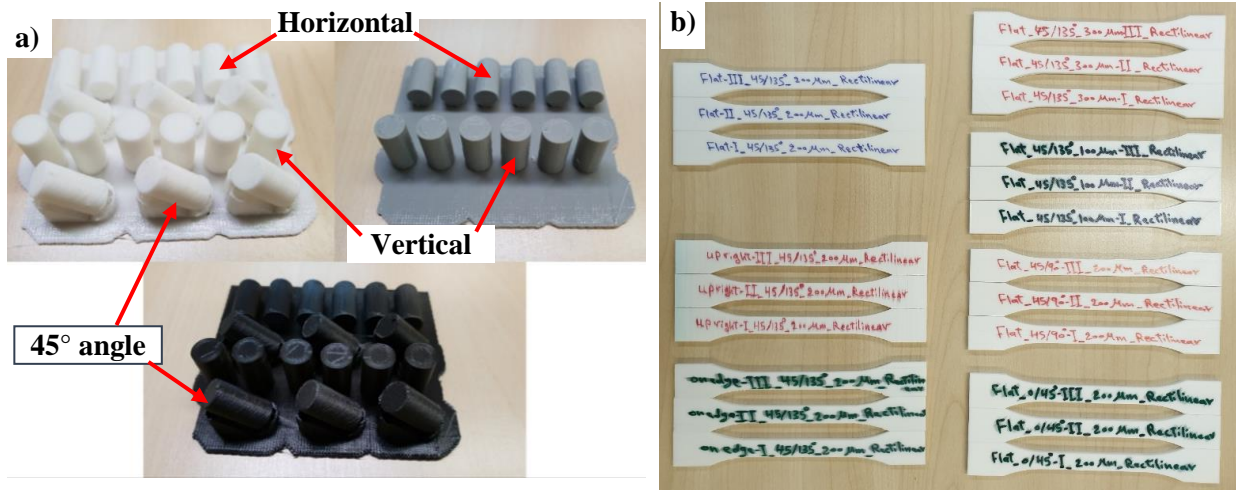


Fig. 3.3. Physical appearance for the 3D-printed PLA samples, a) tribology test pieces manufactured in different orientations, and b) tensile specimens prior to the test

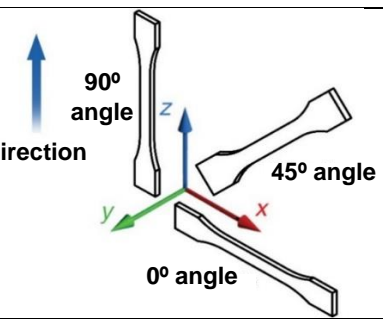
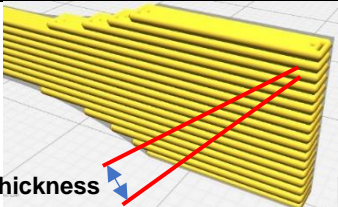
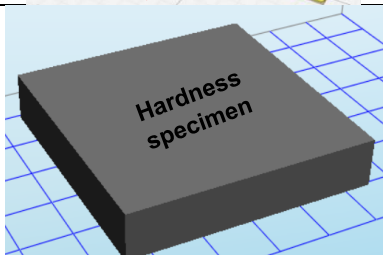
### 3. Materials and methods

Table 3.1. Matrix for the illustrations of 3D printing parameters examined throughout the experiments versus the tests carried out and materials used

Test conducted <span style="color: blue;">➔</span>		Tensile				Tribology				Hardness				Surface roughness				Surface structure				Surface energy					
		PLA	Bronze/PLA	Resin	Graphene/resin	PLA	Bronze/PLA	Resin	Graphene/resin	PLA	Bronze/PLA	Resin	Graphene/resin	PLA	Bronze/PLA	Resin	Graphene/resin	PLA	Bronze/PLA	Resin	Graphene/resin	PLA	Bronze/PLA	Resin	Graphene/resin		
Material <span style="color: blue;">➔</span>																											
3D printing parameter <span style="color: blue;">⬇</span>																											
a)		○	○	○	○	●	●	●	●	○	○	○	○	●	○	●	●	●	●	○	○	○	○	○	○	○	○
b)		●	●	○	○	○	○	○	○	●	●	○	○	○	○	○	○	○	○	○	●	○	○	○	○	○	○
c)		●	○	○	○	○	○	○	○	○	○	○	○	○	○	○	○	○	○	○	○	○	○	○	○	○	○



### 3. Materials and methods

		Test conducted				Tensile				Tribology				Hardness				Surface roughness				Surface structure				Surface energy							
		Material		3D printing parameter		PLA	Bronze/PLA	Resin	Graphene/resin	PLA	Bronze/PLA	Resin	Graphene/resin	PLA	Bronze/PLA	Resin	Graphene/resin	PLA	Bronze/PLA	Resin	Graphene/resin	PLA	Bronze/PLA	Resin	Graphene/resin	PLA	Bronze/PLA	Resin	Graphene/resin				
d)		○	○	●	○	○	○	○	○	○	○	○	○	○	○	○	○	○	○	○	○	○	○	○	○	○	○	○	○	○	○	○	○
e)		○	○	○	●	○	○	○	○	○	○	○	○	○	○	○	○	○	○	○	○	○	○	○	○	○	○	○	○	○	○	○	○
f)		○	○	○	○	○	○	○	○	○	○	○	○	○	○	○	○	○	○	○	○	○	○	○	○	○	○	○	○	○	○	○	○

Note: ● refers that this parameter was used while printing the specified material; ○ the parameter was not used while printing the specified material

### 3. Materials and methods

Table 3.2. List of 3D-printed materials using FDM technology, test specimens' printing parameters, and the number of examined samples in each test

Material, Colour	Printing parameter			Number of tested specimens		
	Print orientation	Layer height, $\mu\text{m}$	Raster angle, $^\circ$	**Tribology, roughness, and morphology tests	Tensile test	Hardness test
PLA, Gray	*Horizontal	200	45/135 $^\circ$	6	-	-
	*45 $^\circ$ angle	200	45/135 $^\circ$	6	-	-
	*Vertical	200	45/135 $^\circ$	6	-	-
PLA, Black	*Horizontal	200	45/135 $^\circ$	6	-	-
	*45 $^\circ$ angle	200	45/135 $^\circ$	6	-	-
	*Vertical	200	45/135 $^\circ$	6	-	-
PLA, White	*Horizontal	200	45/135 $^\circ$	6	-	-
	*45 $^\circ$ angle	200	45/135 $^\circ$	6	-	-
	*Vertical	200	45/135 $^\circ$	6	-	-
	Flat	*100	45/135 $^\circ$	-	3	***
		*200	45/135 $^\circ$	-	3	***
		*300	45/135 $^\circ$	-	3	***
		200	*0/45 $^\circ$	-	3	***
		200	*45/135 $^\circ$	-	3	***
		200	*45/90 $^\circ$	-	3	***
	*On-edge	200	45/135 $^\circ$	-	3	***
*Upright	200	45/135 $^\circ$	-	3	***	
Total	17 conditions			54	24	
				78		
Bronze/PLA composite	*Horizontal	200	45/135 $^\circ$	6	-	-
	*45 $^\circ$ angle	200	45/135 $^\circ$	6	-	-
	*Vertical	200	45/135 $^\circ$	6	-	-
	*Flat	200	45/135 $^\circ$		3	***
	*On-edge	200	45/135 $^\circ$		3	***
	*Upright	200	45/135 $^\circ$		3	***
Total	6 conditions			18	9	
				27		
Overall	23 conditions			105		

\*The variable parameter for each examined condition

\*\* The tribology tests were conducted under two loads (150 and 200 N), three identical specimens was tested under each load

\*\*\*The same tensile testing specimens were used for hardness tests

#### 3.3.2. Bronze/PLA composite filament printed by FDM technique

The commercially manufactured bronze/PLA filaments having a diameter of 1.75 mm were used to fabricate the 3D-printed tribology and tensile test specimens. The bronze/PLA filaments with a bronze content of 8% were purchased from a commercial 3D filament manufacturer (eSUN, 2018). The test pieces were produced using the commercial 3D printer WANHAO Duplicator 6 with a nozzle diameter of 0.4 mm. The specimens were printed with a 45/135 $^\circ$  raster angle, 100% infill percentage, and 0.2 mm layer thickness. For slicing purposes, the Simplify 3D software was used. The printing temperature and platform temperature were maintained at 195 $^\circ\text{C}$  and 60 $^\circ\text{C}$ , respectively. Prior to testing, the specimens were conditioned in a climate room with a temperature of 25 $^\circ\text{C}$  and relative humidity of 50%.

### 3. Materials and methods

The tribology test samples were fabricated at three print orientations, which were Horizontal, 45° angle, and Vertical, as illustrated in Table 3.1a. The tensile test specimens were also manufactured at three print orientations, which were Flat (horizontally), On-edge, and Upright (vertically), as exhibited in Table 3.1b. In the case of On-edge print orientation, the 3D-printed samples were fabricated with supporter beneath the gage section due to the vast space. The actual physical appearance of tribology and tensile test pieces is shown in Fig. 3.4a and Fig. 3.4b, respectively. The numbers of all printed bronze/PLA composite specimens, with different process parameters, examined on each test are listed in Table 3.2 (lower part of the table).

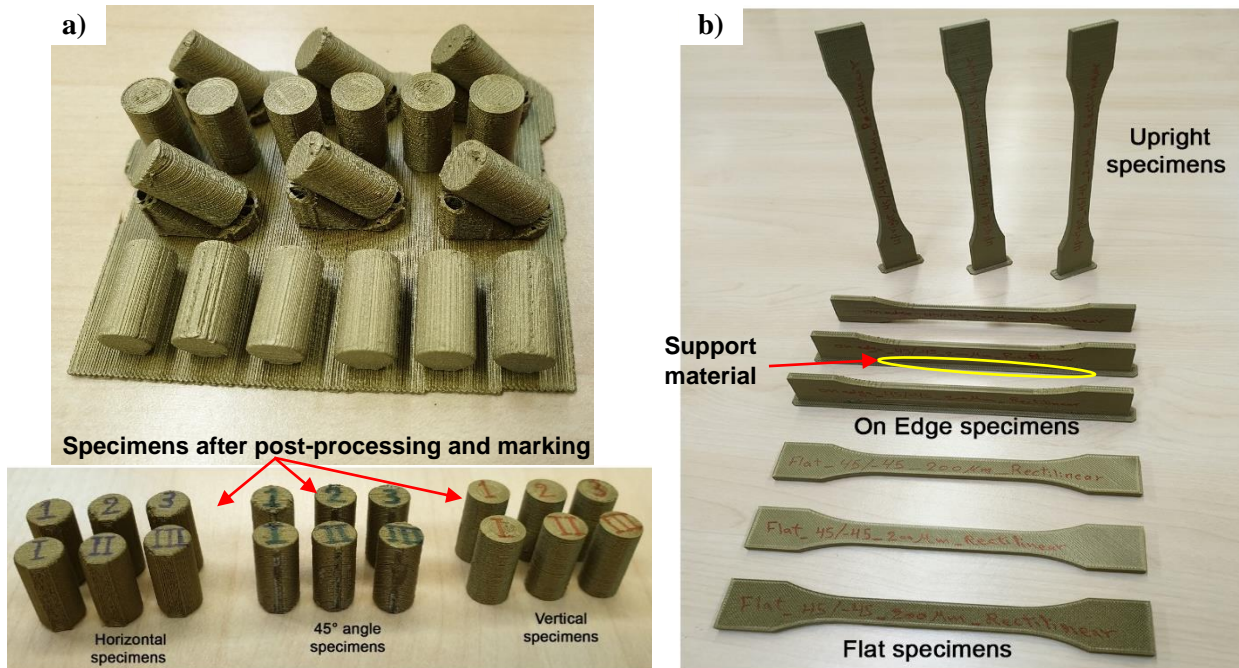


Fig. 3.4. The real specimens of bronze/PLA composite material 3D-printed at different build orientations for a) tribology tests, and b) tensile testing

#### 3.3.3. WANHAO neat resin printed by DLP technique

The tensile and tribology test specimens produced utilizing a commercial 3D printer WANHAO D7. This 3D printer uses digital light processing (DLP) technology, which works in accordance with the photo-polymerization mechanism. CreationWorkshop (which its file extension format is "cws") is the recommended software by the manufacturer was used for the slicing purpose. The commercially manufactured Wanhao UV resin (light-curable chemical liquid) were used in the fabricate of the test samples. Two different colours (red and white) of this photo-curable resin were inspected, having a viscosity of 120~140 MPa.s and density of 1.12 g/cm<sup>3</sup> at 25 °C (Wanhao, 2017). The chemical composition ingredients of the used resin as described in the datasheet of the product are listed in Appendix A4.

To investigate the effect of print orientation on the tribological properties, the test specimens were manufactured at three print orientations, which were X (Horizontal), 45° angle, and Z (Vertical), as exhibited in Table 3.1a. However, the tensile specimens were fabricated at On-edge build orientation with three sub-build orientation angles which were 0°, 45°, and 90° to the z-axis, as illustrated in Table 3.1d. All the examined samples were printed with a layer thickness of 100 µm and solid inside (100% filling). At least, three similar specimens were manufactured for each material colour and print settings, i.e., for each individual print parameters, three identical samples have been prepared (see Fig. 3.5). The numbers of all DLP printed resin samples, with different colours and parameters as well as post-processing, examined on each test are listed in Table 3.3 (upper part of the table).

### 3. Materials and methods

Table 3.3. List of 3D-printed materials using DLP (with varying material colour and graphene content), test specimen printing parameters, and the number of examined samples for each test

Material	Printing parameter		**Post processing	Number of tested specimens			
	Print orientation	Layer height, $\mu\text{m}$		Tribology, roughness, and morphology tests	Tensile test	Hardness test	
Wanhao resin, Red	Horizontal	100	√	3	-	-	
	45° angle			3	-	-	
	Vertical			3	-	-	
	Horizontal		X	3	-	-	
	45° angle			3	-	-	
	Vertical			3	-	-	
	0° angle		√	-	3	***	
	45° angle			-	3	***	
	90° angle			-	3	***	
	0° angle		X	-	3	***	
90° angle	-	3		***			
Wanhao resin, White	Horizontal	100	√	3	-	-	
	45° angle			3	-	-	
	Vertical			3	-	-	
	0° angle		√	-	3	***	
	45° angle			-	3	***	
	90° angle			-	3	***	
	0° angle		X	-	3	***	
	45° angle			-	3	***	
Total	19 conditions			27	30		
				57			
Neat resin 0.0 wt.% graphene	Horizontal / On-edge	35	√	3	4	3	
		50		3	4		
		100		3	4		
	45° angle	35		3	-	-	
		50		3	-		
		100		3	-		
	Vertical	35		3	-		
		50		3	-		
		100		3	-		
Graphene/ resin composite 0.5 wt.% graphene	Horizontal / On-edge	35	√	3	4		3
		50		3	4		
		100		3	4		
	45° angle	35		3	-	-	
		50		3	-		
		100		3	-		
	Vertical	35		3	-		
		50		3	-		
		100		3	-		
1.0 wt.%	Horizontal / On-edge	35	√	3	4		3
		50		-	4		
		100		-	4		
2.0 wt.%	Horizontal	35		3	-	3	
Total	29 conditions				60	36	12
					108		
Overall	48 conditions				165		

\*\* (√) post-processing was applied; (X) post-processing was not utilised

\*\*\* The same tensile testing specimens were used for hardness tests

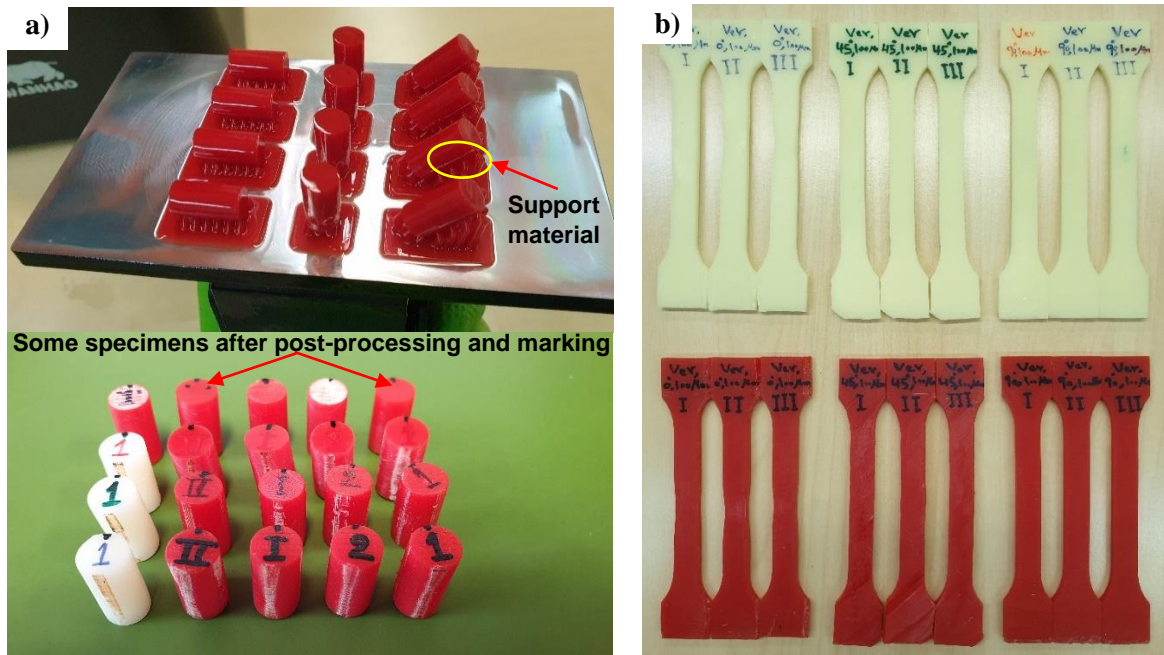


Fig. 3.5. Actual samples of neat resin material DLP 3D-printed, a) tribology test pieces after manufacturing immediately and then after post-processing and marking, and b) tensile test specimens

### 3.3.4. Graphene/resin composite printed by DLP technique

#### Materials

Graphene nanoplatelets consisting of short stacks of platelet-shaped graphene sheets that are in a planar form were obtained from Nanografi Nanotechnology company (Ankara, Turkey) (Inc., 2019). The material has 99.90% purity and is coloured black. The particles have an average thickness of 3 nm and a diameter of 1.5  $\mu\text{m}$ , coupled with a surface area of 800  $\text{m}^2/\text{g}$ . Graphene nanoplatelets are excellent electrical and thermal conductors (1500-1980  $\text{s/m}$ ) because of their pure graphitic composition.

The 3D printing material used as a matrix (binder) for the graphene to create the composite and manufacture the specimens is a photocurable polyurethane-based resin purchased from Esun Industrial Co., Ltd (Shenzhen, China) (Esun Industrial Co., 2019). The utilized resin is a white coloured liquid that could be cured to become solid (light-curable chemical) at a wavelength range between 395–405 nm. This resin has a density of 1.07–1.13  $\text{g}/\text{cm}^3$  and at 25  $^\circ\text{C}$  a viscosity of 200–300  $\text{mPa}\cdot\text{s}$ . The chemical ingredients of the used photopolymer resin material as described in the product's datasheet are tabulated in Appendix A4.

#### Preparation of graphene/resin composite

The flowchart displayed in Fig. 3.6 represents the sequence and steps of the experimental work that was accomplished during the preparation and testing of the graphene/resin composites. The contents ratio of the composite material (the neat resin and graphene powder) was weighed by a Sartorius brand lab balance (Sartorius AG Company, Gottingen, Germany) with an accuracy of 0.001 g. A polypropylene (PP) plastic centrifuge tube, 50 ml in volume and conical bottom shape, was used as a container for the mixture (graphene/resin dispersion) when preparing the composite material. As the capacity of the tube is only up to 50 ml, which is almost 50 mg for the mixture as well, only 50 mg of the dispersion material was prepared each time, which was adequate amount for the vat of the used 3D printer. The ratios of dispersion contents were determined very precisely. First, the tube was placed on the scale, and the tare button was pressed to not include the container within the dispersion contents' weight in the reading. Then the required proportion of graphene

### 3. Materials and methods

was put in the tube (i.e., in the case of 0.5 wt.%, the graphene's weight was 0.25 g). After that, the resin was added according to the remaining weight. A vortex mixer shaker, or vortexer, is a simple device used commonly in laboratories to mix small vials of liquid. In this work, FOUR E's Vortex Mixer (FOUR E's Scientific Co., Ltd, Guangzhou, China) with a shaking speed of 3000 rpm and 50 ml capacity was utilized to mix the graphene with the resin.

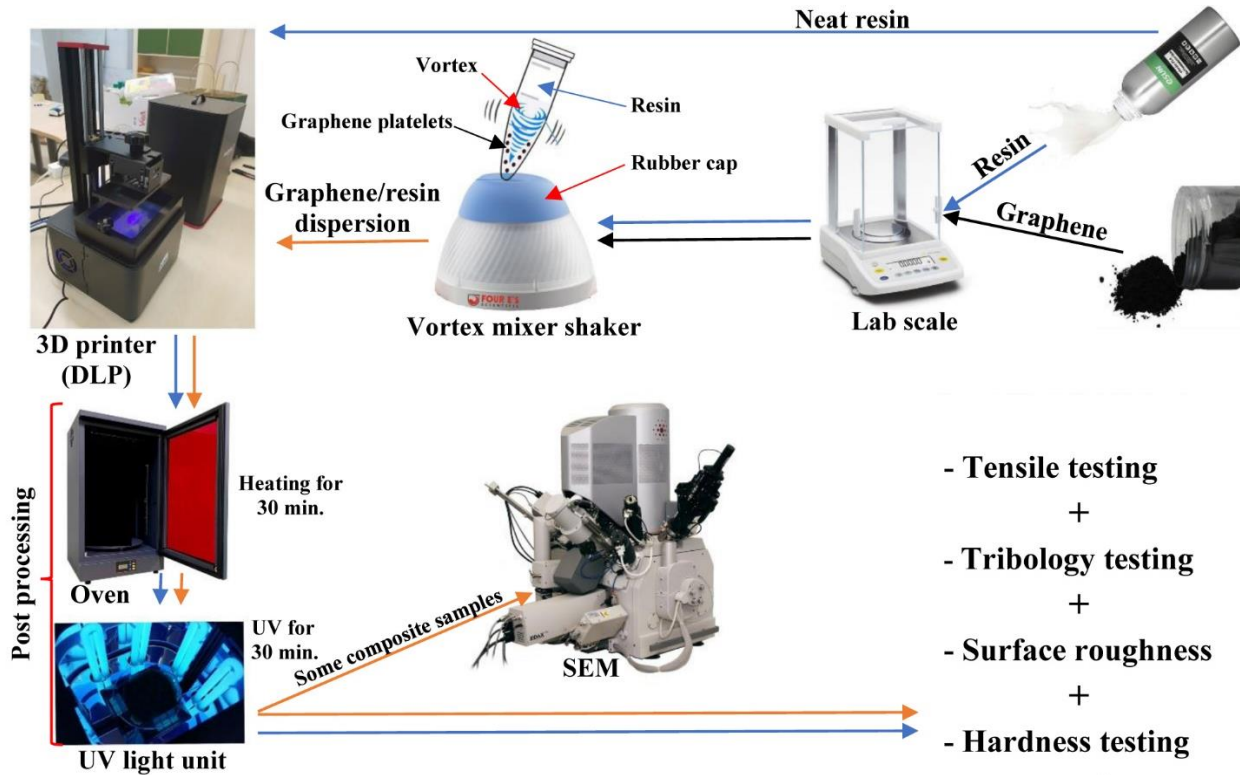


Fig. 3.6. Flowchart for the experimental work sequence

After weighing the materials by scale according to the required concentrations, the centrifuge tube is closed with its high density polyethylene (HDPE) screw cap that is designed to ensure there is no leak. Furthermore, the tube is fully covered by an aluminium foil to make it opaque and to avoid any light from the lab room to transmit to the liquid resin that might cure it. When the conical bottom of the tube is pressed into the vortex mixer's rubber cup attached to an electric motor with the drive shaft, the rubber piece oscillates rapidly in a circular motion because of the running motor. This creates a vortex that then affects the dispersion liquid inside. Despite the pure resin being white in colour, the mixture becomes fully black within a short time (a couple of seconds) of mixing by the vortex mixer. This indicates the distribution of the graphene platelets throughout the resin. The mixing process is continued for five minutes to make sure that the composite is homogeneous.

#### *Producing test specimens*

The tribology, tensile, and hardness test specimens were produced using the commercial 3D printer WANHAO D7. All printed specimens were solid (100% filled). The tribology specimens are cylindrically shaped printed to fit in the tribology testing machine holder. The cylindrical tribology test pieces have a diameter of 8 mm and a length of 15.2 mm. They were fabricated at three layer thicknesses (35, 50, and 100  $\mu\text{m}$ ) and three print orientations. Table 3.1a presents the print orientations that are Horizontal (X), 45° angle, and Vertical (Z). For each print material (pure resin and graphene/resin composites according to the graphene ratio contents) and parameter, three identical specimens were manufactured. That is, for every single print setting, three similar samples were prepared. The same tribological specimens were used for microstructural and surface

### 3. Materials and methods

roughness determinations. However, different test pieces were manufactured for the hardness testing because of the incompatible dimensions (small size) of the tribological samples. For obtaining an appropriate sample for the employed hardness test device, cuboid-shaped specimens were produced (see Table 3.1f). These test pieces are 35 mm in length, 35 mm in width, and 8 mm in height. The actual physical appearance of the printed samples is pictured in Fig. 3.7a.

The tensile test pieces were the dog-bone shape modeled according to the standard ISO 527-2: 2012 type 1BA (International Organization for Standardization, 2012b). The specimens were built at an On-edge orientation owing to the reliability of this build orientation, as confirmed in the author's previous studies (Hanon Marczis et al., 2019, 2020b; Hanon Alshammas et al., 2020). These samples were fabricated at three layer heights (100, 50, and 35  $\mu\text{m}$ ) to investigate the influence of print layer thickness (see Table 3.1e) on the mechanical properties. In terms of the printing materials, neat (pure) resin as well as graphene/resin composite with two different graphene concentrations (0.5 and 1 wt.%) were used for the manufacture of specimens. This was done to assess the effect of graphene platelets' existence. At least, four identical specimens were printed for each print condition (see Fig. 3.7b).

The printing parameters and number of examined samples for each tested condition are presented in Table 3.3 (lower part of the table). As there are multiple variable parameters, the samples were marked with different numbers, colours, and symbols for easier traceability. For tribology specimens, the orientations were designated with Arabic numbers, Roman numerals, and letters for the Horizontal, 45° angle, and Vertical, respectively. Further, the layer thicknesses of 100, 50, and 35  $\mu\text{m}$  were denoted with green, blue, and red colours, respectively. The graphene concentration of the graphene/resin composite specimens has also been recognized using the symbols \*, #, and & for the 0.5, 1, and 2 wt.% ratios, respectively. These identifying codes were highlighted at the top of the specimens, as shown in Fig. 3.7a where the manufactured tribology specimens are presented. Regarding tensile models, the description included the layer height, graphene content, and sample order within the same set. These identifying codes were manifested at the top face of the test pieces, as displayed in Fig. 3.7b.

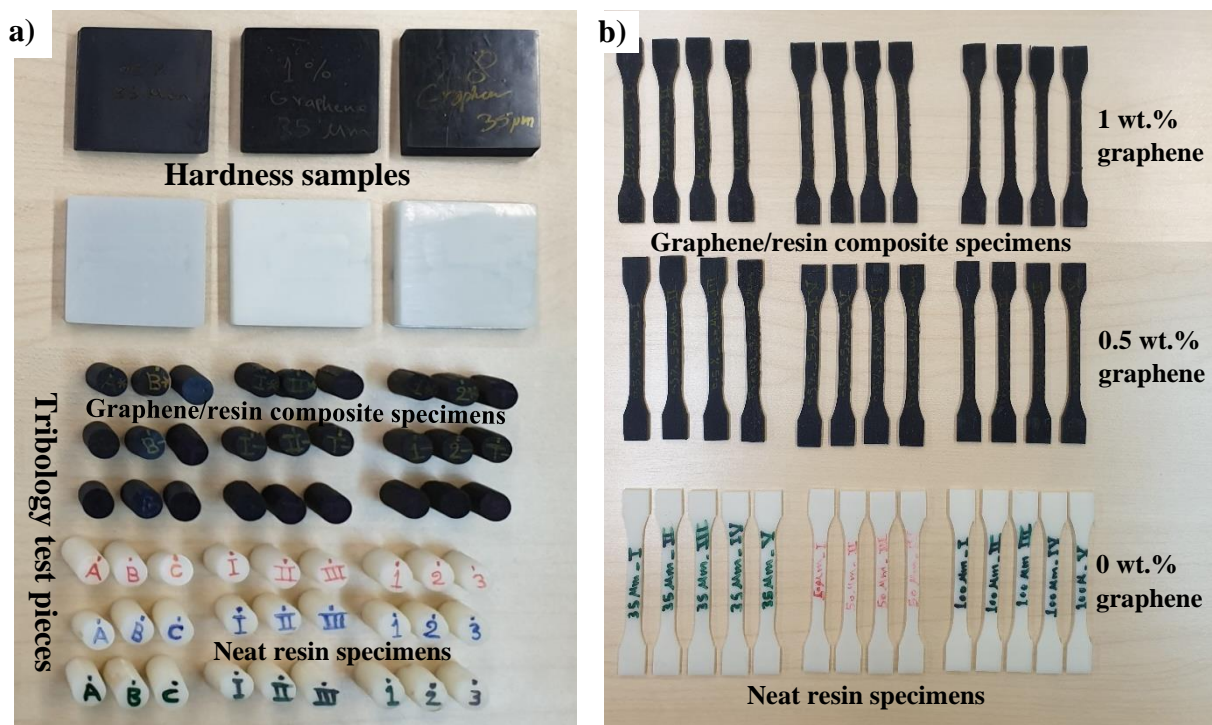


Fig. 3.7. Physical appearance of graphene/resin composite 3D-printed, a) hardness and tribology test specimens with their addressing code, and b) tensile test specimens with different graphene content

### 3.4. Post-processing

After 3D printing, all testing samples were subjected to post-processing. For FDM printed specimens, the post-processing was only to remove the support material (if any) manually by a sharp tool. However, the post-printing process of DLP samples was initiated by heating the specimens in the oven (see Fig. 3.8a) for 30 minutes up to 60 °C. The heated specimens were then exposed to ultraviolet (UV) light at a 405 nm wavelength for 30 minutes, as recommended by Formlabs (Formlabs, 2018). The UV light was supplied inside a UV cure unit. The UV light unit was made from scratch, mainly from a 36 watts nail salon UV lamp (see Fig. 3.8b). It was modified to be fitted into a box to hold up the specimens. To minimize the loss of UV light, the cardboard box was lined with aluminium foil as it increases reflectivity inside the box. Moreover, a transparent plastic sheet was used as a shelf inside the box to ensure that the UV light reaches all sides of the specimens simultaneously. A schematic diagram of the used UV light unit is depicted in Fig. 3.8c.

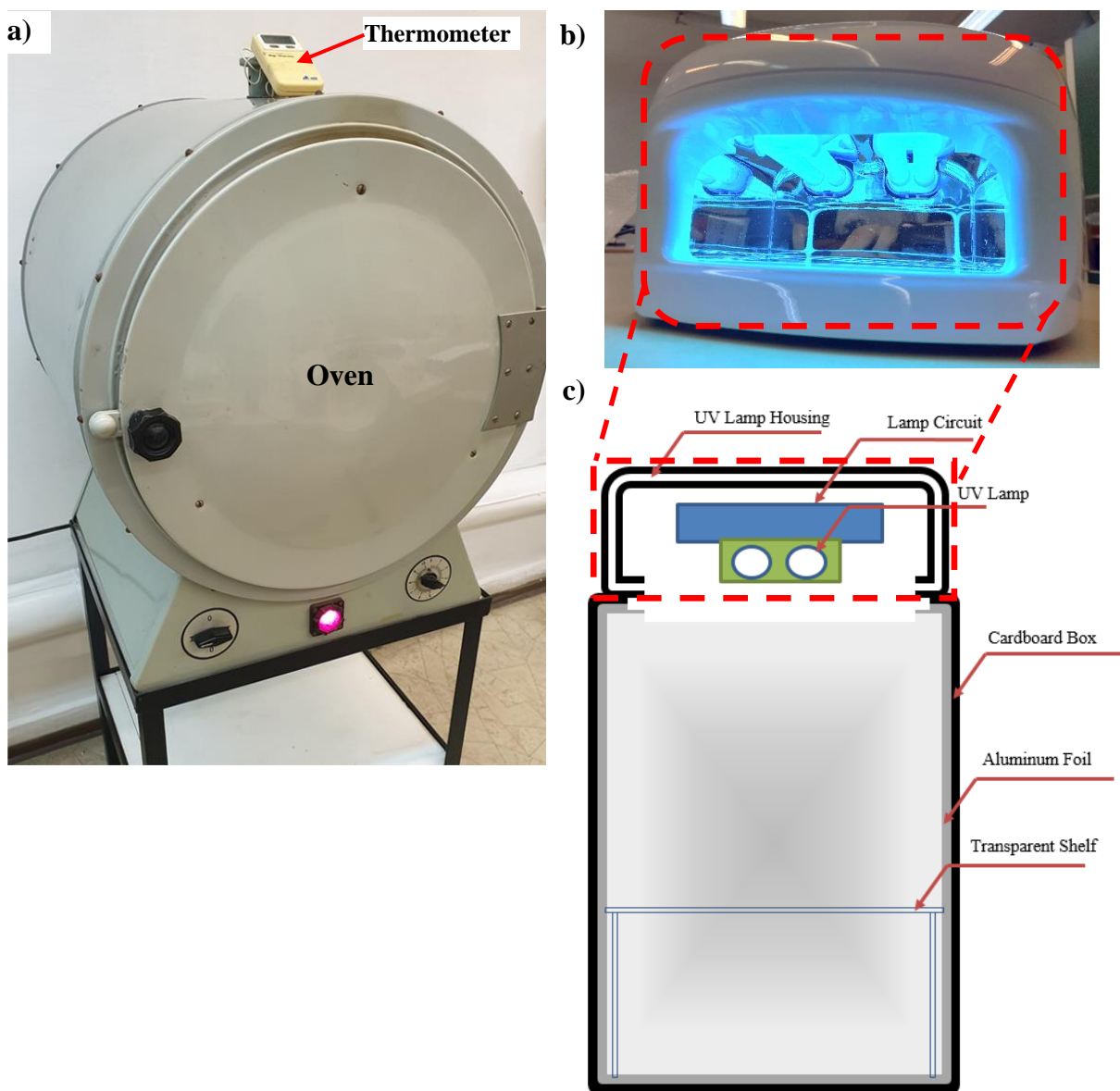


Fig. 3.8. The post-curing process equipment, a) the oven used for heating the specimens, b) nail salon UV lamp, and c) schematic diagram of the ultraviolet light unit



### 3.5. Determination of tribological properties

#### 3.5.1. Tribometer system and procedure of experiments

A cylinder-on-plate tribometer (Fig. 3.9a) with a reciprocating motion was used to assess the wear and friction characteristics of the 3D-printed parts. This model system ensures the creation of high surface pressure even at small dimensions (line contact). However, the alternating sliding means both static (at reversal points) and dynamic (at intermediate slides) friction can be measured side by side due to the two-way sliding friction. This allows the stick-slip tendency to be explored by jointly measuring adhesions and slips. The schematic of the cylinder-on-plate apparatus is shown in Fig. 3.9b. Normal load, frequency, sliding speed, and stroke length can be varied to fit the test requirements. The counterpart is a ground steel plate with a maximum stroke and frequency of 50 mm and 30 Hz, respectively. The employed tribo-test (cylinder-on-plate) is consistent with the standard ASTM G-133 of the reciprocating sliding wear (ASTM International, 2016). The tribological measurements were conducted under dry conditions with no lubricant.

The measuring circuit primarily includes a tribometer, an inverter, Spider 8 (a strain gauge measurement device), and a computer. Alternating motion is provided by a variable speed electric motor using the push rod attached to its axis. This motor provided with an adjustable frequency drive and an eccentric disc. The eccentric disc drives the sliding plate on a linear path by the coupled interchangeable push rod. The inverter is used to set the experiment frequency to the required value precisely. The stroke length could be modified according to the measurement parameters due to the eccentricity of the thrust bar. After adjusting the desired load, the weight can be fixed with a screw on the load arm. The Spider 8 (see Fig. 3.9c) was used to convey the measured data (mainly friction force, wear depth, and the other essential features) from the tribometer into the computer. These data were measured by the sensors fastened to the tribometer. Before each test, the counterpart was cleaned thoroughly from surface impurities (due to the debris of the previously tested specimens) using acetone-dipped cotton. To determine the tribological properties of 3D-printed specimens under reciprocating sliding conditions, it is necessary to carefully select the typical wear test parameters. The parameters implemented during the tribological tests are presented in Table 3.4.

Table 3.4. The performed parameters during the tribological tests

Parameter	Value
Surface roughness of steel counterpart, $R_a$	0.10 – 0.12 $\mu\text{m}$
Load, F	150-200 N
Alternating motion frequency, f	4.583 Hz
Stroke length	6 mm
Relative humidity, Rh	45 – 50 %
Ambient temperature, T	23 – 25 $^{\circ}\text{C}$
Test duration, t	60 min

These parameters were determined based on the previous polymer studies (e.g., (Zsidai et al., 2002; Hanon Kovács et al., 2019; Hanon Alshammas et al., 2020; Hanon Marczis et al., 2020a)). The surface roughness corresponds to the typical roughness of fine surface machining (e.g., grinding, or fine cutting). The load (150-200 N) gives a significant surface pressure (20-40 MPa) in the line contact that follows industrial practice. The short stroke length well localizes the resulting friction temperature and its effect.

### 3. Materials and methods

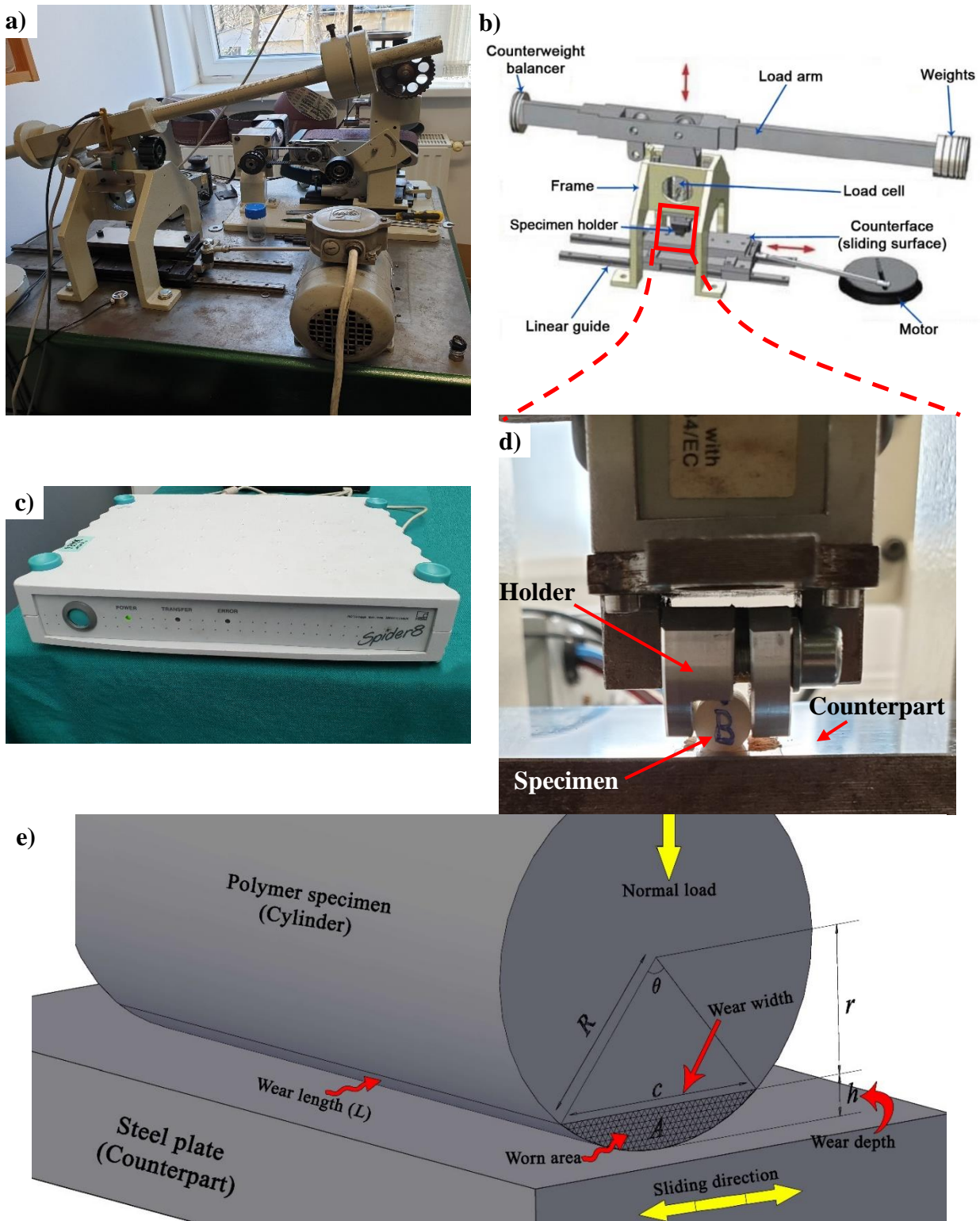


Fig. 3.9. Tribological tests equipment and its experimental setup, a) cylinder-on-plate tribometer, b) schematic of cylinder-on-plate reciprocating tribometer apparatus, c) strain gauge measurement device (Spider 8), d) cylindrical polymer test piece fixed by the sample holder, and e) schematic diagram for the contact of the frictional couple during cylinder-on-plate tribology test

The wear and friction coefficient development as a function of sliding time were transferred by Spider 8 and automatically recorded on the computer. The sampling rate during the measurement is 600 (1/s). The measurements of friction force and wear depth were recorded regularly after every 60 s throughout the tribo-testing for all specimens. Three of the HBM brand (Darmstadt, Germany) sensors were employed during the test. For measuring the applied load, a compact design force

transducer (C9B) was used to set the vertical static load (compression), which measures up to 5 kN with an accuracy of  $\pm 0.5\%$  full scale. In addition, the friction was investigated utilizing (PW6D) load cell having an accuracy of  $\pm 0.0350\%$ . Moreover, the displacement transducer type WETA 1/10 mm measured the samples' wear depth with a maximum linearity deviation of 0.65%.

Three parallel tests were conducted for each condition to assess the average result. The tribology test begins when the cylindrical shape 3D-printed pieces slide against the tribometer's counterpart. The specimens' sliding surface is on its perimeter (on the cylinder perimeter), where a point was already specified prior to the experiments. The cylindrical polymer test piece was fixed by means of the sample holder (see Fig. 3.9d). A schematic diagram for the contact of the frictional couple (the specimen and the counterpart) is shown in Fig. 3.9e. No matter the print orientation, all samples were placed horizontally (laid down) on the counterpart while testing. It is noteworthy here that the cylindrical specimen is fixed and does not rotate in the cylinder on the plate tribological model system, so it always has the same line surface in friction. The cylinder edges thus have no effect on the sliding conditions and friction-coefficient/wear.

### 3.5.2. Tribology test data analysis

The tribology measurements data, including wear development and friction force obtained, are transferred to the computer using Spider 8 (as mentioned in section 3.5.1.). CATMAN software is employed to process the measured data into a Microsoft Office Excel file. Wear depth and the friction force of specimens are obtained as a function of total sliding time. However, it is possible to calculate the sliding distance since the frequency ( $f$ ) and the stroke length (motor diameter, divided by 2 to get radius ( $r$ )) are known. Firstly, by computing the angular velocity ( $\omega$ ) from

$$\omega = 2 * \pi * f, \quad (3.1)$$

then, it is converted to a linear velocity ( $v$ ) through

$$v = r * \omega. \quad (3.2)$$

After that, multiplying  $v$  by the sliding time ( $t$ ) measurements, the sliding distance ( $d$ ) will be found

$$d = v * t. \quad (3.3)$$

The friction force was measured through the load cell deformation, and subsequently the curve obtained was drawn (see Fig. 3.10a). This curve is not yet appropriate for analysis, as it is necessary to extract the static (maximum) and dynamic (motion) friction coefficients per cycle, as demonstrated in Fig. 3.10b. To do that, the measured frictional force ( $F_f$ ) is divided by the load force ( $F_n$ ) in order to obtain the coefficient of friction ( $\mu$ ) (Schmitz, et al., 2005)

$$\mu = \frac{F_f}{F_n}. \quad (3.4)$$

The maximum values of measured points per half period are considered as the static coefficient of friction, while the average is the dynamic friction coefficient (see Fig. 3.10b). Since the observed frictional force is negative in each half period due to the alternating motion system, the absolute value for the acquired negative frictional force should be taken. Fig. 3.10b shows the data of 600 measurements which was recorded in only one second (as aforementioned, sampling rate is 600 1/s). Also, it can be seen that around four and a half waves (cycles) were drawn, considering the alternating motion frequency (4.583 Hz) mentioned in Table 3.4.

The static and dynamic friction coefficient behaviour for one of the specimens during the test is illustrated in Fig. 3.10c. The static friction is always higher than dynamic friction during the running time except for the starting moment. However, at the beginning of measurement appears

### 3. Materials and methods

a slight difference between the static (blue) and dynamic (red) friction values. This can be explained as a measurement error due to the looseness in the sample clamp head of the tribometer. The difference between static and dynamic friction coefficient is increasing throughout the test time, which reveals that the stick-slip phenomenon is existent.

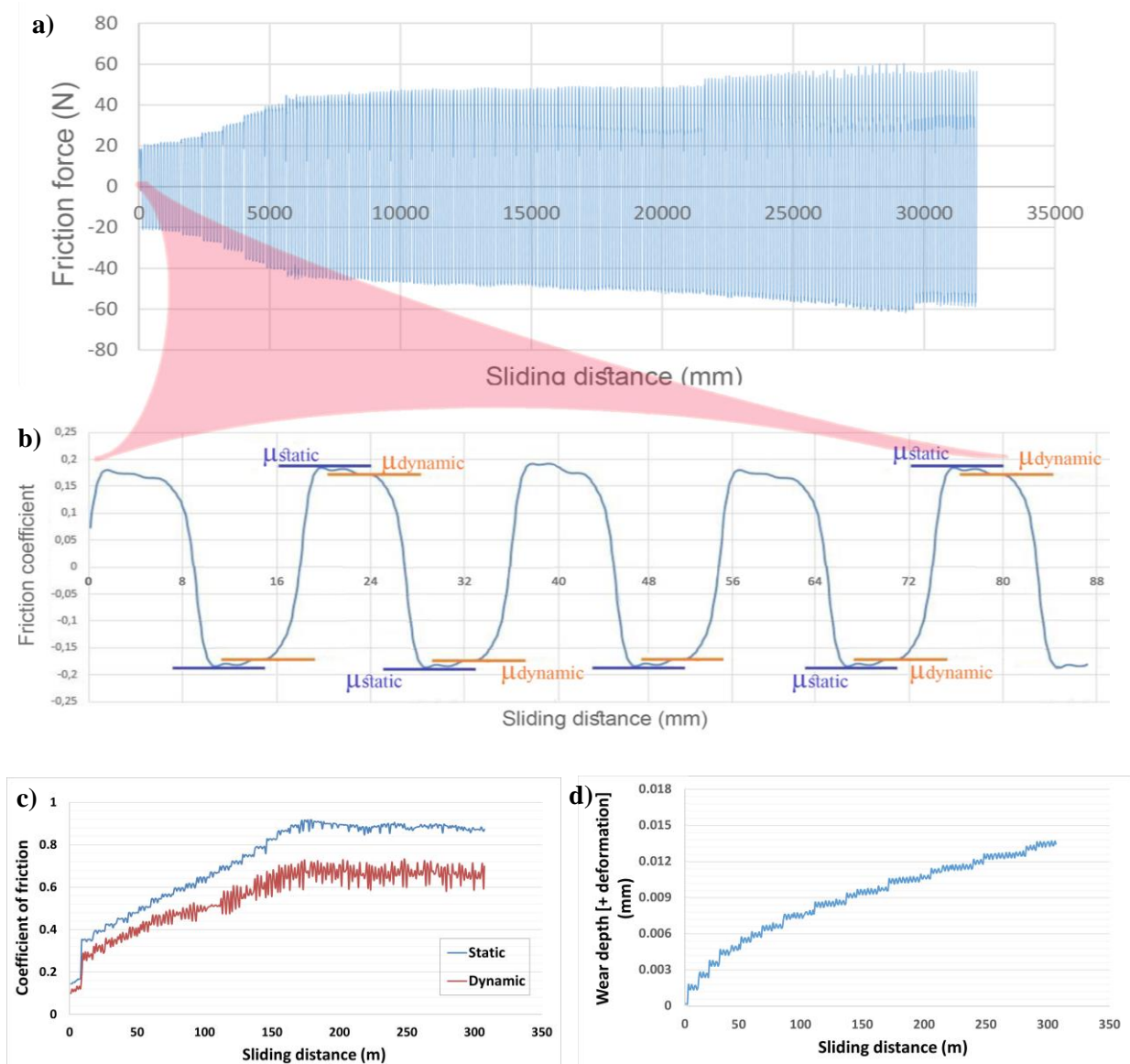


Fig. 3.10. Tribology test data analysis, a) initial results obtained for frictional force measured versus total sliding distance, b) few data (for only 1 s of sliding) was extracted to show the static and dynamic friction coefficient per cycle, c) static and dynamic friction coefficient curves, and d) wear behaviour (specimen: neat resin, horizontally printed, test load 150 N)

The wear behaviour of one of the tested samples during the tribology test is demonstrated in Fig. 3.10d. Most of 3D-printed samples have disclosed a persistent increment tendency in terms of wear rate versus the sliding distance. It can be seen that the wear was represented as "wear depth + deformation". This is because, in this test rig (cylinder-on-plate), the displacement sensor detects the wear and deformation together. Fig. 3.11 clarify how the wear and deformation was measured. Before applying the load (load = 0 N), the specimen was still circular, indicating that neither deformation nor wear took place. The initial deformation (which is the largest) occurs after applying the normal load (load  $\gg$  0 N), approximately after waiting for 5 seconds, but the test did not start yet (distance = 0 m). At this moment, the wear meter was reset to zero (tare option

applied), so the initial (Hertz) deformation was excluded from the measurement, trying to obtain the net wear depth without the deformation effect. After the test starts (distance > 0 m), the initial pressure (Hertz pressure/deformation) will definitely be present in the future due to the counterformal (line/point) contact. However, parallel with increasing wear continuously (contact surface increases), the elastic deformation significantly decreases, a slight kick-back is also expected. As a result, the "recoil" mass of material replaces the worn layers, i.e., less wear is measured than real. Later, with a significant increase in the bearing surface, this effect decreases and remains present to a limited but nearly constant value throughout the measurement. Therefore, the wear in this work was represented as "wear depth + deformation", even if this deformation effect is small in front of the wear magnitude.

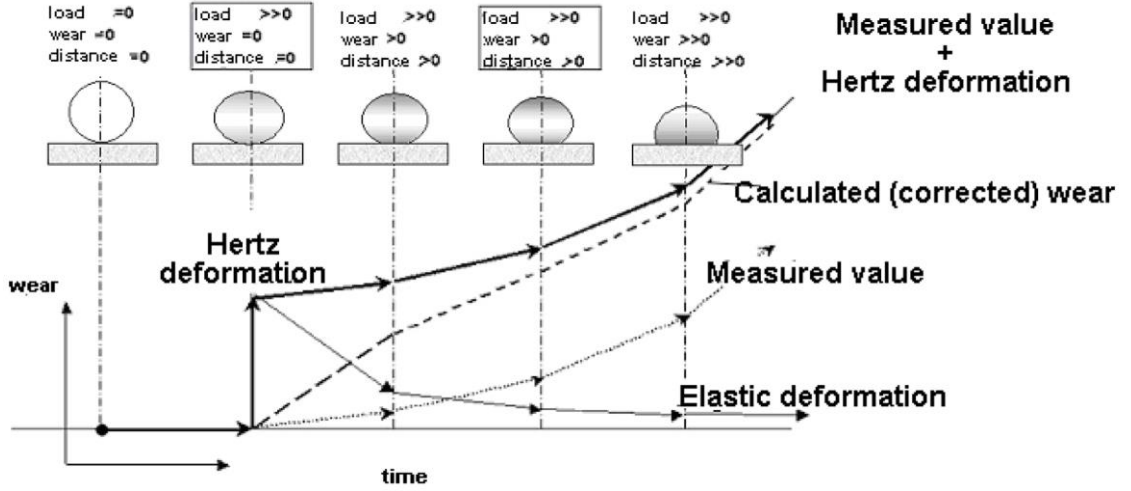


Fig. 3.11. Elastic deformation and wear components of the measured displacement value at the onset of friction and throughout the sliding (Zsidai László, 2005).

In order to calculate the wear volume (then specific wear rate) theoretically, the effect of the deformation was disregarded because its impact by the end of the test is negligible, as mentioned above. Therefore, the remaining effect was considered is the wear depth, which was given by the wear sensor. The wear sensor can measure the vertical movement during the tribo test when development in the wear occurs. The wear depth is observed and calculated through the displacement rate of the probe. Since the wear depth ( $h$ ) was known by measurement, the wear volume ( $\Delta V$ ) can be found via multiplying the area (worn area) by the length ( $l$ ) of the cylinder (see Fig. 3.9e). Equations (3.5) and (3.6) were used to calculate the wear width ( $c$ ) and area ( $A$ ), respectively (Weisstein, 2019)

$$c = 2\sqrt{h(2R - h)}, \quad (3.5)$$

$$A = R^2 \cos^{-1}\left(\frac{R-h}{R}\right) - \frac{c(R-h)}{2}, \quad (3.6)$$

where  $R$  is the radius of the cylindrical specimen.

After calculating the wear volume loss ( $\Delta V$ ) through

$$\Delta V = A * l, \quad (3.7)$$

the Archard's wear equation (Colbert and Sawyer, 2010) was used to compute the specific wear rate ( $K$ )

$$K = \Delta V / F_n d, \quad (3.8)$$

where  $d$  is the total sliding distance and  $F_n$  is the applied normal load.

### 3.6. Tensile testing

The FDM 3D-printed test pieces were produced with dimensions of 150 mm by 20 mm by 4 mm according to the dog-bone tensile test geometry of the ISO 527-2: 2012 standard type 1B sample (International Organization for Standardization, 2012b), as presented in Fig. 3.12a. However, due to insufficiency in the printing dimensions, the DLP printed tensile test pieces were modelled following ISO 527-2, type 1BA, with an overall dimension of 75 mm × 10 mm × 2 mm (length × width × thickness, consecutively).

Prior to measurement, the samples were conditioned for 24 hours in a room with a climatic of 23-25 °C and 45-50% as temperature (T) and relative humidity (Rh), respectively. Humidity has a significant impact on the measured values (Müller et al., 2009), therefore, for match results, it was substantial that all the specimens had the same moisture content. The tensile mechanical properties were examined for all printed specimens by a universal testing machine (Zwick / Roell Z100, Germany), exhibited in Fig. 3.12b, with employing the standard for tensile testing of polymers ISO 527 (International Organization for Standardization, 2012a). During the test, both ends of the sample were attached to the grip, and testing was performed at a velocity of 5 mm/min until the test piece broke down. In order to yield confident data, three samples, at least, were tested for each condition (identical sample in terms of printing settings and material content) and their average was calculated. The essential mechanical properties including Young's modulus (modulus of elasticity), ultimate tensile strength (UTS), elongation at break, and elongation at UTS were obtained from each specimen's stress-strain curve. The modulus of elasticity ( $E$ ) was calculated using Hooke's law, in all stress-strain points

$$E = \sigma / \varepsilon , \quad (3.9)$$

where  $\sigma$  is the tensile stress (applied force " $F$ " / cross-sectional area " $A$ ") and  $\varepsilon$  is the tensile strain (change in length " $\Delta L$ " / initial length " $L$ ").

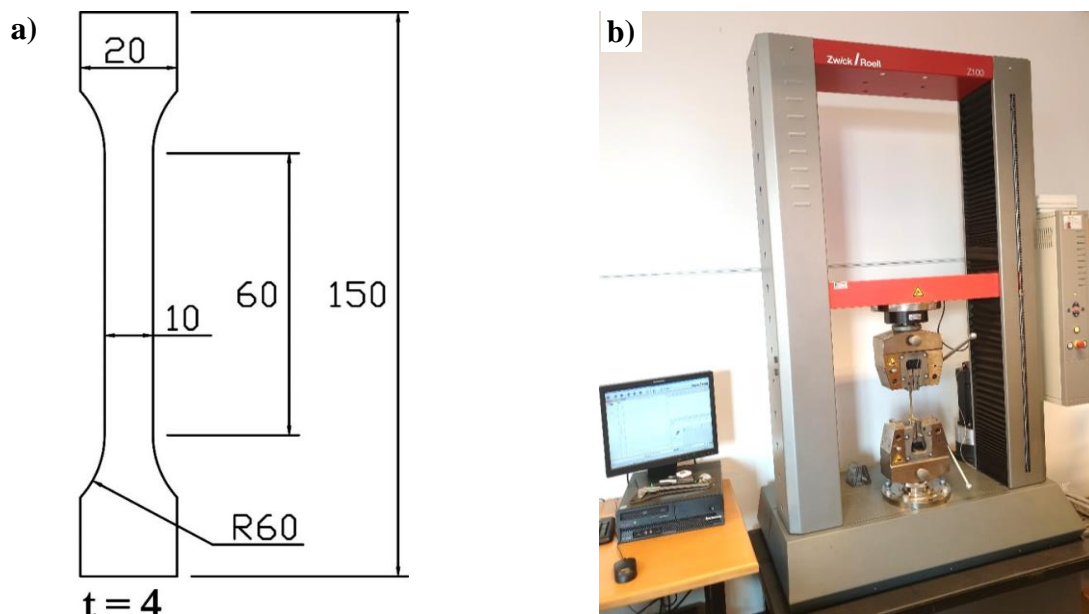


Fig. 3.12. Mechanical tests sample and apparatus, a) dimensions of the dog-bone tensile test piece (ISO 527-2, type 1B, FDM printed), and b) tensile testing machine used

For reliable results, the Young's modulus was determined by taking the gradient of the line on two points fitted at the 10% and 60% in the stress-strain plot. The stress-strain curves gained from specimens were compared to investigate the variance in specimens' mechanical properties fabricated in different conditions.

#### 3.7. Microstructure, hardness, roughness, and surface energy characterizations

A ZEISS brand optical microscope (see Fig. 3.13a) equipped with a mobile stand-alone colour camera type ZEISS Axiocam ERc 5s (Carl Zeiss AG, Oberkochen, Germany) was used to examine the surface morphology of the printed samples before and after the tribology test. The captured images were taken at different magnifications employing four ZEISS magnifying lenses (10x, 20x, 50x, and 100x). The examination is concentrated on the determination of the surface characteristics in terms of printing quality and the presence of scratches and voids at the worn area due to the sliding during the tribology test. Furthermore, in the case of graphene/resin composite material, several images were taken for the microscopic structure of DLP samples that were printed at three different relaxation times after mixing the graphene with resin. The graphene platelets distribution for each relaxation time and the attitude of breaking the samples at various magnifications were examined. The surface morphology was examined using an EVO 40 scanning electron microscope (Carl Zeiss AG, Oberkochen, Germany) at 20 kV acceleration voltage. In all cases, a secondary electron (SE) detector was applied, and the working distance (WD) was 10.5 mm. To avoid electrostatic charging of the surface, the samples were coated with a thin gold layer.

The hardness of the printed test pieces was examined using a shore D hardness device measuring between 0 and 100HD (see Fig. 3.13b). This model of testing instrument is customized for hard rubber, hard plastics, and semi-rigid plastics, and it works in accordance with the ASTM D2240 standard for polymers' durometer hardness testing (ASTM International, 2015). The penetration is carried out when a steel needle (indenter) is pressed into the testing material and the amount of resistance is displayed at the scale. This indenter needle is a conical point shape with a top cone angle of 35° and a tip radius of 0.1 mm. The test can be carried out at a working temperature of 0–40 °C (performed at 25 °C in this study), while the total measure force is up to 8.1 N.

A Mitutoyo portable surface roughness tester type SJ-41 (Mitutoyo Corporation, Sakado, Kanagawa, Japan) connected to a computer was used to measure the surface roughness, as shown in Fig. 3.13c. Zoom in for the measurement sensor (probe), during the test, is displayed on the middle. A scan length of 5 mm and a cut-off of 0.8 mm were used as test conditions to obtain 2D surface roughness ( $R_a$ ) measurements as well as the primary profile. Checking the surface profile helped determine the quality of printing and understand the tested contact surface profile in tribotests. Moreover, if the wear was not measurable by other means, it can be evaluated based on the change in surface profile before and after the test. Therefore, the surface roughness was evaluated for all tribology specimens prior to and after the tests.

The drop shape analyser DSA30 (KRÜSS company, Hamburg, Germany) was used to measure the contact angle and to determine the surface free energy (see Fig. 3.13d). Prior to measurement, the samples were cleaned of any surface impurities with isopropyl alcohol and then with high purity distilled water. The sample then inserted into the instrument with tweezers and closed the lid to ensure that the conditions were consistent. During the measurement, 10  $\mu$ l of liquid droplets were applied to the sample at a rate of 3  $\mu$ l/s using a 0.512 mm diameter needle. The device was calibrated with the diameter of the needle, and a tilt angle of 2° was used. Measurements were conducted at 25 °C. The orientation and fitting method were set as Sessile drop and ellipse, respectively. Two models were used to determine surface free energy which are EoS and Fowkes. For each condition, three parallel measurements were performed, and the average of which was taken into account during the evaluation.

### 3. Materials and methods

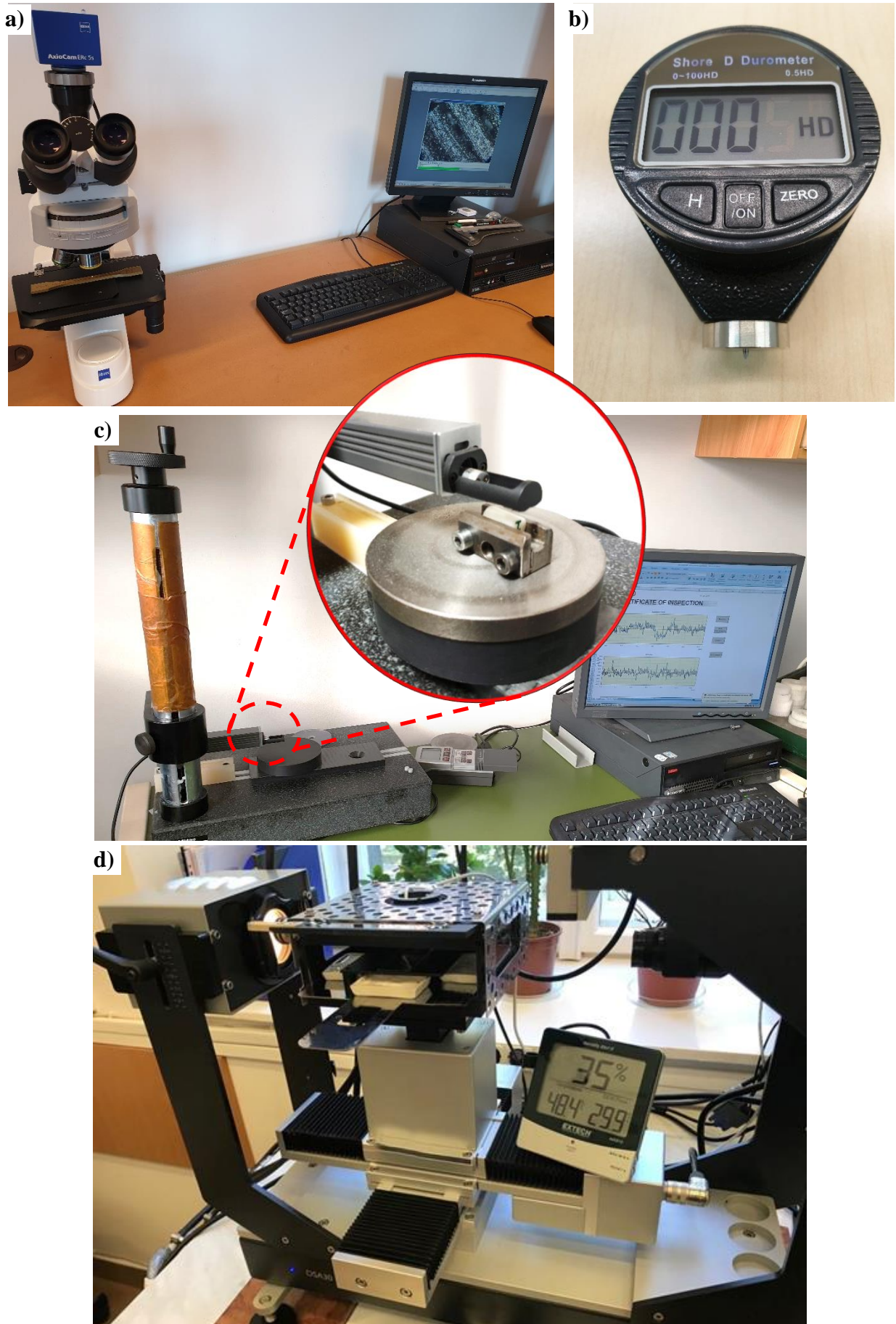


Fig. 3.13. Equipment utilised for the experiments, a) optical microscope, b) hardness test device (Shore D), c) surface roughness test device, and d) drop shape analyser device



### 3. Materials and methods

High-purity distilled water, diiodomethane ( $\text{CH}_2\text{I}_2$ ) and cyclohexane ( $\text{C}_6\text{H}_{12}$ ) were used as measuring liquids. In the form of droplets, these liquids were used to determine the dispersive ( $\gamma^D$ ) and polar ( $\gamma^P$ ) components of the surface energy. By summing the surface tension components, the value of the total surface energy ( $\gamma$ ) was determined (Kalin and Polajnar, 2013)

$$\gamma = \gamma^D + \gamma^P. \quad (3.10)$$

The surface tension and its components for measuring liquids are listed in Table 3.5.

Table 3.5. Surface tension and surface tension components for measuring liquids (Kalin and Polajnar, 2013)

Measuring liquids	Total surface tension, mN/m	Dispersive component, mN/m	Polar component, mN/m
Water	72.8	21.8	51.0
Diiodomethane	50.08	50.8	0
Cyclohexane	25.5	25.5	0

Three interfaces exist when a liquid drop is attached to an ideal (homogeneous) solid surface at an equilibrium contact angle, as illustrated in Fig. 3.14. These interfaces are solid-liquid interfacial ( $\gamma^{sl}$ ), solid-vapor interfacial ( $\gamma^{sv}$ ), and liquid-vapor interfacial ( $\gamma^{lv}$ ) free energies. The Young's equation (Salapare et al., 2015) governs the relationship between the surface free energies and the contact angle, as follows

$$\gamma^{lv} \cos \theta = \gamma^{sv} - \gamma^{sl}. \quad (3.11)$$

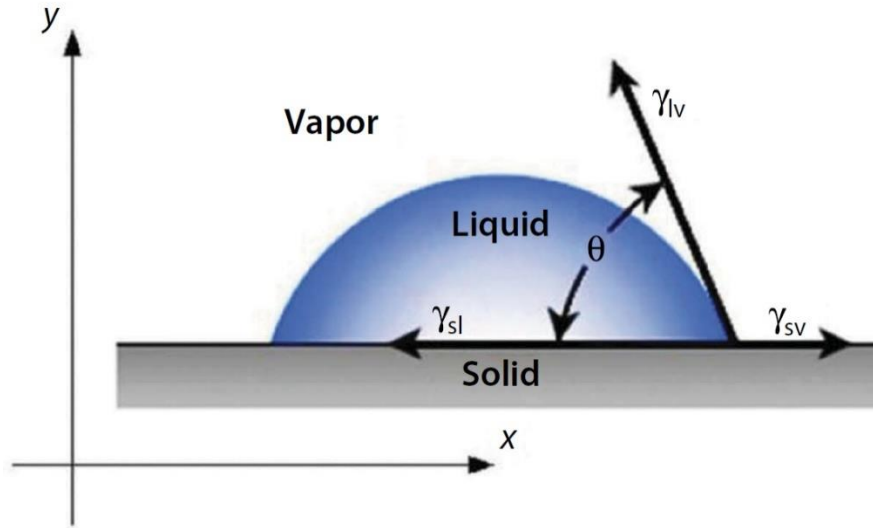


Fig. 3.14. Surface free energies of a liquid drop settling on a solid surface (Salapare et al., 2015)

The specimens prepared for the tests were made by the same 3D printing technologies used throughout this study (FDM and DLP). This is to investigate the surface energy of the components produced with each technique. PLA filament was used for the FDM 3D printing, while the neat resin was utilized for the DLP, and both materials are white.

## 4. RESULTS AND DISCUSSION

The experiments' results are presented in this chapter, as well as discussions suggesting the new findings. These include tribological characteristics for different 3D printing techniques (FDM and DLP) and materials (neat and composite for each technique) by assessing the results of tribology and relevant testing (such as tensile, hardness, surface roughness, surface morphology and microstructure, and surface energy).

### 4.1. Investigation of tribological properties

#### 4.1.1. Tribology of neat PLA material FDM 3D-printed

##### 4.1.1.1. Influence of process parameters and filament colour on friction

The wear and friction behaviour of 3D-printed PLA with different colours was evaluated using a cylinder-on-plate tribometer under dry sliding conditions. The coefficient of friction during tribology test as a function of sliding distance for loads of 150 and 200 N was plotted in Fig. 4.1a and Fig. 4.1b, respectively. The friction coefficient shown in these figures for specimens were printed in three different orientations (Horizontal, 45° angle, and Vertical) besides three various colours (white, black, and grey).

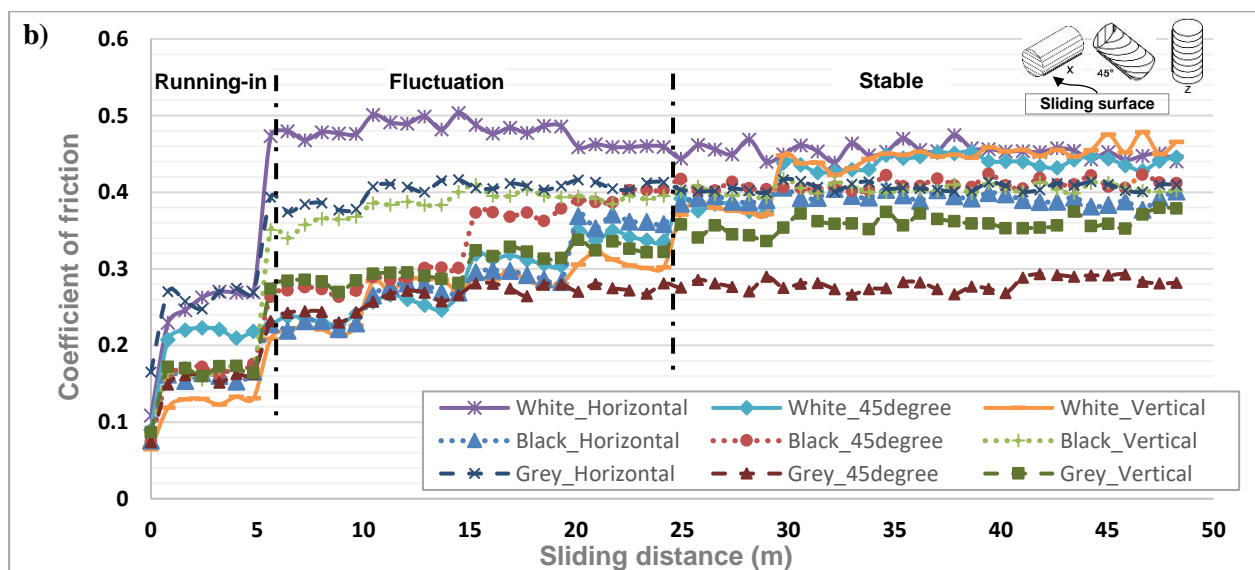
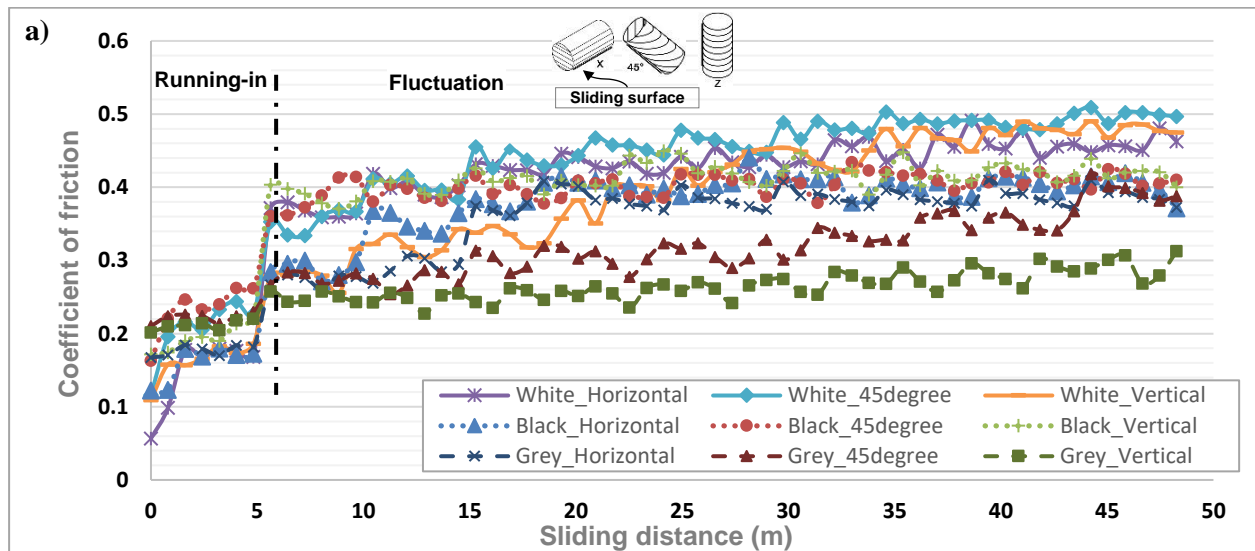


Fig. 4.1. Friction behaviour curves at a) 150 N load, and b) 200 N load

The friction coefficient curve generally goes through variant stages (mainly three stages: running-in stage, fluctuation stage, and stable friction stage (Yang et al., 2018)). Observing the curves obtained from both applied loads 150 and 200 N, the running-in stage has a sharp increase due to the static friction behaviour. It can be clearly seen that this stage has undergone through two rises, including a steady-state period in between. That may take place because the sliding between the 3D-printed surface and the steel counterpart is unstable in the running-in stage (Tsouknidas, 2011), where the surface roughness of the specimen is not polished yet (Hanon Marczis et al., 2020a).

The second stage (fluctuation) was reached after almost six meters of sliding between the surfaces. In the 150 N applied load, the friction coefficient for most of the samples increased steadily until the end of this stage except for the black and grey test pieces, which were printed vertically in which the friction coefficient was increasing and decreasing within the same range. However, in terms of the 200 N applied load, the specimens' friction coefficient was increasing regularly (slightly in some cases and pointedly in others) as well, except for the horizontally printed white colour specimen in which its friction coefficient tends to decrease after a tiny increment. That represented a unique attitude in this stage among other samples.

The stable friction stage of the 150 N load specimens was not so balanced, as the white and grey coloured samples regardless of the print orientation kept increasing, whereas the black coloured test pieces were more or less the same value. Though, the 200 N load specimens showed approximately steady-state attitude, as the samples tendency were either stable or slightly increased. In these curves, particularly in the stable friction stage (as it represents the assessable friction behaviour), the colour has reflected an obvious impact for both applied loads specimens. The white colour samples have reported the highest friction coefficient. The lowest friction coefficient was observed at the grey coloured test pieces, whereas the black colour was in between.

Fig. 4.2. compares the friction behaviour of three identical specimens tested under the same conditions. The friction coefficient behaviour of all samples was in good agreement as their curves were almost consistent throughout the sliding distance. This indicates the reliability of the specimens' manufacturing method and testing procedure.

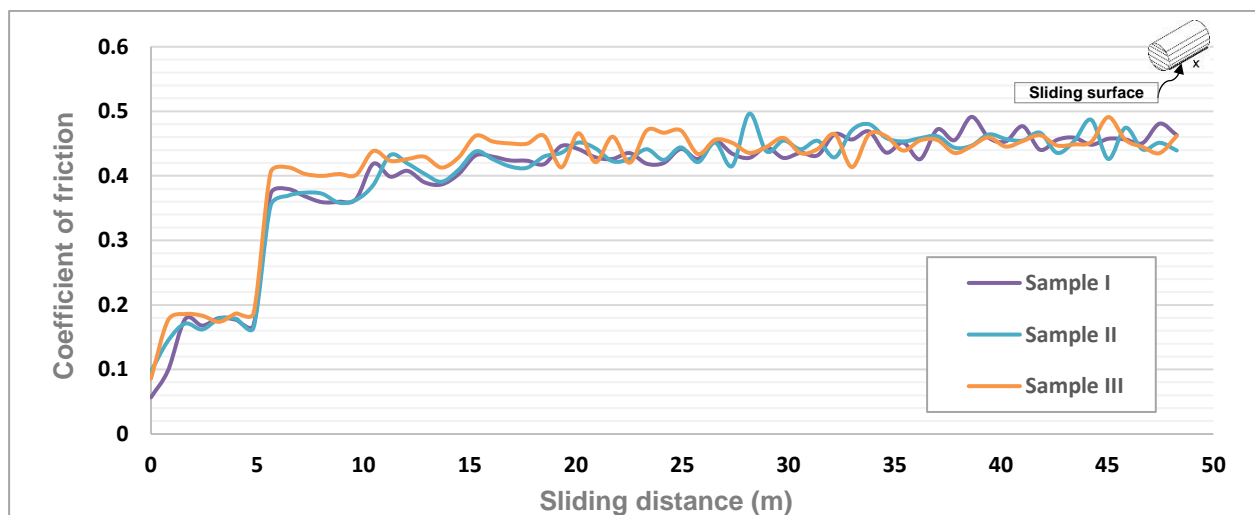


Fig. 4.2. Comparison of friction behaviour curves of three identical specimens (white colour PLA, horizontally printed, and tested under 150 N load).

The averaged values of the dynamic friction coefficient (in the stable stage) for all specimens (three print orientation, three colours, and two applied load) were calculated and presented in Fig. 4.3. In all conditions, the white polymer exhibited the highest friction, while the grey colour samples offered the lowest friction except in the case of Horizontal under 200 N load.

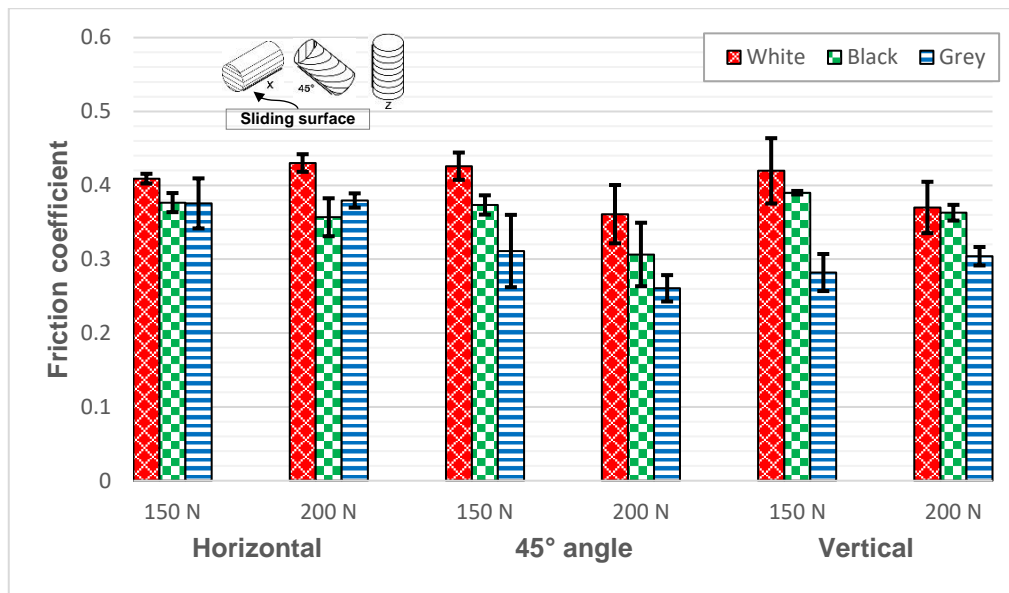


Fig. 4.3. Average dynamic friction coefficient

For 150 N applied load (under lower load), the colour has no significant effect on the Horizontal orientation's friction. However, in the 45° angle and the Vertical, the colour showed notable influence. Concerning the 200 N applied load (under higher load), the colour has affected the test pieces' friction in all orientations.

Comparing the impact of low and high loads (150 and 200 N) among the same print orientation specimens, the friction of white samples in Horizontal orientation increased at higher load. Meanwhile, no considerable effect has been observed in grey and black colours. Nonetheless, the friction coefficient in most of the remaining test pieces (among 45° angle and Vertical orientations each alone) decreased at a higher load. This is because the friction coefficient generally decreases with increasing load for polymers due to an alteration in the dominant friction mechanism (Voyer et al., 2019). The lower load makes less deformation in the contact zone (small contact surface), therefore the contact pressure is higher. In comparison, the higher load leads to bigger deformation in the contact area and thus less contact pressure (Muhammad Nuruzzaman et al., 2011).

Fig. 4.4 exhibits maximum values reached in the static and dynamic friction coefficient. The static coefficient of friction is always higher than the dynamic. Both static and dynamic friction coefficients were plotted in one column for each condition and colour. The reason for showing such a combined column is to figure out the stick-slip tendency of each tested specimen versus different colours, printing orientation, and applied load during the tribotest. The stick-slip phenomenon can be observed by means of the contrast rate between the static and dynamic friction coefficient. The more the variance between the static and dynamic coefficient of friction, the bigger the stick-slip tendency existence (Popov, 2010). From the results demonstrated in the figure, generally, the static friction coefficient under a high load (200 N) was at a decreased rate compared to the lower load (150 N). The distinction between the static and dynamic friction coefficient values under lower applied load was large but within the same range at all orientations and colours. However, the white colour has various ranges in each orientation at a higher load, whereas black and grey were at almost the same moderate rates. The lowest values in terms of the static and dynamic friction coefficient and the divergence between them have been noticed in 45-degree orientation under higher load. The above means that all specimens under low load showed significant stick-slip tendency compared to the high load. This would agree with the research of Voyer et al. (2019), where they found out that at low normal loads, a higher stick-slip tendency was observed for PA6 material.

## 4. Results and discussion

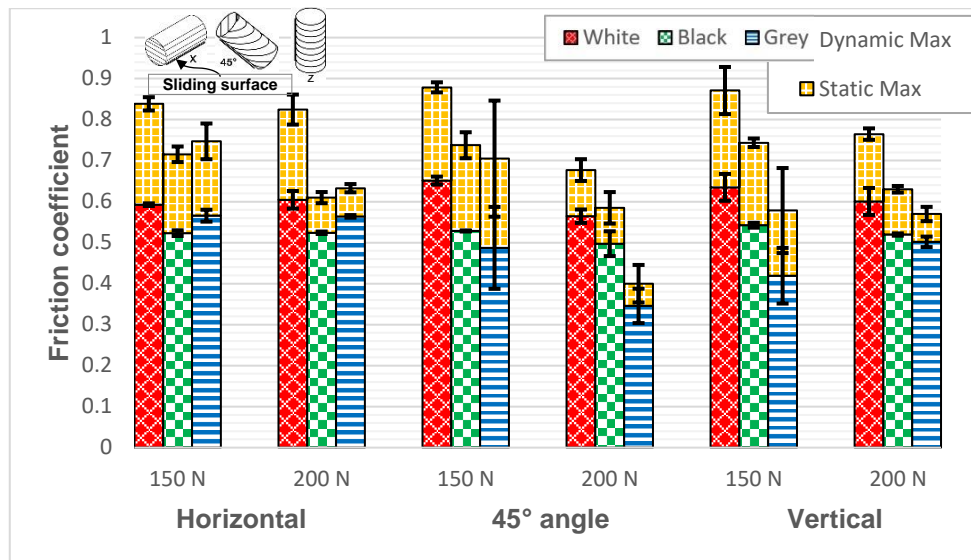


Fig. 4.4. Comparison between maximum static and dynamic friction coefficient

### 4.1.1.2. Influence of process parameters and filament colour on wear

Fig. 4.5 shows a comparison of the average wear depth obtained during the tribology test. Evident from this figure, there is a large effect for the print orientation and applied load on the wear depth of differently coloured samples. It can be clearly seen that the wear of the specimens in 45-degree orientation under high load decreased in all cases, prominently at the black and grey. However, in Horizontal orientation, the wear increases with increasing the load at white and grey cases, but the black decreased. The Vertical orientation test pieces exhibited similar behaviour against each applied load (specifically black and grey), except the white decreased the wear under higher load.

In terms of the effect of various print orientations, the 45° angle workpieces have shown an elevated wear attitude due to the gaps between the printed layers (space between asperities) at the sliding surface, as illustrated in Fig. 4.6, making the contact area smaller. The smaller the contact area with the counterpart (sliding plate), the higher the wear depth behaviour due to increasing the pressure at the junction points. This causes the junction points to wear off faster and thus increases the rate of wear depth.

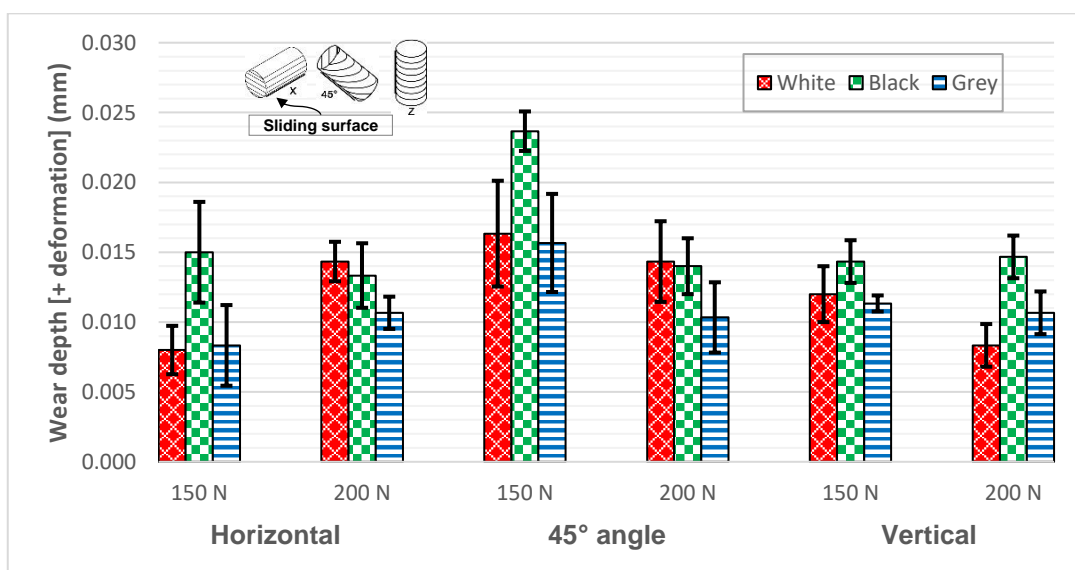


Fig. 4.5. Average wear depth comparison

#### 4. Results and discussion

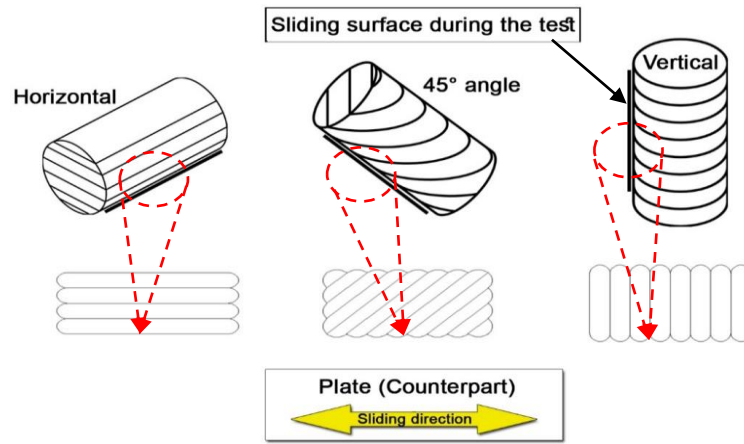


Fig. 4.6. The contact surface structure of different build orientation specimens

The different colours of PLA polymer also showed somewhat an effect on the wear depth. Mainly, the black coloured specimens reported a high wear depth. In contrast, the white and grey test pieces in most cases were within the same moderate range. There is no certain interpretation in literature about why the wear depth of black colour has increased higher than other colour samples. But the author believes that due to the sliding with the counterpart, the frictional heat boosts the temperature (conduction heat transfer) of the specimen's surface. Hence, the black colour samples may be subject to the black body features where maximum heat retains in the test piece's body. When the temperature at the contacts increases, the shear strength of the specimen (polymer) decreases due to the occurrence of thermal softening. As a result of this, transferring films and adhesion became the prevailing wear type rather than micro-cutting and abrasion (Şahin et al., 2017). Therefore, the sliding surface layers melt faster, causing higher wear depth. For proving this, heat conductivity tests were conducted on the same examined tribological specimens to compare the thermal behaviour of different PLA colours. The details about these experiments and their results are explained in section 4.1.1.3. On the other hand, Wittbrodt and Pearce (2015) evaluated the mechanical properties of 3D-printed PLA with five colours (white, black, blue, grey, and natural) to figure out whether different filament colours exhibit various characteristics. Their results have shown a strong relationship between percent crystallinity and tensile strength of 3D-printed samples. Further, they disclosed that for optimizing the crystallinity, a critical printing temperature should be set for each colour. Thus, for the current work, the percent crystallinity of different filament colours might also have a significant influence on the tribological properties of 3D-printed PLA.

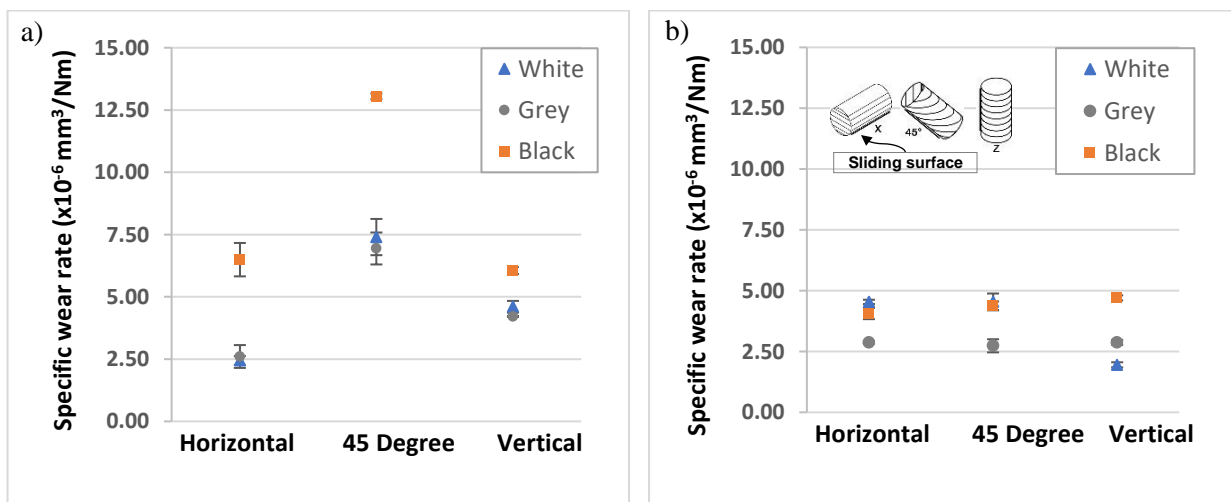


Fig. 4.7. Specific wear rate at a) 150 N load, and b) 200 N load

In general, a higher wear depth and implicitly specific wear rate, as shown in Fig. 4.7, was observed at low applied load. Regarding the high load, not much effect was detected on the specific wear rate at various print orientation. Şahin et al. (2017) studied the influence of four loads (ranged from 50 to 200 N) on the tribological properties of polyacetal. The wear rates of their samples varied from  $0.61 \times 10^{-6}$  to  $1.533 \times 10^{-6}$  mm<sup>3</sup> at the mentioned loads. They figured out that the wear rate reduced with growing the applied load. They attributed this to the impact of  $p\nu$ -value determination on wear rate, where  $\nu$  stands for the velocity and  $p$  for the load.

#### 4.1.1.3. Effect of different colours on thermal conductivity

The friction and wear characteristics basically depend on the generated frictional heat, which could not be directly measured in the present work due to the design of the used tribometer. Therefore, the issue was approached from a different direction. The contact temperature that affects the friction characteristics of the polymers is highly dependent on the thermal conductivity characteristics of the polymer. Different wear and friction values were obtained for various colours (white, black and grey) through the tribological tests on the same testing conditions and steel plate. This was attributed to the differences in heat conduction conditions due to the effect of different colours and their associated additives. To substantiate this hypothesis, the polymers of different colours were subjected to a simple test to determine whether the frictional heat is indeed more difficult to dissipate from the surface of different colouring (white, black, and grey) for the same PLA polymer. A schematic of the experimental setup used in this test is shown in Fig. 4.8.

As shown in Fig. 4.8, a constant heat input was created with an electronically controlled industrial heat gun. The different heating curves were obtained by measuring the heating effect of the heat input at the same points. This was done through a thermocouple pair placed into holes close to the two opposite faces of the cylindrical specimen (by computer evaluation).

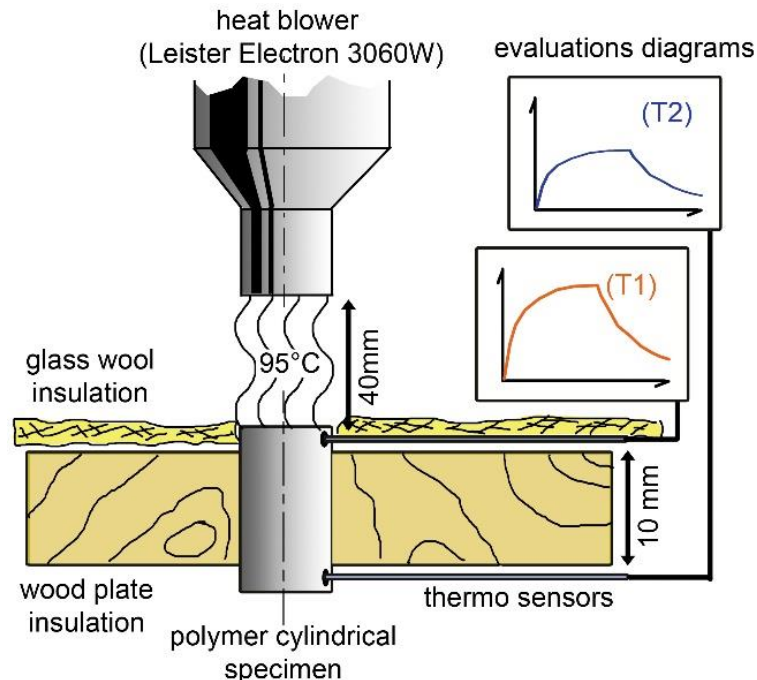


Fig. 4.8. Rapid test method for determining which colour (pigment) has a worse effect on heat conduction ( $T_{\max}$  - maximum temperature at the point of heat input,  $T_1$  - temperature closer to heat input,  $T_2$  - temperature on the other side of the specimen farther from heat input)

Fig. 4.9 helps to understand the different thermal conductivities caused by different colourings with the surface temperature change over time. The diagrams contain three curves, the temperatures of the "heated" and "cold" sides and their difference as a function of time. After

#### 4. Results and discussion

reaching  $T_{\max}$  ( $\approx 90-95$  °C) during heating (this was also the set value on the heating blower), the heating source was switched off at  $T_d = 47$  °C for the temperature difference between the two opposite surfaces. The specimens were then allowed to cool until the temperatures on both sides equalized.

The results show that white PLA needed the shortest time (230 seconds) for reaching the required temperature difference (47 °C) and for cooling (638 seconds). For grey and black PLA, a longer time was observed for achieving the temperature difference wanted (grey 458 seconds and black 310 seconds) and for cooling (grey 889 seconds and black 909 seconds). In summary, the thermal conductivity of the white-coloured PLA raw material is clearly more favourable than that of the grey-coloured and black-coloured raw material.

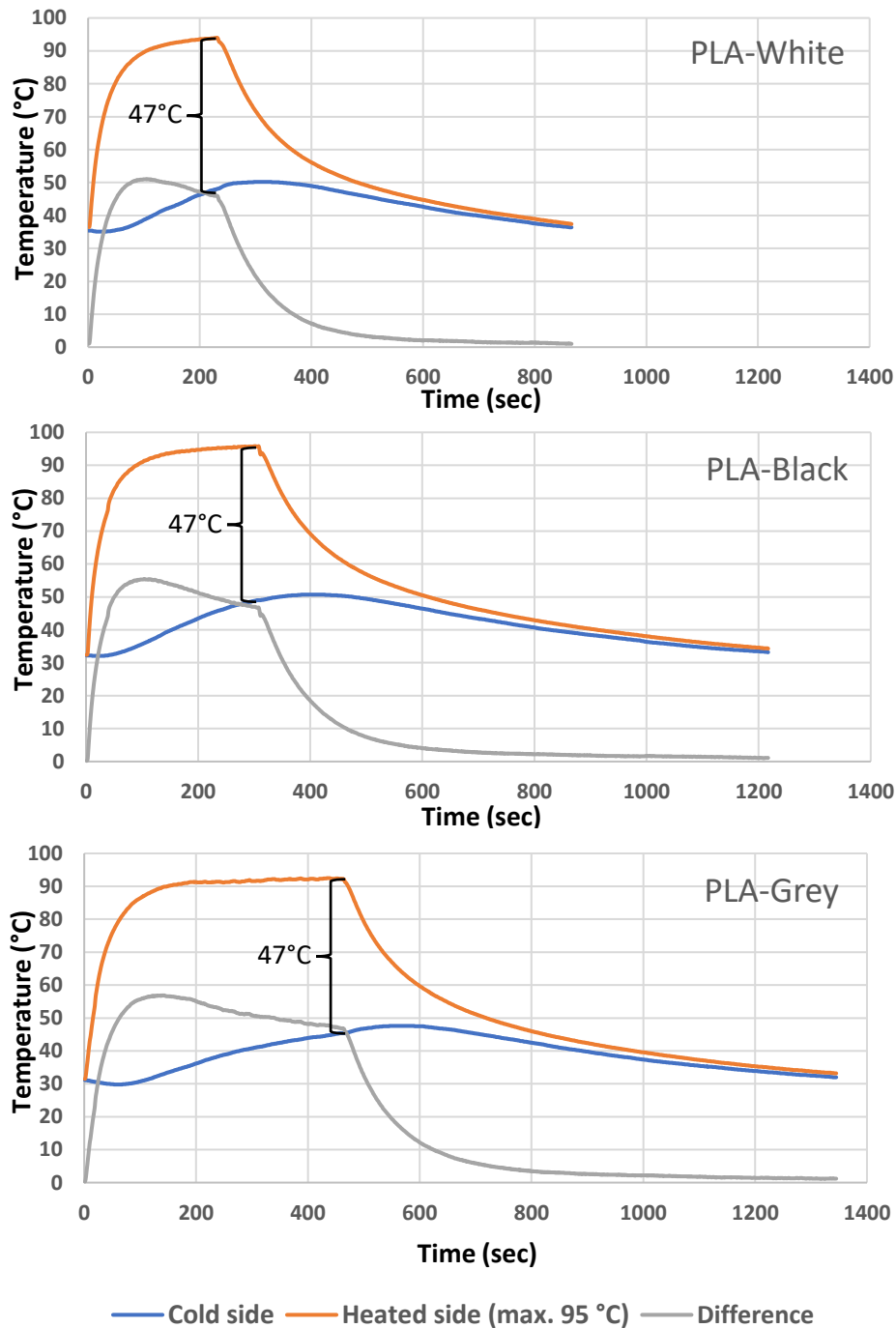


Fig. 4.9. Results of thermal conductivity tests for differently coloured PLA polymer specimens



Observations point to some obstruction of heat conduction in the case of black and grey staining, which means the formation of higher temperatures between the contact surfaces. The effect of this can be well traced to higher wear in most cases of black-stained PLA. When the material retains heat for a longer time during the cylinder-on-plate tribology system test, the sample body cannot cool down while reciprocating movement (change sliding direction) but continues to increase the heat as the sliding progresses. Therefore, the black keep increasing heat, softening the contact surface and causing higher wear depth. However, it has the opposite effect on the friction behaviour order, as the white then black and the lowest grey PLA sequence showing higher friction can also be attributed to the heat conduction order.

#### 4.1.2. Tribology of bronze/PLA composite material FDM 3D-printed

After evaluating the tribology test data results, the static and dynamic friction coefficient has been obtained. The main points of the investigated data are summarized in Fig. 4.10. Considering both loads (150 N and 200 N) results, it can be seen that Horizontal and 45° angle have the least dynamic friction coefficient, whereas the Vertical offered the highest friction coefficient values. This can be expounded due to the layers' structure, which is in contact with the sliding surface. However, it can be noticed a bigger difference between the dynamic and static friction coefficients under the load 150 N. What means that sliding under lower loads, increase the tendency for occurring stick-slip phenomenon. As it was possible to hear higher noise while testing Vertical specimens, which indicates the happening of this phenomenon as well. Bearing in mind that under the higher load (200 N), these differences decreased. Therefore, the instability of the sliding also decreases. The friction strongly depends on the sliding surface structure. It is apparent in Fig. 4.6 that various print orientations result in different surface roughness. The smoothest surface is given by Horizontal and the roughest by Vertical orientation. This basically determines the pressure between the two paired surfaces, which denotes the importance of the surface structure.

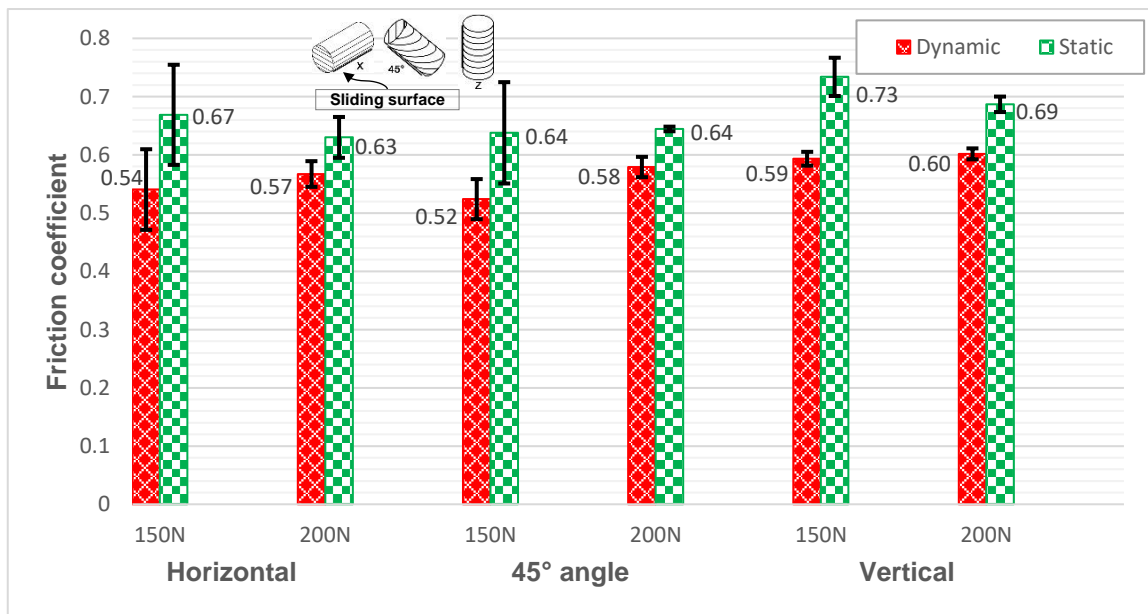


Fig. 4.10. Comparison of average static-dynamic friction coefficient

Comparison among the average wear depth that occurred during the tribology test is displayed in Fig. 4.11. The test pieces exhibited similar behaviour in all orientations against each applied load (150 and 200 N). At the lower load, less wear was observed. The Vertically oriented samples showed the least wear, due to the layer structure. Since its contact area with the sliding counterpart is smaller than the other print orientation samples. Whereas the 45° angle and Horizontal

workpieces have offered elevated wear attitude. This is because a bigger surface area is in contact with the sliding plate. Certainly, the lower wear rate specimens are preferable for many implementations.

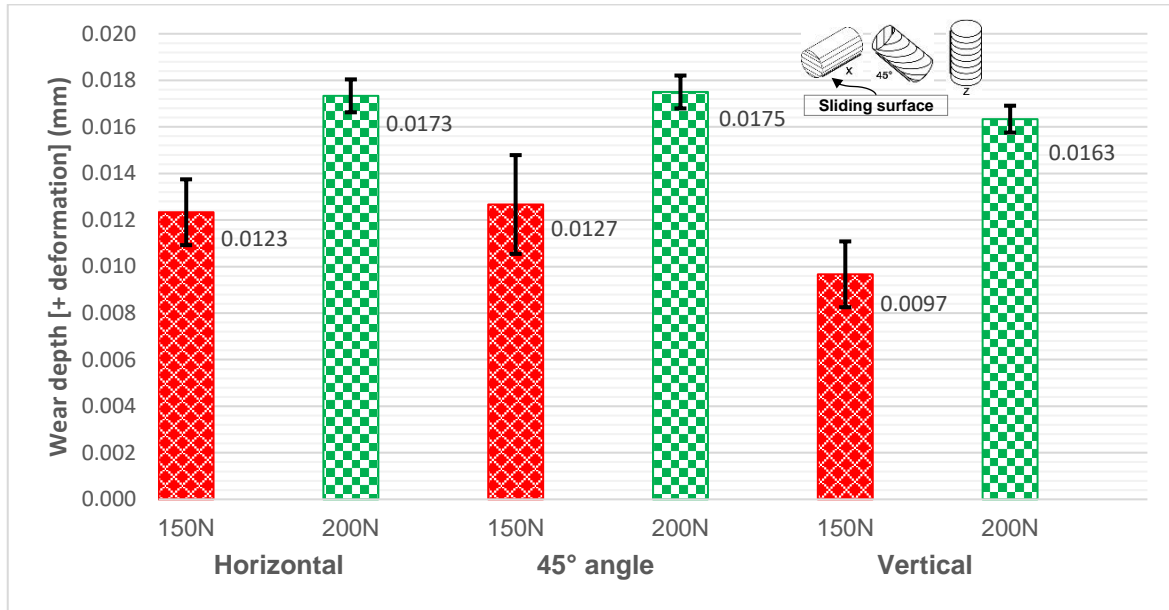


Fig. 4.11. Comparison of average wear depth for each print orientation

The above demonstrates the considerable effect of the layer structure for the sliding contact surfaces on both friction coefficient and wear. This finding suggests optimizing the print orientation to be more suitable for each case of usage to choose whether the whole print orientation of the product must be changed or only at the required working surface.

The dynamic friction coefficient of all examined orientations for the used material (bronze/PLA) has ranged with an average of (0.52 - 0.6). The measured wear depth has averaged with values between (9.7 to 17.5  $\mu\text{m}$ ). These wear depth values give a specific wear rate about (3.3 - 6.1  $\text{mm}^3/\text{N}\cdot\text{mm} \times 10^{-9}$ ), respectively. Hence, in order to determine the influence of bronze existence on the tribological properties, the findings should be compared with wear and friction of neat PLA achieved in literature. Hanon et al. (2019) reviewed the tribological behaviour of 3D-printed PLA with two different colours. In general, the coefficient of friction for PLA has ranged with a value of approximately (0.5). While the wear depth of the white PLA was measured about (150  $\mu\text{m}$ ). The specific wear rate for neat PLA was calculated by Bajpai et al. (2013). When employing a relatively low load (30 N), the specific wear rate reached  $3.2 \times 10^{-9} \text{mm}^3/\text{N}\cdot\text{mm}$ . Comparing the present results with the prior studies indicate that bronze addition has improved the wear behaviour of PLA but kept the friction coefficient at the same range. This trend corresponds with what mention by Unlu et al. (2010) and Unal et al. (2010), where the reinforcement by bronze has improved the wear resistance even if the friction more or less remains the same. Guo et al. (2018) evaluated the influence of post-processing on tribology performance and surface characteristics of Polyamide 12 (PA12) specimens manufactured by selective laser sintering. The authors proposed subjecting the surfaces to the so-called magnetic field assisted finishing (MFAF) as a post-processing method that comes after precision grinding. The processed surfaces presented a better tribology performance demonstrated by higher wear resistance and a lower coefficient of friction. This indicates the possibility of employing such post-processing methods to improve the tribological properties of 3D-printed polymers.

#### 4.1.3. Tribology of neat resin material DLP 3D-printed

The tribological tests were investigated for specimens at each build orientation (X-Horizontal, 45° angle, and Z-Vertical) in parallel with the post-curing process presence. These two factors were examined in order to determine their effect on the friction and wear behaviour.

As shown in Fig. 4.12a, the dynamic friction coefficient obtained from the post-curing process specimens exhibited no significant difference (between 0.72-0.79) among the samples of various print orientations. Nevertheless, the tendency for occurring stick-slip phenomenon has notably increased. This specifically occurred in the red colour 45°, and white colour Horizontal and Vertical build orientation specimens, where the static friction coefficient reached very high values. In contrast, relatively reduced values were observed in the friction coefficient (whether static or dynamic) of the non-cured specimens for all build orientations.

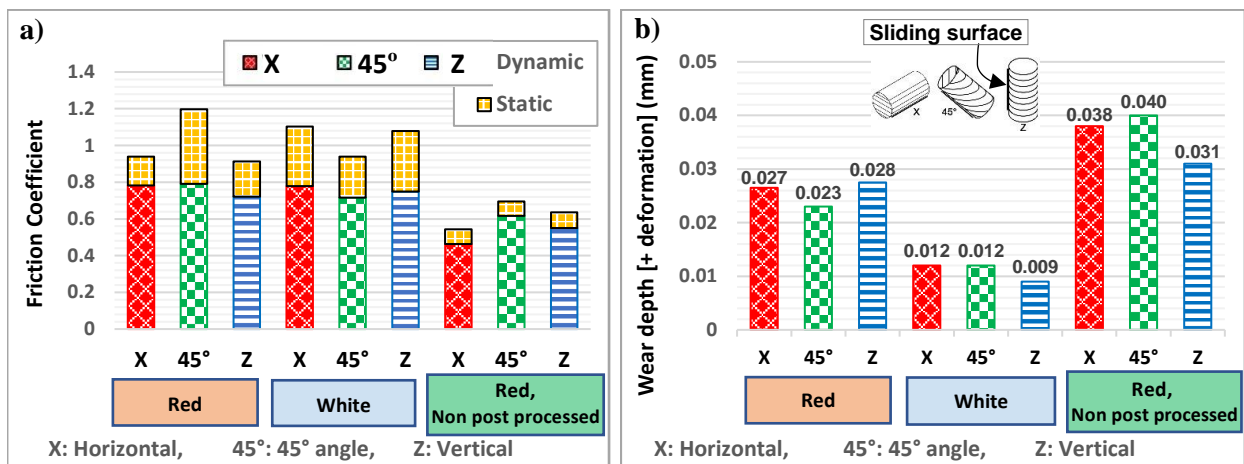


Fig. 4.12. Comparison of the tested specimens at each print orientation angle and UV post-curing process concerning the a) friction coefficient, and b) wear depth

Comparison of the wear depth among the tested prototypes in terms of print orientation and the post-curing process is displayed in Fig. 4.12b. The non-cured specimens demonstrated the highest wear depth as compared to the post-curing test pieces. This indicates the impact of the post-curing process on the hardness (increased) of the surface, that gave the cured specimens better wear resistance. As well as the effect of the post-curing process, a new factor influenced the wear results, which is the colour of the material. The red coloured specimens revealed higher wear depth values in front of the white specimens. This could be explained due to the existence of pigments in the samples' material. Therefore, the presence of these pigments might increase the temperature of the sliding surfaces during the test and subsequently boost the wear tendency. On the other hand, no remarkable impact on the wear behaviour was reflected regarding the different build orientations when compared with the specimens of the same colour and post-curing state.

#### 4.1.4. Tribology of graphene/resin composite material DLP 3D-printed

Specimens were made of neat resin was tested first, followed by the graphene/resin composite specimens. The graphene/resin composite testing procedure has been divided into two phases because of the diversity of variables in the experiment (print orientation, layer thickness, and the graphene content ratio in the mixture). In phase one, tribological tests were used to examine the specimens in different print orientations and layer thicknesses with the same graphene content ratio (0.5 wt.%). According to the best results obtained during phase one tests, phase two proceeds where different graphene content ratios were assessed (1 and 2 wt.%) after manufacturing new specimens using only the optimal print parameters obtained. The static and dynamic coefficients

of friction were obtained after evaluating the test's recorded data. The difference between the maximum values of the dynamic and static friction coefficient help determine the stick-slip tendency (Popov, 2010).

### 4.1.4.1. Friction coefficient behaviour profile

Comparison of the profiles of friction coefficient during tribology tests under a load of 150 N is presented in Fig. 4.13a–d as a function of sliding distance. The coefficient of friction presented in Fig. 4.13a–c concerns the layer thicknesses of 35, 50, and 100  $\mu\text{m}$ , respectively. These compared specimens were made of neat resin and graphene/resin composite with graphene content of 0.5 wt.%. However, the comparison among the friction coefficient of different graphene content ratios (0, 0.5, 1, and 2 wt.%) for only the horizontally printed pieces with a layer thickness of 35  $\mu\text{m}$  are shown in Fig. 4.13d.

Generally, the friction coefficient profile curves go through three stages called running-in, fluctuation, and stable friction, as aforementioned in section 4.1.1.1. The curves show a sharp increase in the running-in stage because of the static friction behaviour. At the beginning of the friction, there is initially a clear polymer-metal contact. The polymer then quickly begins to build a film layer (transfer film) due to the adhesion mechanism of friction to the metal surface. Polymer-polymer/metal contact is thus rapidly formed. Friction between materials with the same chemical composition is higher, meaning it quickly increases at the very beginning of the sliding. This is mostly applicable for the pairing of soft-hard materials, especially polymers. This stage terminated almost by the end of the first ten meters of the sliding distance in all curves.

The length of the fluctuation stage differed for different curves as some of them lasted up to 40 m (e.g., most of the 100  $\mu\text{m}$  and some of the 35  $\mu\text{m}$  layer thickness specimens), 80 m (most of 50  $\mu\text{m}$ ), and 120 m (some of 35  $\mu\text{m}$ ) of sliding distance. Further, a few of them remained unstable roughly until the end of the test (such as 0.5 wt.% graphene specimens at "50  $\mu\text{m}$  in thickness and 45° angle orientation" and "100  $\mu\text{m}$  in thickness and Vertical orientation"). Moreover, the fluctuation stage entirely disappeared in all 0.5 wt.% graphene specimens that printed horizontally irrespective of the layer thickness.

The stable friction stage is regarded as the assessable period for friction behaviour as it represents the balanced phase. The curves obtained show that most of the neat resin test pieces reported an elevated dynamic coefficient of friction ranging from 0.6 to 0.7 in the stable stage. However, the addition of graphene significantly impacted the attitude of the friction coefficient. The coefficient of friction was reduced tremendously in most of the specimens that contained graphene than in those without it, primarily in the horizontally oriented samples regardless of the layer thickness.

The stick-slip phenomenon involves vibration and noise while friction. It occurs when there is a significant difference between the static and dynamic friction coefficients for a given material. It is noticeable with high sliding friction and is also observed when low sliding friction is coupled with higher adhesion friction. A dry friction coefficient value of 0.4-0.5 does not count as small (this is otherwise normal for plastics at this value). Low dry friction could be between metal and metal, e.g., a value of 0.1. However, this can go below 0.05 for lubricated systems. On the other hand, the stick-slip phenomenon can also be detected by a significant difference between the measured values of the friction and adhesion coefficients. This is why this work investigated the friction in a reciprocating system, where the adhesive friction at each change of direction (momentary stop) alternates with the motion (sliding) friction between the two endpoints. With this model system, the two values can be detected together.

#### 4. Results and discussion

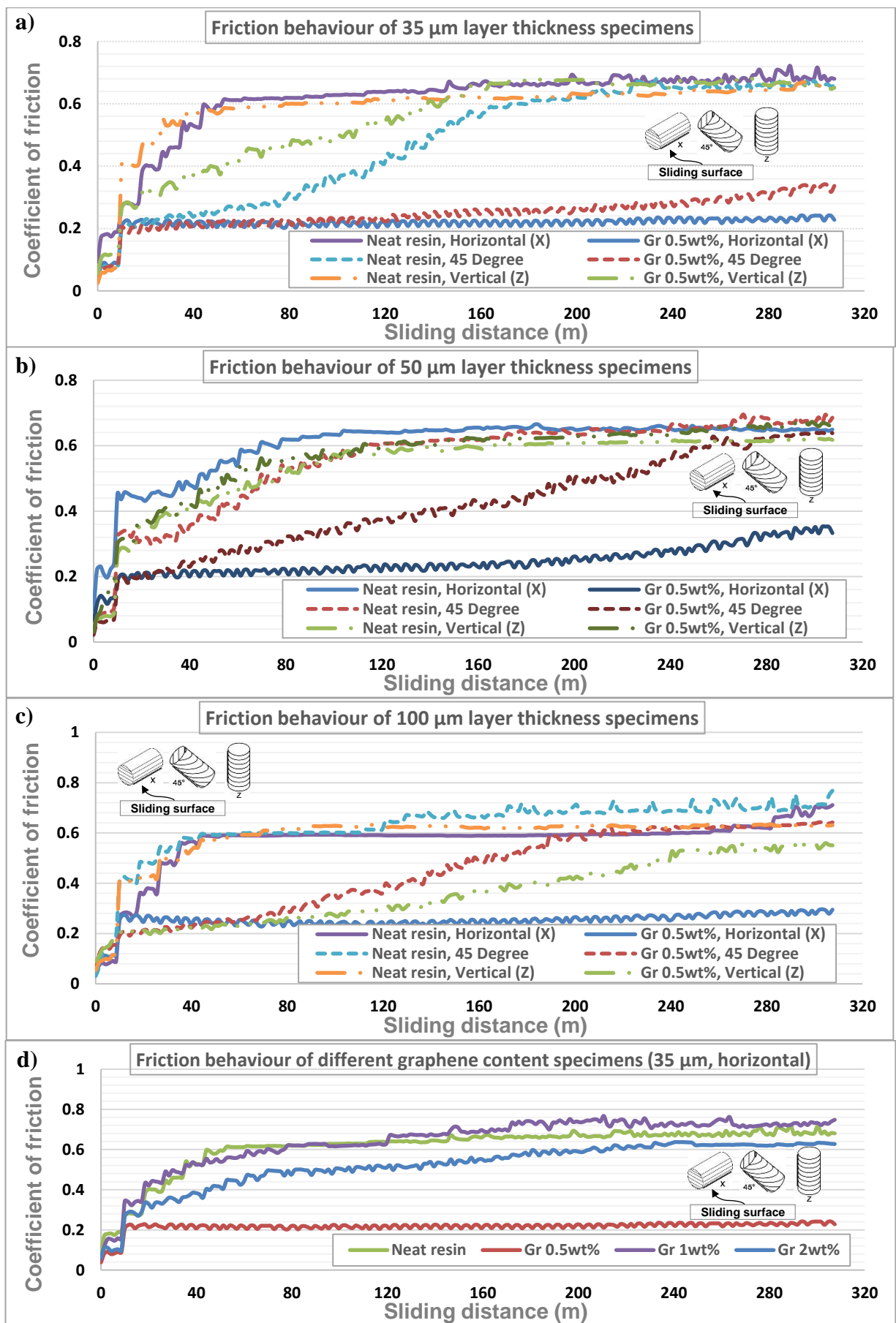


Fig. 4.13. Comparison of the friction behaviour profile of specimens with a layer thickness of a) 35  $\mu\text{m}$ , b) 50  $\mu\text{m}$ , c) 100  $\mu\text{m}$  made of neat resin (0 wt.% graphene) and graphene/resin composite (0.5 wt.% graphene), and d) 35  $\mu\text{m}$  for materials with different graphene ratios (0, 0.5, 1, and 2 wt.%)

## 4.1.4.2. Static and dynamic friction coefficient

Friction-wear testing is a dynamic process as the coefficient of friction continues to fluctuate throughout the sliding. The behaviour of friction can be plotted versus the sliding distance/time as a continuous curve until the sliding ends (as demonstrated in Fig. 4.13). A few of the tested specimens can therefore be represented by these curves (maximum one sample for each condition). There are two reasons for this: from one side, it is difficult to follow multiple curves in a single graph. For this reason, the curves of Fig. 4.13 were split between four graphs. On the other hand, it is impossible to show the standard deviation of the results for the three identical samples that were examined for each tested condition. The friction and wear outcomes were therefore presented in column graphs (see Figs. 4.14 and 4.16) in order to compare all the specimen results and their standard deviations. To extract a single value representing the average friction coefficient for each specimen, a point was selected within the curve's stable stage (in particular, at 200 m of sliding distance). For the present work, the stable stage was generally considered the last third of the curve.

The max (static and dynamic) friction coefficient and dynamic average friction coefficient are compared in Fig. 4.14a and Fig. 4.14b, respectively. The compared results involve both neat resin and graphene (0.5 wt.)/resin composite material specimens at all tested parameters (print orientations and layer thicknesses). For neat resin specimens, static max and dynamic max friction coefficients have reached significantly high values because of the characteristic of DLP 3D-printed resin material products where the property of adhesion increase (M M Hanon and Zsidai, 2020). Therefore, the dynamic max disclosed a friction coefficient ranging from 0.7 to 0.96. Regarding the distinction between the static max and dynamic max values, the Vertical (all) and 45° angle (only 0.5 wt.% graphene) specimens exhibited a larger difference, thus indicating an increase in the stick-slip phenomenon (Popov, 2010). Nevertheless, Horizontal (almost all) and 45° angle (only neat resin) specimens revealed almost moderate variance between static and dynamic max. In terms of the dynamic average friction coefficient comparison between samples with and without graphene content, a significant difference was observed in the coefficient of friction because of graphene. The values clearly decreased and roughly reached, in some cases (particularly in the Horizontal), to half of the corresponding value in the neat resin material chart. This may be because of the effect of graphene as a solid lubricant (Berman et al., 2014). Despite all values of 0.5 wt.% graphene specimens decreasing compared with pure resin, the friction coefficient of Vertical and 45° angle pieces remained somewhat raised because of the surface structure of these orientations. These surfaces have asperities and cavities (rough surface) at the contact area of the tribology test (see Fig. 4.15b). Such asperities boost the friction coefficient by increasing the pressure caused by reducing the contact area (Dawoud et al., 2015; Nirmal et al., 2015). This led to the augmented values observed for the friction coefficient despite the presence of graphene.

The effect of process parameters was mainly investigated on the neat resin specimens where the influence of graphene platelets has not yet existed. The layer thickness was not found to impact the friction coefficient much as its values were comparable among the specimens having the same print orientation. However, a notable effect on the friction was observed regarding different print orientations. For Horizontal, higher friction was provided as there would be greater adhesion on a large sliding area (contact surface between the sample and the counterpart) (Yu et al., 2011).

Fig. 4.14c presents the comparison of the dynamic average friction coefficient between neat resin and different graphene contents. This second round of tribological tests was performed solely to examine the impact of increased graphene content, but not the printing process parameters. As they showed the best results in phase one, Horizontal orientation and layer thickness of 35 µm were chosen as the printing parameters for phase two. The results showed that increasing the percentage of graphene beyond 0.5% by weight did not reduce the coefficient of friction. Hence,

#### 4. Results and discussion

for the used graphene/resin composite material in this work, the graphene percentage of 0.5 wt.% was considered the optimum ratio for attaining the best friction behaviour results.

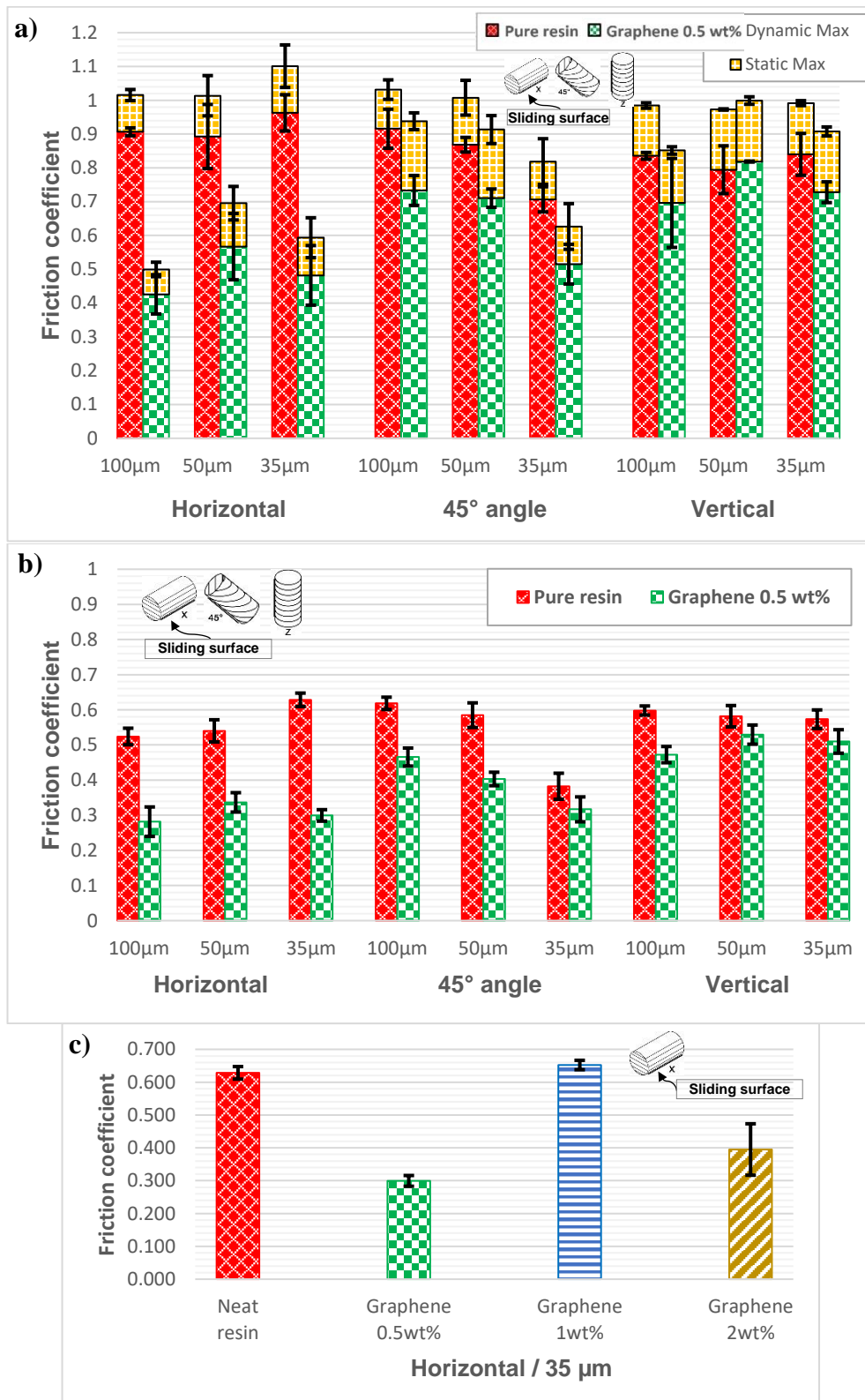


Fig. 4.14. Comparison of a) maximum value of static and dynamic friction coefficients among the specimens of neat resin (0 wt.% graphene) and 0.5 wt.% graphene concentration, b) dynamic average friction coefficient of pure resin (0 wt.% graphene) and 0.5 wt.% graphene content samples, and c) dynamic average friction coefficient of pieces with various graphene ratios (0, 0.5, 1, and 2 wt.%)

## 4.1.4.3. Wear depth and specific wear rate

The irregularities on the friction surface of the printed specimen (roughness peaks resulting from the printing layers) come into contact with the opposing surface on a small surface when the slip starts. The surface pressure will therefore be high at start-up, and the wear will increase intensively. These irregularities are later smoothed out (or elastically deformed, possibly melted) as a result of the initial rapid wear, so the surface pressure decreases due to the increased contact zone. This has a positive effect on wear (increased load-bearing surface), so the wear curve usually flattens out after the initial rapid rise (running in stage zone) and wear slows down.

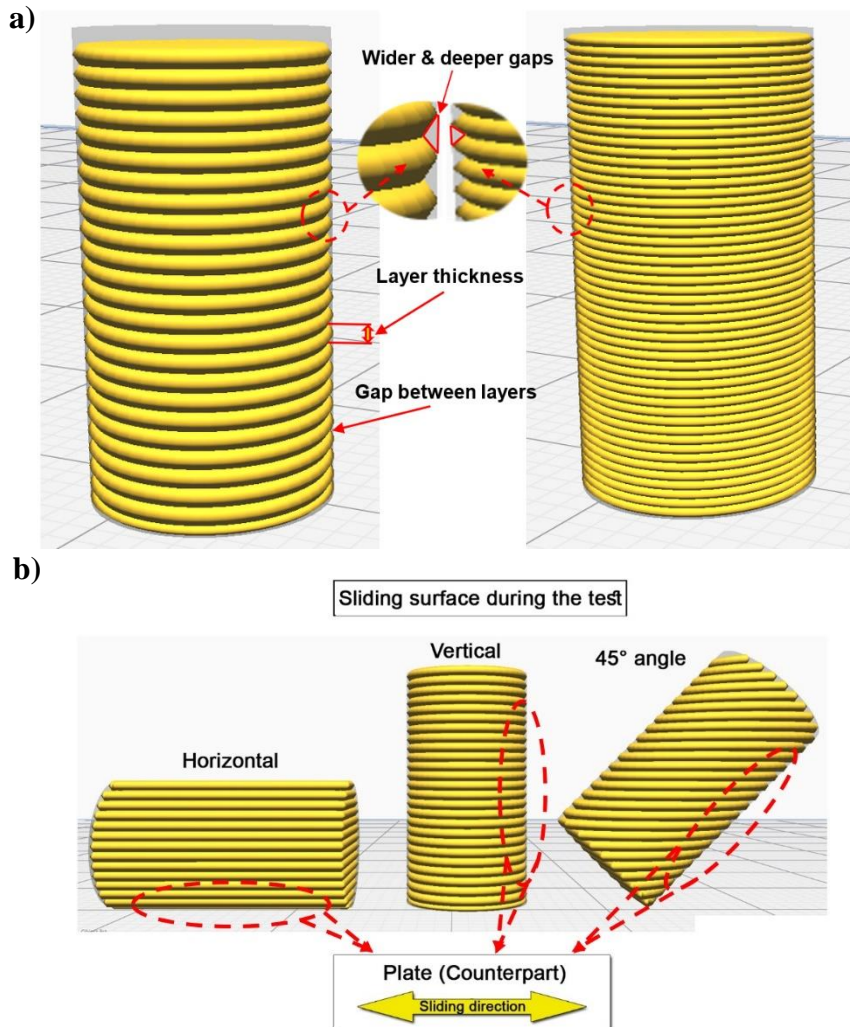


Fig. 4.15. Illustration of a) gaps among layers for specimens printed with a layer thickness of 100 μm (left) and 35 μm (right), and b) sliding surface roughness of different print orientations

For deeper insights into the influence of the 3D printing process settings on wear testing, see Fig. 4.15 for the surface structure of different layer thickness and print orientation specimens. Fig. 4.15a reveals that, despite the number of gaps among the layers of 35 μm thickness being significantly more than in the 100 μm layer height, the surface of 100 μm specimens is rougher than the 35 μm one. This is because the gaps among the 100 μm layers (larger thickness) are wider and deeper than the 35 μm. As in the friction coefficient, the wear also depends on the contact area (Hanon Marcisz et al., 2020a). Therefore, these deeper gaps cause the surface during the tribo-test to keep wearing off until the peaks disappear and reach a smooth surface. This may be regarded, in the case of graphene (0.5 wt.)/resin composite, as the reason for the increase in the wear at 100 μm layer thickness and decrease in the 35 μm samples. Fig. 4.15b illustrates how the sliding



face of the Horizontal sample is considerably smoother than that of the 45° angle and Vertical sample. The surface roughness is increased by the hills (peaks) and valleys (gaps) among layers that are not present in horizontally DLP 3D-printed faces (Muammal M. Hanon and Zsidai, 2020). These peaks wear off rapidly because of the increasing pressure applied by the normal load because of the smaller contact area (Hanon Alshammas et al., 2020). Accordingly, an elevated wear level was detected in the Vertical surface against the Horizontal.

The wear depth (measured by the displacement sensor) and the specific wear rate are the wear characteristic representatives in this work. Fig. 4.16a illustrates a comparison of wear depth for neat resin and graphene (0.5 wt.)/resin composite specimens under all tested printing settings (orientations and thicknesses). Concerning the Horizontal build orientation, generally, the graphene/resin composite specimens offered lower wear depth values than the neat resin specimens. This is because of the existence of graphene platelets in the sample's sliding surface. As the sliding surface of horizontally printed pieces is smoother, the presence of these graphene particles may provide better resistance to the specimen's surface (because of the harder surface of graphene) (Pang et al., 2018). However, the smoothness of the pure resin surface (horizontally orientated) makes the adhesion effect dominant (Zhiani Hervan et al., 2020), thus boosting wear tendency, which was obviously reduced by graphene. Therefore, when graphene/resin composite samples were compared with the identical ones of neat resin, it showed a remarkable influence on the wear behaviour. This subsequently resulted in the reduction of wear depth up to 27.2% and 31% at 50  $\mu\text{m}$  and 35  $\mu\text{m}$  thicknesses, respectively. This can be also connected to the alignment direction of graphene nanoplatelets within the polymer matrix. When the specimen is manufactured, the arrangement of graphene inside the polymer bulk resembles the isostress (see Fig. 4.17a) configuration. Hence, the alignment direction tends to have the lower surface area of graphene platelets facing the printing platform top surface. A similar approach to the proposed mechanism has been mentioned in other published research (Zhao et al., 2010; Li et al., 2016) regarding the graphene nanoplatelets' dispersion pattern. They indicated that the graphene oxide flakes were generally aligned parallel to the nanocomposite polymer matrix's top surface.

Based on the above, when testing the horizontally printed specimen, the graphene platelets in this print orientation have larger contact area during the tribo-test considering its arrangement direction at the specimen's bottom (Fig. 4.17a, sliding surface view). This large area helps to enable these platelets to act as a solid lubricant (Berman et al., 2014) and decrease the wear. On the other hand, the samples' wear depth of graphene/resin composite at 45° angle and Vertical orientations increased compared with that of the neat resin by 98% and 64% at the 100  $\mu\text{m}$  and 50  $\mu\text{m}$  layer thicknesses, respectively. This may be because of the surface roughness of these orientations' specimens, as their sliding surface (at the cylinder perimeter) is rougher than in the Horizontal (see Fig. 4.42a), which would cause significant wear from deformation (Myshkin and Kovalev, 2018). Furthermore, the graphene platelets' arrangement orientation caused the nanoplatelets' cross-section to face the sliding surface (see Fig. 4.17b) because the specimens of Vertical/45° orientation are placed to the flat (plane) position while testing. This makes the contact area much smaller and increases the roughness and the wear. This causes more wear of graphene specimens at these orientations than in neat resin.

Fig. 4.16b exhibits the wear depth of various graphene content (0, 0.5, 1, and 2 wt.%) for horizontally built orientation samples at a layer thickness of 35  $\mu\text{m}$ . The impact of increasing the graphene content on the wear depth was examined. The results showed that the most favourable wear depth was at graphene percentage of 0.5 wt.%, as increasing the graphene ratio to 1 wt.% or 2 wt.% did not improve the wear attitude. This may be because of the difficulty of curing the resin completely by ultraviolet light while increasing the graphene percentage, as curing depth is

#### 4. Results and discussion

diminished by graphene platelets. This leads to a fast deterioration of the specimen at the beginning of the wear test, and these graphene platelets can serve as a solid lubricant layer that protects from further wear.

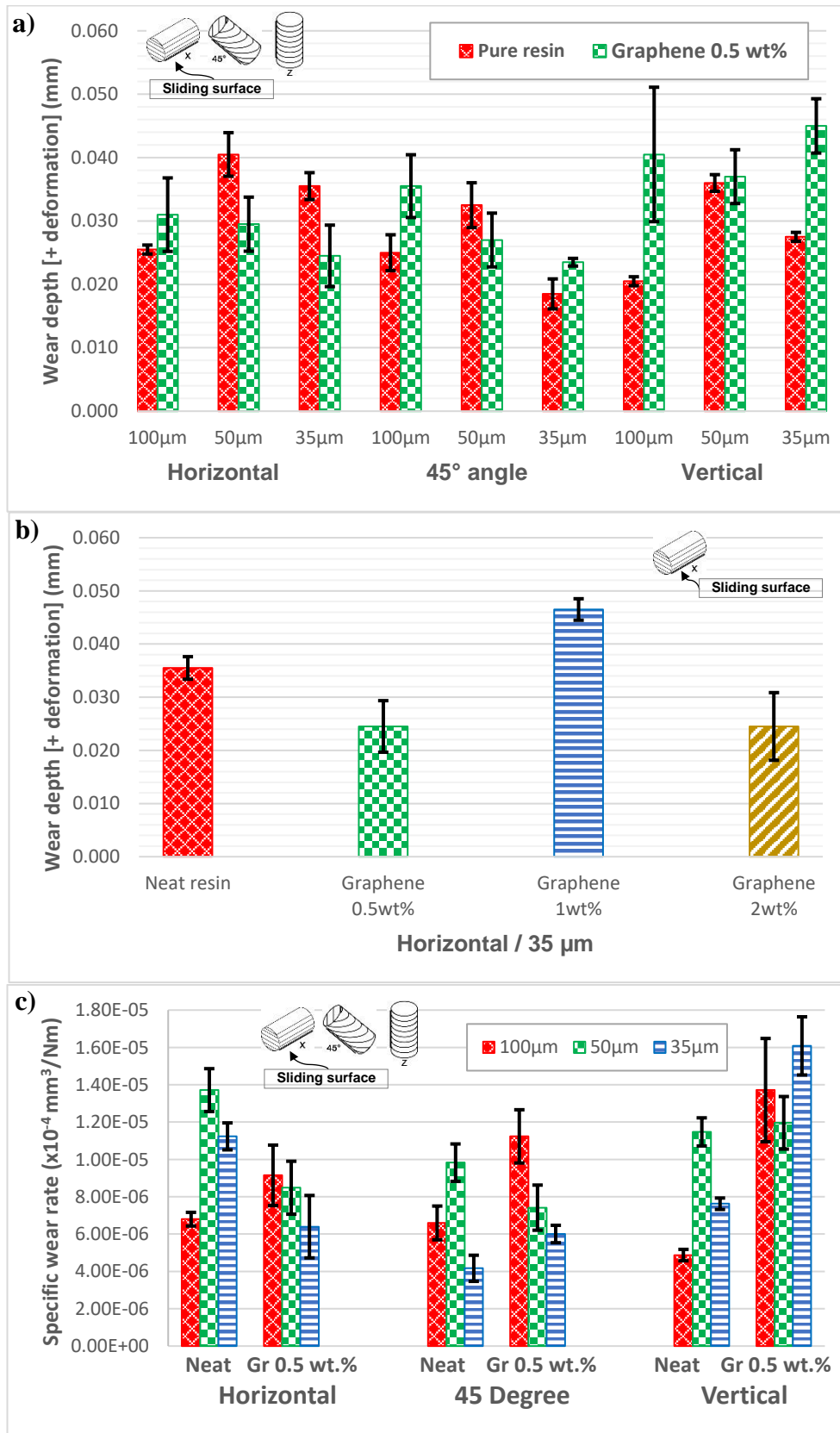


Fig. 4.16. Comparison of a) wear depth among samples of neat resin (0 wt.% graphene) and 0.5 wt.% graphene content, b) wear depth of specimens with varying graphene content (0, 0.5, 1, and 2 wt.%), and c) the specific wear rate of neat resin (0 wt.% graphene) and 0.5 wt.% graphene content pieces

In terms of the impact of graphene on the specific wear rate, Fig. 4.16c presents a comparison between the neat resin and graphene (0.5 wt.)/resin composite under various process parameters. The results confirm that the specific wear rate obtained is in agreement with wear depth results. The graphene/resin specimens at Horizontal build orientation reported a decline in the values of specific wear rate compared with that in the neat resin ones. On the other hand, its values inflated in the test pieces of 45° angle and Vertical print orientations, irrespective of the layer thickness. This suggests that graphene impacts the wear behaviour. Nevertheless, the printing process parameters seems to have more influence on the wear than the existence of graphene.

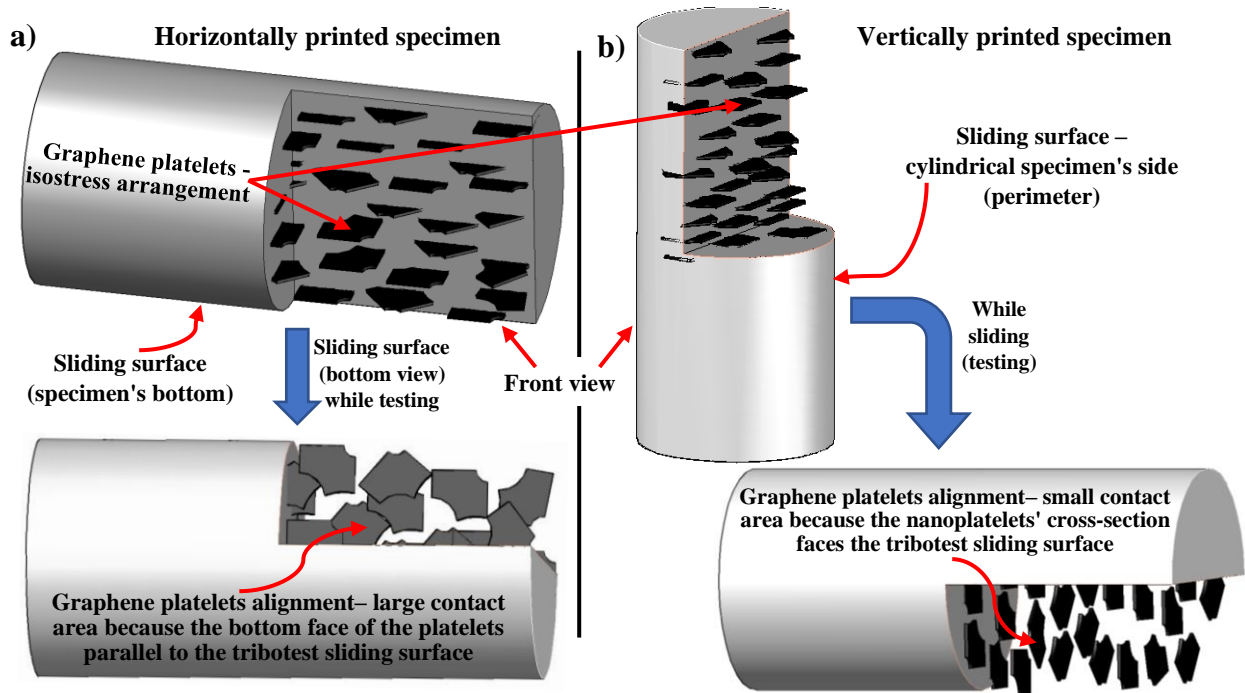


Fig. 4.17. Schematic of graphene platelets alignment in a) Horizontal and b) Vertical build orientation specimens

#### 4.1.5. Theoretical sliding surfaces as a function of measured wear

In the following, the wear (sliding) surfaces belonging to the given wear depths are determined by an approximate method using 3D CAD modelling. This is used to compare the effect of the macrogeometric layer orders created by the different printing orientations on the friction surface. To do this, the friction surface layers were first modelled in 3D using a parametric SolidWorks CAD program. Subsequently, the wear is simulated by cutting at given depths and the resulting wear surfaces are determined.

##### 4.1.5.1. Overview

In the present modelling study, the models are treated as a rigid body, taking into account only the wear and not the deformation. This is because the deformation (Hertz deformation) is well suited to be determined in metals with ideal geometries, but it is unsatisfactory here due to the viscoelastic properties of the polymers. The exact simulation is further complicated by the fact that the deformation of the corrugated surface due to the construction of the layer is only a part, followed by the deformation of the block material above the corrugated/wavy surfaces. In summary, this deformation consists of two parts, a gaped corrugated layer and a solid deformation above it. The solution could be to use the FEM method, but firstly, testing the polymer specimen's deformation properly would be required (e.g., an optical stress test used in mechanics). To do this, poly (methyl methacrylate) - also known as PMMA plexiglass - models would have to be used on each sheet formed with macro-surface roughness. Finite element simulations can then be performed with the

same PMMA material setting. This validation can only be started by simulating deformations and exploring (mathematical) regularities in other polymers. This goes beyond the scope and objectives of the current PhD work; it is a separate area of research. The modelling is justified by the corrugated surfaces created due to the construction of the FDM technology layer, which is negligible in DLP technology due to its smoother surface.

#### 4.1.5.2. Approximate definition of cross-section and creation of basic models

The cross-section of the FDM printed layer used in the present work was first determined. The diameter of the printer nozzle hole is 0.4 mm. It can be seen in Fig. 4.18 (left) that the free melting of the filament was based on a circular cross-section, while printing was based on a longitudinally deformed shape lying on the lower surface due to the layer thickness (0.2 mm). The flattened cross-section (shown on the right side in Fig. 4.18) was determined by calculating the two different contours with the same area.

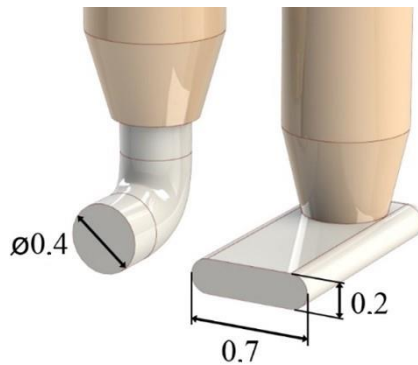


Fig. 4.18. Schematic of the filament's dimensions during the FDM 3D printing in context of, free-flowing (left) and layer printed in the layer thickness according to the initial cross-sectional area (right)

Using the layer cross-section thus determined, the surface layer models of the Horizontal, 45° angle, and Vertical orientations were created. Fig. 4.19 shows the three basic models.

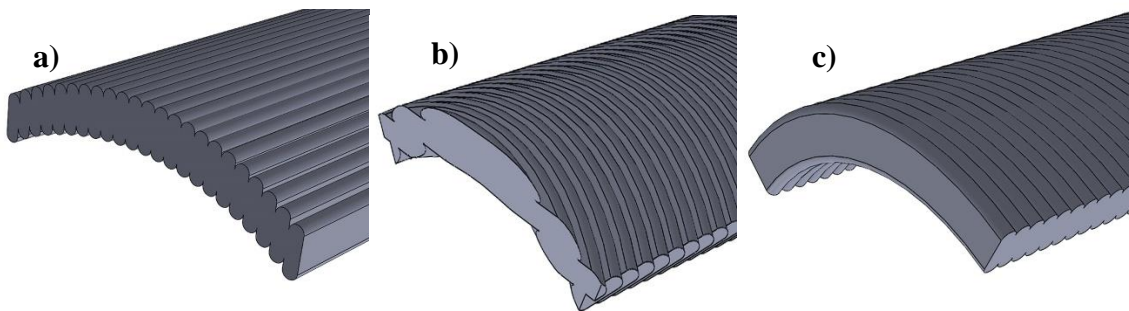


Fig. 4.19. Surface structure models of a) Horizontal, b) 45° angle, and c) Vertical orientations

The juxtaposition of the layers is done by simplification, along the sintering connection lines.

#### 4.1.5.3. Results of the approximate determination of wear surfaces

In the finished models, wear on the assumed sliding zone was achieved by cutting at different depths. An example of this is illustrated in Fig. 4.20, where the result of a 0.05 mm cut can be seen in red on the surface layers as it represents the friction contact surface.

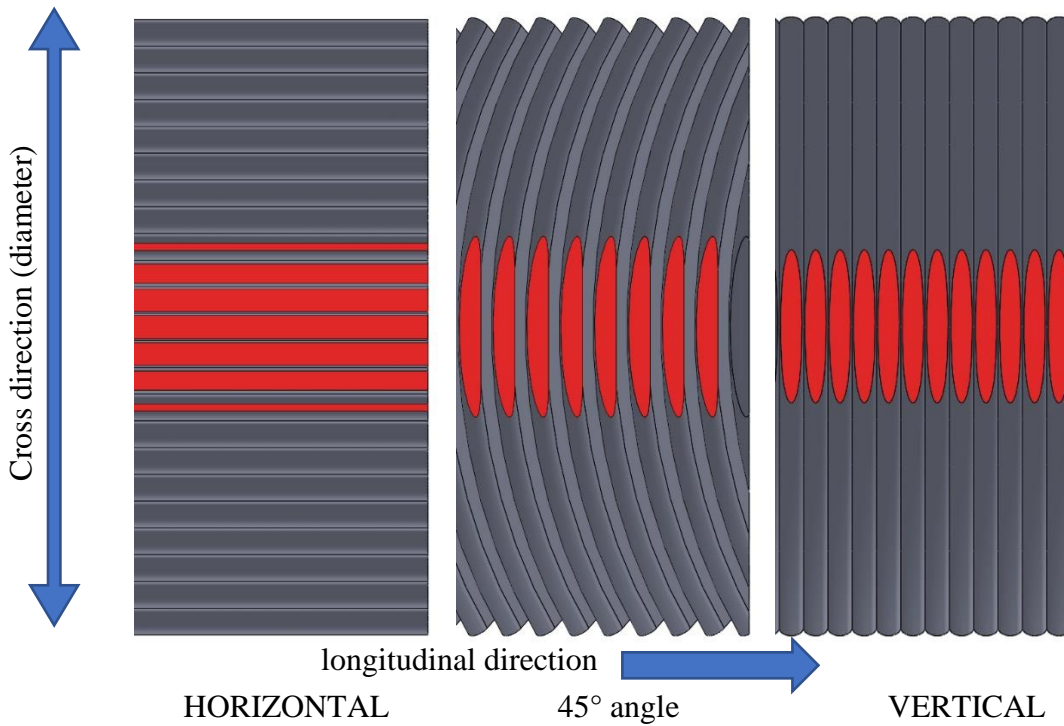


Fig. 4.20. Theoretical wear surfaces (marked in red) on the models' sliding area after cutting depth up to 0.05 mm

To approximate the no-load (deformation-free) contact surface at rest, a small (0.0001 mm) abrade was made, and surfaces were measured, the results of which are shown in Fig. 4.21. The figure shows that the Horizontal arrangement establishes the largest initial contact. Accordingly, the surface pressure and the expected initial deformation are the lowest here. The most significant deformation is assumed for the Vertical arrangement.

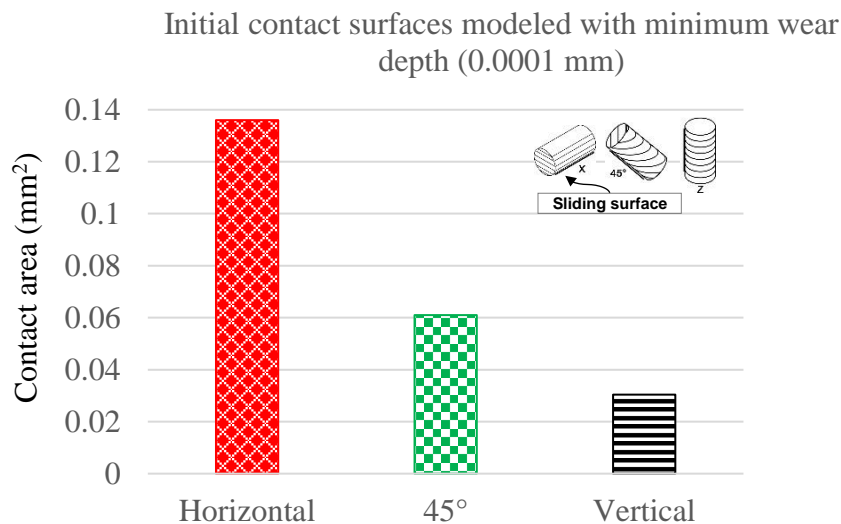


Fig. 4.21. Approximate modelling of the initial (static) contact surface at a small wear depth (0.0001 mm)

Fig. 4.22 shows the area of the cut/worn surfaces obtained after increasing wear with successive increments. The effect of wear depth up to 0.2 mm in 0.005 mm increments is exhibited in Fig. 4.22a. Further, Fig. 4.22b displays the initial detail of the previous figure marked with a square, simulated in 0.0025 mm increments up to 0.025 mm, which corresponds to the wear range measured in our experimental studies.

#### 4. Results and discussion

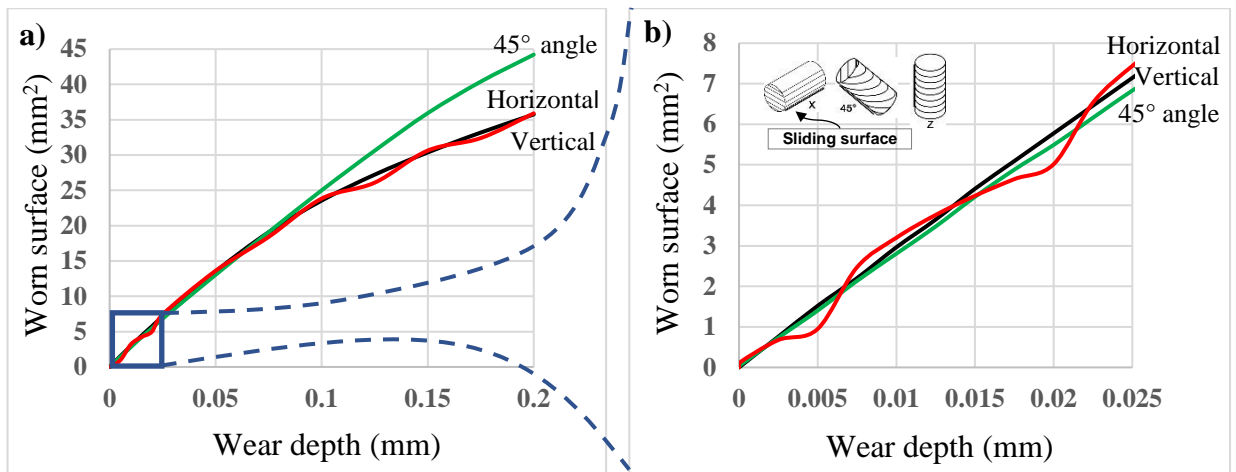


Fig. 4.22. Theoretical wear surface area values as a function of wear depth obtained with a total depth of cut of a) 0.2 mm, and b) 0.025 mm

It can be seen in Fig. 4.22a that at a high wear depth, a significantly larger surface area of more than 20% is created at the 45° angle orientation compared to the others. Horizontal and Vertical have nearly equal values over the entire wear depth range. In Fig. 4.22b, almost identical surfaces are obtained in the wear range of our experimental measurements. The Horizontal is undulating due to facing newer and newer layer lines, while the Vertical gives a slightly larger surface compared to 45° angle.

In Fig. 4.23, the wear values (from minimum to maximum) of different orientations measured during the actual tribological experiments (the framed parts) were placed on the simulated wear-contact surface curves (for the purpose of comparison) at two loads (150 and 200 N).

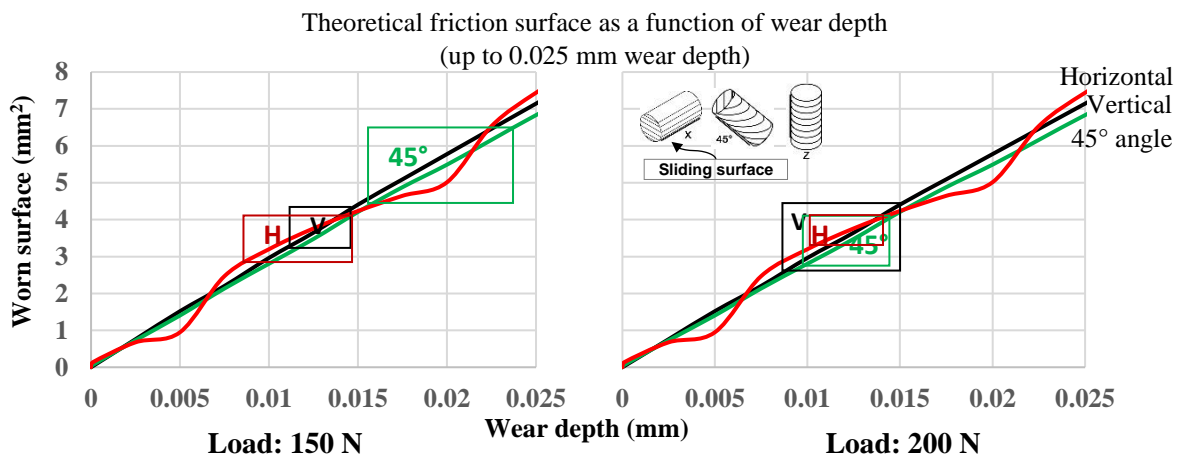


Fig. 4.23. Comparison of wear depths measured at different loads and the theoretical wear surface

The figure shows that at a lower load (150 N), the 45° angle orientation is associated with greater wear offering the largest surface in the tested wear range. This may also be related to the greater difference between static and dynamic friction (stick-slip tendency) through increased adhesion. At higher loads, the orientation influencing the surfaces has no effect, the increased role of the deformation component can be assumed. The nearly identical theoretical surfaces of the Horizontal and Vertical orientations can also be observed on the correspondence of their friction results under both mentioned load categories.

It is considered worthwhile to carry out further development and refinement on the results presented above, supplemented by deformation studies, within the framework of another research.

### 4.1.6. Summary and conclusions on the investigation of tribological properties

In this chapter (4.1.), the tribological behaviours of materials FDM (neat PLA and bronze/PLA composite) and DLP (neat resin and graphene/resin composite) 3D-printed were studied comprehensively. The influences of three different colours (for PLA filament), the attendance of bronze (for bronze/PLA composite), UV post-curing process (for neat resin), and layer thicknesses as well as graphene platelets' existence (for graphene/resin composite) were examined. Three print orientations (Horizontal, 45° angle, and Vertical) were used during the tribology specimens' manufacture for all materials. The tribological tests were performed under a dry condition and reciprocating sliding movement. Two applied loads were employed throughout the experiments of tribological tests. Based on the observations of the obtained results, the consequent conclusions can be drawn:

For FDM 3D-printed PLA

- The filament's colour reflected an obvious impact on test pieces' friction coefficient under all conditions. The white colour samples have offered the highest friction coefficient, whereas the lowest was observed at the grey. The black coloured specimens reported a high wear depth rate. This might be associated with the black body features where maximum heat retains in the sample's body, causing thermal softening and the sliding surface layers melt faster.
- All specimens under low load displayed significant stick-slip tendency compared to high load. Further, the wear depth and implicitly specific wear rate reduced with growing the applied load.
- The friction coefficient of 45° angle and Vertical orientation samples decreased at higher load due to the deformation in the contact area. Moreover, an elevated wear rate has been shown at the 45° angle pieces under low load because of greater gaps between the printed layers which resulting in a smaller contact area. Thus, increasing the pressure at the junction points.

For FDM 3D-printed bronze/PLA composite

- The structure of the sliding surfaces played a key role in determining wear and friction. The smaller the contact area (rough surface) between the sliding surfaces the higher the coefficient of friction (due to the high pressure) but the lower the wear rate was, and vice versa. The vertically oriented test pieces showed the highest friction but the least wear.
- The occurrence of the stick-slip phenomenon was more likely in the context of sliding under low loads, but wear was diminished.
- The presence of bronze particles as a reinforcement for the PLA material improved the tribological properties since the wear depth was significantly decreased as compared with the literature. Nevertheless, the friction remained more or less the same, since the matrix of the polymer composite was filled with hard particles.

For DLP 3D-printed resin

- The non-cured specimens demonstrated the highest wear depth and lowest friction coefficient as compared to the cured ones.

For DLP 3D-printed graphene/resin composite

- The dynamic coefficient of friction in the 0.5 wt.% graphene specimens disclosed a significant decrease (reached roughly 50% at the horizontally printed irrespective of the layer thickness) compared with the corresponding samples of the neat resin material. This was attributed to the effect of graphene as it may have acted as a solid lubricant.

- The graphene percentage of 0.5 wt.% was suggested as the optimum ratio for attaining the best tribological behaviour results in this work.
- Due to different print orientations, the surface structure displayed an influence on friction coefficient, particularly for Vertical and 45° angle pieces. This is because of their asperities that boost the friction coefficient due to the increased pressure caused by reducing the contact areas. This was also reflected in the large distinction between their static and dynamic max values, thus indicating an increase in the stick-slip phenomenon.
- In terms of the layer thickness impact, the wider and deeper gaps among the 100 µm layers cause the surface during the tribo-test to keep wearing off until the peaks disappear, which caused the increase in the wear at 100 µm layer thickness samples and a decrease in the 35 µm.

As a general conclusion concerning the tribological characteristics for materials reviewed, the occurrence of the stick-slip phenomenon was more likely in the context of sliding under low loads. Also, the asperities of the Vertical and 45° angle pieces boosted the friction coefficient due to the increased pressure caused by reducing the contact areas. However, the friction coefficient decreased at higher load due to the deformation in the contact area. Furthermore, different materials' colours, the post-processing, and the presence of additives obviously impacted the tribological properties (both friction and wear).

**The findings mentioned above are published in [1], [6], [13], and one more article is under review in the Journal of Materials and Design (IF: 7.99), see list of publications (Appendix A2).**

### 4.2. Investigation of mechanical characteristics

#### 4.2.1. Tensile of neat PLA material FDM 3D-printed

The influence of print orientation, raster direction angle, and layer thickness on the tensile strength of white PLA is studied in this section. Curves of applied engineering stress versus strain under tensile testing load are presented in Fig. 4.24. In terms of the build orientation effect (Fig. 4.24a), vertically aligned samples (Upright) displayed brittle failure and distinctly inferior tensile strength (only 15.64 MPa) compared with horizontally aligned (Flat) and On-edge samples (averaging less than 61% and 68%, respectively), which both displayed more or less ductile failure. This is due to the orientation of the Upright infill layer perpendicular to the applied load, that in turn, permits individual layers disengaging under the load (Rybachuk et al., 2017). The strain recorded for the Upright tensile samples was quite low at a value below 1.4%, which was remarkably lower than the strain obtained for Flat and On-edge samples owing to various failure modes.

When evaluating the strength of different raster angle specimens (Fig. 4.24b), the [45/90°] specimens had the highest value (44.97 MPa), while [45/135°] raster direction angle appeared to affect strength as 10.5% weaker. However, [0/45°] demonstrated a lower strength proportion of 30.1% and 21.9% than [45/90°] and [45/135°] test pieces, consecutively. This notable decline can be explained due to the infill raster angle of the [0/45°] sample is perpendicular to the tensile test load, which leads to dismantling the print lines with modest strength and elongation. A similar tendency was reported by Hanon et al. (2019) concerning the raster direction angle effect but for PETG polymer. As their lowest strength values were obtained at the specimens that contain perpendicular raster angle to the tensile test load direction, whereas the highest values were gained from the ones that comprise parallel and 45° rasters.

Regarding layer thickness impact (Fig. 4.24c), the highest tensile strength was observed in the lowest layer thickness specimens. This is due to the strength of FDM parts improves with



#### 4. Results and discussion

increasing the total number of layers (Anoop K. Sood et al., 2012), since the number of layers increases as the layer thickness decreases. Thus, an ultimate strength of 44.4 MPa was offered as an average for the 0.1 mm test pieces, while a weaker value of 4.4% was noticed for the 0.2 mm and a much weaker rate of 38.5% for 0.3 mm as compared to the 0.1 mm specimens. Rankouhi et al. (2016) and Ayrlmis et al. (2019) stated that the tensile properties of 3D-printed specimens improve significantly as printing layer thickness decreases. They ascribed this to bigger gaps that can be caused as the layer thickness increases. This in turn provokes the porosity to increase in the cross-section of the sample, which results in lower mechanical properties. More clarifications about the structure (inner and outer) of the tensile specimens manufactured with different print orientations can be seen in Fig. 4.27 and Fig. 4.28. Also, further details are explained in section 4.2.2 about the effect of fibres/raster angle and the number of contours (in connection with load direction) on the tensile strength behaviour.

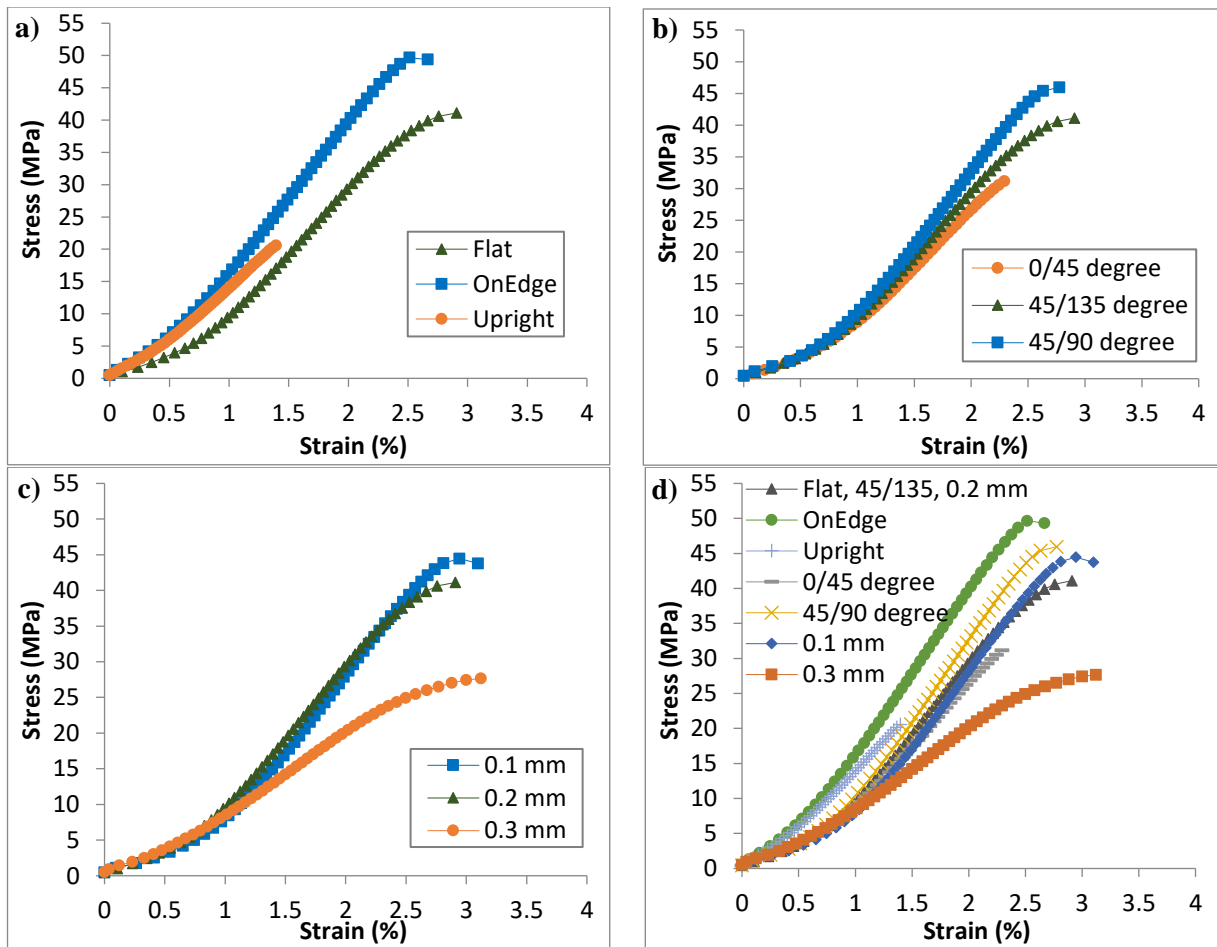


Fig. 4.24. The stress-strain curves at different a) build orientation, b) raster direction angle, c) layer thickness, and d) Comparison among all of them

A comparison of tensile properties for all tested parameters is presented in Fig. 4.24d. This figure was primarily concerned with stress versus strain for tensile specimens of each print condition. However, to give a comprehensive insight into the overall material behaviour, Young's modulus, ultimate tensile strength (UTS), elongation at UTS, and elongation at break were all calculated for the average of each sample set and presented in Table 4.1.

Among all the tested specimens, it can be seen that the highest Young's modulus and ultimate tensile strength values were observed in the On-edge sample ( $1.896 \pm 0.044$  GPa and  $49.12 \pm 0.78$  MPa, respectively). This phenomenon because of the inter-layer (fibres/roads) bonding, which contributes to enhancing the overall strength of a complicated structure. Besides, the surface of the

#### 4. Results and discussion

samples contains well bonded shells (contours) parallel to the testing load direction. More load can be afforded when fibres/roads are loaded axially in the FDM fabricated parts (Keleş et al., 2017). The best elongation at break results was found in the 0.1 mm layer height specimens (3.13%) due to the increase in the number of layers. Hence, when the number of layers increases, the tensile load is uniformly distributed across all bonded layers (including surfaces and inner fibres), thus balancing the internal stresses, which are generally associated with a laminate structure (Rybachuk et al., 2017). Shubham et al. (2016) attributed the reduction in elongation at break and ultimate tensile strength (in their work) to the negative effect of large layer thickness. As the smaller the layer thickness the better inter-layer bonding, because layers are closely stacked together, consequently a higher tensile strength and elongation. Conversely, larger layer thickness specimens have poor inter-layer bonds due to bigger microvoids, which leads to lower tensile strength.

Table 4.1. Average values and standard deviation of experimental data obtained from the tensile and hardness tests

Printing parameter			Young's modulus (GPa)	SD ±	UTS (MPa)	SD ±	Elongation at UTS (%)	SD ±	Elongation at break (%)	SD ±
Orientation	Raster angle (°)	Layer height (µm)								
*Flat	45/135	200	1.499	0.083	40.25	0.77	2.69	0.20	3.04	0.05
*On-edge	45/135	200	1.896	0.044	49.12	0.78	2.59	0.02	2.73	0.02
*Upright	45/135	200	1.322	0.145	15.64	5.23	1.16	0.28	1.17	0.28
Flat	*0/45	200	1.371	0.074	31.44	0.85	2.30	0.08	2.30	0.07
Flat	*45/135	200	1.499	0.083	40.25	0.77	2.69	0.20	3.04	0.05
Flat	*45/90	200	1.680	0.113	44.97	1.15	2.68	0.15	2.84	0.26
Flat	45/135	*100	1.425	0.076	42.12	2.13	2.96	0.06	3.13	0.18
Flat	45/135	*200	1.499	0.083	40.25	0.77	2.69	0.20	3.04	0.05
Flat	45/135	*300	0.931	0.139	25.91	1.88	2.84	0.56	2.85	0.57

(\*) is the variable in the current condition.

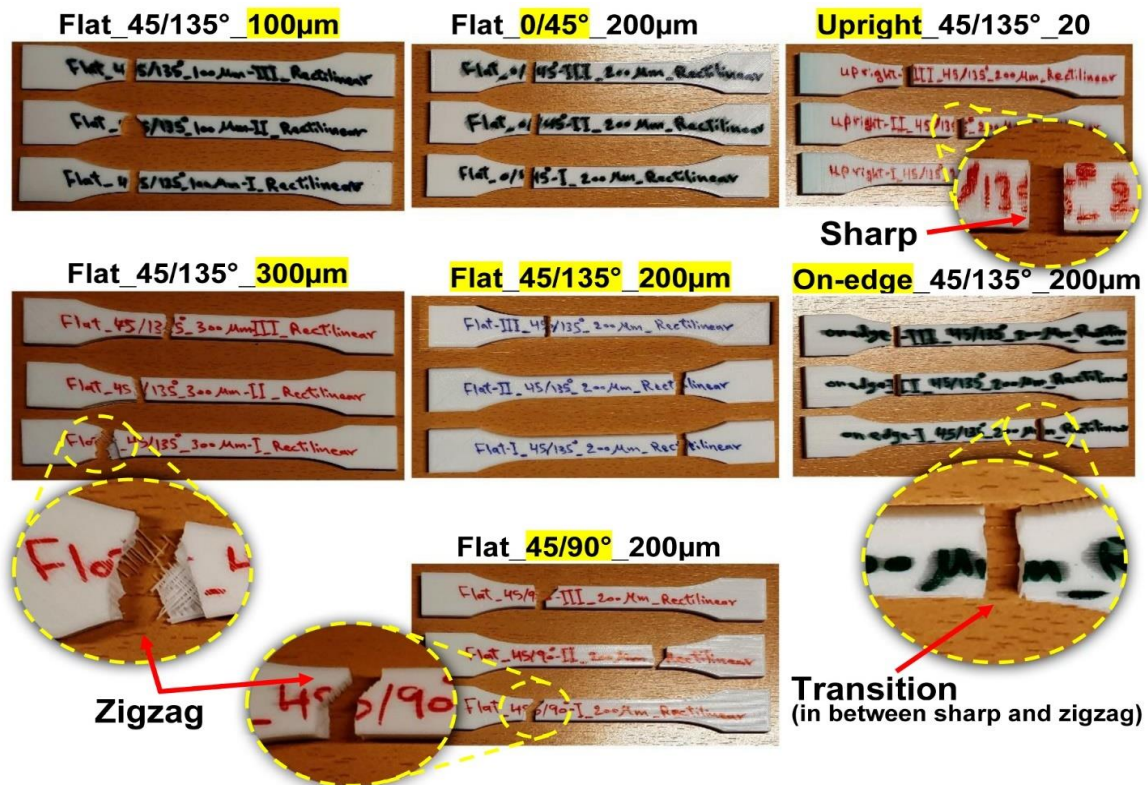


Fig. 4.25. The fracture profile of the tensile test specimens after testing, \*the text highlighted with yellow colour refers to the variable parameter

The physical appearances of specimens after the tensile test are shown in Fig. 4.25. The figure shows that at Flat specimens which were printed with  $[45/135^\circ]$  and  $[45/90^\circ]$  raster angle, the fracture profile was kind of zigzag. This is due to the inner construction where the lines (rasters) of the layers have alternately formed either parallel and  $45^\circ$  or  $45^\circ$  and  $-45^\circ$  ( $135^\circ$ ) angle to the tensile applied load. Meanwhile, the break of the Upright and Flat  $[0/45^\circ]$  samples was quite sharp because half/all of the built layers were normal to the tensile load. This means that the shape of the fracture follows the angle of the lines (fibres) that form the structure of the sample. The only exceptional failure pattern is in the On-edge test pieces which were in between the sharp and zigzag. This is due to the short length of printed rasters of each layer that makes the structure of the inner lines is more robust (Hanon Alshammas et al., 2020).

#### 4.2.2. Tensile of bronze/PLA composite FDM 3D-printed

The tensile test results are revealed in Fig. 4.26. It can be clearly seen that curves are categorized into three groups in accordance with the tensile properties. Among the tested specimens, the Flat was the most ductile, whereas the On-edge is the strongest, meanwhile, the Upright was the most brittle. The On-edge specimens obviously could withstand almost double of the stress load that has been applied on the Flat and Upright ones.

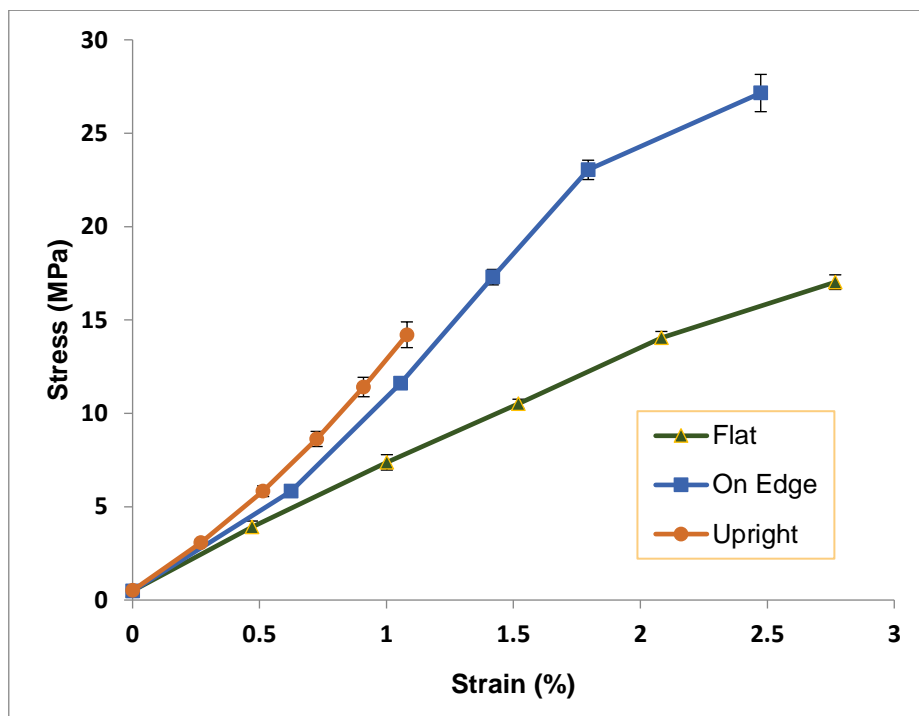


Fig. 4.26. Average of stress-strain curves for the specimens of different print orientation

For a better understanding of these groups' tendencies, the structure of the printed tensile test specimens is displayed in Fig. 4.27. Every layer contains the contour (shell) and the inner lines. In the case of Flat test pieces, the direction of the layers' contour is parallel with the applied force of the tensile test. As the long inner lines were built at a  $45^\circ$  angle with a moderate number of layers, that increases the possibility of these samples for more elongation (higher strain). The On-edge workpiece has a complicated structure since its cross-section possesses a relatively small size contour with a massive number of layers and short inner lines. This interprets the high strength that these samples offered when pulled during the test. Concerning the Upright samples, the layers are built vertically up to each other and are not interlocked by the printed inner lines but only by the adhesion among layers. Therefore, these specimens are quickly fractured when stretched by the applied force, which makes its attitude brittle.

#### 4. Results and discussion

The provided results are in good agreement with the prior studies. Zaldivar et al. (2017) examined the influence of print orientation on the mechanical behaviour of ULTEM 9085 material. They stated that On-edge samples obtained the highest measured tensile strengths with a difference of over 84% against the lowest tensile strengths which were observed in the Upright specimens. Nevertheless, the tensile strengths of Flat test pieces increased with an average of 21% than the Upright. These findings prove an almost similar trend in terms of the effect of print orientation as compared to the current work. The mechanical properties of Polycarbonate parts FDM printed were studied by Domingo-Espin et al. (2015). They explained the deformation behaviour at the break of printed specimens in different orientations. Flat and On-edge samples revealed a significant plastic behaviour since the deposited filaments are organized in the same direction where the specimen is being pulled. Hence, contour and raster are longitudinally pulled. However, the fracture of the Upright specimen is fragile because not much plastic deformation was observed. This is due to the applied tension load during the test being perpendicular to the built layers, where bonding strength in between is weaker than the resistance of pulled contours. Thus, the orientation of layer formation is fundamental in terms of strength. The results clearly show that the tensile strength of the bonding between the layers is significantly less than the strength of the inner lines.

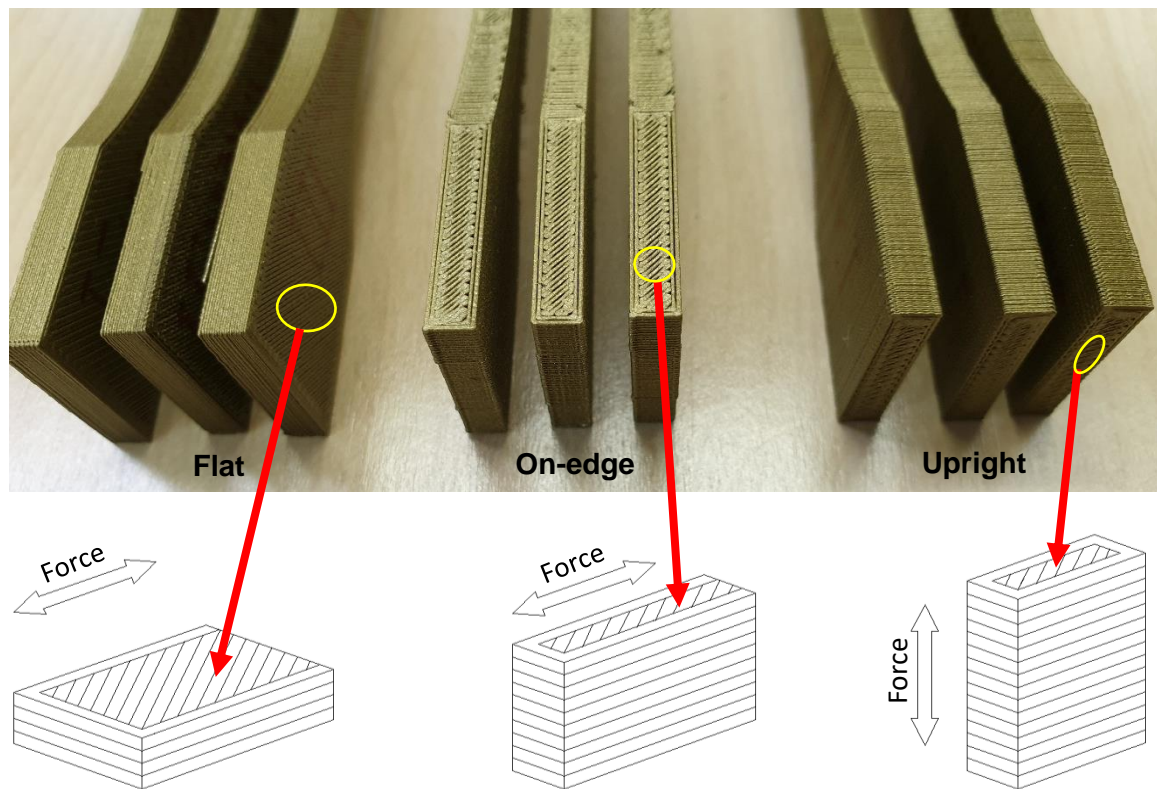


Fig. 4.27. Structure of 3D-printed tensile test specimens

This can also be explained further in Fig. 4.28, where the samples are shown after the fracture. The Flat specimen (left side) was broken with an angle of  $45^\circ$  which is similar to its raster direction angle structure. For all specimens of this print orientation, it can be noticed that the shell was dislocated after the tensile test. However, the robust construction of the inner lines, as well as the doubled shell layers, giving the On-edge test piece (at the middle) a higher tensile strength. Obviously, the Upright sample (right side) was fractured in a sharp form. This is due to the fabric of the layers being built vertically (up to each other) and perpendicular to the tension force. That leads to separate the bonding between layers without any deformation in the shell or the inner lines.

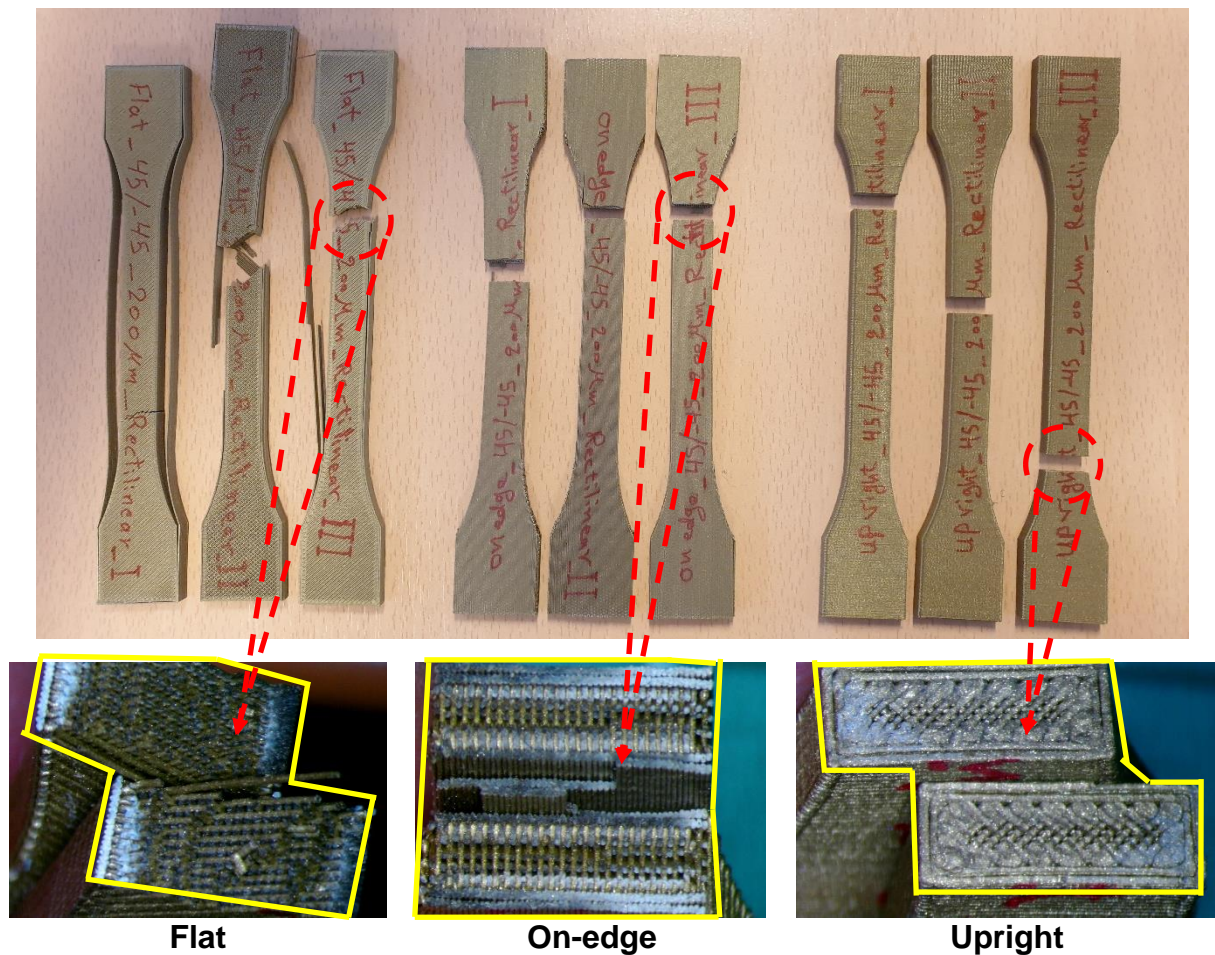


Fig. 4.28. The fracture form of specimens after the tensile test

#### 4.2.3. Tensile of neat resin DLP 3D-printed

The stress-strain curves of the On-edge specimens at each build orientation angle are represented in Fig. 4.29a and Fig. 4.29b for samples after and without post-curing process, respectively. In general, the white coloured specimens offered tensile stress slightly higher than the red coloured specimens. According to the results, it can be clearly seen that  $0^\circ$  build orientation angle specimens demonstrate much greater mechanical properties as compared to the  $45^\circ$  and  $90^\circ$  build orientations specimens, no matter whether were undergone post-curing. This could be explained that the adhesion within the layer of the material (i.e., XY-plane) is much more robust than the adhesion between the layers (i.e., Z-axis). In addition, the specimens built in  $0^\circ$  orientation angle have a higher number of built layers which are parallel to the direction of applied load during the tensile test, that leads to greater mechanical strength.

Regarding the impact of post-processing, it is obviously shown in the results that the tensile stress of DLP specimens improved remarkably by the UV post-curing process. In contrast, the value of elongation at the break was significantly decreased for the UV post-cured specimens in front of the non-cured ones. The obtained stress-strain curves for the UV post-curing specimens display brittle attitude since the majority of these specimens have an elongation at the break before 5 percent strain. However, the non-cured specimens could be classified as a ductile tendency material due to the relatively high percentage of the strain, particularly in the  $0^\circ$  angle prototypes. The improvement in the mechanical properties after the UV post-curing could imply that the partially cured and remaining uncured Wanhao UV resin required more time for being fully cured. From the results, Wanhao UV curable resin is considered anisotropy beyond processed by DLP 3D printing.

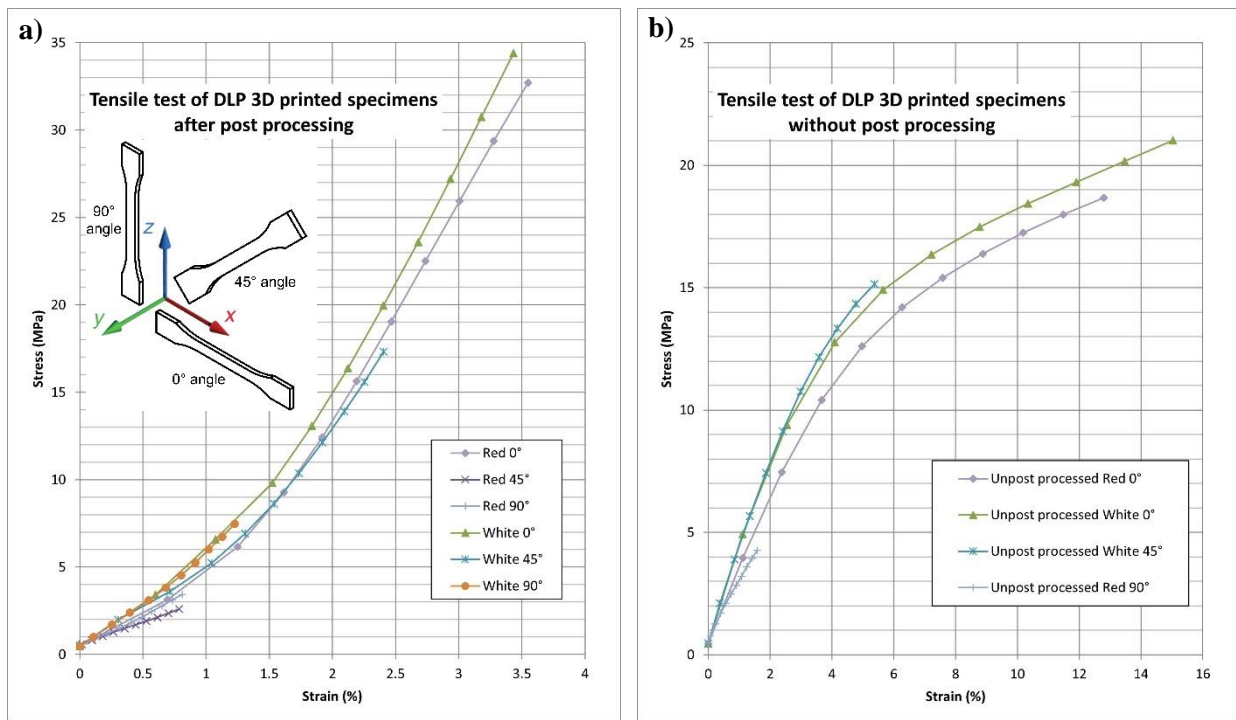


Fig. 4.29. Stress-strain curves of specimens a) UV post-cured, and b) non-cured

#### 4.2.4. Tensile of graphene/resin composite DLP 3D-printed

The mechanical behaviour of DLP 3D-printed components is discussed in this chapter. To investigate the effect of strengthening the polymer composite, using graphene, on the mechanical properties, tensile test samples were 3D-printed under different printing conditions. The variables of the experiment included the print layer thickness (height) and the graphene concentration to resin. Three print layer heights (35, 50, and 100  $\mu\text{m}$ ) were examined and two graphene ratios (0.5, and 1 wt.%) were assessed. An average of four identical test pieces was taken for each inspected condition. The mechanical properties were reviewed through evaluating the stress-strain curves which implicitly assisted to obtain Young's modulus, ultimate tensile strength (UTS), elongation at break, and elongation at UTS for each specimen's data. The subsequent sections present the influence of layer thickness firstly, and then followed by the impact of graphene attendance.

##### 4.2.4.1. Impact of layer thickness

The stress versus strain curves under a load of tensile testing for different layer thickness (35, 50, and 100  $\mu\text{m}$ ) specimens are demonstrated in Fig. 4.30. The layer thickness effect can be better observed in Appendix A5, where curves for materials with 0 (neat resin), 0.5, and 1 wt.% graphene ratios are displayed. In general, the highest tensile strength attitude was observed in the layer thickness of 35  $\mu\text{m}$  (lowest height). This is because the strength of 3D-printed objects enhances with the increase in the number of the layers (Anoop K. Sood et al., 2012), as the lower the layer height the more the number of layers. Therefore, the neat resin specimens reported a reduction of 11.62% and 22.1% in the average values of the tensile stress for 50 and 100  $\mu\text{m}$  layer thickness, consecutively, as compared to the 35  $\mu\text{m}$ . Further, a decrease of "7.25% and 25.78%" for the 50  $\mu\text{m}$  layer height and "23.13% and 35.52%" for the 100  $\mu\text{m}$  was noticed in the 0.5 wt.% and 1 wt.% graphene content samples, respectively, against the 35  $\mu\text{m}$  specimens. This improvement in the 3D-printed parts' tensile properties when the printing layer thickness reduces was also observed in other published research (Rankouhi et al., 2016; Ayrilmis et al., 2019). They attributed the weaker mechanical properties of the greater layer thickness to the bigger existed gaps. Which in turn prompts the porosity to develop in the element's cross-section and accelerates the failure.

#### 4. Results and discussion

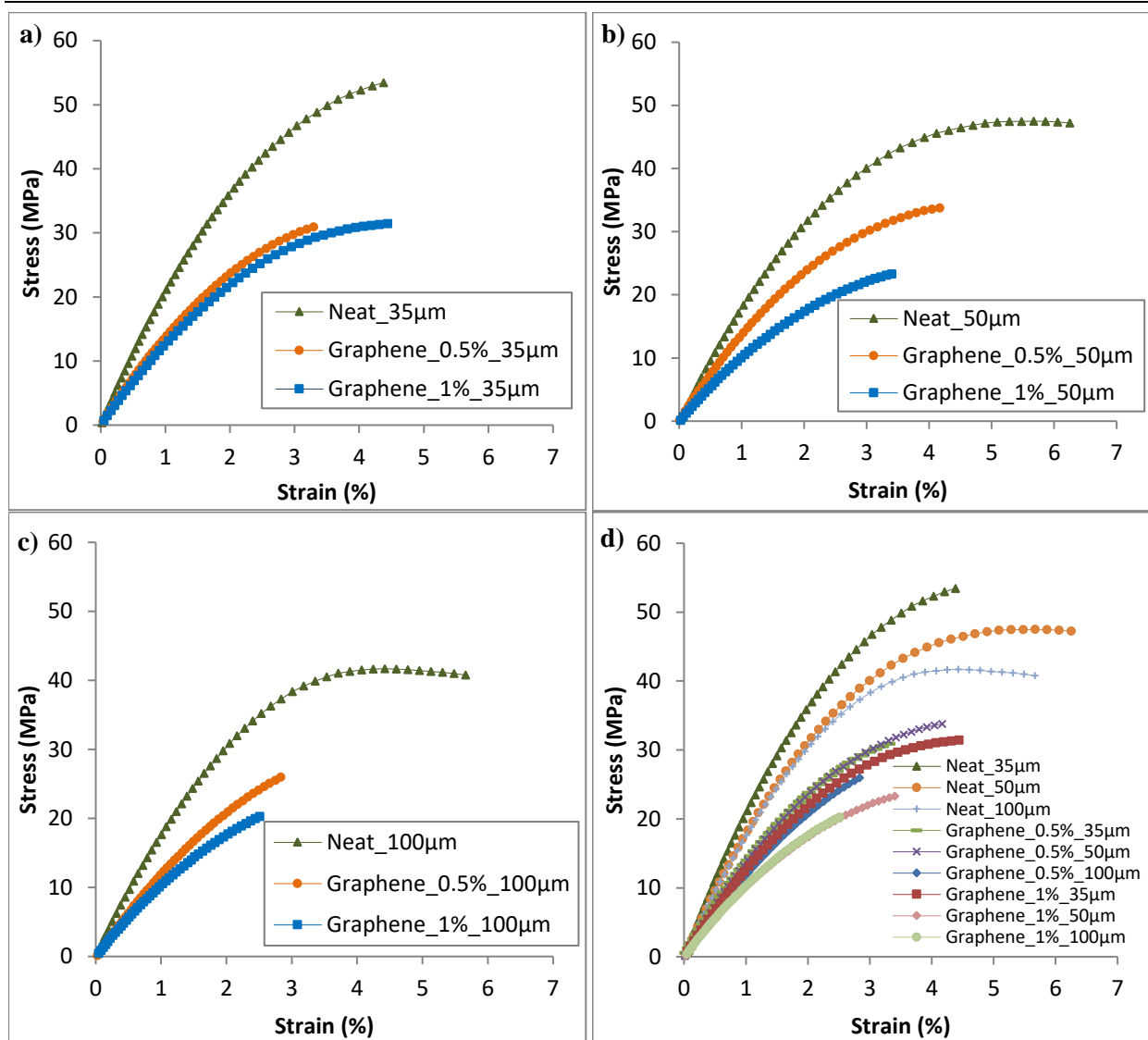


Fig. 4.30. Tensile stress-strain curves of various graphene concentration (0, 0.5, 1 wt.%) specimens at layer thickness of a) 35  $\mu\text{m}$ , b) 50  $\mu\text{m}$ , c) 100  $\mu\text{m}$ , and d) comparison among all the used conditions

##### 4.2.4.2. Influence of graphene existence

Two different graphene concentrations of 0.5 and 1 wt.% were tested. The charts in Fig. 4.30 demonstrate how the addition of graphene, has affected the tensile stress and strain of DLP 3D-printed resin, at various layer heights. The layer thickness specimen curves of 35, 50, and 100  $\mu\text{m}$  are drawn in Fig. 4.30a, Fig. 4.30b and Fig. 4.30c, respectively. Moreover, Fig. 4.30d displays a comparison of stress-strain curves among all examined conditions. Based on these results, Young's modulus, UTS, elongation at UTS and elongation at break were calculated and represented in Appendix A6. Furthermore, the values of all results with their standard deviation (SD), were summarized and tabulated in Table 4.2.

Despite the graphene is characterized with high mechanical qualities, however, it can be seen throughout the whole obtained results that the mechanical behaviour was not improved when the graphene nanoplatelets were integrated. Also, it was noticed that with increasing the graphene concentration further, a much worse mechanical attitude was acquired. This might be attributed to the bubbles created within the matrix bulk during the DLP 3D printing due to the addition of graphene. Considering that the graphene contributes to scattering the UV light and decreases the curing which results in the presence of adjacent unpolymerized regions. In turn, played a role to boost the porosity existence, and subsequently, the effects of graphene platelets' stiffening and

#### 4. Results and discussion

strengthening were critically hampered (Markandan and Lai, 2020). Markandan and Lai (2020) have observed large pores at higher graphene content (through microscopy images) of SLA-printed graphene/polymer composites. These pores caused an increase in the porosity in consistence with graphene concentration increment, where the overall porosity was generally around 8%.

Table 4.2. Average values aside with their standard deviation (SD) of Young's modulus, ultimate tensile strength (UTS), elongation at UTS, and elongation at break of samples manufactured in all tested conditions

Printing parameter			Young's modulus (MPa)	SD [±]	UTS (MPa)	SD [±]	Elongation at UTS (%)	SD [±]	Elongation at break [%]	SD (%)
Material	Graphene content (wt.%)	Layer height (µm)								
Neat resin	0	35	917.66	116.80	49.17	3.96	5.39	0.49	6.79	2.17
		50	847.46	1.81	45.17	3.31	5.33	0.38	7.40	0.73
		100	841.78	132.46	45.16	4.88	5.48	1.44	7.42	2.45
Graphene composite	0.5	35	890.87	98.25	28.74	3.30	3.23	0.27	3.24	0.28
		50	864.79	132.81	34.82	0.79	4.09	0.59	4.09	0.59
		100	807.09	63.90	26.66	2.80	3.30	0.15	3.31	0.16
	1	35	715.85	101.54	29.76	1.96	4.23	0.78	4.27	0.82
		50	635.78	65.69	20.53	3.82	3.22	0.36	3.22	0.37
		100	611.06	221.48	18.23	4.22	3.18	0.72	3.19	0.72

On the contrary, the neat resin prototypes reported better mechanical properties (as compared to the graphene/resin composite) irrespective of the layer heights. The Young's modulus and UTS have revealed a difference of 33.41% and 62.92%, respectively, between the highest (in 35 µm neat resin) and lowest (in 100 µm graphene 1 wt.%) given values (see Appendix A6). Meanwhile, the distinction between the highest (in 100 µm, neat resin) and lowest (in 100 µm, graphene 1 wt.%) values were approaching 41.97% and 57.01% for the elongation at UTS and elongation at break, sequentially. The reduction values (variance) overall reviewed mechanical characteristics (Young's modulus, UTS, elongation at UTS, and elongation at break) in terms of the effect of layer thickness and the graphene incorporation are listed in Appendix A7. The 35 µm layer thickness specimens (in case of investigating the layer thickness effect) and neat resin specimens (in case of graphene content influence) were considered the reference for comparing.

A similar attitude was recognized by some researchers in recently published studies when mechanical properties of 3D-printed graphene/polymer composites were investigated. A reduction in the tensile strength, the flexural strength, the tensile modulus of elasticity, and the flexural modulus of elasticity was detected with the increase in the graphene nanoplatelets (GnP) concentration uploaded to ABS polymer (Vidakis et al., 2020). The mechanical response and tensile strength of a pure thermoplastic PLA proved a better performance as compared to graphene/PLA composite (Vidakis et al., 2019). The addition of 0.5% of graphene oxide (GO) to the matrix of DLP 3D-printed resin caused a decrease of the mechanical features, as a higher amount of GO negatively influenced the curing process (Chiappone et al., 2017). Several parameters can influence the mechanical characteristics of graphene-based composites including the preparation method, the structure of the filler, the dispersion of the graphene in the matrix, the orientation of the nanoplatelets (filler), and the filler matrix interactions (Papageorgiou et al., 2017). In terms of the preparation methods effect, many studies have reviewed the mechanical



properties of graphene-based polymer composites prepared with various procedures other than 3D printing. Vallés et al. (2016) have incorporated graphene oxide (GO) into an epoxy resin (matrix) at loadings from 0.5 to 5 wt.% using sonication bath and then mechanical stirring. Tensile testing revealed moderate reinforcement of the polymer up to an optimal loading of 1 wt.%. However, higher loadings beyond 1 wt.% caused the mechanical features of the composites to deteriorate due to agglomeration of the GO flakes. Another published research reported a comparable approach when polyurethane (PU) nanocomposites incorporated with graphene sheets (D-Graphene) by solution blending method. For this composite (D-Graphene/PU), the tensile strength enhanced up to a certain limit of graphene loading (0.24 vol%) but then reduced as loading increased (Yang et al., 2013). This indicates that neither 3D printing, nor other preparation methods can be considered free of disadvantages while graphene incorporated in a composite form. As 3D printing suffered from porosity existing whereas other methods showed filler flakes agglomeration which both contributed to weakening the mechanical features. Nevertheless, 3D printing has the advantage of manufacturing complex structures with a relatively shorter time and less material consumption.

### *4.2.5. Summary and conclusions on the investigation of mechanical characteristics*

The present chapter (4.2.) comprehensively reviewed the mechanical behaviour of materials FDM (neat PLA and bronze/PLA composite) and DLP (neat resin and graphene/resin composite) 3D-printed. The tensile tests were investigated on specimens manufactured with varying three processing parameters (build orientation, raster direction angle, and layer thickness - for PLA filament), print orientation (for bronze/PLA composite), build orientation angle as well as UV post-curing process (for neat resin), and layer thicknesses as well as graphene platelets' existence (for graphene/resin composite). The ultimate tensile strength (UTS), Young's modulus, elongation at UTS, and elongation at break have been assessed in consistence with the behaviour gained from the examined print settings. According to the results obtained, the following conclusions can be drawn:

For FDM 3D-printed PLA

- The Young's modulus and UTS are maximum at On-edge print orientation due to its robust construction, while elongation at UTS and elongation at break are better at Flat orientation.
- The lower the layer thickness (a layer thickness within a specimen's total height) the higher the tensile strength due to the increase in the entire number of layers.
- The print orientation has the highest contribution parameter which affects mechanical features of the used PLA material compared to the other examined 3D printing process factors.
- The fracture profile of specimens after the tensile test followed/(affected by) the inner structure, which was either in the shape of zigzag or quite sharp.

For FDM 3D-printed bronze/PLA composite

- The On-edge print orientation revealed maximum tensile stress of 28 MPa, which was almost twice the stress value as compared to Flat and Upright specimens.
- The Upright sample showed a very fragile behaviour, with extremely rapid fracturing of the printed layers with 1.1% elongation at the break point. Meanwhile, the Flat and On-edge samples exhibited a more plastic behaviour, with an elongation of 2.5-3% at the break point.

For DLP 3D-printed resin

- The results revealed that the specimens printed at different orientation angles ( $0^\circ$ ,  $45^\circ$ , and  $90^\circ$ ) influenced the mechanical properties, where the most robust specimens in terms of the tensile strength were obtained at  $0^\circ$  angle (On-edge position).
- The UV post-curing process played a significant role in the augmentation of the tensile stress value, but meanwhile diminution the elongation at the break.

For DLP 3D-printed graphene/resin composite

- The highest tensile strength attitude was observed in the lowest layer thickness ( $35\ \mu\text{m}$ ) specimens, due to the increase in the number of layers. The greatest decrease (35.52%) was noticed in the  $100\ \mu\text{m}$  layer thickness, against the  $35\ \mu\text{m}$  (at 1 wt.% graphene content samples).
- The mechanical properties were not improved, when the graphene nanoplatelets were integrated throughout the obtained results. Also, a much worse mechanical attitude was gained when increasing the graphene concentration further, owing to the porosity increase.

As a general conclusion regarding the mechanical properties for materials examined, the On-edge print orientation exhibited maximum tensile strength due to its robust inner construction. In addition, the tensile strength increases with decreasing the layer thickness within a specimen's total height. Moreover, the UV post-curing process improved the tensile stress, but meanwhile reduced the elongation. Further, the mechanical properties were not improved after introducing additives.

**The findings mentioned above are published in [2], [6], [11], and [13], see list of publications (Appendix A2).**

### 4.3. Hardness test observation

Plastics in general as in other soft materials, have a relatively low hardness (Hong et al., 2017). The effect of hardness on polymer wear is convoluted by the fact that various wear mechanisms can dominate depending upon the manufacturing conditions. However, the adhesive junction created during sliding at a given load condition is induced by the decreasing hardness of pair junctions (Equbal et al., 2010). Thus, the material's hardness can be considered a contributing factor in terms of the wear volume loss distinction of two sliding surfaces (Bustillos et al., 2017). According to many researchers in literature, the hardness of 3D-printed polymers was affected when the parts were fabricated with various manufacturing settings (Chari et al., 2018; Ramesh and Panneerselvam, 2020; Zhiani Hervan et al., 2020). This intimates the importance of assessing the influence of production parameters such as build orientation, raster direction angle, and layer thickness on the hardness of 3D-printed elements. In turn, leading to a better comprehending of their tribological properties.

In this study, the hardness of the manufactured samples was evaluated employing the hardness measurement method Shore D. The hardness tests were conducted on the same tensile test specimens for all examined materials; except for the graphene/resin composite, the samples tested were cuboid-shaped (see Table 3.1f and Fig. 3.7a). Regardless of the specimens' manufacturing parameters, the hardness measurements were only performed on the top view face of the samples (when positioned in a Flat orientation, like in Table 3.1b). The top face was chosen because the measuring area is not enough in the faces of the front and side view. The required measuring space is a circular area of at least  $18\ \text{mm}^2$ , as stated in the equipment used. Moreover, the measurements for different print orientation specimens (Flat, On-edge, and Upright) make the examination covering the structure of other sides (shell and filling). When assessing the hardness on tensile

specimens, the tests were accomplished on three sections (gripping, curvature, and gauge, see the illustrations in Appendix A8). Three results were obtained on each measurement area and then averaged. In the case of Flat orientation specimens, the bed side was almost flattened (ironed) owing to the direct contact with the print platform. Therefore, the print top face was assigned for measurement, as this would give more reliable and fair results considering the measuring surface of On-edge and Upright pieces was not pressed.

#### 4.3.1. Hardness of neat PLA material FDM 3D-printed

As mentioned in section 3.3.1, the PLA specimens were manufactured at three different printing parameters (build orientation, raster angle, and layer thickness) with three levels for each. The obtained hardness results, as well as the illustrations about where the measurements were performed (at the gripping, curvature, and gauge sections), are presented in Appendix A8. Three points of measurement were conducted on each section investigated, and the average was calculated. The hardness value ranges in Shore D (77.5 – 78.5), (78 – 80), and (74.5 – 75), for Flat, On-edge, and Upright print orientation, (78.5 – 81), (77.5 – 78.5), and (77.5 – 78.5) for [0/45°], [45/135°], and [45/90°] raster direction angle, and (81), (77.5 – 78.5), and (79.5 – 80.5) for 0.1 mm, 0.2 mm, and 0.3 mm layer thickness specimens, respectively (see all results compared in Fig. 4.31).

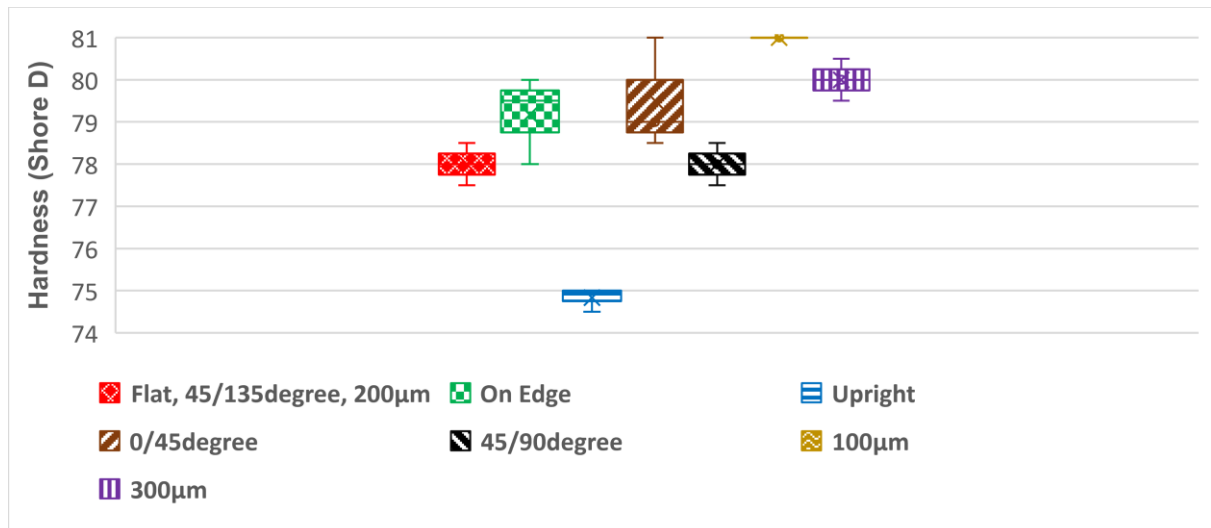


Fig. 4.31. Comparison of hardness average values in various print parameters

The results of build orientation specimens show that the On-edge exhibited the highest hardness value (see Appendix A8 - Fig. 8.3a). This can be ascribed to the contour (the shell of each layer) of this specimen, as it was in contact with the penetration indenter (test needle). Owing to the fact that the shell is fundamentally much rigid compared to the filling face, the hardness therefore increases. On the other hand, lower hardness values were offered by the Upright orientation samples, despite the indenter was also facing (in contact with) the shell during the tests. This is due to the construction of the Upright specimens where the adhesion between layers is the only structural bond that hold the layers above each other vertically, while the inner lines that interlock the layers with each other (fibres in between layers) are absent here (Hanon Alshammas et al., 2020). Thus, the indenter might penetrate into a gap (space) after crossing the shell. That is completely different than the On-edge workpiece where its complicated structure offers a massive number of inner lines among layers. Further, the Flat specimens were halfway, since there was no shell existed at the test point. Accordingly, the test indenter hit the filling face's inner lines which are not as hard as the shell, as mentioned before. The hardness consequence of Flat and Upright

specimens confirms the significance of both the first layer (facing layer) and inner filling (inner lines), as the deficiency of any one of them leads to weakening the hardness. Comparing to the results shown in Fig. 4.24a, it seems that the tensile strength of print orientation parameter specimens was in increase as the hardness increased. Since the On-edge samples reported the highest hardness and tensile strength as well, followed by the Flat, whilst the lowest values were detected in the Upright for both properties (tensile and hardness). This indicates that there is good agreement in terms of the correlation between the tensile strength of the print orientation parameter and the hardness property.

In terms of raster angle specimens,  $[45/135^\circ]$  and  $[45/90^\circ]$  displayed almost the same values with even similar standard deviation (see Appendix A8, Fig. 8.3b). However, the  $[0/45^\circ]$  angle showed slightly higher hardness. Since these samples are all Flat, thus there is no shell in the testing points. Though, the hardness value variance might be due to the stability of the short inner lines of  $[0/45^\circ]$  pieces, as  $0^\circ$  lines were built towards the transverse (cross-section) of the specimen (see Table 3.1c and Appendix A8 -Fig.8.3b). While  $45^\circ$  and  $90^\circ$  (longitudinal towards the sample length) are much longer which gives the possibility to deviate when facing the indenter. Subsequently, no specific behaviour to follow concerning the relation between hardness and tensile strength when the raster angle is varied (based on the comparison with Fig. 4.24b). This refers that the angle of the rasters seems not to be an influential factor on the hardness as the print orientation and layer thickness.

The layer thickness samples revealed the best hardness in the 0.1 mm specimen (see Appendix A8 - Fig. 8.3c). This result was expected which can be interpreted due to the presence of fewer voids when the number of layers is more. Based on that, a 0.3 mm sample is supposed to have the least hardness among the layer thickness specimens owing to the formation of irregular structure (Ramesh and Panneerselvam, 2020). Nevertheless, it manifested a value in between the test pieces of 0.1 and 0.2 mm. Hence, the hardness under different layer thicknesses showed no specific tendency, which is consistent with the outcomes of a published study (Ramesh and Panneerselvam, 2020). Moreover, no proportional relation between hardness and layer thickness was diagnosed (compared to Fig. 4.24c) when the 3D printing variable is the layer thickness.

#### 4.3.2. Hardness of bronze/PLA composite FDM 3D-printed

The hardness of three FDM manufactured specimens (with different print orientations) was estimated using Shore D hardness measurements. The test was done on three points (gripping, curvature, and gauge sections) for each sample. The hardness ranges (63 – 67), (70 – 72), and (72.5 – 76) Shore D for Flat, On-edge, and Upright print orientation specimens respectively, as shown in Fig. 4.32. The highest values were reported at the Upright and On-edge samples because the test penetration needle was in contact with the shell of the print, which is harder, as mentioned in section 4.3.1. In contrast, the needle was in contact with the filling face in the Flat test piece.

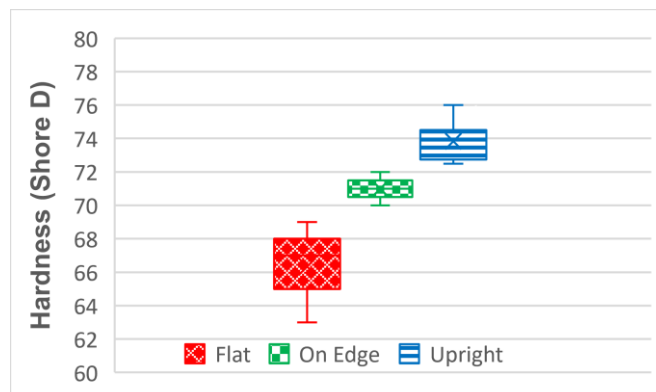


Fig. 4.32. The average of hardness results for different print orientations

#### 4.3.3. Hardness of neat resin material DLP 3D-printed

Fig. 4.33a shows the hardness outcomes of specimens that were evaluated after post-processing, whereas Fig. 4.33b shows the results of samples that were not post-treated. This helped examine the effect of post-processing on the hardness of the tested pieces. It can be clearly seen that the hardness of the post-processed samples is higher. The hardness increased as an obvious consequence of the post-processing. On the contrary, the hardness measurement recorded a decline when the tested specimens were not post-processed.

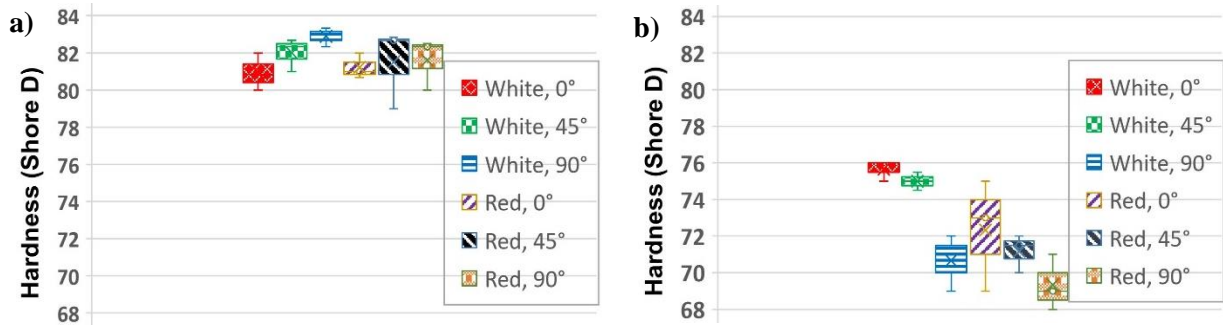


Fig. 4.33. Comparison of the hardness results for specimens a) after post-processing, and b) without post-curing process

#### 4.3.4. Hardness of graphene/resin composite DLP 3D-printed

The hardness of the material can be considered a contributing factor for the wear volume loss disparity of the two sliding surfaces (Bustillos et al., 2017). This suggests the importance of how adding a second material (during the production to have composite) affects the hardness of 3D-printed parts. Moreover, a better understanding concerning their tribological properties is needed. The specimens were printed with 35  $\mu\text{m}$  layer thickness and Horizontal orientation and were made of neat resin material and graphene/resin composite with three various graphene concentrations (0.5, 1, and 2 wt.%). This helped examine the effect of graphene ratio on the hardness of the tested pieces. The Shore D hardness value for the neat resin specimen reached nearly 78, while for the specimens of graphene/resin composite the hardness fluctuated around 78.5–79, 77.5–78, and 79.5–80.5 for graphene content of 0.5, 1, and 2 wt.%, respectively, as displayed in Fig. 4.34. It can be seen that the hardness value increased as the graphene ratio increased, except in the case of 1 wt.%. The highest value was detected in the specimen of 2 wt.% graphene concentration. The hardness increased as a clear consequence of the existence of graphene, which is much harder than the polymer matrix. This shows that the presence of graphene at a low percentage (even if only up to 1 wt.%, as shown in previous studies (Chen et al., 2012; Pérez-Bustamante et al., 2014; Tabandeh-Khorshid et al., 2016)) can increase the hardness value of the composite material.

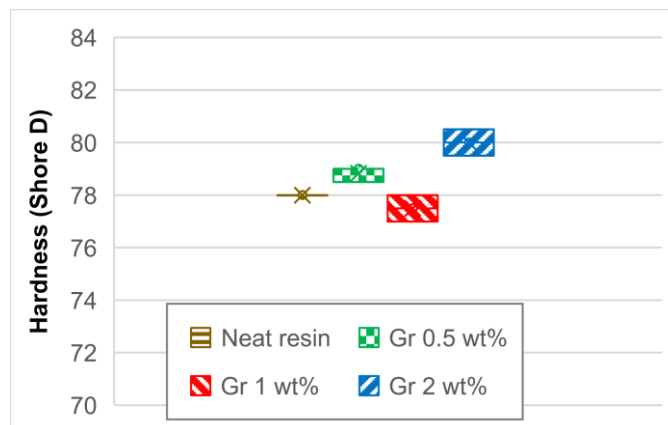


Fig. 4.34. Hardness at different graphene content levels

### 4.3.5. Summary and conclusions on the investigation of hardness

This chapter (4.3.) presented the investigation of the hardness of 3D printing components. The specimens were 3D-printed using FDM (neat PLA and bronze/PLA composite) and DLP (neat resin and graphene/resin composite) technologies together with varying processing parameters. These parameters are three processing settings build orientation, raster direction angle, and layer thickness (for PLA filament), print orientation (for bronze/PLA composite), build orientation angle as well as UV post-curing process (for neat resin), and graphene platelets ratio (for graphene/resin composite). Hardness tests were performed on tensile testing specimens for all examined materials except the graphene/resin as cuboid-shaped specimens was used. Based on the experimental results, the following conclusions can be formed:

For FDM 3D-printed PLA

- The On-edge reported the highest hardness among the print orientation samples, followed by the Flat and then the Upright. Since this attitude is the same for the tensile strength, indicating that the correlation between the hardness and tensile strength is directly proportional when the print orientation parameter is the variable.
- Maximum hardness was observed with decreasing the layer thickness (the thickness of layers within a specimen's total height), as the 0.1 mm thickness revealed the best hardness compared to other layer height specimens.

For FDM 3D-printed bronze/PLA composite

- The Upright and On-edge samples disclosed a higher hardness, which could be attributed to the fact that the test needle was in contact with the shell of the print, which was more solid. Meanwhile, the Flat samples displayed lower hardness due to the contact with the inner print filling, which was less reliable than the shell.

For DLP 3D-printed resin

- The hardness of non-post treated samples was reduced by 11.4 percent as compared to post-processed specimens.

For DLP 3D-printed graphene/resin composite

- The Shore D hardness tests for the specimens of pure resin and graphene/resin composite showed that hardness increased with the increase in graphene ratio. This shows that the presence of graphene even at a low percentage can alter the hardness value of the composite material.

As a general conclusion regarding the hardness of the materials examined, hardness increased when the test needle was in contact with the shell (e.g., in case of On-edge and Upright), owing to the higher rigidity of the contour. In addition, maximum hardness was observed with decreasing the layer thickness. Furthermore, the UV post-curing and incorporating the additives enhanced the hardness.

**The findings mentioned above are published in [6], [11], [15], and one more article is under review in the Journal of Materials and Design (IF: 7.99), see list of publications (Appendix A2).**

#### 4.4. Determination of surface roughness

In addition to the surface roughness issue, the shape of the samples from the 3D printing process reveals a form error or waviness. Accordingly, showing the primary profiles of the specimens investigated, as well as the surface roughness ( $R_a$ ) value determination, are unavoidable. Therefore, both (profile and  $R_a$ ) are demonstrated for all examined materials in the current work. The measurements were accomplished on the tribology specimens, as well as the counterpart plate in some cases, before and after the test. The dark line illustrated aside from the cylinders in Fig. 4.6 represents the surface roughness measurement path where the tribological tests were done as well. That means the measuring test line was carried out within/align-with the sliding area of the tribological test. This is to figure out the influence of surface roughness of 3D-printed parts on the tribological behaviour. The only exception regarding the shape of samples tested is for the case of bronze/PLA composite, where measurements were conducted on tensile pieces. This investigates the roughness caused by different print orientations on the face where the shell exists specifically.

##### 4.4.1. Surface roughness of neat PLA material FDM 3D-printed

All samples (Horizontal, 45° angle, and Vertical) were produced at the layer thickness of 0.2 mm with a cylindrical form. The results presented in Fig. 4.35 and Fig. 4.36 disclose that the primary profile and the  $R_a$  values were in good compatibility. The measured profiles of specimens examined before the tribology test (see Fig. 4.35a) demonstrate that the Horizontal samples were much smoother than the 45° angle and Vertical ones, where a significant fluctuation (hills and valleys) was noticed, indicating an obvious waviness on these orientations' surfaces. Further, the samples'  $R_a$  values were averaging (2.68  $\mu\text{m}$ ), (13.16  $\mu\text{m}$ ), and (13.73  $\mu\text{m}$ ) for the Horizontal, 45° angle, and Vertical, consecutively. Meanwhile, the  $R_a$  of the counterpart is (0.09  $\mu\text{m}$ ). Looking simply at Fig. 4.6, these results were expected. Since the building orientation of the Horizontal pieces is parallel to the measuring direction. This makes the surface roughness value lower because the measuring sensor (probe) is aligned with the inner printed lines, and no wrinkles are facing it. In comparison, Upright and 45° angle specimens revealed a rough surface. This is due to the test line being perpendicular to the layers' construction where the probe runs across the valleys and peaks of the entire layers.

Alsoufi and Elsayed (2017) have reviewed the influence of measuring direction on the surface roughness of 3D-printed PLA+ parts manufactured by the FDM method with the variance of layer thickness. They have examined three different measuring directions (0°, 45°, 90°), which makes their work almost similar to the current study. When tests were done on the 0.2 mm specimens, they came out with surface roughness values of (2.6  $\mu\text{m}$ ), (23.5  $\mu\text{m}$ ), and (21.2  $\mu\text{m}$ ) for the 0°, 45°, and 90° angle measuring direction, respectively, which are in good agreement with the provided results. Ayrilmis (2018) surveyed the impact of layer thickness on the surface roughness of 3D-printed wood flour/PLA filament. The surface roughness was measured parallelly and perpendicularly to the printing direction of the 3D-printed specimens. For the layer thickness of 0.2 mm, the parallel to printing direction samples (the same as Horizontal) offered a surface roughness  $R_a$  of ~ 6  $\mu\text{m}$ . At the same time, the perpendicular to printing direction was approaching of ~ 12  $\mu\text{m}$ . This outcome also demonstrates a similar range of roughness as compared to the present work.

After the tribological tests, the surface roughness measurements were achieved again. The results displayed a significant change in the measured profile and reduction in all specimens'  $R_a$  values, ranged between (75.37 to 85.21%) against the results prior to the test. This evidence the occurrence of wear by removing the facing rough layers during the tribological test. In contrast, the  $R_a$  value of the counterpart was increased by 25%, which indicates the presence of abrasive wear.

#### 4. Results and discussion

The surface roughness influences the tribological properties as following; the more the surface roughness due to the asperities, the smaller the sliding contact area, which leads to a higher pressure and implicitly a higher friction coefficient, and vice versa. This was reflected on the friction coefficient of the specimens (particularly at the running-in stage, no matter what is the colour) when a lower load was applied (see Fig. 4.1a). Hence, all the 45° and Vertical samples showed an elevated friction coefficient (due to the rougher surface resulting in a higher pressure). In comparison, the Horizontal exhibited lower (smoother surface gives rise to bigger sliding contact area, and then less pressure). This trend cannot be noticed in the case of higher applied load, as the high applied load terminates the running-in stage much shortly, and such a phenomenon arduous to be recognized.

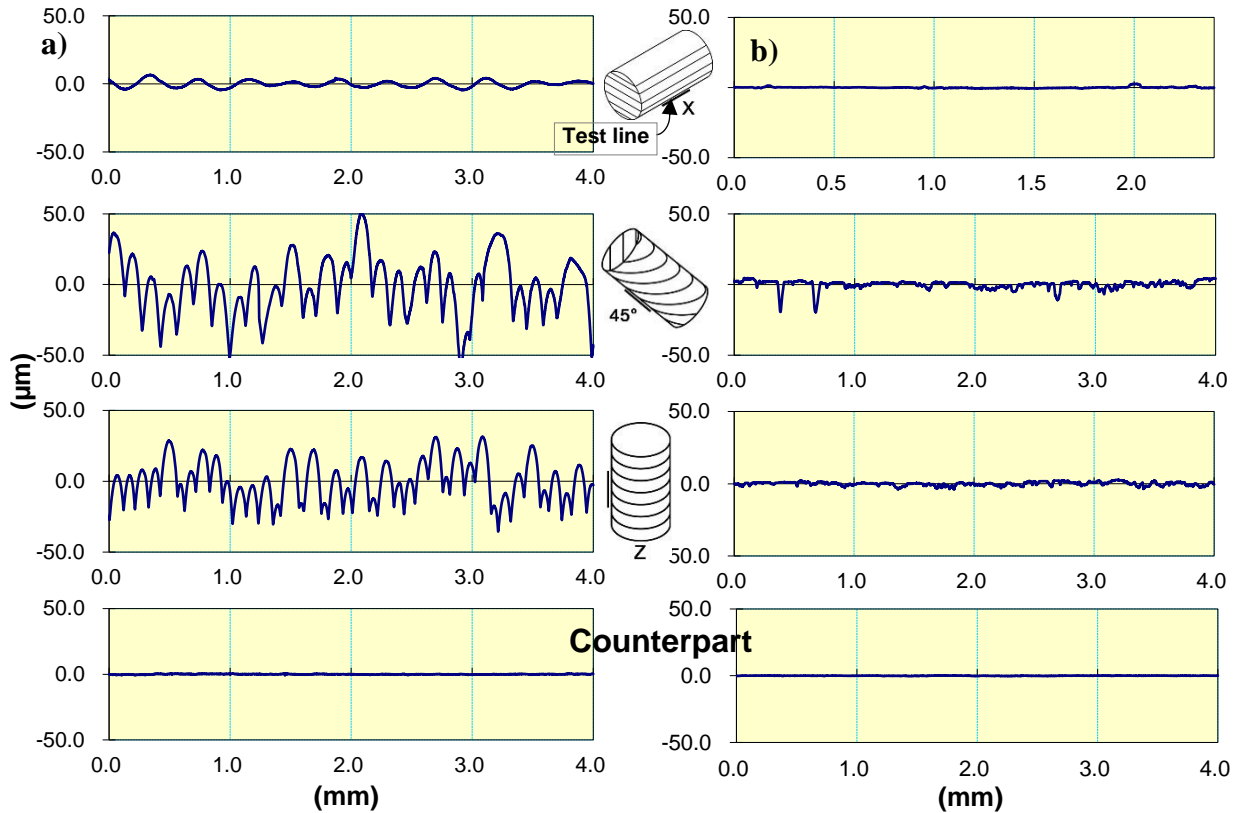


Fig. 4.35. Comparison of the measured profile at each print orientation specimens, a) before the tribology test, and b) after tribology tests

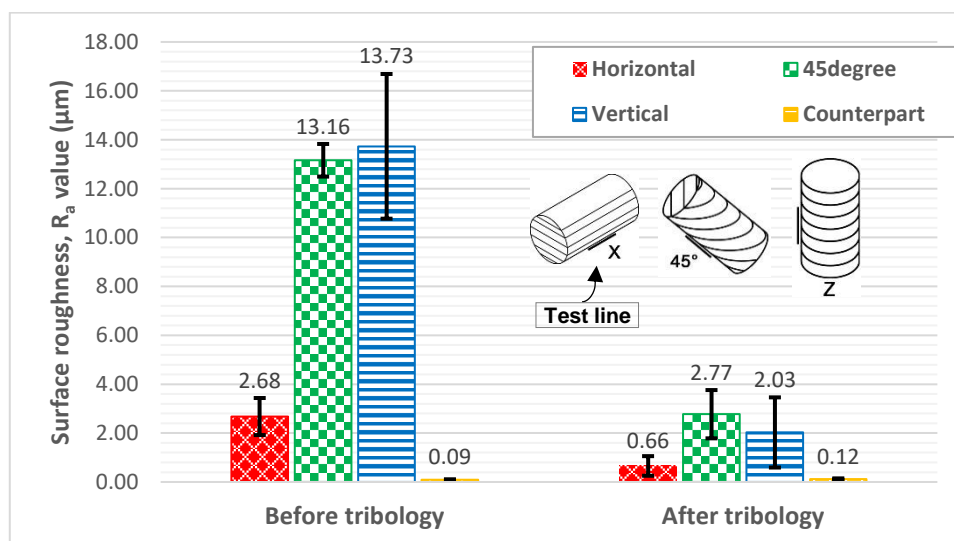


Fig. 4.36. Surface roughness ( $R_a$ ) value of tribology specimens before and after the test



#### 4.4.2. Surface roughness of bronze/PLA composite FDM 3D-printed

The measurements were performed on tensile test samples produced in three orientations. The measured profile of each print orientation is shown in Fig. 4.37. The dark line at the right side of the figure illustrates the path of the measurement and the surface face where the test was done. In all cases, the measurement track was perpendicular to the layers build direction where the shell can be found. The surface roughness ( $R_a$ ) values were verified based on the average of  $R_a$  results for each print orientation at the layer thickness of 200  $\mu\text{m}$ . It can be clearly seen that a slight difference has been observed among the tested surfaces ranged between (12.6 - 16.8  $\mu\text{m}$ ), as shown in Fig. 4.38. The smoothest surface was noticed at the On-edge sample. This is due to peaks and valleys of the entire layers seem quite uniform and its depth is insignificant. While Upright specimen reflected the roughest surface since the structure contains non-regulated layers due to the stacking of the printed material. Lee et al. (2016) have demonstrated a similar range of roughness (12.6  $\mu\text{m}$ ) for a microfluidic channel wall FDM-printed at a 90° inclined angle (alike the present shell). They mentioned that surfaces generated through FDM printers are rather rough, where the profile of roughness is distinguished by a stepping feature. As for the bronze particles influence, Balaji et al. (2006) inspected the surface roughness of mild steel substrate coated by bronze/PTFE composite. They concluded that  $R_a$  values vary in accordance with the content of the bronze and polymer deposit. The higher the bronze content the smoother the surface roughness, and vice versa. Finally, the obtained values of surface roughness ( $R_a$ ) in this research can be improved by means of post-processing procedures like surface polishing.

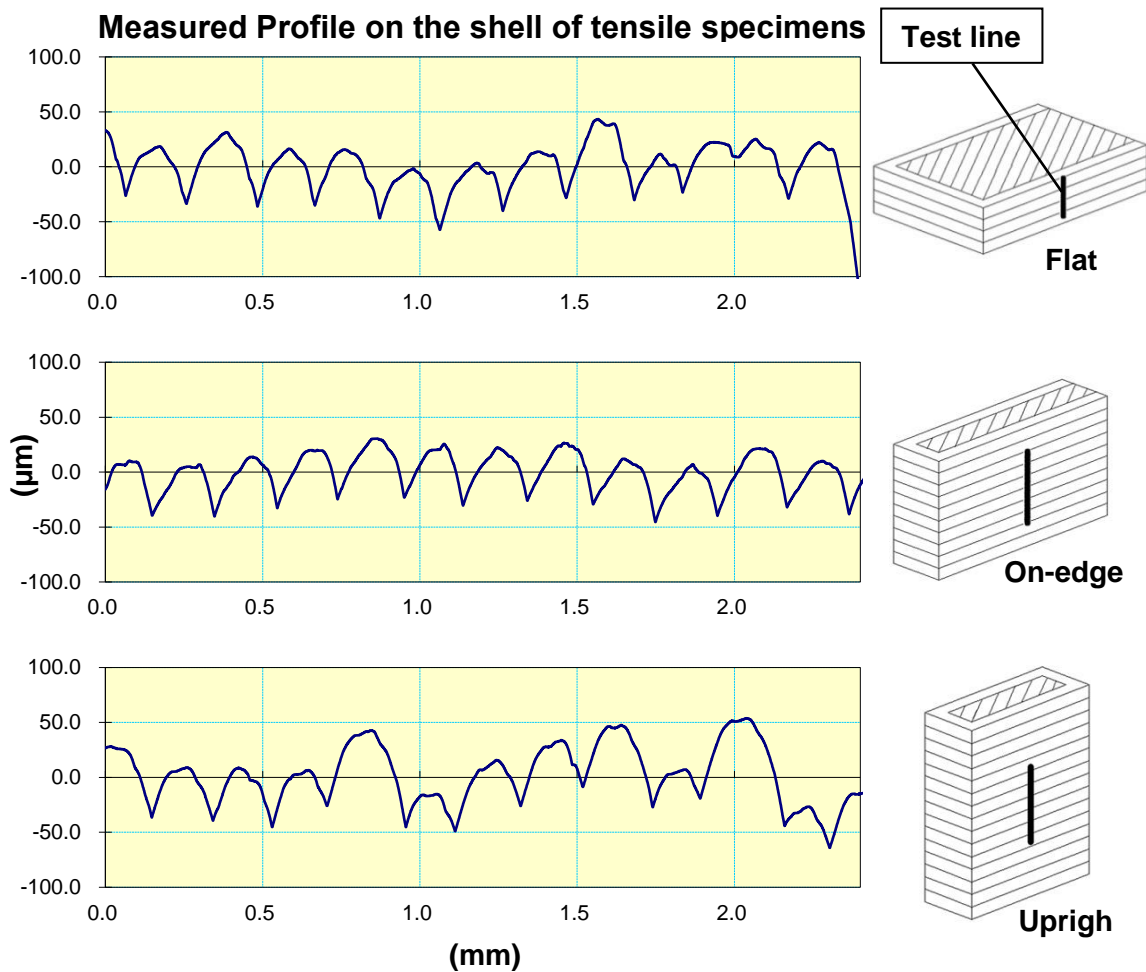


Fig. 4.37. Surface roughness measured profile comparison

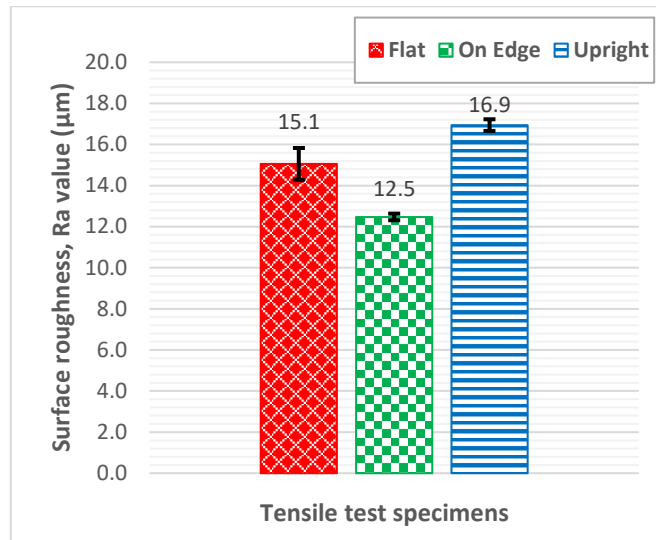


Fig. 4.38. Surface roughness ( $R_a$ ) results of tensile test specimens printed in different orientations

#### 4.4.3. Surface roughness of neat resin material DLP 3D-printed

The surface roughness tests were done for the cylindrical tribology specimens fabricated in three orientations (X,  $45^\circ$ , and Z). Fig. 4.39 depicts the measured profile for each print orientation. Before the tribological tests (Fig. 4.39a), obviously, the smoothest surface could be seen at the X (Horizontal) specimen. This is because the measurement sensor (probe) during the test likely has passed over the bottom layer (quite smooth) which was in contact with the printing platform (first printed layer). While Z (Vertical) specimen offered a rougher surface due to the layer structure of the examined surface (like valleys and hills). In addition to these valleys and hills, an angle of  $45^\circ$  is noticed among the lines of the built layers for the  $45^\circ$  specimen makes it the roughest among the inspected surfaces. The surface roughness ( $R_a$ ) results for the three examined orientations before and after tribological tests are provided in Fig. 4.40. Certainly, the surface roughness value of the worn area due to the tribology test is smaller than the virgin surface. This is because of the abrading of the rough layers from the original surface. The same attitude was offered in the measured profile of specimens after the tribological tests (Fig. 4.39b), as fluctuation in these curves was remarkably smoothed out (more evident in the case of  $45^\circ$ , and Z specimens) due to the wear.

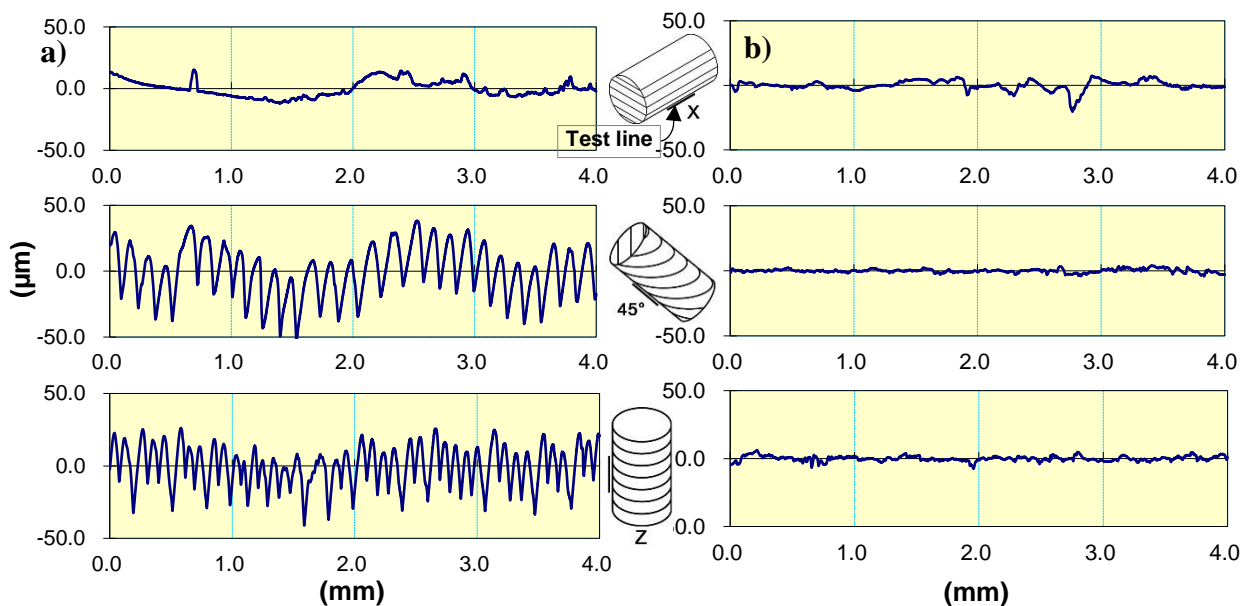


Fig. 4.39. Measured profile of tribology specimens a) before the test, and b) after testing

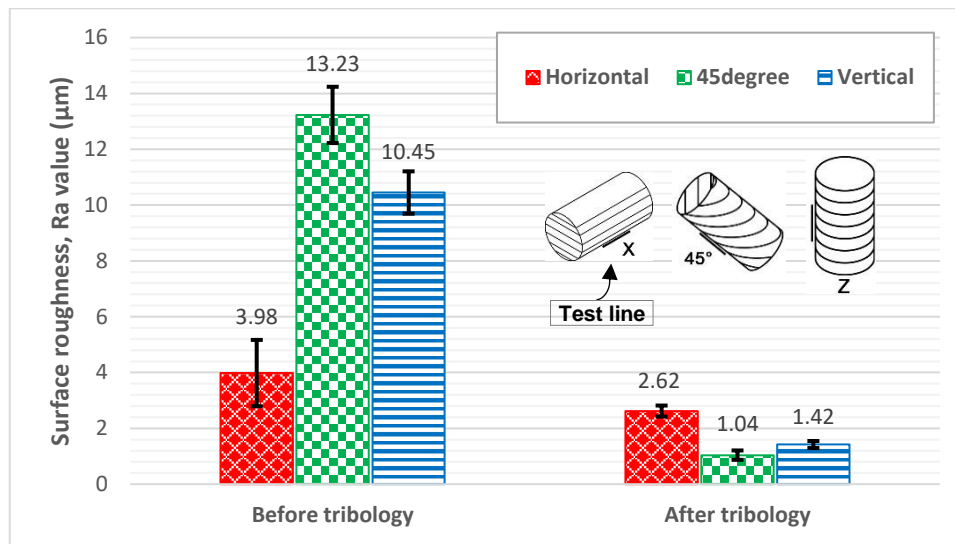


Fig. 4.40. Surface roughness ( $R_a$ ) value at various print orientation samples before and after tribology test

#### 4.4.4. Surface roughness of graphene/resin composite DLP 3D-printed

##### 4.4.4.1. Surface roughness of the test specimens

The examined samples were fabricated in different print orientations (Horizontal,  $45^\circ$  angle, and Vertical), layer thicknesses (35, 50, and  $100 \mu\text{m}$ ), and graphene ratios (0, 0.5, 1, 2 wt.%). The measured profiles (Fig. 4.41) showed a tendency similar to the previously examined materials (see Fig. 4.35 and Fig. 4.39) regarding the notable smoothness of the Horizontal specimen than other orientations and polishing the surfaces of all samples after the tribological tests owing to the wear.

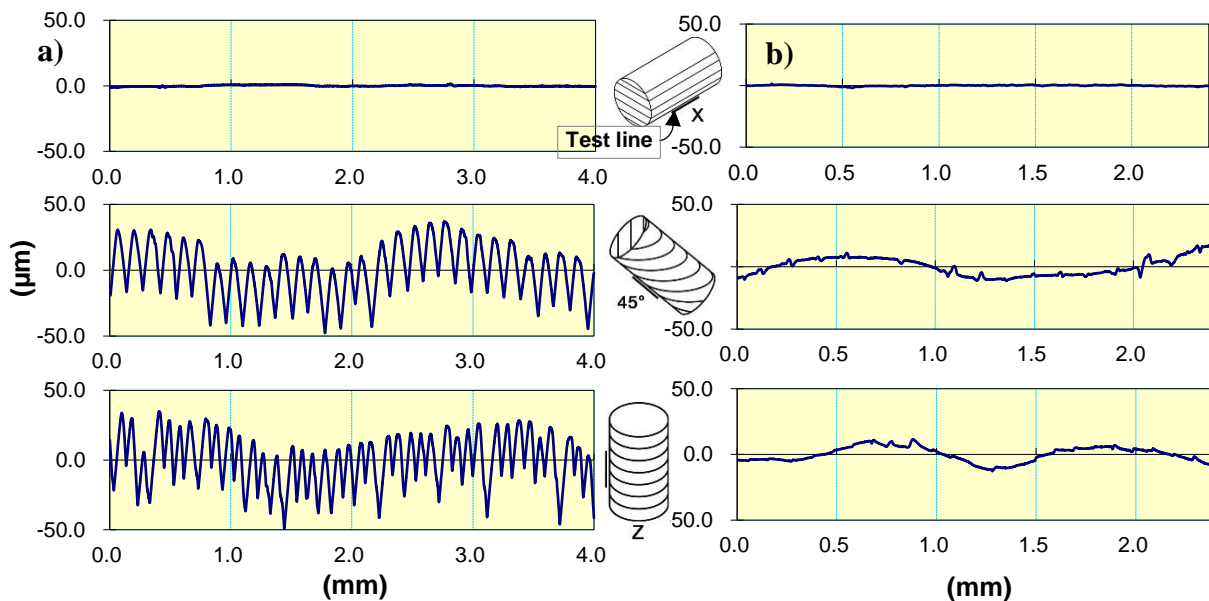


Fig. 4.41. Measured profile of graphene (0.5 wt.%) / resin composite at each print orientation for specimens printed with a layer thickness of  $100 \mu\text{m}$ , a) before the tribology test, and b) after tribology

The obtained  $R_a$  results (see Fig. 4.42) generally revealed a significant increase in the samples' roughness of  $45^\circ$  angle and Vertical compared with that in the Horizontal. This increase included both materials that were used (neat resin and graphene/resin composite), regardless of the layer thickness. For example, on average, the roughness of the Horizontal was inferior by 98% to  $45^\circ$  angle and Vertical at  $100 \mu\text{m}$ . Similar trends were observed in literature (M M Hanon and Zsidai, 2020; Muammel M. Hanon and Zsidai, 2020) concerning the effect of different print orientations on the surface roughness of DLP printed parts.

#### 4. Results and discussion

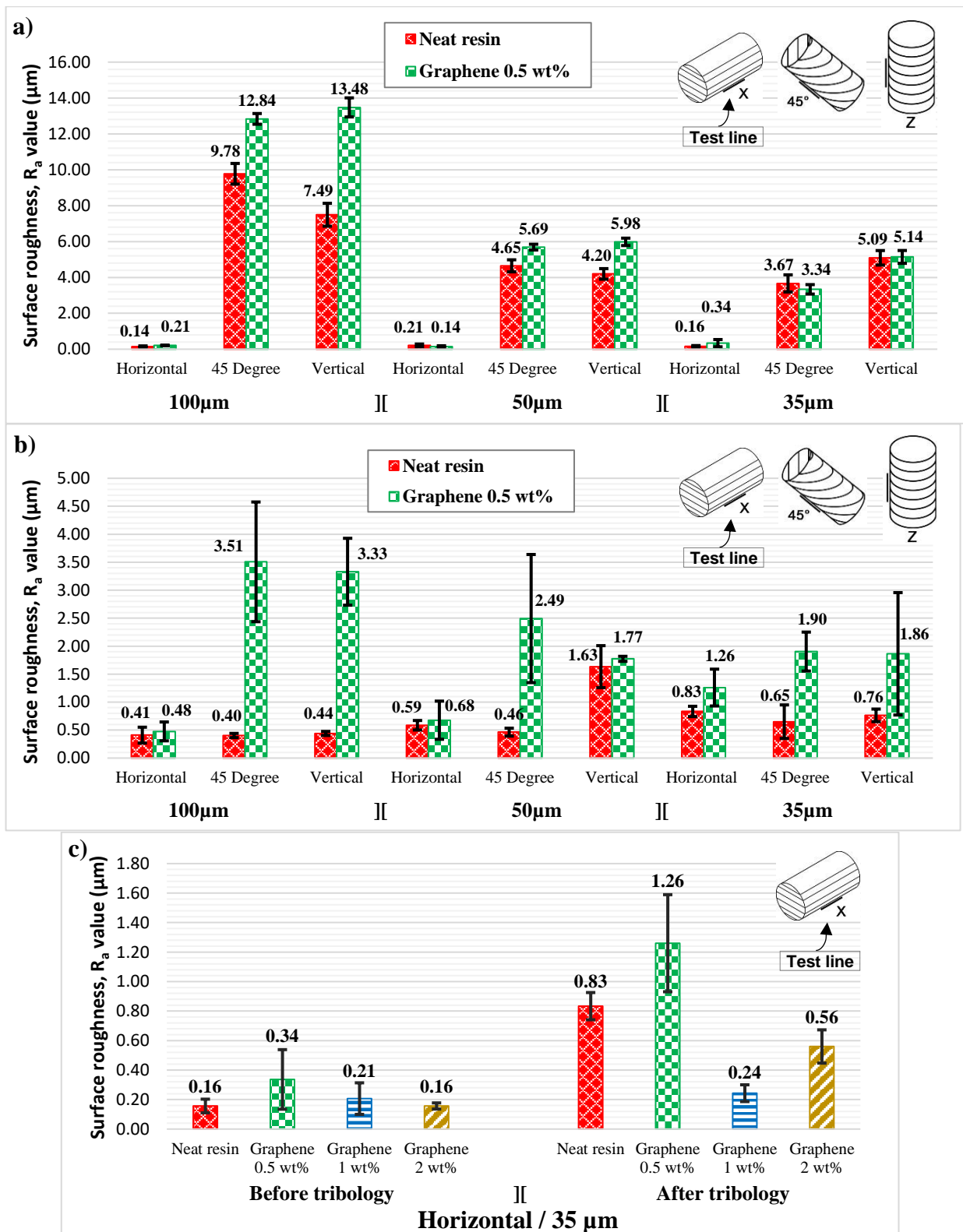


Fig. 4.42. Surface roughness of tribological specimens, a) prior to tests, b) after tests, and c) with different graphene content levels before and after tests

The results shown in Fig. 4.42a were expected because, for the Horizontal piece, the measurement probe of the roughness test passed only over the first built layer at the specimen's bottom, as mentioned in section 4.4.3. This layer was in direct contact with the smooth surface metallic platform during the manufacturing when the liquid resin was illuminated by the UV light and then solidified (Mu et al., 2017). Therefore, the surface of this layer takes the shape (smoothness) of the platform. Even the presence of graphene platelets in the Horizontal orientation graphene/resin

composite specimens did not increase the roughness before the tribology test. This is because the smooth metallic plate (build platform) pushed these platelets inside the layer during the print. Thus, no peaks or wrinkles remained on the surface. On the other hand, the significant increase in roughness of the 45° angle and Vertical samples compared with that in the Horizontal within the same layer thickness is also justifiable as the measuring path is perpendicular to the construction of the specimen where the test probe runs across the peaks (hills) and valleys (gaps) of the entire layers (Hanon Alshammas et al., 2020). In terms of the layer thickness' impact on surface roughness, the highest increment was observed in the layer thickness of 100 µm. Compared with the layer thicknesses of 50 µm and 35 µm, the surface roughness of 100 µm thickness increased by 54% and 69% for 45° angle specimens and by 52% and 51% for Vertical specimens. This would agree with the outcome of a published research (Ayrilmis, 2018) that assessed the influence of layer thickness on surface characteristics of 3D-printed materials. The study observed that the specimens' surface roughness increased with the increase of printing layer thickness. The reason for this increase was explained in section 4.1.4.3. and further illustrated in Fig. 4.15a, as the gaps among the layers of 100 µm are wider and deeper than those at 50 µm and 35 µm. This was reflected in the tribological behaviour by augmenting the wear of 100 µm layer thickness samples while lowering it at 35 µm.

The results of surface roughness ( $R_a$ ) after tribology are shown in Fig. 4.42b. As previously stated, the horizontally printed samples' surface was extremely smooth before tribology, but its roughness grew after tribology. This was certainly because of the tracks of the worn area caused by the tribology. The roughness mean values (for both neat resin and graphene/resin composite materials) after tribology increased to 61%, 72%, and 70% in the layer thicknesses of 100 µm, 50 µm, and 35 µm, respectively, compared with their pristine surface before tribology. This implies that the average increment in the surface roughness of Horizontal pieces after tribology (irrespective of the used material and layer thickness) is 68% compared with the roughness of the virgin surface. Fig. 4.42c displays the surface roughness of samples with differing graphene content (0, 0.5, 1, and 2 wt.%). These specimens were fabricated in phase two, which included only one printing condition (Horizontal orientation at a layer thickness of 35 µm). They therefore exhibited similar behaviour to other Horizontal samples with respect to increasing the roughness of their surface after tribological testing compared with the roughness of the same surface prior to testing.

On the contrary, for all thicknesses, the surface roughness was decreased remarkably for the specimens of 45° angle and Vertical orientations after the tribological tests. The roughness mean values for pure resin material samples reduced by 95%, 76%, and 84% in the layer thicknesses of 100 µm, 50 µm, and 35 µm, respectively, after tribology against the roughness values for the same specimens before the tribology. Meanwhile, the roughness values of graphene/resin pieces decreased by 74%, 63%, and 56% in the 100 µm, 50 µm, and 35 µm, respectively. This considerable reduction was caused by the abrading of the peaks and valleys (rough layers) from the original surface as a result of the tribology test (Muammal M. Hanon and Zsidai, 2020). As seen above, the reduction in the roughness of 45° angle and Vertical orientations was evident in the samples of pure resin (total average of 85%) than in the graphene/resin composite (total average of 64.3%), regardless of the layer thickness. This variance in the roughness is because the cross-section of graphene platelets faces the sliding surface (because of their alignment direction while testing) for the samples of 45° angle and Vertical orientations, as illustrated in Fig. 4.17b. These graphene platelets apparently act as harsh chips after rubbing off the rough layers (peaks and valleys) of the matrix material because of the wear. Thus, they contribute to increasing the roughness, and thus the wear. Therefore, the graphene/resin composite offered higher roughness than the neat resin. The overall average drop in the surface roughness of 45° angle and Vertical

pieces after tribology (irrespective of the used material and layer thickness) is 74.7% compared with the roughness of the fresh surface.

#### 4.4.4.2. Surface roughness of the counterpart

The surface roughness ( $R_a$ ) of the counterpart was also examined before and after the tribology tests for both investigated materials (neat resin and graphene/resin composite). It was observed that the roughness value after testing all pure resin specimens increased to more than twice of the starting surface roughness (see Fig. 4.43). This indicates the presence of the transfer layer phenomenon during the tribological tests. The transfer layer (from the specimen's material) either fills the asperities that exist on the counterpart surface or adds to its additional layers (Chang et al., 2014), thus changing the roughness. In contrast, no significant difference in the  $R_a$  value of the counterpart was observed after testing the graphene/resin composite material, except a slight increase that may be caused by some gentle scratches that occurred due to the friction with the graphene platelets (harsh chips) when the samples of  $45^\circ$  angle and Vertical orientations were examined.

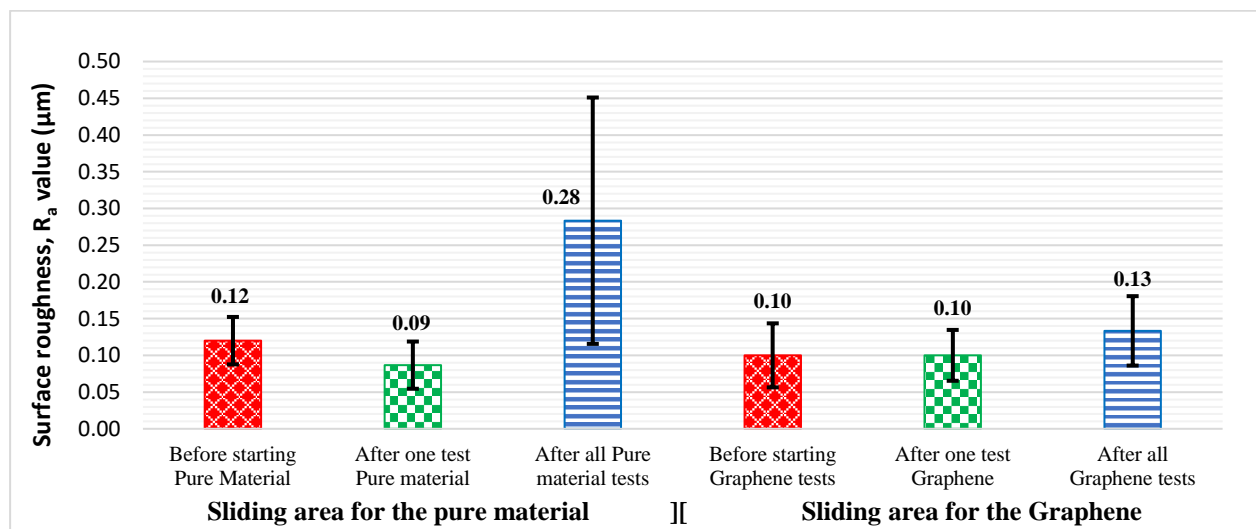


Fig. 4.43. Surface roughness of counterpart plate before and after tribological tests

#### 4.4.5. Summary and conclusions on the investigation of surface roughness

The current chapter (4.4.) presented the investigation of the surface roughness of 3D printing elements. The measurements were conducted on tribology specimens (except for bronze/PLA composite, on tensile samples), as well as the counterpart in some cases, before and after the test. The specimens were 3D-printed using FDM (neat PLA and bronze/PLA composite) and DLP (neat resin and graphene/resin composite) technologies together with varying processing parameters (mainly build orientation, as well as layer thickness and additive ratio in the case of graphene/resin composite). Based on the assessment of the results, the following observations can be drawn:

For FDM 3D-printed PLA

- The surface roughness of the Horizontal pieces was lower because the measuring sensor (probe) is aligned with the inner printed lines, and no wrinkles are facing it. In comparison, Upright and  $45^\circ$  angle specimens revealed a rough surface due to the probe runs across the valleys and peaks of the entire layers (test path is perpendicular to the layers' construction).
- A significant reduction was revealed in the surface roughness ( $R_a$ ) values for all specimens after tribological tests, ranged between (75.37% to 85.21%) against the virgin surface. This confirms the occurrence of wear by removing the facing rough layers.

For FDM 3D-printed bronze/PLA composite

- A slight difference in the roughness has been observed of the tested surfaces, ranging between (12.6 - 16.8  $\mu\text{m}$ ), as all specimens were measured from a side containing shell.

For DLP 3D-printed resin

- The horizontally printed specimens have offered the smoothest surface as compared to other build orientation samples. This is because the measurement sensor during the test has passed on the bottom layer which was, in the case of Horizontal, in contact with the printing platform while manufacturing.

For DLP 3D-printed graphene/resin composite

- The surface roughness ( $R_a$ ) of the Horizontal samples before tribology was inferior by 98% (at 100  $\mu\text{m}$ ) compared with the 45° angle and Vertical because of the extremely smooth layer where the measuring was done.

The horizontally printed samples' surface roughness grew after tribology (68% compared with the virgin surface) because of the tracks of the worn area caused by the test. On the contrary, the surface roughness was decreased remarkably for the specimens of 45° angle and Vertical orientations after the tribological tests. As a general conclusion about the surface roughness of the materials studied, the horizontally printed specimens have offered the smoothest surface as compared to other build orientation samples. Further, a considerable reduction was observed in the surface roughness ( $R_a$ ) values after tribological tests against the virgin surface, confirming the occurrence of wear by removing the facing rough layers.

**The findings mentioned above are published in [1], [6], [13], and one more article is under review in the Journal of Materials and Design (IF: 7.99), see list of publications (Appendix A2).**

### 4.5. Surface structure observation

#### 4.5.1. Surface structure of neat PLA material FDM 3D-printed

Micrographs for the sliding area surface of PLA cylindrical specimens prior to and after the tribological tests under a 150 N load are shown in Figs. 4.44-4.46. The samples were manufactured in Horizontal, 45° angle, and Vertical directions to examine the impact of these different build orientations on the printed parts' morphology.

Fig. 4.44a and Fig. 4.44b displays the optical images of the Horizontal test piece. Obviously, the FDM printing lines (infill at the sliding area) before the tribology test were polished after the experiment, indicating material removal due to wear. As mentioned in the surface roughness observations, Horizontal specimens' sliding area has a smoother surface than other test pieces due to its structure. This led to a larger contact area with the mating surface and produced a higher wear rate, which was apparent in the test pieces' burnished surface. The wear track toward the sliding direction can be seen clearly. A lot of molten and then resolidified debris are noticeable as well. The edge of the Horizontal sample is presented in Fig. 4.44c and Fig. 4.44d. These images evidence that the contact between sliding surfaces was considerably uniform up to the specimen's edge.

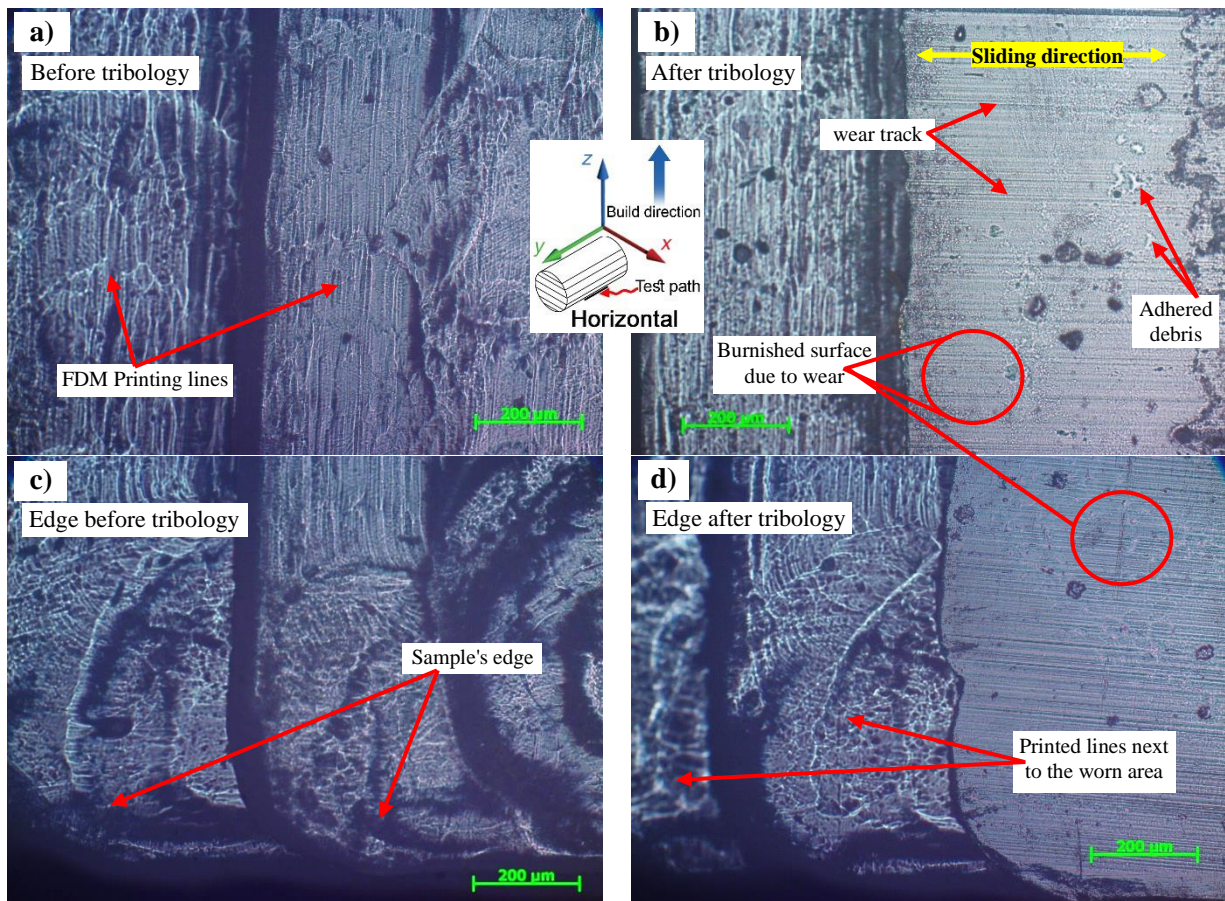


Fig. 4.44. Surface morphology of Horizontal print orientation specimen before and after tribology test

Fig. 4.45a-d shows the microphotographs for  $45^\circ$  angle specimens before and after tribological tests. In this sample, the shell (contour) is the facing side with the counterpart during the test (see Fig. 4.45a). When the build orientation is at an angle of  $45^\circ$ , the rasters are deposited in an oblique form. That may lead to gap formation among rasters of the contact area throughout the tribology test, as pictured in Fig. 4.45b-d. This is due to the relative motion and the compressive force sustained for contact. Consequently, these voids may also be responsible for grooves emergence demonstrated at the worn area (see Fig. 4.45b and Fig. 4.45d). Therefore, the wear surface having grooves can be clearly visible in these microphotographs. Further, deep or shallow pits may be formed because of the repeated sliding contact of the surface asperities due to relative motion. Fig. 4.45c shows that contact between the sliding surfaces was not entirely uniform. Some zones were even out of contact due to the disadvantage of constructing the layers in an oblique form.

Fig. 4.46a shows the layer-by-layer structure of the Vertically oriented specimens (before the experiment), where the layers built upwardly. Due to the shell texture (which represents the sliding surface in this sample), all layers have peaks, and between every two layers there is a valley. These peaks and valleys act as asperities, as the surface becomes rougher due to them. During the sliding between the test piece's surface and the counterpart, these peaks and valleys deform and contribute to originate the worn surface. Severe wear scars were detected on the specimens' surface after the test, as depicted in Fig. 4.46b and Fig. 4.46d. The propagation of these scars can be attributed due to the deep asperities of the original surface. Furthermore, the extreme edge exhibited in Fig. 4.46c is not incorporated within the worn area, which indicates the nonuniformity of the sliding contacts.



#### 4. Results and discussion

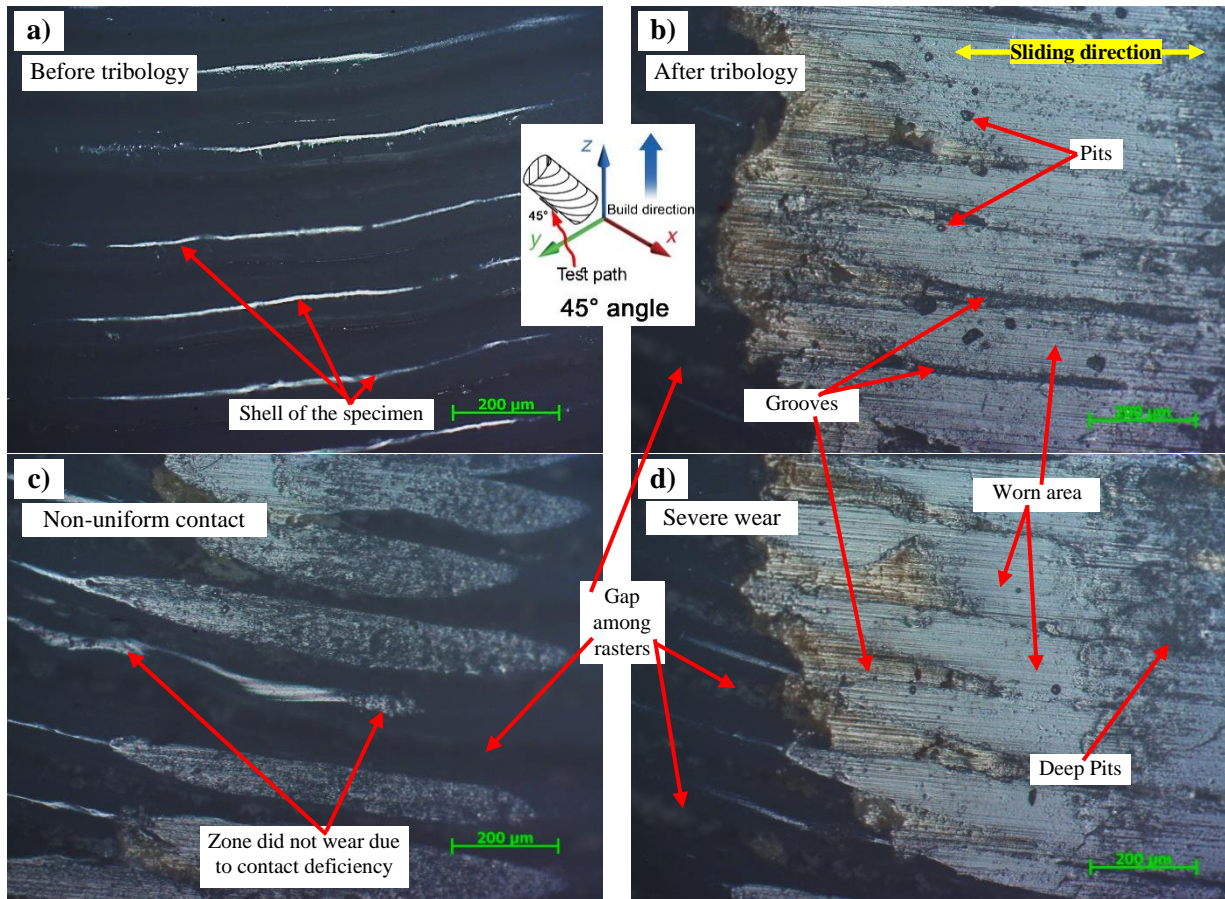


Fig. 4.45. Surface structure of 45° angle build orientation sample prior to and after tribology test

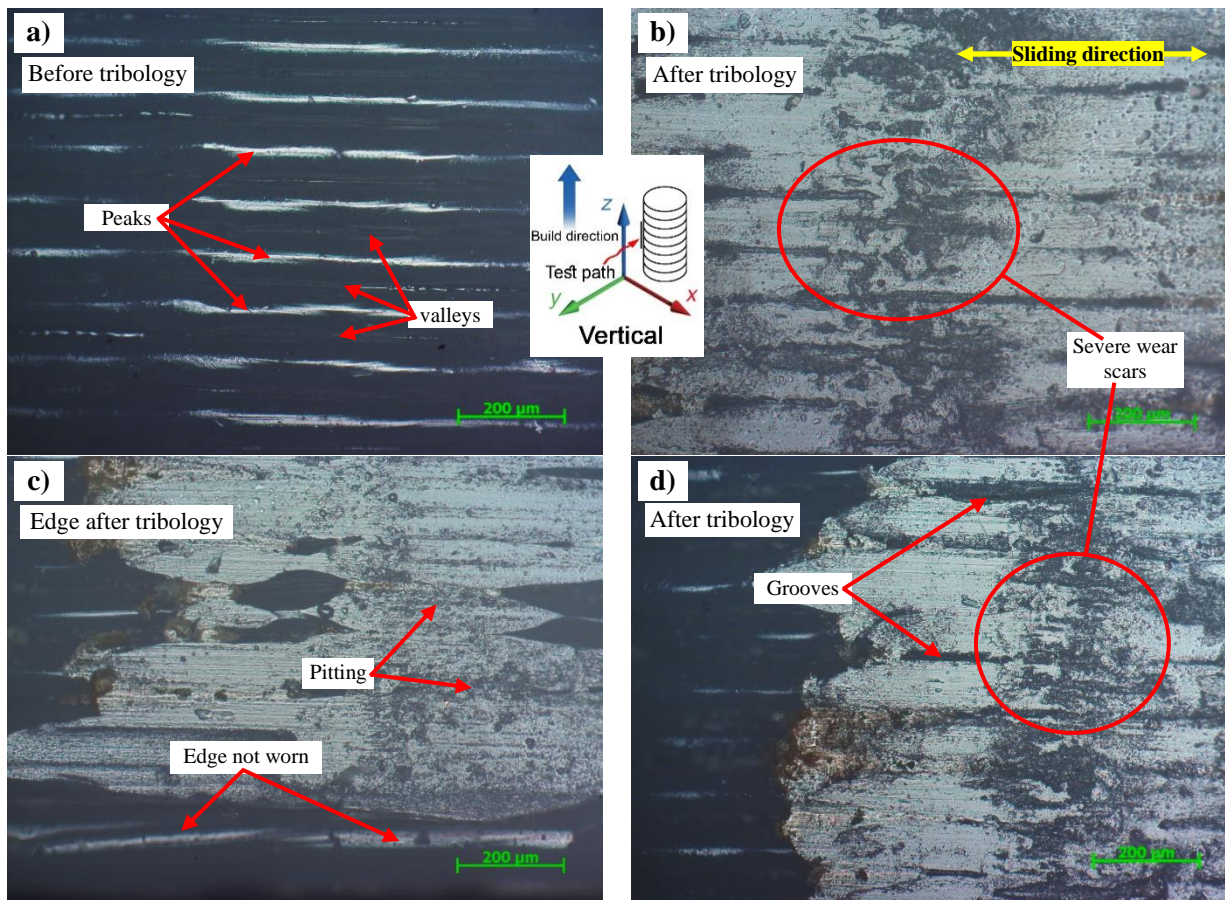


Fig. 4.46. Microscopic examination of the Vertically aligned printed specimen before and after tribological testing

Based on these observations, the wear mechanism of the 45° angle and Vertical test pieces (where the shell side is the mating surface) can be classified as abrasive wear. This was confirmed by the existence of marks of scar, pitting, and groove, which impacted the tribological behaviour. However, the Horizontal (where the inner infill side is the sliding surface) can be classified as adhesive wear with a slight amount of debris. The sliding area extent influences the surface roughness and consequently the wear behaviour. When the test piece's surface has a higher roughness (due to less contact area, like the 45° angle and Vertical specimens), the superficial layers wear off easily, resulting in a higher wear rate. In contrast, a larger sliding area decreases the wear rate (the same as Horizontal). This was suitably remarked in the specimens' tribological examinations under 150 N load, which are employed for the surface structure investigation. As Horizontal samples provided a reduction in the wear depth and specific wear rate compared to the other orientation pieces. Therefore, the texturing of the Horizontal specimen's surface is more appropriate to improve wear and friction performance.

#### 4.5.2. Surface structure analysis of bronze/PLA composite FDM 3D-printed

Micrographs of the surface morphology are shown in Figs. 4.47–4.49. The surface structure images of Flat orientation 3D-printed bronze/PLA specimen from the front and top view (when placed as in On-edge position) are offered in Fig. 4.47a–d. The random distribution of the bronze particles is clearly observed in the specimens. The layers were printed with a raster direction angle of 45°/135° (i.e., one layer with 45° while the upper one is 135° and so on). This direction angle as well as the curvature at the end of every built line have been illustrated. Despite the print infill setting is 100%, but spaces among lines have been observed in the specimens, which indicates the anisotropy of the FDM method. These lines in every layer are surrounded by a double strap of the shell (contour). The shell texture from the front and top view are also exhibited.

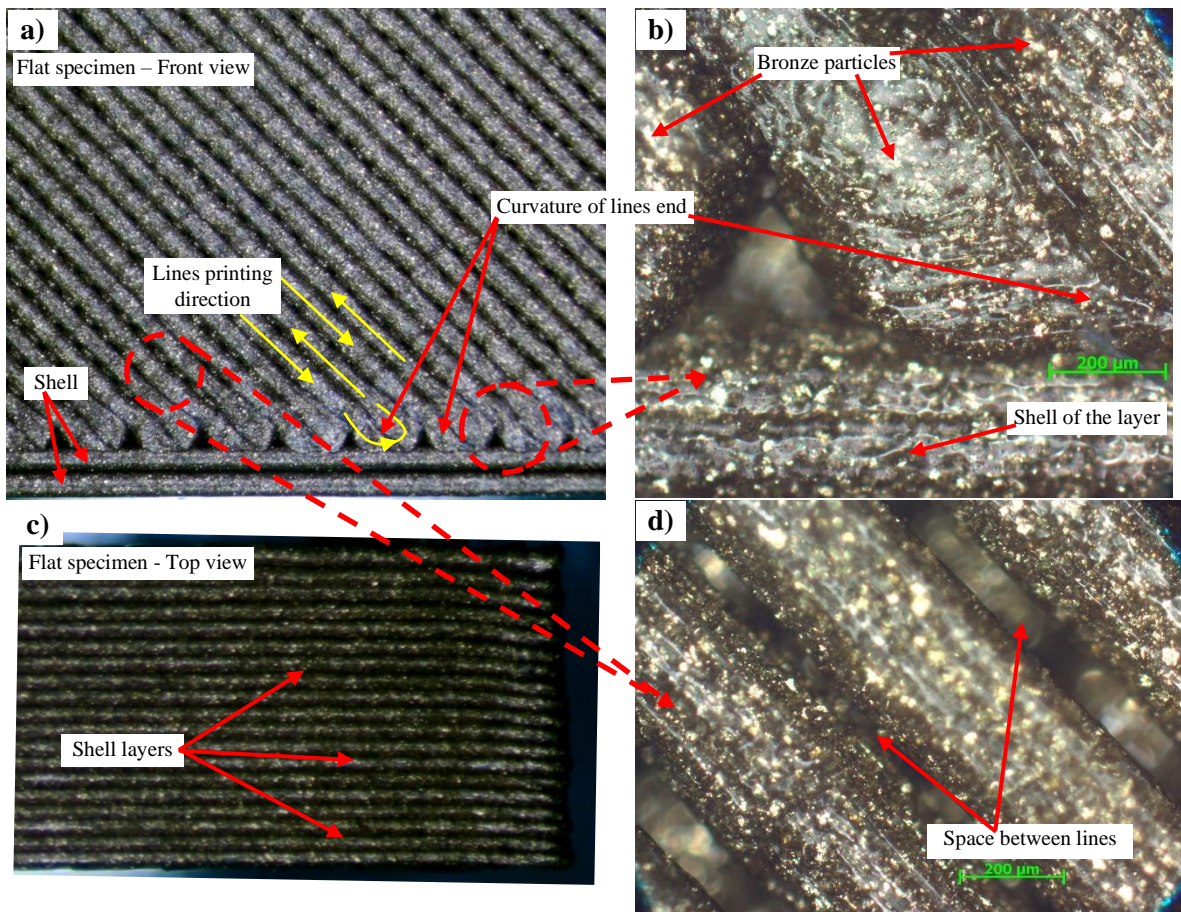


Fig. 4.47. Surface structure images of the 3D-printed sample in Flat orientation

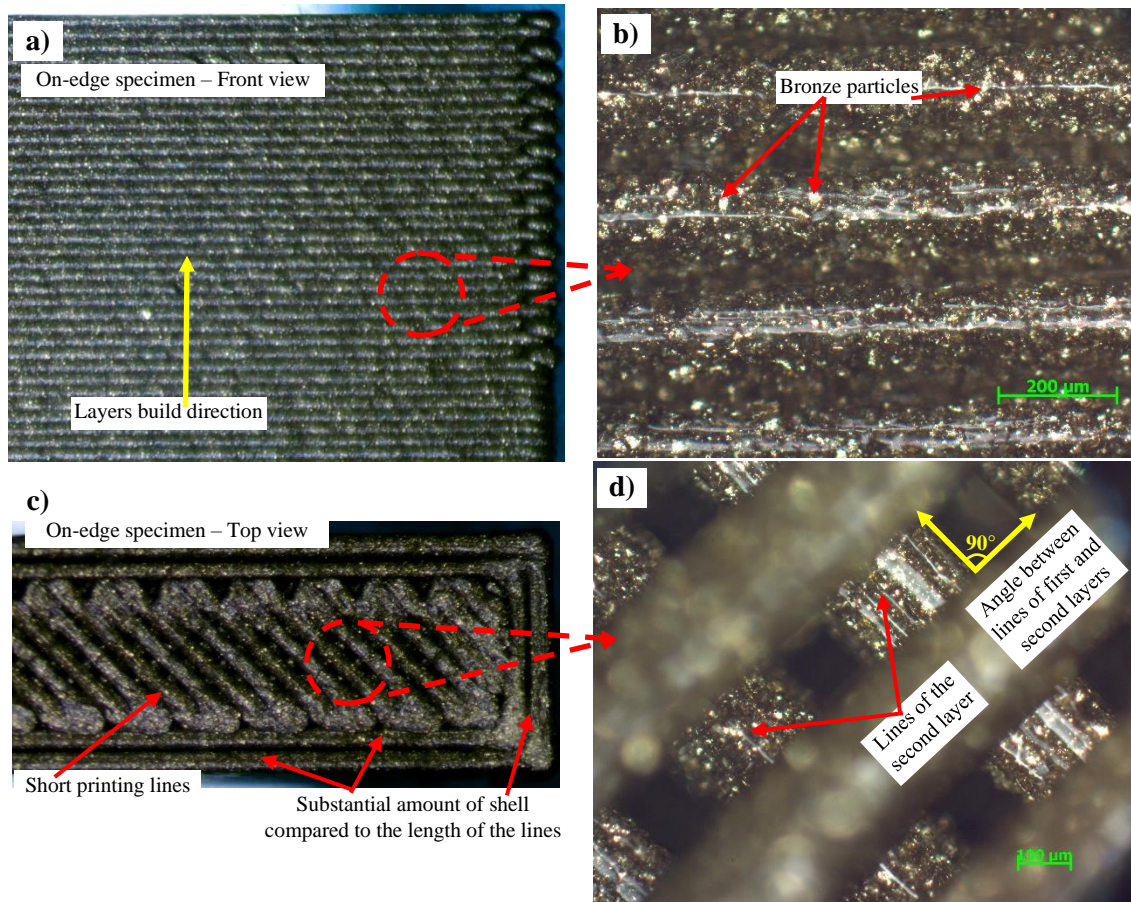


Fig. 4.48. Microscopic examination of On-edge orientation specimen

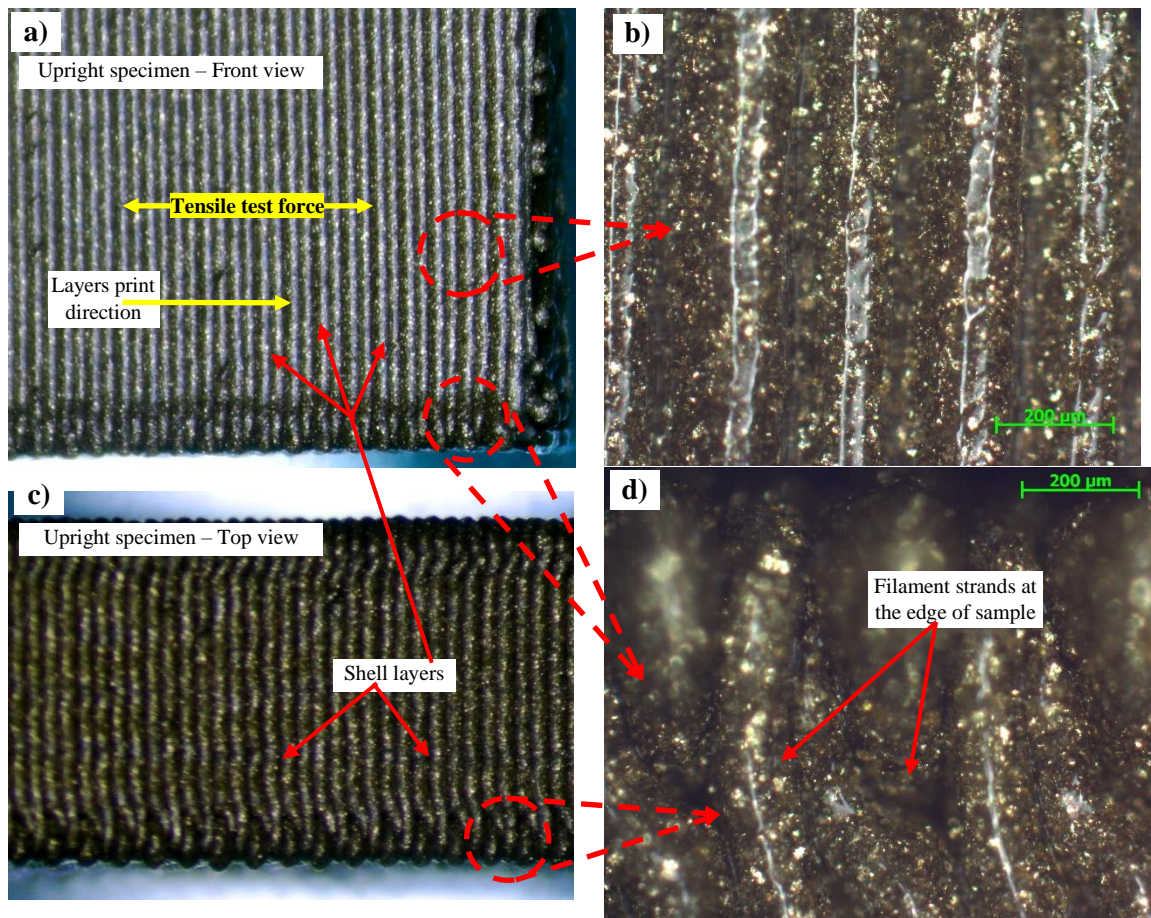


Fig. 4.49. The surface structure of the Upright specimen from the front and top view

The microscopic examination of the On-edge orientation specimen is shown in Fig. 4.48a–d. Short printing lines have been observed at the top view (seen in Fig. 4.48c). These short lines are supported by the interlocked layers (which were built layer by layer) as well as the assist of the shell. The samples of this orientation possess a substantial amount of shell compared to the length of the lines in every layer. These factors (short lines, the interlocking of layers, and the shell amount feature) grant the On-edge specimen strength more than other orientation specimens. This interprets why the On-edge specimens could afford twice the applied tensile load in comparison with the others. The angle between lines of layers was confirmed as  $90^\circ$  (manifested in Fig. 4.48d) since the angle of the raster direction for the first layer is  $45^\circ$ , while the second is  $135^\circ$ .

The front and top view of the Upright specimen have been demonstrated in Fig. 4.49a-d. A unique construction like the strands has been observed at the edges (binds the shell layers) of this sample (presented in Fig. 4.49c and Fig. 4.49d). The Upright sample has been characterized by a weak tensile strength. This due to the layers of the test piece were built perpendicular to the applied force of the tensile test. As the adhesion bonding is the only linkage since there are no merged lines or fibres among the layers.

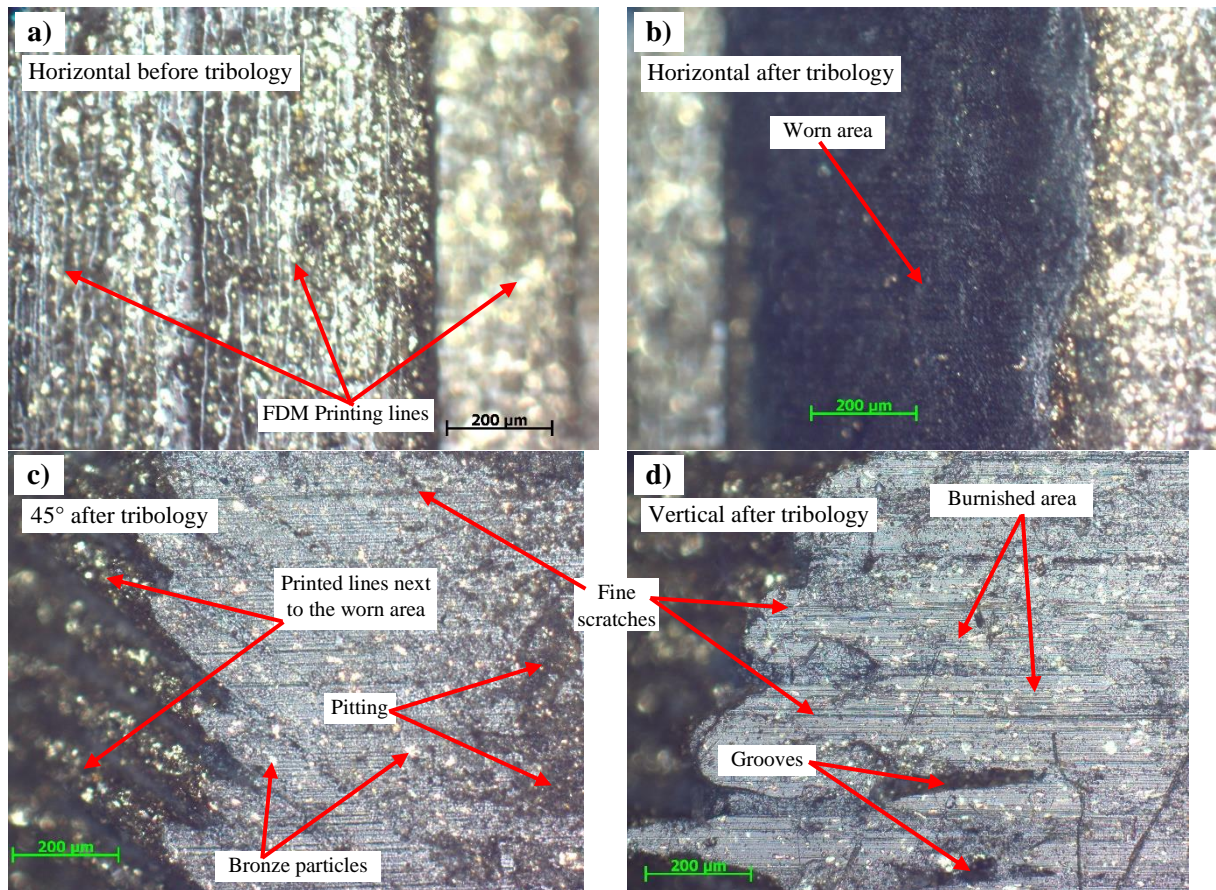


Fig. 4.50. Surface morphology of FDM specimens printed in Horizontal,  $45^\circ$  angle, and Vertical orientation before and after tribology test

Micrographs of the perimeter morphology of bronze/PLA cylindrical specimens before and after the tribology test are shown in Fig. 4.50a–d. The surface structure after the tribology test for the Horizontal,  $45^\circ$  angle, and Vertical print orientation samples has been exhibited in Fig. 4.50b, Fig. 4.50c and Fig. 4.50d, respectively. The essential points associated with the surface morphology of the worn area were demonstrated. At the Horizontal print orientation sample, the worn area is pigmented with black colour (displayed in Fig. 4.50b). This is because of the large contact area with the counterpart, which results in a higher wear rate for test pieces. It can be observed that

after sliding at different conditions, most of the bronze particles are still in its locations. These particles are in good condition, and no pull out or detachment was noticed. The existence of an abrasive wear mechanism was confirmed by the microscope images of different print orientations, which showed marks of pitting and grooves (as disclosed in Fig. 4.50c and Fig. 4.50d). Those asperities contributed to alteration of the surface roughness, which influenced the tribological behaviour. In the obtained tribology results, the decreased wear loss of the vertically-orientated sample, despite the higher coefficient of friction, was due to the higher roughness of the surface. This confirmed the high pressure prevailing between the sliding surfaces due to the lower contact area. In contrast, the horizontally-orientated test piece revealed a relatively lower surface roughness that caused a higher wear depth but a lower friction coefficient. The extent of sliding distance also affects the surface roughness and, implicitly, the wear behaviour. When wear occurs, the surface of the specimen has a higher roughness. Hence, the top layer wears off easily, presenting a higher wear rate. As the sliding distance increase, the high slope of the wear rate decreases. As wear progresses, a glaze forms on the specimen sliding surface, which cause a significant reduction in the rate of wear.

### *4.5.3. Surface morphology analysis of neat resin material DLP 3D-printed*

The surface morphology of DLP specimens has been exhibited in Fig. 4.51a-f, as an optical microscope was used for this purpose. The microscopic images are depicting the surface structure of different orientation specimens (X, 45°, and Z) before and after the tribological testing.

The surface topography of the X (Horizontal build orientation) printed specimens has been illustrated in Fig. 4.51a and Fig. 4.51b for prior and later the tribological testing, respectively. It can be clearly seen that the worn surface became burnished after the test. Also, re-adhered material was observed at the gaps among the burnished lines. This adhered material was created from the wear debris, which was deposited between the sliding bodies. As wear time increased, debris reaches sufficient volume and then re-adhere to the worn area. As a consequence, the adhered material fills the voids and grooves.

Fig. 4.51c and Fig. 4.51d demonstrates the 45° angle specimen after wear testing. The border between the worn surface and the non-worn lines (lines which are next to the sliding area) is displayed in Fig. 4.51c. In this figure, the marks of adhesion wear mechanism could be noticed. The load pressure and the heat promote the softened polymer film to adhere to the metallic counterface and then work as a lubricant. This leads to lower the specific wear rate, which was evinced in the post-curing specimens.

The vertically (Z) printed specimens before and after tribological testing are represented in Fig. 4.51e and Fig. 4.51f, consecutively. Uncured resin particles were manifested at the vertically printed lines before examining the wear. This indicates the insufficient UV curing time during the manufacturing process. Creation of surface asperities and cavities in the sliding surface have been observed following the tribology test. These asperities (rough surface) contribute to reducing the contact areas. Thus, the friction coefficient augments due to increasing the pressure. This interprets the high values that were reported for the coefficient of friction.

## 4. Results and discussion

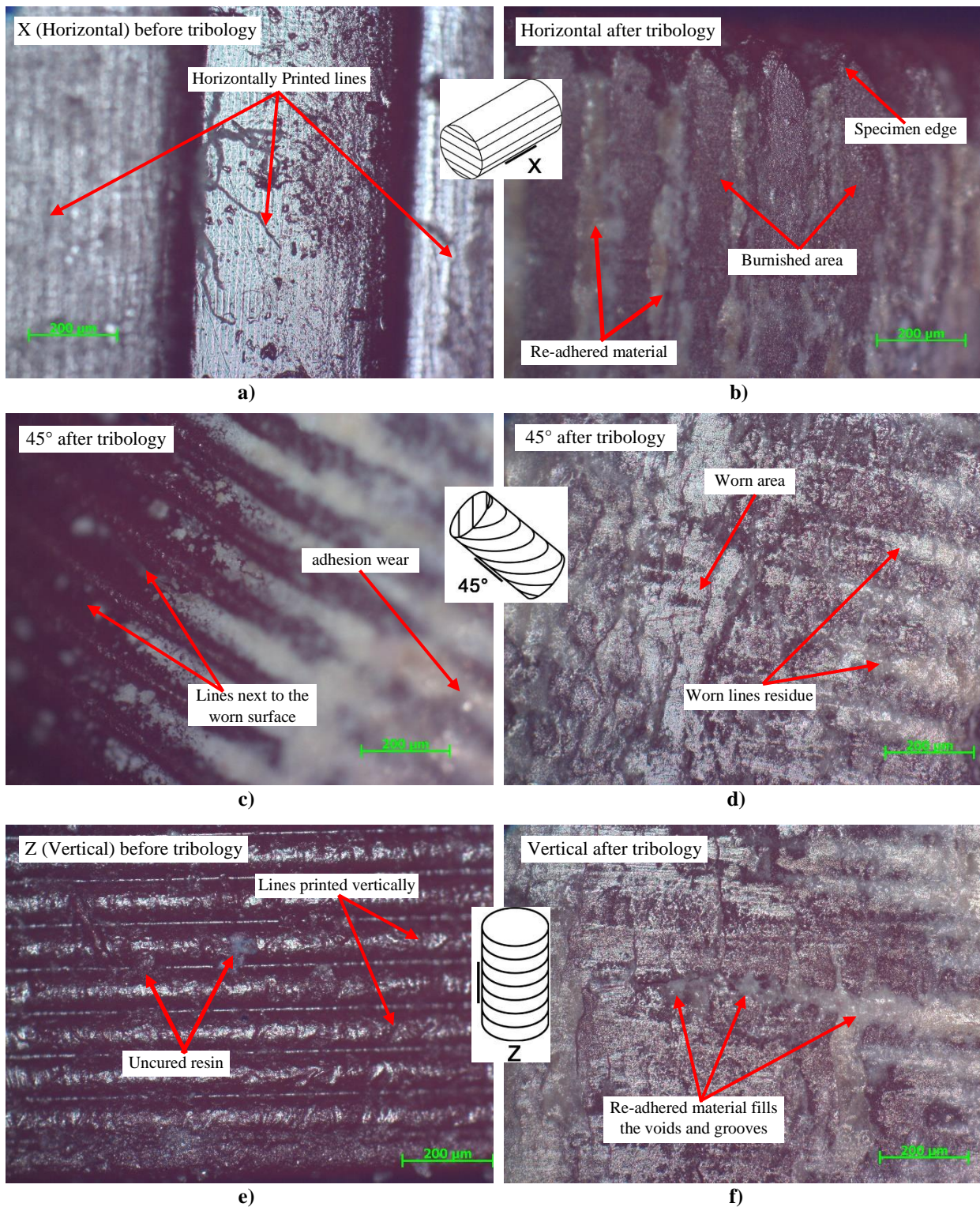


Fig. 4.51. Microscopic images for the surface morphology of DLP specimens 3D-printed in X, 45°, and Z orientations prior and later tribological testing

### 4.5.4. SEM of graphene/resin composites prepared with different relaxation times

Three different relaxation times after mixing the graphene with resin (matrix) by vortex mixer shaker were implemented for printing pretest specimens. These times are freshly made (printing the specimens immediately after mixing), after one day, and after one week. Fig. 4.52a-d shows the SEM images of different relaxation time specimens. The graphene/resin composite used for the microstructure examination is the one with 0.5 wt.% graphene. The graphene platelets are tiny as its particles have an average thickness of 3 nm and a diameter of 1.5 μm. Fig. 4.52a and Fig.

#### 4. Results and discussion

4.52b show that graphene particles were found on the samples (freshly mixed) and successfully incorporated into the ultimate printed structure. The graphene platelets also appear to be distributed evenly throughout the surface, with some minor pits visible.

The SEM image in Fig. 4.52c (after one day of mixing) is somehow consistent with the details shown in Fig. 4.52a regarding the presence and distribution of the graphene particles throughout the specimen surface. However, the amount of graphene platelets in Fig. 4.52c is hardly less than that shown in Fig. 4.52a. Besides, some wrinkles are more noticeable on the surface. These observations indicate the effect of relaxation time after one day of mixing. The surface view of the printed sample after one week of mixing (graphene/resin composite) clearly depicts the aggregations' formation of precipitated graphene particles (Fig. 4.52d). This suggests that graphene platelets have lost their uniform distribution over the sample's body structure after one week. The above observations were based on many SEM images taken from different spots.

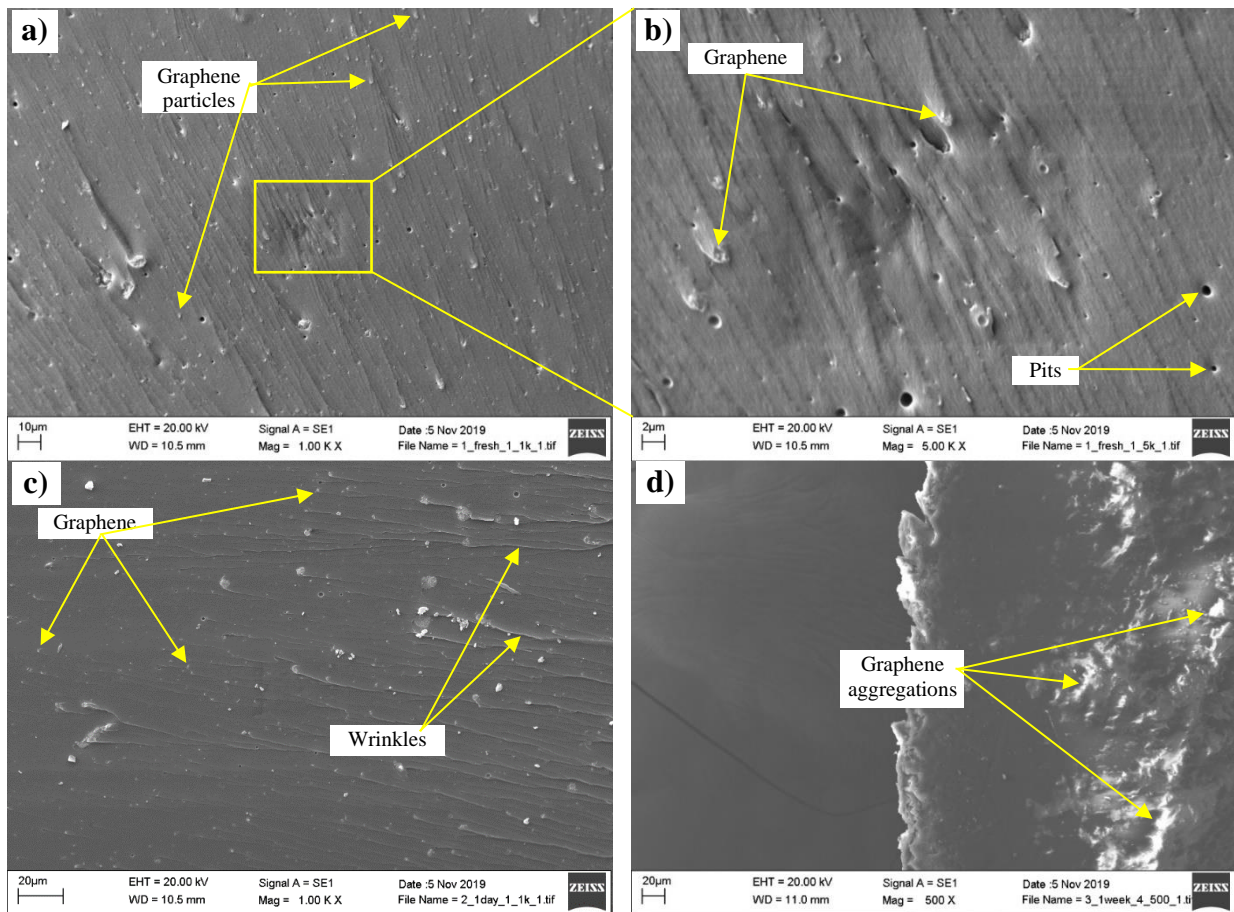


Fig. 4.52. The microstructure of specimens that were printed after a) and b) freshly mixing graphene with resin, c) one day of mixing graphene with resin, and d) one week of mixing graphene with resin

The term 'freeze fracturing' refers to the technique of freezing and then breaking a specimen to reveal its internal structure. The properties of a heterogeneous polymer system could be determined by interfacial interactions that SEM on a fractured surface can easily follow. The most frequent micromechanical deformation mechanism is debonding (which is an interfacial interaction) in particulate-filled polymers. If the adhesion between the polymer matrix and the filler is weak, the separation of the interface occurs under load/stress. The samples were therefore frozen and fractured in liquid nitrogen to create a proper surface for SEM and to decrease the painted area with gold, which is needed for the examination.

#### 4. Results and discussion

The pieces were submerged in liquid nitrogen for approximately 5 minutes to ensure they were completely frozen. The temperature was the boiling point of nitrogen,  $-195\text{ }^{\circ}\text{C}$ . The specimens were then removed from the liquid nitrogen and immediately snapped with two pairs of tweezers. The fracture behaviour of the freshly mixed specimen is depicted in Fig. 4.53a and Fig. 4.53b. While the surfaces in general are almost smooth, sharp edges can be seen in the breakage areas. Fig. 4.53c highlights the morphology of the fractured cross-section (one-day sample) and shows an interesting phenomenon of the fracture pattern in a saw-teeth form. The saw-teeth formation may be resulted from the final separation of aggregated graphene platelets. This is because the graphene congregation area is weaker and the fracture carries out in the points that connect two ridges. The saw-teeth shape formation is also obvious in the one-week specimen at the fractured cross-section surface, exhibited in Fig. 4.53d. This further confirms the role of graphene particles' aggregations in causing such a phenomenon.

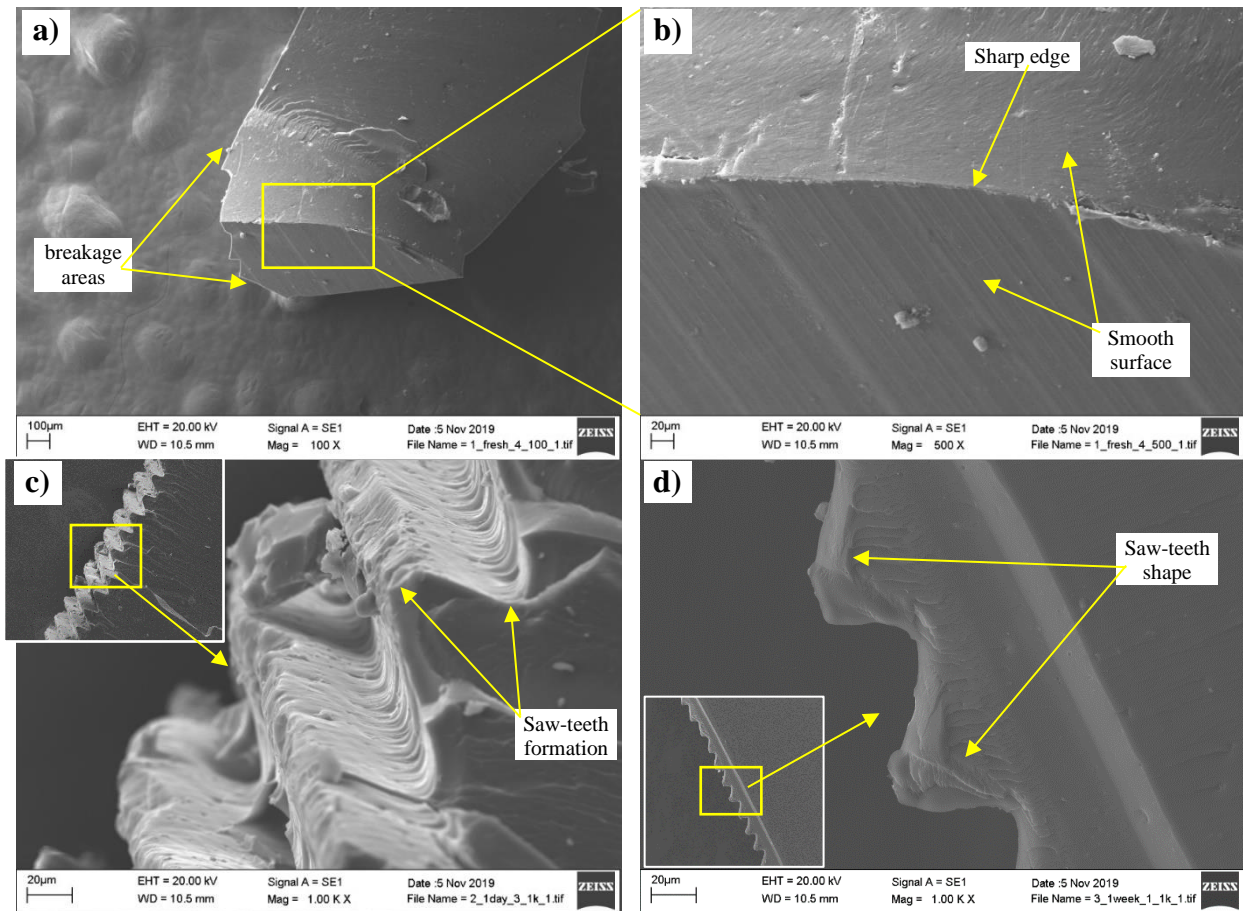


Fig. 4.53. Fracture morphology of graphene/resin composite specimens that were printed after a) and b) freshly mixing, c) one day of mixing, and d) a week of mixing

The relaxation time may have a negative effect on the homogeneity of the composite, as the graphene nanoplatelets tend to precipitate or colligate with each other. This eventually decreases the effectiveness of the graphene distribution over the polymer matrix. Furthermore, the relaxation time is important as it allows the air bubbles to escape from the mixture without the need for a vacuum chamber. It was thus necessary to investigate how different relaxation times affect the composite's homogeneity. It was evident in the freshly mixed sample (Fig. 4.52[a and b] and Fig. 4.53[a and b]) that the graphene platelets were homogeneously distributed and had a smooth fracture surface. In contrast, the specimens printed after a while (whether one day or a week later) showed a saw-teeth shape formation at the fracture cross-section, thus demonstrating that, at these relaxation times, distinctly after a week, most graphene platelets were precipitated. Therefore, all



test pieces used in the experiments were printed with a fresh mixing for graphene/resin composite. This helped ensure that graphene particles are homogeneously distributed and that there are no problems in the surface and interior morphology.

On the other hand, the addition of graphene to the polymer matrix had a side effect as it made it difficult for the ultraviolet light to fully cure the resin. This difficulty increased with an increase in the graphene concentration in the composite. Hence, more than 2 wt.% of graphene was arduous to be printed because the graphene particles caused the light to scatter. Moreover, the graphene platelets are black coloured, and it led to light energy of the UV light leaving the resin semi-cured being absorbed, despite the post-processing that included further UV light curing and heat treatment. Nevertheless, approaching a graphene ratio of 2 wt.% to be printed by photopolymerization technique is considered an outstanding achievement. Several works in literature report that polymer composite 3D objects can be developed through light-based printing systems (photopolymerization) by using a low concentration of carbon nanoparticles (such as graphene or carbon nanotube). The ratio of these particles within the composite reached up to 0.1 wt.% of graphene (Markandan and Lai, 2020; Lai et al., 2021), 0.5 wt.% of graphene oxide (GO) (Lin et al., 2015; Chiappone et al., 2017), 0.01 wt.% of single-wall carbon nanotube (SWCNT) (Ushiba et al., 2013), 0.2 wt.% and 1.5 wt.% of multi-walled carbon nanotube (MWCNT) (Liu et al., 2016; Y. Zhang et al., 2018), and 0.3 wt.% of CNT (Gonzalez et al., 2017). This indicates the efficiency of the composite's preparation method in this work with the vortex mixer shaker.

### *4.5.5. Summary and conclusions on the investigation of surface morphology*

In this chapter (4.5.), the surface morphology and the microstructure of 3D-printed parts were discussed. The specimens were 3D-printed using FDM (neat PLA and bronze/PLA composite) and DLP (neat resin and graphene/resin composite) technologies together with varying processing parameters (mainly build orientation). The microscopic images were taken for the specimens before and after the tribology tests. The essential points associated with the surface morphology of the worn area were demonstrated. Also, SEM images were carried out to determine the integration and distribution of additives throughout the polymeric matrix. Based on the obtained results, the following conclusions can be drawn:

For FDM 3D-printed PLA

- The optical microscope images disclosed that 45° and Vertical samples presented abrasive wear mechanism confirmed by marks of scar, pitting, and groove owing to the deep asperities. However, adhesive wear was offered by the smooth surface of Horizontal pieces where larger contact area with the mating surface producing a higher wear rate.

For FDM 3D-printed bronze/PLA composite

It can be observed that after sliding at different conditions, most of the bronze particles are still in its locations. These particles are in good condition, and no pull out or detachment was noticed. For DLP 3D-printed resin

- The sliding surface became burnished after the tribological tests, indicating the occurrence of wear.
- Adhered material was observed filling the voids and grooves among the burnished printing lines. These attached materials were created from the wear debris deposited between the sliding bodies.

For DLP 3D-printed graphene/resin composite

- Based on the SEM images, the freshly mixed sample showed a uniform distribution for graphene platelets with a smooth fracture surface. In contrast, the specimens printed after one day or a week showed saw-teeth shape formation at the fracture cross-section because most graphene platelets were precipitated.

**The findings mentioned above are published in [1], [6], [13], and one more article is under review in the Journal of Materials and Design (IF: 7.99), see list of publications (Appendix A2).**

#### 4.6. Determination of surface energy

The Eos (single-liquid) and Fowkes (two-liquid) methods were used for the evaluation. As a measuring liquid, water was utilized for the Eos method, whereas diiodomethane and cyclohexane were employed for Fowkes. The PLA samples' surface was dissolved when introduced to the diiodomethane and cyclohexane. Therefore, it was not possible to determine its surface free energy values by the two-liquid (Fowkes) method. Accordingly, the PLA was only examined by the single-liquid (Eos) method using water.

##### 4.6.1. FDM 3D-printed PLA - single-liquid measurement results

The surface free energy value was calculated with the Eos model. During the measurement, well-examined, constant-volume droplets that did not flow were obtained. The measurement results are tabulated in Table 4.3. In addition, the measurement recordings are given in Fig. 4.54. The calculated surface free energy value is  $\gamma = 9.64$  (mN/m).

Table 4.3. PLA - water measurement results

Edge angle	Measurement number		
	1	2	3
Left edge angle (°)	132.66	129.72	115.95
Right edge angle (°)	131.28	128.81	116.03
Edge angle average (°)	131.97	129.26	115.99

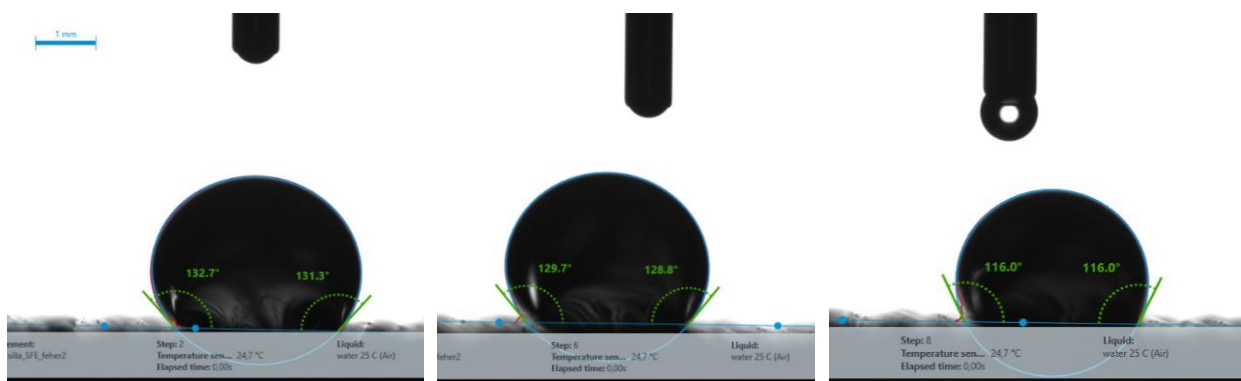


Fig. 4.54. Photograph of a water drop residing on FDM 3D-printed PLA surface during the measurement using the Eos method, for three tests at identical conditions

##### 4.6.2. DLP 3D-printed Resin - single-liquid measurement results

The measurement results are listed in Table 4.4. The calculated surface free energy value is  $\gamma = 41.09$  (mN/m). The measurement recordings are given in Fig. 4.55.

## 4. Results and discussion

Table 4.4. Resin - water measurement results

Edge angle	Measurement number		
	1	2	3
Left edge angle (°)	78.81	76.82	60.54
Right edge angle (°)	78.52	76.26	63.82
Edge angle average (°)	78.67	76.54	62.18

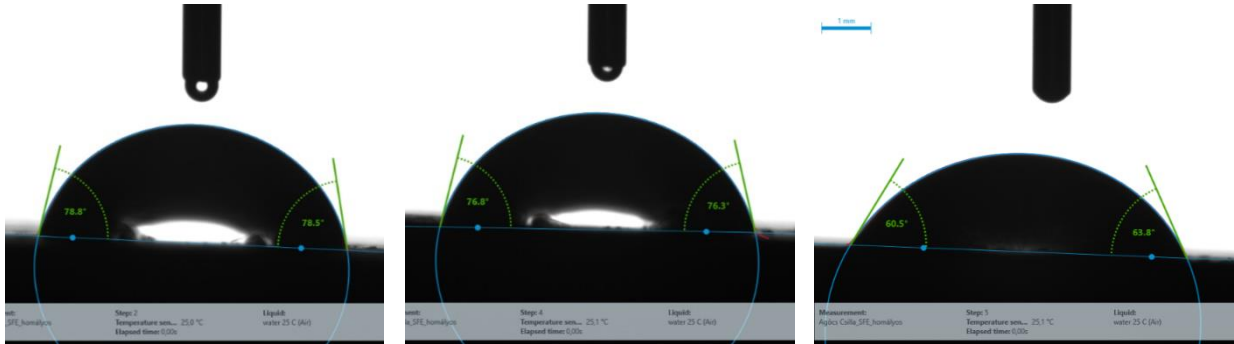


Fig. 4.55. Photograph of a water drop residing on DLP 3D-printed resin surface during the measurement using the Eos method, for three tests at identical conditions

### 4.6.3. DLP 3D-printed Resin - two-liquid measurement results

The surface free energy value was calculated with the Fowkes model. The measurement results are presented in Table 4.5. In addition, the measurement recordings are depicted in Fig. 4.56. The calculated surface free energy value is  $\gamma = 38.30$  (mN/m).

Table 4.5. Resin - diiodomethane measurement results

Edge angle	Measurement number		
	1	2	3
Left edge angle (°)	49.26	60.11	58.51
Right edge angle (°)	63.52	67.63	69.35
Edge angle average (°)	56.39	63.87	63.93



Fig. 4.56. Photograph of a diiodomethane drop residing on DLP 3D-printed resin surface during the measurement using the Fowkes method, for three tests at identical conditions

The measurement results show that DLP 3D-printed resin has a high surface free energy (41.09 mN/m). High surface energy means a stronger tendency to adhesion, and greater friction thus may

occur during sliding. On the other hand, the FDM 3D-printed PLA exhibited a low surface free energy value (9.64 mN/m), indicating that this material is likely well suited for plastic-plastic friction, as the lubricant does not stick to the surface. Fig. 4.57 displays the relation between the coefficient of friction (obtained from the tribological testing) and surface free energy for the same materials made by FDM and DLP 3D printing techniques. The figure shows that the coefficient of friction has increased as the surface energy increase, which supports the expectation mentioned above.

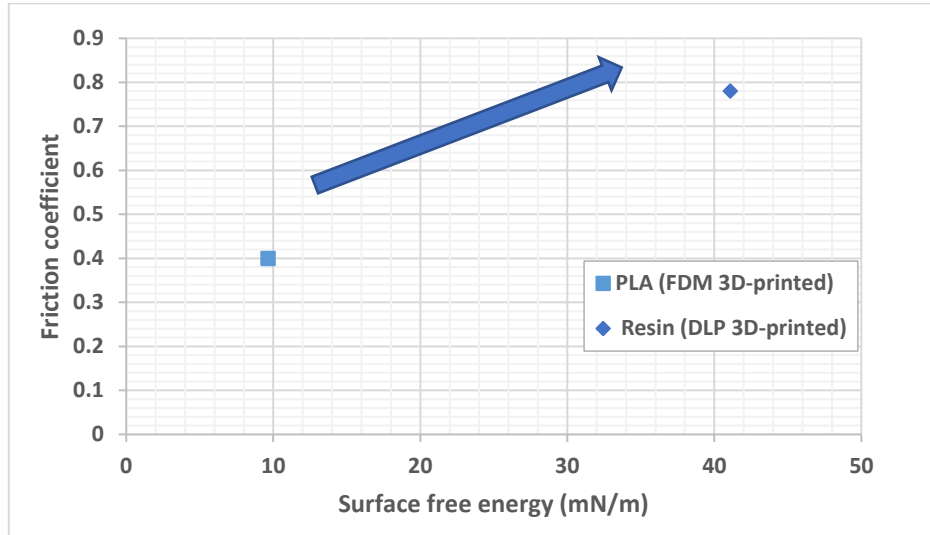


Fig. 4.57. The relationship between the coefficient of friction and surface free energy when water is the measuring liquid using the Eos method

#### 4.7. New scientific results

The tribological and mechanical characteristics of 3D-printed polymers and polymer composites were comprehensively investigated in this study. The following points are noteworthy to be mentioned:

##### 1. Correlation between the manufacturing process parameters and the tribological properties

I found that the 3D printing parameters (build orientation and layer thickness), strongly influence tribological characteristics in the context of surface waviness/roughness.

Print orientation has an effect on wear based on the surface's macro geometry formed. The Horizontal orientation is smooth compared to other build orientations (e.g., the surface roughness ( $R_a$ ) of Horizontal is 65–98% lower than the 45° angle and Vertical). Accordingly, I confirmed that if the surface of the specimen is more rough (due to the smaller contact area), the surface layers will wear easily, resulting in a higher abrasion rate (around 32%). Also, I have created a 3D CAD model utilizing the same print orientations examined, focusing on the sliding surfaces' macro geometry. I found that the wear depths of the model's surfaces are in good agreement with the results obtained experimentally.

As the print layer thickness increases, the surface roughness increases, where the rough peaks suffer further and faster wear compared to the smoother surfaces. These findings are supported by my tribological test results, where the wear depth was reduced by 27.2% and 31% for the 50 and 35  $\mu\text{m}$  layer thicknesses, respectively, compared to the 100  $\mu\text{m}$  samples.

### *2. The impact of composite fillers on the tribological and mechanical characteristics*

I have established that the addition of graphene (which can act as a solid lubricant) significantly impacted the coefficient of sliding friction, which was reduced by up to 50% in the graphene-containing samples (mainly in the Horizontal position regardless of layer thickness) compared to the neat resin samples. I found that the optimal graphene volume in the matrix when its concentration does not exceed 0.5 wt.% as it provides better tribology characteristics and also does not reduce the mechanical behaviour.

I observed that graphene resulted in different behaviour in terms of its mechanical properties. Graphene nanoplates did not improve Young's modulus and UTS. Upon further increase of the graphene concentration, worse mechanical properties (almost 24.7%) were obtained due to the increase in porosity. This clearly shows that the preferred tribological characteristics of the graphene/polymer composite plain bearing are coupled with poorer mechanical features.

I investigated composites with high graphene concentrations prepared with an efficient mixing method (lab vortex procedure). I was able to print composites with a graphene ratio of 2 wt.% by the photopolymerization technique. I proved the reliability of the satisfactory mixing method of the uniformly distributed graphene platelets, which was confirmed by the microstructural SEM images. I have shown that the freshly mixed sample is uniformly distributed on graphene plates with a smooth fracture surface. However, the pieces printed after one day or one week of resting showed a saw-teeth shape formation in the cross-section of the fracture, as most of the graphene platelets were detached.

### *3. The effect of graphene platelets alignment on friction and wear behaviour*

I found a correlation between the effect of adjusting graphene platelets and the friction and wear behaviour. The arrangement of graphene in the polymer is similar to the isostress configuration (the lower surface of the graphene platelet faces the upper surface of the printing platform). When testing a horizontally printed specimen, the graphene platelets have a larger contact area during the tribo test, taking into account its orientation at the bottom of the specimen. This large area allows these platelets to act as a solid lubricant and reduce friction and abrasion. As a result, the coefficient of friction has been significantly reduced, and in some cases (especially horizontally) has reached roughly half the value of pure resin material.

I showed that the wear depth of the graphene/resin composite samples increased by 98% and 64%, respectively, at an angle of 45° and a Vertical orientation at a layer thickness of 100 µm and 50 µm, respectively. This is due to the fact that the cross-section of the nano-platelets face the sliding surface due to the arrangement orientation of the graphene platelets, as the samples in the Vertical/45° orientation are placed in a flat (plane) position during the test. This will make the contact area much smaller and increase roughness and wear.

### *4. The influence of material's colour*

I ascertained that the filaments with various colours, due to different additives, reflects an obvious impact on the coefficient of friction of the test pieces. White colour samples gave the highest coefficient of friction while the lowest gave grey. Black specimens reported high wear depth. I stated that this could be related to the characteristics of the black body, where the maximum heat retains in the body of the sample, causing thermal softening and faster melting of the sliding surface layers. I proved this through some heat-conductive tests were carried out on the same examined tribology specimens. The black kept the heat for a longer time, indicating the formation of higher temperatures and therefore determining the tribological behaviour.

## 5. CONCLUSION AND SUGGESTIONS

In this study, the tribological and mechanical behaviour of FDM and DLP 3D printing polymer and polymer composites were reviewed exhaustively. Based on the assessment of the results, the following observations can be drawn:

In the FDM 3D printing:

- The Young's modulus and UTS are maximum at On-edge print orientation due to its robust construction, while elongation at UTS and elongation at break are better at Flat orientation.
- The print orientation has the highest contribution parameter which affects mechanical features compared to the other examined 3D printing process factors.
- The fracture profile of specimens after the tensile test followed/(affected by) the inner structure, which was either in the shape of zigzag, sharp, or transition.
- The occurrence of the stick-slip phenomenon was more likely in the context of sliding under low loads, but wear was diminished.
- The friction coefficient of 45° angle and Vertical orientation samples decreased at higher load due to the deformation in the contact area caused by the rough surface.
- The Upright and On-edge samples disclosed a higher hardness, due to the test needle was in contact with the shell which is more solid than the inner print filling.

In the DLP 3D printing

- Based on the SEM images, the freshly mixed sample showed a uniform distribution for graphene platelets with a smooth fracture surface.
- The most robust specimens in terms of the tensile strength were obtained at 0° angle as compared to 45° and 90° orientation angles.
- In terms of layer thickness influence, the highest tensile strength attitude was observed in the lowest layer thickness (35 µm) specimens, due to the increase in the number of layers.
- The UV post-curing process played a significant role in the augmentation of the tensile stress value, but meanwhile diminution the elongation at the break. Also, the non-cured specimens demonstrated the highest wear depth and lowest friction coefficient and hardness in comparison with the cured ones.
- The dynamic coefficient of friction in the 0.5 wt.% graphene specimens disclosed a significant decrease (reached up to 50%) as the graphene acted as a solid lubricant.
- The horizontally printed specimens have offered the smoothest surface as compared to other build orientation samples.

This topic is extremely fertile to be further explored, as quite a lot of aspects are still not covered yet. To highlight some of which, numerous recommendations can be suggested. In the same used cylinder-on-plate tribometer, varying more testing parameters (e.g., sliding speed) should be conducted to investigate its influence, in the context of 3D printing settings, on wear and friction. Also, further studies on the performance of 3D-printed objects under other tribo systems (e.g., pin-on-disk, block-on-ring, etc.) should be carried out. Moreover, applying additional machining/chemical-post-processing on the surfaces of 3D manufactured elements is likely to improve its tribological behaviour. Besides, much more composite materials (including bio-composites) can be tested as well.

## 6. SUMMARY

### THE EFFECT OF 3D PRINTING STRUCTURES AND SURFACES ON THE TRIBOLOGICAL BEHAVIOR OF POLYMER AND POLYMER COMPOSITES

In summary, the tribological and mechanical behaviour of two 3D printing technologies (FDM and DLP) were studied comprehensively. Four different polymer materials were examined (neat PLA and bronze/PLA composite for FDM, and neat resin and graphene/resin composite for DLP). Various print settings (build orientation, raster direction angle, and layer thickness) and material colours (white, grey, black, and red) were used during the specimens' manufacture. For DLP, the specimens were inspected with and without post-processing (heating and UV post-curing). The experiments of tribological tests were performed in alternative reciprocating sliding under dry conditions. Two applied loads (150 N and 200 N) were employed throughout the experiments of tribological tests. The effect of 3D printing parameters and additives' existence on the coefficient of friction, wear depth, and specific wear rate were evaluated. The tensile tests were investigated on 3D-printed specimens, and the tensile strength, UTS, elongation at UTS, and elongation at break have been assessed in consistence with the behaviour gained from the examined print settings. SEM and optical microscope were used to study the microstructure and the surface morphology of printed components prior to and after the tribological tests. Hardness and surface roughness of specimens were also tested and analysed for their association with tribological behaviour.

For FDM 3D-printed specimens, the results showed that the white colour samples have offered the highest friction coefficient, whereas the lowest was observed at the grey. The black coloured specimens reported a high wear depth rate. The occurrence of the stick-slip phenomenon was more likely in the context of sliding under low loads. Further, the wear depth and implicitly specific wear rate reduced with growing the applied load. The friction coefficient of 45° angle and Vertical orientation samples decreased at higher load due to the deformation in the contact area. The Young's modulus and UTS are maximum at On-edge print orientation due to its robust construction, while elongation at UTS and elongation at break are better at Flat orientation. Meanwhile, the Upright sample showed a very fragile behaviour, with extremely rapid fracturing of the printed layers at the break point. The print orientation has the highest contribution parameter which affects mechanical features of the used materials compared to the other examined 3D printing process factors.

For DLP 3D printing, the non-cured specimens demonstrated the highest wear depth and lowest friction coefficient as compared to the cured ones. Based on the SEM images, the freshly mixed sample showed a uniform distribution for graphene platelets with a smooth fracture surface, unlike the specimens printed after one day or a week. The graphene percentage of 0.5 wt.% was suggested as the optimum ratio for attaining the best tribological behaviour results in this work, as it decreased the friction coefficient roughly 50%. The highest tensile strength attitude was observed in the lowest layer thickness (35 µm) specimens, due to the increase in the number of layers. A worse mechanical attitude was gained when increasing the graphene concentration, owing to the porosity increase. The horizontally printed specimens have offered the smoothest surface as compared to other build orientation samples. The hardness of post-processed specimens has increased by 11.4% comparing to non-post treated samples. Also, the hardness increased with the increase in graphene ratio. This shows that the presence of graphene even at a low percentage can alter the hardness value of the composite material.

## 7. ÖSSZEFOGLALÁS (SUMMARY IN HUNGARIAN)

### 3D NYOMTATÁSI STRUKTÚRÁK ÉS FELÜLETEK HATÁSA POLIMER ÉS POLIMER KOMPOZITOK TRIBOLÓGIAI VISELKEDÉSÉRE

Átfogóan tanulmányoztam két eltérő 3D nyomtatási technológia (FDM és DLP) hatását a tribológiai és mechanikai viselkedésre. Négy különböző polimer anyagot vizsgáltam (natúr PLA és bronz/PLA kompozit FDM nyomtatással, valamint natúr gyanta és grafit/gyanta kompozit DLP nyomtatással). A minták gyártása során különféle nyomtatási beállításokat (rétegépítés tájolása, raszteres irányszög és rétegvastagság) és anyagszíneket (fehér, szürke, fekete és piros) alkalmaztam. A DLP esetében a mintákat utófeldolgozással (hevítés és UV utókezelés) és anélkül is ellenőriztem. A tribológiai tesztek kísérleteit henger-síkon modell rendszerben, alternáló csúszó súrlódással, kenésmentes körülmények között végeztem. A tribológiai vizsgálatok során két terhelést (150 N és 200 N) alkalmaztam. Értékeltem a 3D nyomtatási paraméterek és az adalékanyagok hatását a súrlódási tényezőre, a kopásmélységre és a fajlagos kopási sebességre. A szakítóvizsgálatokat 3D-nyomtatott mintákon vizsgáltam, és a szakítószilárdságot, az UTS-t, az UTS-beli nyúlást és a szakadási nyúlást a vizsgált nyomtatási beállításokból nyert viselkedéssel összehangban értékeltem. SEM és optikai mikroszkóp segítségével vizsgáltam a nyomtatott alkatrészek mikroszerkezetét és felületi morfológiáját a tribológiai vizsgálatok előtt és után. A próbatestek keménységét és felületi érdességét is teszteltem és elemeztem a tribológiai viselkedéssel való összefüggésük szempontjából.

Az FDM 3D-nyomtatott mintáknál az eredmények azt mutatták, hogy a fehér színű minták adják a legmagasabb súrlódási együtthatót, míg a legalacsonyabbat a szürke színnél figyeltem meg. A fekete színű mintáknál nagy kopásmélységet tapasztaltam. A „stick-slip” jelenség előfordulása inkább kis terhelés melletti csúszás esetén volt megfigyelhető. Ugyanakkor a kopási mélység és az implicit fajlagos kopási sebesség csökkent a normál terhelés növekedésével. A 45°-os szögben és a függőleges orientációban készült minták súrlódási tényezője nagyobb terhelésen csökkent az érintkezési területen fellépő deformáció miatt. A Young modulusa és az UTS maximális az „on edge” élen történő nyomtatási tájolásnál, a robusztus felépítésnek köszönhetően, míg az UTS nyúlása és a szakadási nyúlás „flat” lapon történő tájolás esetén kedvezőbb. Az „Upright”, függőlegesen nyomtatott minta sérülékeny viselkedést mutatott, a nyomtatott rétegek könnyed elválása miatt. A többi vizsgált 3D nyomtatási folyamat tényezőhöz képest a nyomtatási orientáció rendelkezik a legnagyobb járulékos paraméterrel, amely befolyásolja a felhasznált anyagok mechanikai tulajdonságait.

A DLP 3D nyomtatott próbatestek közül a nem utókezelt minták mutatták a legnagyobb kopási mélységet és a legalacsonyabb súrlódási együtthatót szemben az utókezelt mintákhoz képest. A grafit lemezek bekeverését követően rögtön nyomtatott próbatesteken elvégzett SEM-felvételeken jól látszik az egyenletes eloszlás és a sima törésfelület, ellentétben az egy nap vagy egy hét után nyomtatott mintákkal. Ebben a munkában a 0,5 tömeg%-os grafit százalékos arányt javasoltam optimális aránynak a legjobb tribológiai viselkedési eredmények eléréséhez, mivel ez közel 50%-kal csökkentette a súrlódási együtthatót. Ugyanakkor a legnagyobb szakítószilárdsági viszonyt a legkisebb rétegvastagságú (35  $\mu\text{m}$ ) próbatesteknél tapasztaltuk, a rétegszám növekedése miatt. A grafit koncentráció növelésekor a porozitás növekedése miatt rosszabb mechanikai jellemzőket kaptunk. A vízszintesen nyomtatott minták a legsimább felületet adják a többi építési tájolású mintához képest. Az utókezelt minták keménysége 11,4%-kal nőtt a nem utókezelt mintákhoz képest. A keménység is nőtt a grafit arány növekedésével, ez azt mutatja, hogy a grafit jelenléte még kis százalékban is megváltoztathatja a kompozit anyag keménységi értékét.



## 8. APPENDICES

### A1: Bibliography

1. Abdelbary, A. (2014): Polymer tribology, in *Wear of Polymers and Composites*. Elsevier, 1–36. <https://doi.org/10.1533/9781782421788.1>
2. Ahn, D., Kweon, J. H., Choi, J., and Lee, S. (2012): Quantification of surface roughness of parts processed by laminated object manufacturing, *Journal of Materials Processing Technology*, 212(2), 339–346. <https://doi.org/10.1016/j.jmatprotec.2011.08.013>
3. Akhoundi, B., and Behraves, A. H. (2019): Effect of Filling Pattern on the Tensile and Flexural Mechanical Properties of FDM 3D Printed Products, *Experimental Mechanics*, 59(6), 883–897. <https://doi.org/10.1007/s11340-018-00467-y>
4. Alaimo, G., Marconi, S., Costato, L., and Auricchio, F. (2017): Influence of meso-structure and chemical composition on FDM 3D-printed parts, *Composites Part B: Engineering*, 113, 371–380. <https://doi.org/10.1016/j.compositesb.2017.01.019>
5. Alsoufi, M. S., and Elsayed, A. E. (2017): How Surface Roughness Performance of Printed Parts Manufactured by Desktop FDM 3D Printer with PLA+ is Influenced by Measuring Direction, *American Journal of Mechanical Engineering*, 5(5), 211–222. <https://doi.org/10.12691/ajme-5-5-4>
6. Appleyard, D. (2015): Powering up on powder technology, *Metal Powder Report*, 70(6), 285–289. <https://doi.org/10.1016/j.mprp.2015.08.075>
7. Arif, M. F., Alhashmi, H., Varadarajan, K. M., Koo, J. H., Hart, A. J., and Kumar, S. (2020): Multifunctional performance of carbon nanotubes and graphene nanoplatelets reinforced PEEK composites enabled via FFF additive manufacturing, *Composites Part B: Engineering*, 184, 107625. <https://doi.org/10.1016/j.compositesb.2019.107625>
8. Ashby, M. F., and Jones, D. R. H. (2005): *Engineering Materials 2: An Introduction to Microstructures, Processing and Design*. 3rd edn. Britain, UK: Butterworth-Heinemann. Available at: <https://www.elsevier.com/books/engineering-materials-2/jones/978-0-7506-6381-6>
9. ASTM International (2013): F2792-12a - Standard Terminology for Additive Manufacturing Technologies, Rapid Manufacturing Association, 10–12. <https://doi.org/10.1520/F2792-12A.2>
10. ASTM International (2015): *ASTM D2240-15e1, Standard Test Method for Rubber Property—Durometer Hardness*, ASTM Standard. <https://doi.org/10.1520/D2240-15E01>
11. ASTM International (2016): *ASTM G133-05:2016 - Standard Test Method for Linearly Reciprocating Ball-on-Flat Sliding Wear*. <https://doi.org/10.1520/G0133-05R16>
12. Attar, H., Calin, M., Zhang, L. C., Scudino, S., and Eckert, J. (2014): Manufacture by selective laser melting and mechanical behavior of commercially pure titanium, *Materials Science and Engineering: A*, 593, 170–177. <https://doi.org/10.1016/j.msea.2013.11.038>
13. Attaran, M. (2017): The rise of 3-D printing: The advantages of additive manufacturing over traditional manufacturing, *Business Horizons*, 60(5), 677–688. <https://doi.org/10.1016/j.bushor.2017.05.011>
14. Aw, Y., Yeoh, C., Idris, M., Teh, P., Hamzah, K., and Sazali, S. (2018): Effect of Printing Parameters on Tensile, Dynamic Mechanical, and Thermoelectric Properties of FDM 3D Printed CABS/ZnO Composites, *Materials*, 11(4), 466. <https://doi.org/10.3390/ma11040466>

15. Ayrlimis, N. (2018): Effect of layer thickness on surface properties of 3D printed materials produced from wood flour/PLA filament, *Polymer Testing*, 71, 163–166. <https://doi.org/10.1016/j.polymertesting.2018.09.009>
16. Ayrlimis, N., Kariz, M., Kwon, J. H., and Kitek Kuzman, M. (2019): Effect of printing layer thickness on water absorption and mechanical properties of 3D-printed wood/PLA composite materials, *The International Journal of Advanced Manufacturing Technology*, 102(5–8), 2195–2200. <https://doi.org/10.1007/s00170-019-03299-9>
17. Bahadur, S. (2000): The development of transfer layers and their role in polymer tribology, *Wear*, 245(1–2), 92–99. [https://doi.org/10.1016/S0043-1648\(00\)00469-5](https://doi.org/10.1016/S0043-1648(00)00469-5)
18. Bajpai, P. K., Singh, I., and Madaan, J. (2013): Tribological behavior of natural fiber reinforced PLA composites, *Wear*, 297(1–2), 829–840. <https://doi.org/10.1016/j.wear.2012.10.019>
19. Balaji, R., Pushpavanam, M., Kumar, K. Y., and Subramanian, K. (2006): Electrodeposition of bronze–PTFE composite coatings and study on their tribological characteristics, *Surface and Coatings Technology*, 201(6), 3205–3211. <https://doi.org/10.1016/j.surfcoat.2006.06.039>
20. Balla, V. K., DeVasConCellos, P. D., Xue, W., Bose, S., and Bandyopadhyay, A. (2009): Fabrication of compositionally and structurally graded Ti–TiO<sub>2</sub> structures using laser engineered net shaping (LENS), *Acta Biomaterialia*, 5(5), 1831–1837. <https://doi.org/10.1016/j.actbio.2009.01.011>
21. Bandyopadhyay, A., Krishna, B. V., Xue, W., and Bose, S. (2009): Application of Laser Engineered Net Shaping (LENS) to manufacture porous and functionally graded structures for load bearing implants, *Journal of Materials Science: Materials in Medicine*, 20(S1), 29–34. <https://doi.org/10.1007/s10856-008-3478-2>
22. Bartenev, G. M., and Lavrentev, U. U. (1981): *FRICTION AND WEAR OF POLYMERS*, Tribology Series. Netherlands: Elsevier. [https://doi.org/10.1016/S0167-8922\(08\)70731-4](https://doi.org/10.1016/S0167-8922(08)70731-4)
23. Beaman, J. J., Barlow, J. W., Bourell, D. L., Crawford, R. H., Marcus, H. L., and McAlea, K. P. (1997): *Solid Freeform Fabrication: A New Direction in Manufacturing*, *Jom*. <https://doi.org/10.1007/978-1-4615-6327-3>
24. Berman, B. (2012): 3-D printing: The new industrial revolution, *Business Horizons*, 55(2), 155–162. <https://doi.org/10.1016/j.bushor.2011.11.003>
25. Berman, D., Erdemir, A., and Sumant, A. V. (2014): Graphene: a new emerging lubricant, *Materials Today*, 17(1), 31–42. <https://doi.org/10.1016/j.mattod.2013.12.003>
26. Bhushan, B. (2013a): *Principles and Applications to Tribology*. The Atrium, Southern Gate, Chichester, West Sussex, PO19 8SQ, UK: John Wiley & Sons, Ltd. <https://doi.org/10.1002/9781118403020>
27. Bhushan, B. (2013b): Wear, in *Principles and Applications to Tribology*. The Atrium, Southern Gate, Chichester, West Sussex, PO19 8SQ, UK: John Wiley & Sons, Ltd, 447–544. <https://doi.org/10.1002/9781118403020.ch8>
28. Bhushan, B., and Caspers, M. (2017): An overview of additive manufacturing (3D printing) for microfabrication, *Microsystem Technologies*, 23(4), 1117–1124. <https://doi.org/10.1007/s00542-017-3342-8>
29. Biron, M. (2013): Plastics Solutions for Practical Problems, in *Thermoplastics and Thermoplastic Composites*. Elsevier, 831–984. <https://doi.org/10.1016/B978-1-4557-7898-0.00007-X>

30. Bourell, D., Kruth, J. P., Leu, M., Levy, G., Rosen, D., Beese, A. M., and Clare, A. (2017): Materials for additive manufacturing, *CIRP Annals - Manufacturing Technology*, 66(2), 659–681. <https://doi.org/10.1016/j.cirp.2017.05.009>
31. Bowers, R. C., Clinton, W. C., and Zisman, W. A. (1953): *Frictional Behavior of Polyethylene, Polytetrafluoroethylene, and Halogenated Derivatives*. NRL report. United States: Naval research. Available at: <https://books.google.com/books?id=b67XSAAACAAJ>
32. Briscoe, B. J., and Sinha, S. K. (2002): Wear of polymers, in *Proc. Inst. Mech. Eng., Part J: J. Eng. Tribol.*, 401–413
33. Briscoe, B. J., and Sinha, S. K. (2013): *Tribological applications of polymers and their composites – past, present and future prospects*, *Tribology of Polymeric Nanocomposites*. <https://doi.org/10.1016/B978-0-444-59455-6.00001-5>
34. Briscoe, B. J., and Tabor, D. (1978): Friction and wear of polymers: The role of mechanical properties, *British Polymer Journal*, 10(1), 74–78. <https://doi.org/10.1002/pi.4980100114>
35. Brostow, W., Kovačević, V., Vrsaljko, D., and Whitworth, J. (2010): Tribology of polymers and polymer-based composites, *Journal of Materials Education*, 2010(Vol.32 (5-6): 273-290), 273–290. Available at: 2010 Tribology of polymers and polymer-based composites\_UNT\_EDU\_.pdf
36. Bustillos, J., Montero, D., Nautiyal, P., Loganathan, A., Boesl, B., and Agarwal, A. (2017): Integration of graphene in poly(lactic) acid by 3D printing to develop creep and wear-resistant hierarchical nanocomposites, *Polymer Composites*, 16(2), 101–113. <https://doi.org/10.1002/pc.24422>
37. Cantrell, J. T., Rohde, S., Damiani, D., Gurnani, R., DiSandro, L., Anton, J., Young, A., Jerez, A., Steinbach, D., Kroese, C., and Ifju, P. G. (2017): Experimental characterization of the mechanical properties of 3D-printed ABS and polycarbonate parts, *Rapid Prototyping Journal*, 23(4), 811–824. <https://doi.org/10.1108/RPJ-03-2016-0042>
38. Cao, S., Qiu, Y., Wei, X.-F., and Zhang, H.-H. (2015): Experimental and theoretical investigation on ultra-thin powder layering in three dimensional printing (3DP) by a novel double-smoothing mechanism, *Journal of Materials Processing Technology*, 220, 231–242. <https://doi.org/10.1016/j.jmatprotec.2015.01.016>
39. Cazón, A., Morer, P., and Matey, L. (2014): PolyJet technology for product prototyping: Tensile strength and surface roughness properties, *Proceedings of the Institution of Mechanical Engineers, Part B: Journal of Engineering Manufacture*, 228(12), 1664–1675. <https://doi.org/10.1177/0954405413518515>
40. Chanda, M., and Roy, S. K. (2007): *Plastics Technology Handbook*. New York: Taylor & Francis Group. Available at: <http://allaboutmetallurgy.com/wp/wp-content/uploads/2016/11/Plastic-Technology-Handbook.pdf>
41. Chang, L., Friedrich, K., and Ye, L. (2014): Study on the Transfer Film Layer in Sliding Contact Between Polymer Composites and Steel Disks Using Nanoindentation, *Journal of Tribology*, 136(2). <https://doi.org/10.1115/1.4026174>
42. Chari, V. S., Venkatesh, P. R., Krupashankar, and Dinesh, V. (2018): Effect of processing parameters on FDM process, in, 020061. <https://doi.org/10.1063/1.5029637>
43. Chen, Y., Qi, Y., Tai, Z., Yan, X., Zhu, F., and Xue, Q. (2012): Preparation, mechanical properties and biocompatibility of graphene oxide/ultrahigh molecular weight polyethylene composites, *European Polymer Journal*, 48(6), 1026–1033. <https://doi.org/10.1016/j.eurpolymj.2012.03.011>

44. Chiappone, A., Roppolo, I., Naretto, E., Fantino, E., Calignano, F., Sangermano, M., and Pirri, F. (2017): Study of graphene oxide-based 3D printable composites: Effect of the in situ reduction, *Composites Part B: Engineering*, 124, 9–15. <https://doi.org/10.1016/j.compositesb.2017.05.049>
45. Cho, Y. H., Lee, I. H., and Cho, D.-W. (2005): Laser scanning path generation considering photopolymer solidification in micro-stereolithography, *Microsystem Technologies*, 11(2–3), 158–167. <https://doi.org/10.1007/s00542-004-0468-2>
46. Chua, C. K., and Leong, K. F. (2014): *3D Printing and Additive Manufacturing*. WORLD SCIENTIFIC. <https://doi.org/10.1142/9008>
47. Cifuentes, S. C., Frutos, E., Benavente, R., Lorenzo, V., and Gonzalez-Carrasco, J. L. (2017): Assessment of mechanical behavior of PLA composites reinforced with Mg micro-particles through depth-sensing indentations analysis, *Journal of the Mechanical Behavior of Biomedical Materials*, 65(July 2016), 781–790. <https://doi.org/10.1016/j.jmbbm.2016.09.013>
48. Cirino, M., Friedrich, K., and Pipes, R. B. (1988): Evaluation of polymer composites for sliding and abrasive wear applications, *Composites*, 19(5), 383–392. [https://doi.org/10.1016/0010-4361\(88\)90126-7](https://doi.org/10.1016/0010-4361(88)90126-7)
49. Colbert, R. S., and Sawyer, W. G. (2010): Thermal dependence of the wear of molybdenum disulphide coatings, *Wear*, 269(11–12), 719–723. <https://doi.org/10.1016/j.wear.2010.07.008>
50. Comb, J. W., Priedeman, W. R., and Turley, P. W. (1994): FDM technology process improvements, in *Proceedings of Solid Freeform Fabrication Symposium*. Austin: Stratasys, Inc., 42–49
51. Cooperstein, I., Layani, M., and Magdassi, S. (2015): 3D printing of porous structures by UV-curable O/W emulsion for fabrication of conductive objects, *Journal of Materials Chemistry C*, 3(9), 2040–2044. <https://doi.org/10.1039/C4TC02215G>
52. Crawford, R. J. (1998): *Plastics Engineering 3rd Edition*, 530
53. Dawoud, M., Taha, I., and Ebeid, S. J. (2015): Effect of processing parameters and graphite content on the tribological behaviour of 3D printed acrylonitrile butadiene styrene, *Materialwissenschaft und Werkstofftechnik*, 46(12), 1185–1195. <https://doi.org/10.1002/mawe.201500450>
54. Department of Education and Science (1966): *Lubrication (tribology), education and research a report on the present position and industry's needs*. H. M. Stationery Off.
55. Domack, M. S., and Baughman, J. M. (2005): Development of nickel-titanium graded composition components, *Rapid Prototyping Journal*, 11(1), 41–51. <https://doi.org/10.1108/13552540510573383>
56. Domingo-Espin, M., Puigoriol-Forcada, J. M., Garcia-Granada, A. A., Llumà, J., Borros, S., and Reyes, G. (2015): Mechanical property characterization and simulation of fused deposition modeling Polycarbonate parts, *Materials and Design*, 83, 670–677. <https://doi.org/10.1016/j.matdes.2015.06.074>
57. Duan, B., Hockaday, L. A., Kang, K. H., and Butcher, J. T. (2013): 3D Bioprinting of heterogeneous aortic valve conduits with alginate/gelatin hydrogels, *Journal of Biomedical Materials Research Part A*, 101A(5), 1255–1264. <https://doi.org/10.1002/jbm.a.34420>
58. Dutta, B., Singh, V., Natu, H., Choi, J., and Mazumder, J. (2011): Additive Manufacturing by Direct Metal Deposition, *Adv. Mater. Process*, 167(3), 33–36. Available at: <http://mbraun.com/images/201/POM Group.pdf>

59. Ebewe, R. O. (2000): *Polymer Science and Technology*. New York: CRC Press. Available at: <https://www.crcpress.com/Polymer-Science-and-Technology/Ebewe/p/book/9780849389399>
60. Ehrmann, G., and Ehrmann, A. (2021): Investigation of the Shape-Memory Properties of 3D Printed PLA Structures with Different Infills, *Polymers*, 13(1), 164. <https://doi.org/10.3390/polym13010164>
61. Equbal, A., Sood, A. K., Toppo, V., Ohdar, R. K., and Mahapatra, S. S. (2010): Prediction and analysis of sliding wear performance of fused deposition modelling-processed ABS plastic parts, *Proceedings of the Institution of Mechanical Engineers, Part J: Journal of Engineering Tribology*, 224(12), 1261–1271. <https://doi.org/10.1243/13506501JET835>
62. Ertane, E. G., Dorner-Reisel, A., Baran, O., Welzel, T., Matner, V., and Svoboda, S. (2018): Processing and Wear Behaviour of 3D Printed PLA Reinforced with Biogenic Carbon, *Advances in Tribology*, 2018, 1–11. <https://doi.org/10.1155/2018/1763182>
63. eSUN (2018): *Safety Data Sheet of PLA Bronze filament*. Shenzhen, China, retrieved from: [http://www.esunchina.net/UploadFiles/Download/MSDS\\_eSUN\\_PLA Bronze filament.pdf](http://www.esunchina.net/UploadFiles/Download/MSDS_eSUN_PLA%20Bronze%20filament.pdf) [Accessed: 29/12/2019].
64. Esun Industrial Co., L. (2019): *eResin-LC1001, Material Safety Data Sheet*, eResin-LC1001, Material Safety Data Sheet. Shenzhen, China. Available at: [http://www.esun3d.net/UploadFiles/Download/MSDS\\_eSUN\\_LCD eResin-PLA.pdf](http://www.esun3d.net/UploadFiles/Download/MSDS_eSUN_LCD%20eResin-PLA.pdf)
65. Fahad, M., Dickens, P., and Gilbert, M. (2013): Novel polymeric support materials for jetting based additive manufacturing processes, *Rapid Prototyping Journal*, 19(4), 230–239. <https://doi.org/10.1108/13552541311323245>
66. Ferreira, R. T. L., Amatte, I. C., Dutra, T. A., and Bürger, D. (2017): Experimental characterization and micrography of 3D printed PLA and PLA reinforced with short carbon fibers, *Composites Part B: Engineering*, 124, 88–100. <https://doi.org/10.1016/j.compositesb.2017.05.013>
67. Feygin, M., and Hsieh, B. (1991): Laminated object manufacturing: A simpler process, in *Proceedings of the 2nd Solid Freeform Fabrication Symposium (SFF)*. Austin: TX, 123–130. Available at: <http://sffsymposium.engr.utexas.edu/Manuscripts/1991/1991-16-Feygin.pdf> <http://sffsymposium.engr.utexas.edu/1991TOC>
68. Fisher, L. W. (2005): *Selection of engineering materials and adhesives*. CRC Press. Available at: <https://www.crcpress.com/Selection-of-Engineering-Materials-and-Adhesives/Fisher-PE/p/book/9780824740474>
69. FLOM, D. G., and PORILE, N. T. (1955): Effects of Temperature and High-speed Sliding on the Friction of ‘Teflon’ on ‘Teflon’, *Nature*, 175(4459), 682–682. <https://doi.org/10.1038/175682a0>
70. Formlabs (2018): *Form Cure Time and Temperature Settings*, Form Cure Time and Temperature Settings. Available at: [https://support.formlabs.com/s/article/Form-Cure-Time-and-Temperature-Settings?language=en\\_US](https://support.formlabs.com/s/article/Form-Cure-Time-and-Temperature-Settings?language=en_US) (Accessed: 22 June 2019)
71. Fort, T. (1962): ADSORPTION AND BOUNDARY FRICTION ON POLYMER SURFACES, *The Journal of Physical Chemistry*, 66(6), 1136–1143. <https://doi.org/10.1021/j100812a040>
72. Garcia, C. R., Correa, J., Espalin, D., Barton, J. H., Rumpf, R. C., Wicker, R., and Gonzalez, V. (2012): 3D PRINTING OF ANISOTROPIC METAMATERIALS, *Progress In Electromagnetics Research Letters*, 34, 75–82. <https://doi.org/10.2528/PIERL12070311>

73. Gibson, I., Rosen, D., and Stucker, B. (2015a): Directed Energy Deposition Processes, in *Additive Manufacturing Technologies*. New York, NY: Springer New York, 245–268. [https://doi.org/10.1007/978-1-4939-2113-3\\_10](https://doi.org/10.1007/978-1-4939-2113-3_10)
74. Gibson, I., Rosen, D., and Stucker, B. (2015b): Sheet Lamination Processes, in *Additive Manufacturing Technologies*. New York, NY: Springer New York, 219–244. [https://doi.org/10.1007/978-1-4939-2113-3\\_9](https://doi.org/10.1007/978-1-4939-2113-3_9)
75. Gonzalez, G., Chiappone, A., Roppolo, I., Fantino, E., Bertana, V., Perrucci, F., Scaltrito, L., Pirri, F., and Sangermano, M. (2017): Development of 3D printable formulations containing CNT with enhanced electrical properties, *Polymer*, 109, 246–253. <https://doi.org/10.1016/j.polymer.2016.12.051>
76. Guessasma, S., Belhabib, S., and Nouri, H. (2019): Understanding the microstructural role of bio-sourced 3D printed structures on the tensile performance, *Polymer Testing*, 77, 105924. <https://doi.org/10.1016/j.polymertesting.2019.105924>
77. Guo, J., Bai, J., Liu, K., and Wei, J. (2018): Surface quality improvement of selective laser sintered polyamide 12 by precision grinding and magnetic field-assisted finishing, *Materials & Design*, 138, 39–45. <https://doi.org/10.1016/j.matdes.2017.10.048>
78. Guo, N., and Leu, M. C. (2013): Additive manufacturing: Technology, applications and research needs, *Frontiers of Mechanical Engineering*, 8(3), 215–243. <https://doi.org/10.1007/s11465-013-0248-8>
79. Gustafsson, E. (2013): Investigation of friction between plastic parts, Master's thesis in Polymer tribology, Chalmers university of technology
80. Hanon, M. M., Alshammas, Y., and Zsidai, L. (2020): Effect of print orientation and bronze existence on tribological and mechanical properties of 3D-printed bronze/PLA composite, *The International Journal of Advanced Manufacturing Technology*, 108(1–2), 553–570. <https://doi.org/10.1007/s00170-020-05391-x>
81. Hanon, M. M., Kovács, M., and Zsidai, L. (2019): Tribology behaviour investigation of 3D printed polymers, *International Review of Applied Sciences and Engineering*, 10(2), 173–181. <https://doi.org/10.1556/1848.2019.0021>
82. Hanon, M. M., Marczis, R., and Zsidai, L. (2019): Anisotropy Evaluation of Different Raster Directions, Spatial Orientations, and Fill Percentage of 3D Printed PETG Tensile Test Specimens, *Key Engineering Materials*, 821, 167–173. <https://doi.org/10.4028/www.scientific.net/KEM.821.167>
83. Hanon, M. M., Marczis, R., and Zsidai, L. (2020a): Impact of 3D-printing structure on the tribological properties of polymers, *Industrial Lubrication and Tribology*, 72(6), 811–818. <https://doi.org/10.1108/ILT-05-2019-0189>
84. Hanon, M. M., Marczis, R., and Zsidai, L. (2020b): Influence of the 3D Printing Process Settings on Tensile Strength of PLA and HT-PLA, *Periodica Polytechnica Mechanical Engineering*, 65(1), 38–46. <https://doi.org/10.3311/PPme.13683>
85. Hanon, M M, and Zsidai, L. (2020): Sliding surface structure comparison of 3D printed polymers using FDM and DLP technologies, *IOP Conference Series: Materials Science and Engineering*, 749, 012015. <https://doi.org/10.1088/1757-899X/749/1/012015>
86. Hanon, Muammel M., and Zsidai, L. (2020): Tribological and mechanical properties investigation of 3D printed polymers using DLP technique, *AIP Conference Proceedings*, 2213, 020205. <https://doi.org/10.1063/5.0000267>

87. Hausman, K., and Horne, R. (2014): *3D Printing For Dummies*. Hoboken, New Jersey: John Wiley & Sons, Inc. Available at: <http://eu.wiley.com/WileyCDA/WileyTitle/productCd-1118660757.html%5Cn>
88. Herzog, D., Seyda, V., Wycisk, E., and Emmelmann, C. (2016): Additive manufacturing of metals, *Acta Materialia*, 117, 371–392. <https://doi.org/10.1016/j.actamat.2016.07.019>
89. Hong, Y., Zhang, P., Lee, K.-H., and Lee, C.-H. (2017): Friction and wear of textured surfaces produced by 3D printing, *Science China Technological Sciences*, 60(9), 1400–1406. <https://doi.org/10.1007/s11431-016-9066-0>
90. Inc., N. N. (2019): *Graphene Nanoplatelet-NG01GNP0109, Material Safety Data Sheet*. Ankara, Turkey. Available at: [https://drive.google.com/file/d/1C3t\\_aZjgdLKr6TzNpTh6hy8oBEDoYi1H/view](https://drive.google.com/file/d/1C3t_aZjgdLKr6TzNpTh6hy8oBEDoYi1H/view)
91. International Organization for Standardization (2012a): *ISO 527-1:2012 - Plastics -- Determination of tensile properties -- Part 1: General principles*. Available at: [http://www.iso.org/iso/catalogue\\_detail.htm?csnumber=56045](http://www.iso.org/iso/catalogue_detail.htm?csnumber=56045)
92. International Organization for Standardization (2012b): *ISO 527-2:2012: Plastics - Determination of tensile properties - Part 2: Test conditions for moulding and extrusion plastics*. Available at: <https://www.iso.org/standard/56046.html>
93. Jacobs, P. F. (1992): *Rapid Prototyping & Manufacturing: Fundamentals of Stereolithography*. Dearborn: SME publication. Available at: <https://books.google.com/books?hl=en&lr=&id=-y33AwAAQBAJ&pgis=1>
94. Jafari, M. A., Han, W., Mohammadi, F., Safari, A., Danforth, S. C., and Langrana, N. (2000): A novel system for fused deposition of advanced multiple ceramics, *Rapid Prototyping Journal*, 6(3), 161–175. <https://doi.org/10.1108/13552540010337047>
95. Kalacska, G. (2013): An engineering approach to dry friction behaviour of numerous engineering plastics with respect to the mechanical properties, *Express Polymer Letters*, 7(2), 199–210. <https://doi.org/10.3144/expresspolymlett.2013.18>
96. Kalin, M., and Polajnar, M. (2013): The correlation between the surface energy, the contact angle and the spreading parameter, and their relevance for the wetting behaviour of DLC with lubricating oils, *Tribology International*, 66, 225–233. <https://doi.org/10.1016/j.triboint.2013.05.007>
97. Kang, H.-W., Lee, S. J., Ko, I. K., Kengla, C., Yoo, J. J., and Atala, A. (2016): A 3D bioprinting system to produce human-scale tissue constructs with structural integrity, *Nature Biotechnology*, 34(3), 312–319. <https://doi.org/10.1038/nbt.3413>
98. Keleş, Ö., Blevins, C. W., and Bowman, K. J. (2017): Effect of build orientation on the mechanical reliability of 3D printed ABS, *Rapid Prototyping Journal*, 23(2), 320–328. <https://doi.org/10.1108/RPJ-09-2015-0122>
99. King, R., and Tabor, D. (1953): The effect of temperature on the mechanical properties and the friction of plastics, in *Proceedings of the Physical Society. Section B*, 728. Available at: <http://iopscience.iop.org/0370-1301/66/9/302>
100. Kumar, A., and Gupta, R. K. (2003): Introduction, *Fundamentals of Polymer Engineering, Revised and Expanded*, 1–44. <https://doi.org/10.1201/9780203911891.ch1>
101. Kumar, R., Singh, R., Singh, M., and Kumar, P. (2020): ZnO nanoparticle-grafted PLA thermoplastic composites for 3D printing applications: Tuning of thermal, mechanical, morphological and shape memory effect, *Journal of Thermoplastic Composite Materials*, 089270572092511. <https://doi.org/10.1177/0892705720925119>

102. Kumar, S., and Kruth, J.-P. (2010): Composites by rapid prototyping technology, *Materials & Design*, 31(2), 850–856. <https://doi.org/10.1016/j.matdes.2009.07.045>
103. Kumar, S., Sharma, V., Choudhary, A. K. S., Chattopadhyaya, S., and Hloch, S. (2013): Determination of layer thickness in direct metal deposition using dimensional analysis, *The International Journal of Advanced Manufacturing Technology*, 67(9–12), 2681–2687. <https://doi.org/10.1007/s00170-012-4683-1>
104. Kuo, C.-C., Liu, L.-C., Teng, W.-F., Chang, H.-Y., Chien, F.-M., Liao, S.-J., Kuo, W.-F., and Chen, C.-M. (2016): Preparation of starch/acrylonitrile-butadiene-styrene copolymers (ABS) biomass alloys and their feasible evaluation for 3D printing applications, *Composites Part B: Engineering*, 86, 36–39. <https://doi.org/10.1016/j.compositesb.2015.10.005>
105. Labeaga-Martínez, N., Sanjurjo-Rivo, M., Díaz-Álvarez, J., and Martínez-Frías, J. (2017): Additive manufacturing for a Moon village, *Procedia Manufacturing*, 13, 794–801. <https://doi.org/10.1016/j.promfg.2017.09.186>
106. Lai, C. Q., Markandan, K., Luo, B., Lam, Y. C., Chung, W. C., and Chidambaram, A. (2021): Viscoelastic and high strain rate response of anisotropic graphene-polymer nanocomposites fabricated with stereolithographic 3D printing, *Additive Manufacturing*, 37, 101721. <https://doi.org/10.1016/j.addma.2020.101721>
107. Lanzotti, A., Grasso, M., Staiano, G., and Martorelli, M. (2015): The impact of process parameters on mechanical properties of parts fabricated in PLA with an open-source 3-D printer, *Rapid Prototyping Journal*. Edited by D. Eujin Pei, 21(5), 604–617. <https://doi.org/10.1108/RPJ-09-2014-0135>
108. Larsen, T. R. Ø., Vigild, M. E., and Løgstrup Andersen, T. (2007): *Tribological Studies of Polymer-matrix-composites*, Phd Thesis. DTU - Technical University of Denmark. Available at: <http://findit.dtu.dk/en/catalog/2185768830>
109. Laureto, J. J., and Pearce, J. M. (2018): Anisotropic mechanical property variance between ASTM D638-14 type i and type iv fused filament fabricated specimens, *Polymer Testing*, 68, 294–301. <https://doi.org/10.1016/j.polymertesting.2018.04.029>
110. Lee, H., Lim, C. H. J., Low, M. J., Tham, N., Murukeshan, V. M., and Kim, Y. J. (2017): Lasers in additive manufacturing: A review, *International Journal of Precision Engineering and Manufacturing - Green Technology*, 4(3), 307–322. <https://doi.org/10.1007/s40684-017-0037-7>
111. Lee, J. M., Zhang, M., and Yeong, W. Y. (2016): Characterization and evaluation of 3D printed microfluidic chip for cell processing, *Microfluidics and Nanofluidics*, 20(1), 5. <https://doi.org/10.1007/s10404-015-1688-8>
112. Li, Zheling, Young, R. J., Wilson, N. R., Kinloch, I. A., Vallés, C., and Li, Zheng (2016): Effect of the orientation of graphene-based nanoplatelets upon the Young's modulus of nanocomposites, *Composites Science and Technology*, 123, 125–133. <https://doi.org/10.1016/j.compscitech.2015.12.005>
113. Ligon, S. C., Liska, R., Stampfl, J., Gurr, M., and Mülhaupt, R. (2017): Polymers for 3D Printing and Customized Additive Manufacturing, *Chemical Reviews*, 117(15), 10212–10290. <https://doi.org/10.1021/acs.chemrev.7b00074>
114. Lin, D., Jin, S., Zhang, F., Wang, C., Wang, Y., Zhou, C., and Cheng, G. J. (2015): 3D stereolithography printing of graphene oxide reinforced complex architectures, *Nanotechnology*, 26(43), 434003. <https://doi.org/10.1088/0957-4484/26/43/434003>



115. Liu, Y., Xiong, W., Jiang, L. J., Zhou, Y. S., and Lu, Y. F. (2016): Precise 3D printing of micro/nanostructures using highly conductive carbon nanotube-thiol-acrylate composites, in Gu, B., Helvajian, H., and Piqué, A. (eds), 973808. <https://doi.org/10.1117/12.2214862>
116. Ludema, K. C., and Tabor, D. (1966): The friction and visco-elastic properties of polymeric solids, *Wear*, 9(5), 329–348. [https://doi.org/10.1016/0043-1648\(66\)90018-4](https://doi.org/10.1016/0043-1648(66)90018-4)
117. Manapat, J. Z., Chen, Q., Ye, P., and Advincula, R. C. (2017): 3D Printing of Polymer Nanocomposites via Stereolithography, *Macromolecular Materials and Engineering*, 302(9). <https://doi.org/10.1002/mame.201600553>
118. Markandan, K., and Lai, C. Q. (2020): Enhanced mechanical properties of 3D printed graphene-polymer composite lattices at very low graphene concentrations, *Composites Part A: Applied Science and Manufacturing*, 129, 105726. <https://doi.org/10.1016/j.compositesa.2019.105726>
119. Markstedt, K., Mantas, A., Tournier, I., Martínez Ávila, H., Hägg, D., and Gatenholm, P. (2015): 3D Bioprinting Human Chondrocytes with Nanocellulose–Alginate Bioink for Cartilage Tissue Engineering Applications, *Biomacromolecules*, 16(5), 1489–1496. <https://doi.org/10.1021/acs.biomac.5b00188>
120. Matthews, A., and Holmberg, K. (2009): *Coatings tribology: properties, mechanisms, techniques and applications in surface engineering*. 2nd edn. Edited by B. J. Briscoe. Oxford, UK: Elsevier B.V.
121. Maurath, J., and Willenbacher, N. (2017): 3D printing of open-porous cellular ceramics with high specific strength, *Journal of the European Ceramic Society*, 37(15), 4833–4842. <https://doi.org/10.1016/j.jeurceramsoc.2017.06.001>
122. Mazumder, J., Schifferer, A., and Choi, J. (1999): Direct materials deposition: Designed macro and microstructure, *Materials Research Innovations*, 3(3), 118–131. <https://doi.org/10.1007/s100190050137>
123. Melchels, F. P. W., Feijen, J., and Grijpma, D. W. (2010): A review on stereolithography and its applications in biomedical engineering, *Biomaterials*, 31(24), 6121–6130. <https://doi.org/10.1016/j.biomaterials.2010.04.050>
124. Meyer, T., and Keurentjes, J. T. F. (2005): *Handbook of Polymer Reaction Engineering*, Handbook of Polymer Reaction Engineering. Weinheim: WILEY-VCH Verlag GmbH & Co. <https://doi.org/10.1002/9783527619870>
125. Min, C., He, Z., Liang, H., Liu, D., Dong, C., Song, H., and Huang, Y. (2020): High mechanical and tribological performance of polyimide nanocomposite reinforced by fluorinated graphene oxide, *Polymer Composites*, 41(4), 1624–1635. <https://doi.org/10.1002/pc.25484>
126. Mu, Q., Wang, L., Dunn, C. K., Kuang, X., Duan, F., Zhang, Z., Qi, H. J., and Wang, T. (2017): Digital light processing 3D printing of conductive complex structures, *Additive Manufacturing*, 18, 74–83. <https://doi.org/10.1016/j.addma.2017.08.011>
127. Muhammad Nuruzzaman, D., Asaduzzaman Chowdhury, M., and Lutfar Rahaman, M. (2011): Effect of duration of rubbing and normal load on friction coefficient for polymer and composite materials, *Industrial Lubrication and Tribology*, 63(5), 320–326. <https://doi.org/10.1108/00368791111154931>
128. Müller, C. M. O., Laurindo, J. B., and Yamashita, F. (2009): Effect of cellulose fibers on the crystallinity and mechanical properties of starch-based films at different relative humidity values, *Carbohydrate Polymers*, 77(2), 293–299. <https://doi.org/10.1016/j.carbpol.2008.12.030>

- 
129. Myshkin, N. K., and Kovalev, A. V. (2009): ADHESION AND FRICTION OF POLYMERS, in *Polymer Tribology*. IMPERIAL COLLEGE PRESS, 3–37. [https://doi.org/10.1142/9781848162044\\_0001](https://doi.org/10.1142/9781848162044_0001)
130. Myshkin, N. K., Petrokovets, M. I., and Kovalev, A. V. (2005): Tribology of polymers: Adhesion, friction, wear, and mass-transfer, *Tribology International*, 38(11-12 SPEC. ISS.), 910–921. <https://doi.org/10.1016/j.triboint.2005.07.016>
131. Myshkin, N., and Kovalev, A. (2018): Adhesion and surface forces in polymer tribology—A review, *Friction*, 6(2), 143–155. <https://doi.org/10.1007/s40544-018-0203-0>
132. N. Turner, B., Strong, R., and A. Gold, S. (2014): A review of melt extrusion additive manufacturing processes: I. Process design and modeling, *Rapid Prototyping Journal*, 20(3), 192–204. <https://doi.org/10.1108/RPJ-01-2013-0012>
133. Ngo, T. D., Kashani, A., Imbalzano, G., Nguyen, K. T. Q., and Hui, D. (2018): Additive manufacturing (3D printing): A review of materials, methods, applications and challenges, *Composites Part B: Engineering*, 143(December 2017), 172–196. <https://doi.org/10.1016/j.compositesb.2018.02.012>
134. Nie, B., Yang, L., Huang, H., Bai, S., Wan, P., and Liu, J. (2015): Femtosecond laser additive manufacturing of iron and tungsten parts, *Applied Physics A*, 119(3), 1075–1080. <https://doi.org/10.1007/s00339-015-9070-y>
135. Nirmal, U., Hashim, J., and Megat Ahmad, M. M. H. (2015): A review on tribological performance of natural fibre polymeric composites, *Tribology International*, 83, 77–104. <https://doi.org/10.1016/j.triboint.2014.11.003>
136. Notta-Cuvier, D., Odent, J., Delille, R., Murariu, M., Lauro, F., Raquez, J. M., Bennani, B., and Dubois, P. (2014): Tailoring polylactide (PLA) properties for automotive applications: Effect of addition of designed additives on main mechanical properties, *Polymer Testing*, 36, 1–9. <https://doi.org/10.1016/j.polymertesting.2014.03.007>
137. Ocylok, S., Alexeev, E., Mann, S., Weisheit, A., Wissenbach, K., and Kelbassa, I. (2014): Correlations of Melt Pool Geometry and Process Parameters During Laser Metal Deposition by Coaxial Process Monitoring, *Physics Procedia*, 56, 228–238. <https://doi.org/10.1016/j.phpro.2014.08.167>
138. Osswald, T. A., and Menges, G. (2012): Structure of Polymers, in *Materials Science of Polymers for Engineers*. München: Carl Hanser Verlag GmbH & Co. KG, 49–82. <https://doi.org/10.3139/9781569905241.003>
139. P. Suh, N. (1973): The delamination theory of wear, *Wear*, 25(1), 111–124. [https://doi.org/10.1016/0043-1648\(73\)90125-7](https://doi.org/10.1016/0043-1648(73)90125-7)
140. Pang, W., Ni, Z., Wu, J., and Zhao, Y. (2018): Investigation of tribological properties of graphene oxide reinforced ultrahigh molecular weight polyethylene under artificial seawater lubricating condition, *Applied Surface Science*, 434, 273–282. <https://doi.org/10.1016/j.apsusc.2017.10.115>
141. Papageorgiou, D. G., Kinloch, I. A., and Young, R. J. (2017): Mechanical properties of graphene and graphene-based nanocomposites, *Progress in Materials Science*, 90, 75–127. <https://doi.org/10.1016/j.pmatsci.2017.07.004>
142. Pérez-Bustamante, R., Bolaños-Morales, D., Bonilla-Martínez, J., Estrada-Guel, I., and Martínez-Sánchez, R. (2014): Microstructural and hardness behavior of graphene-nanoplatelets/aluminum composites synthesized by mechanical alloying, *Journal of Alloys and Compounds*, 615, S578–S582. <https://doi.org/10.1016/j.jallcom.2014.01.225>

143. Persson, B. N. J. (2000): *Sliding Friction: Physical Principles and Applications*. 2nd edn. Berlin, Heidelberg: Springer Berlin Heidelberg (NanoScience and Technology). <https://doi.org/10.1007/978-3-662-04283-0>
144. Pope, J. E. (1996): *Rules of Thumb for Mechanical Engineers: A manual of quick, accurate solutions to everyday mechanical engineering problems*. Elsevier. Available at: <http://scholar.google.com/scholar?hl=en&btnG=Search&q=intitle:Rules+of+Thumb+for+MEchanical+Engineers#0>
145. Popov, V. L. (2010): *Contact Mechanics and Friction*. Berlin, Heidelberg: Springer Berlin Heidelberg. <https://doi.org/10.1007/978-3-642-10803-7>
146. Postiglione, G., Natale, G., Griffini, G., Levi, M., and Turri, S. (2015): Conductive 3D microstructures by direct 3D printing of polymer/carbon nanotube nanocomposites via liquid deposition modeling, *Composites Part A: Applied Science and Manufacturing*, 76, 110–114. <https://doi.org/10.1016/j.compositesa.2015.05.014>
147. Ram, A. (1997): *Fundamentals of Polymer Engineering*. 1st edn. Springer
148. Ramesh, M., and Panneerselvam, K. (2020): PLA-Based Material Design and Investigation of Its Properties by FDM, in, 229–241. [https://doi.org/10.1007/978-981-32-9433-2\\_20](https://doi.org/10.1007/978-981-32-9433-2_20)
149. Rankouhi, B., Javadpour, S., Delfanian, F., and Letcher, T. (2016): Failure Analysis and Mechanical Characterization of 3D Printed ABS With Respect to Layer Thickness and Orientation, *Journal of Failure Analysis and Prevention*, 16(3), 467–481. <https://doi.org/10.1007/s11668-016-0113-2>
150. Rayna, T., and Striukova, L. (2016): From rapid prototyping to home fabrication: How 3D printing is changing business model innovation, *Technological Forecasting and Social Change*, 102, 214–224. <https://doi.org/10.1016/j.techfore.2015.07.023>
151. Redwood, B., Schöffner, F., and Garret, B. (2017): *The 3D printing handbook: technologies, design and applications*. 3D Hubs B.V.
152. Revati, R., Majid, M. S. A., Ridzuan, M. J. M., Basaruddin, K. S., Rahman Y., M. N., Cheng, E. M., and Gibson, A. G. (2017): In vitro degradation of a 3D porous Pennisetum purpureum/PLA biocomposite scaffold, *Journal of the Mechanical Behavior of Biomedical Materials*, 74(March), 383–391. <https://doi.org/10.1016/j.jmbbm.2017.06.035>
153. Rezayat, H., Zhou, W., Siriruk, A., Penumadu, D., and Babu, S. S. (2015): Structure–mechanical property relationship in fused deposition modelling, *Materials Science and Technology*, 31(8), 895–903. <https://doi.org/10.1179/1743284715Y.0000000010>
154. Robbins, J. B., Gorgen, V., Min, P., Shepherd, B. R., and Presnell, S. C. (2013): A novel in vitro three-dimensional bioprinted liver tissue system for drug development, *FASEB J*, 27, 872.12
155. Roesler, J., Harders, H., and Baeker, M. (2006): *Mechanical Behavior of Engineering Materials*. <https://doi.org/10.1007/978-3-540-73448-2>
156. Rybachuk, M., Alice Mauger, C., Fiedler, T., and Öchsner, A. (2017): Anisotropic mechanical properties of fused deposition modeled parts fabricated by using acrylonitrile butadiene styrene polymer, *Journal of Polymer Engineering*, 37(7). <https://doi.org/10.1515/polyeng-2016-0263>
157. Şahin, Y., Yalçınkaya, S., and Mirzayev, H. (2017): The effect of load on the tribological property of polyacetal and metallographic observation, in *Proceedings of the International Symposium of Mechanism and Machine Science*. Baku, Azerbaijan: Azerbaijan Technical University, 167–174. Available at: <http://web.iyte.edu.tr/~gokhankiper/ISMMS/Sahin1.pdf>

158. Salapare, H. S., Tiquio, M. G. J. P., and Ramos, H. J. (2015): RF Plasma Treatment of Neptune Grass (*Posidonia oceanica*): A Facile Method to Achieve Superhydrophilic Surfaces for Dye Adsorption from Aqueous Solutions, in *Advances in Contact Angle, Wettability and Adhesion*. Hoboken, NJ, USA: John Wiley & Sons, Inc., 305–332. <https://doi.org/10.1002/9781119117018.ch12>
159. Schmidt, M., Merklein, M., Bourell, D., Dimitrov, D., Hausotte, T., Wegener, K., Overmeyer, L., Vollertsen, F., and Levy, G. N. (2017): Laser based additive manufacturing in industry and academia, *CIRP Annals*, 66(2), 561–583. <https://doi.org/10.1016/j.cirp.2017.05.011>
160. Schmitz, T. L., Action, J. E., Ziegert, and, J. C., and Sawyer, W. G. (2005): The Difficulty of Measuring Low Friction: Uncertainty Analysis for Friction Coefficient Measurements, *Journal of Tribology*, 127(3), 673–678. <https://doi.org/10.1115/1.1843853>
161. Senatov, F. S., Niaza, K. V., Zadorozhnyy, M. Y., Maksimkin, A. V., Kaloshkin, S. D., and Estrin, Y. Z. (2016): Mechanical properties and shape memory effect of 3D-printed PLA-based porous scaffolds, *Journal of the Mechanical Behavior of Biomedical Materials*, 57, 139–148. <https://doi.org/10.1016/j.jmbbm.2015.11.036>
162. Serra, T., Planell, J. A., and Navarro, M. (2013): High-resolution PLA-based composite scaffolds via 3-D printing technology, *Acta Biomaterialia*, 9(3), 5521–5530. <https://doi.org/10.1016/j.actbio.2012.10.041>
163. Shahzad, K., Deckers, J., Zhang, Z., Kruth, J.-P., and Vleugels, J. (2014): Additive manufacturing of zirconia parts by indirect selective laser sintering, *Journal of the European Ceramic Society*, 34(1), 81–89. <https://doi.org/10.1016/j.jeurceramsoc.2013.07.023>
164. Shooter, K. V., and Tabor, D. (1952): The Frictional Properties of Plastics, in *Pro. Phys. Soc.*, 661
165. SHOOTER, K. V, and THOMAS, P. H. (1949): Frictional properties of some plastics., *Research; a journal of science and its applications*, 2(11), 533–5. Available at: <http://www.ncbi.nlm.nih.gov/pubmed/15393900>
166. Shubham, P., Sikidar, A., and Chand, T. (2016): The Influence of Layer Thickness on Mechanical Properties of the 3D Printed ABS Polymer by Fused Deposition Modeling, *Key Engineering Materials*, 706, 63–67. <https://doi.org/10.4028/www.scientific.net/KEM.706.63>
167. Sidambe, A. T. (2014): Biocompatibility of advanced manufactured titanium implants-A review, *Materials*, 7(12), 8168–8188. <https://doi.org/10.3390/ma7128168>
168. Singh, S., Ramakrishna, S., and Singh, R. (2017): Material issues in additive manufacturing: A review, *Journal of Manufacturing Processes*, 25, 185–200. <https://doi.org/10.1016/j.jmapro.2016.11.006>
169. Smerdova, O. (2012): *Interfacial and bulk friction-induced dissipation in composites - PhD Thesis*. Bauman Moscow State Technical University. Available at: [http://bibli.ec-lyon.fr/exl-doc/TH\\_T2293\\_osmerdova.pdf](http://bibli.ec-lyon.fr/exl-doc/TH_T2293_osmerdova.pdf)
170. Song, Y., Li, Y., Song, W., Yee, K., Lee, K. Y., and Tagarielli, V. L. (2017): Measurements of the mechanical response of unidirectional 3D-printed PLA, *Materials and Design*, 123, 154–164. <https://doi.org/10.1016/j.matdes.2017.03.051>
171. Sood, Anoop Kumar, Equbal, A., Toppo, V., Ohdar, R. K., and Mahapatra, S. S. (2012): An investigation on sliding wear of FDM built parts, *CIRP Journal of Manufacturing Science and Technology*, 5(1), 48–54. <https://doi.org/10.1016/j.cirpj.2011.08.003>

- 172.Sood, Anoop K., Ohdar, R. K., and Mahapatra, S. S. (2012): Experimental investigation and empirical modelling of FDM process for compressive strength improvement, *Journal of Advanced Research*, 3(1), 81–90. <https://doi.org/10.1016/j.jare.2011.05.001>
- 173.Srinivas, M., and Babu, B. S. (2017): A Critical Review on Recent Research Methodologies in Additive Manufacturing, *Materials Today: Proceedings*, 4(8), 9049–9059. <https://doi.org/10.1016/j.matpr.2017.07.258>
- 174.Stachowiak, G. W., and Batchelor, A. W. (2005): *Engineering Tribology*. 3rd edn. Burlington, USA: Elsevier Butterworth-Heinemann
- 175.Stansbury, J. W., and Idacavage, M. J. (2016): 3D printing with polymers: Challenges among expanding options and opportunities, *Dental Materials*, 32(1), 54–64. <https://doi.org/10.1016/j.dental.2015.09.018>
- 176.Sugavaneswaran, M., and Arumaikkannu, G. (2015): Analytical and experimental investigation on elastic modulus of reinforced additive manufactured structure, *Materials & Design (1980-2015)*, 66, 29–36. <https://doi.org/10.1016/j.matdes.2014.10.029>
- 177.Sun, Q., Rizvi, G. M., Bellehumeur, C. T., and Gu, P. (2008): Effect of processing conditions on the bonding quality of FDM polymer filaments, *Rapid Prototyping Journal*, 14(2), 72–80. <https://doi.org/10.1108/13552540810862028>
- 178.Sun, S., Yang, M., Kostov, Y., and Rasooly, A. (2010): ELISA-LOC: lab-on-a-chip for enzyme-linked immunodetection, *Lab on a Chip*, 10(16), 2093. <https://doi.org/10.1039/c003994b>
- 179.Tabandeh-Khorshid, M., Ferguson, J. B., Schultz, B. F., Kim, C.-S., Cho, K., and Rohatgi, P. K. (2016): Strengthening mechanisms of graphene- and Al<sub>2</sub>O<sub>3</sub>-reinforced aluminum nanocomposites synthesized by room temperature milling, *Materials & Design*, 92, 79–87. <https://doi.org/10.1016/j.matdes.2015.12.007>
- 180.Tabor, D. (1992): Friction as a Dissipative Process, in *Fundamentals of Friction: Macroscopic and Microscopic Processes*. Dordrecht: Springer Netherlands, 3–24. [https://doi.org/10.1007/978-94-011-2811-7\\_1](https://doi.org/10.1007/978-94-011-2811-7_1)
- 181.Takezawa, A., and Kobashi, M. (2017): Design methodology for porous composites with tunable thermal expansion produced by multi-material topology optimization and additive manufacturing, *Composites Part B: Engineering*, 131, 21–29. <https://doi.org/10.1016/j.compositesb.2017.07.054>
- 182.Tanaka, K. (1984): Kinetic friction and dynamic elastic contact behaviour of polymers, *Wear*, 100(1–3), 243–262. [https://doi.org/10.1016/0043-1648\(84\)90015-2](https://doi.org/10.1016/0043-1648(84)90015-2)
- 183.Tekinalp, H. L., Kunc, V., Velez-Garcia, G. M., Duty, C. E., Love, L. J., Naskar, A. K., Blue, C. A., and Ozcan, S. (2014): Highly oriented carbon fiber–polymer composites via additive manufacturing, *Composites Science and Technology*, 105, 144–150. <https://doi.org/10.1016/j.compscitech.2014.10.009>
- 184.Tofail, S. A. M., Koumoulos, E. P., Bandyopadhyay, A., Bose, S., O’Donoghue, L., and Charitidis, C. (2017): Additive manufacturing: Scientific and technological challenges, market uptake and opportunities, *Materials Today*, 21(1), 22–37. <https://doi.org/10.1016/j.mattod.2017.07.001>
- 185.Totten, G. E., and Liang, H. (2004): *Mechanical tribology : materials, characterization, and applications*. New York, USA: Marcel Dekker (CRC Press). Available at: <https://www.crcpress.com/Mechanical-Tribology-Materials-Characterization-and-Applications/Totten-Liang/p/book/9780824748739>

- 
186. Tran, P., Ngo, T. D., Ghazlan, A., and Hui, D. (2017): Bimaterial 3D printing and numerical analysis of bio-inspired composite structures under in-plane and transverse loadings, *Composites Part B: Engineering*, 108, 210–223. <https://doi.org/10.1016/j.compositesb.2016.09.083>
187. Travitzky, N., Bonet, A., Dermeik, B., Fey, T., Filbert-Demut, I., Schlier, L., Schlordt, T., and Greil, P. (2014): Additive Manufacturing of Ceramic-Based Materials, *Advanced Engineering Materials*, 16(6), 729–754. <https://doi.org/10.1002/adem.201400097>
188. Tromborg, J. K., Sveinsson, H. A., Scheibert, J., Thogersen, K., Amundsen, D. S., and Malthé-Sorensen, A. (2014): Slow slip and the transition from fast to slow fronts in the rupture of frictional interfaces, *Proceedings of the National Academy of Sciences*, 111(24), 8764–8769. <https://doi.org/10.1073/pnas.1321752111>
189. Tsouknidas, A. (2011): Friction Induced Wear of Rapid Prototyping Generated Materials: A Review, *Advances in Tribology*, 2011, 1–7. <https://doi.org/10.1155/2011/746270>
190. Tymrak, B. M., Kreiger, M., and Pearce, J. M. (2014): Mechanical properties of components fabricated with open-source 3-D printers under realistic environmental conditions, *Materials and Design*, 58, 242–246. <https://doi.org/10.1016/j.matdes.2014.02.038>
191. Unal, H., Kurtulus, E., Mimaroglu, A., and Aydin, M. (2010): Tribological Performance of PTFE Bronze Filled Composites under Wide Range of Application Conditions, *Journal of Reinforced Plastics and Composites*, 29(14), 2184–2191. <https://doi.org/10.1177/0731684409345617>
192. Ünlü, B. S., Uzkut, M., and Atik, E. (2010): Tribological Behaviors of Polymer-based Particle-reinforced PTFE Composite Bearings, *Journal of Reinforced Plastics and Composites*, 29(9), 1353–1358. <https://doi.org/10.1177/0731684409103952>
193. Ushiba, S., Shoji, S., Masui, K., Kuray, P., Kono, J., and Kawata, S. (2013): 3D microfabrication of single-wall carbon nanotube/polymer composites by two-photon polymerization lithography, *Carbon*, 59, 283–288. <https://doi.org/10.1016/j.carbon.2013.03.020>
194. Utela, B., Storti, D., Anderson, R., and Ganter, M. (2008): A review of process development steps for new material systems in three dimensional printing (3DP), *Journal of Manufacturing Processes*, 10(2), 96–104. <https://doi.org/10.1016/j.jmapro.2009.03.002>
195. Vaithilingam, J., Kilsby, S., Goodridge, R. D., Christie, S. D. R., Edmondson, S., and Hague, R. J. M. (2015): Functionalisation of Ti6Al4V components fabricated using selective laser melting with a bioactive compound, *Materials Science and Engineering: C*, 46, 52–61. <https://doi.org/10.1016/j.msec.2014.10.015>
196. Vallés, C., Beckert, F., Burk, L., Mülhaupt, R., Young, R. J., and Kinloch, I. A. (2016): Effect of the C/O ratio in graphene oxide materials on the reinforcement of epoxy-based nanocomposites, *Journal of Polymer Science Part B: Polymer Physics*, 54(2), 281–291. <https://doi.org/10.1002/polb.23925>
197. Vidakis, N., Maniadi, A., Petousis, M., Vamvakaki, M., Kenanakis, G., and Koudoumas, E. (2020): Mechanical and Electrical Properties Investigation of 3D-Printed Acrylonitrile–Butadiene–Styrene Graphene and Carbon Nanocomposites, *Journal of Materials Engineering and Performance*, 29(3), 1909–1918. <https://doi.org/10.1007/s11665-020-04689-x>

198. Vidakis, N., Petousis, M., Savvakis, K., Maniadi, A., and Koudoumas, E. (2019): A comprehensive investigation of the mechanical behavior and the dielectrics of pure polylactic acid (PLA) and PLA with graphene (GnP) in fused deposition modeling (FDM), *International Journal of Plastics Technology*, 23(2), 195–206. <https://doi.org/10.1007/s12588-019-09248-1>
199. Vinogradov, G. V., Bartenev, G. M., El'kin, A. I., and Mikhaylov, V. K. (1970): Effect of temperature on friction and adhesion of crystalline polymers, *Wear*, 16(3), 213–219. [https://doi.org/10.1016/0043-1648\(70\)90229-2](https://doi.org/10.1016/0043-1648(70)90229-2)
200. Voyer, J., Klien, S., Velkavrh, I., Ausserer, F., and Diem, A. (2019): Static and Dynamic Friction of Pure and Friction-Modified PA6 Polymers in Contact with Steel Surfaces: Influence of Surface Roughness and Environmental Conditions, *Lubricants*, 7(2), 17. <https://doi.org/10.3390/lubricants7020017>
201. Wang, D., Huang, X., Li, J., He, B., Liu, Q., Hu, L., and Jiang, G. (2018): 3D printing of graphene-doped target for 'matrix-free' laser desorption/ionization mass spectrometry, *Chemical Communications*, 54(22), 2723–2726. <https://doi.org/10.1039/C7CC09649F>
202. Wang, X., Jiang, M., Zhou, Z., Gou, J., and Hui, D. (2017): 3D printing of polymer matrix composites: A review and prospective, *Composites Part B: Engineering*, 110, 442–458. <https://doi.org/10.1016/j.compositesb.2016.11.034>
203. Wanhao (2017): *Wanhao UV Resin msds sheet*, Wanhao Premium UV Resin. Available at: [https://www.3djake.nl/wanhao-3d-printers-onderdelen/uv-hars?sai=3277&gclid=EAIaIQobChMIrNb4uJ2a2wIVBN-yCh3KEQ6dEAYYAIBEGJGq\\_D\\_BwE](https://www.3djake.nl/wanhao-3d-printers-onderdelen/uv-hars?sai=3277&gclid=EAIaIQobChMIrNb4uJ2a2wIVBN-yCh3KEQ6dEAYYAIBEGJGq_D_BwE) (Accessed: 16 June 2019)
204. WANHAO 3D PRINTER, C. (2016): *WANHAO Duplicator 6*. Available at: <https://www.wanhao3dprinter.com/Unboxin/ShowArticle.asp?ArticleID=163> (Accessed: 22 November 2021)
205. WANHAO 3D PRINTER, C. (2018): *WANHAO Duplicator 7*. Available at: <https://www.wanhao3dprinter.com/Unboxin/ShowArticle.asp?ArticleID=164> (Accessed: 22 November 2021)
206. Weisstein, E. W. (2019): Circular Segment. From MathWorld—A Wolfram Web Resource. accessed 21/5/2019. Available at: <http://mathworld.wolfram.com/CircularSegment.html>
207. Wen, Y., Xun, S., Haoye, M., Baichuan, S., Peng, C., Xuejian, L., Kaihong, Z., Xuan, Y., Jiang, P., and Shibi, L. (2017): 3D printed porous ceramic scaffolds for bone tissue engineering: a review, *Biomaterials Science*, 5(9), 1690–1698. <https://doi.org/10.1039/C7BM00315C>
208. Wieleba, W. (2002): The statistical correlation of the coefficient of friction and wear rate of PTFE composites with steel counterface roughness and hardness, *Wear*, 252(9–10), 719–729. [https://doi.org/10.1016/S0043-1648\(02\)00029-7](https://doi.org/10.1016/S0043-1648(02)00029-7)
209. Williams, S. W., Martina, F., Addison, A. C., Ding, J., Pardal, G., and Colegrove, P. (2016): Wire + Arc Additive Manufacturing, *Materials Science and Technology*, 32(7), 641–647. <https://doi.org/10.1179/1743284715Y.0000000073>
210. Withell, A., Diegel, O., and Grupp, I. (2011): Porous ceramic filters through 3D printing, *Innovative Developments in Virtual and Physical Prototyping*, 115–120. Available at: [http://books.google.com/books?hl=en&lr=&id=Q002\\_TiMJ6kC&oi=fnd&pg=PA313&dq=Porous+ceram](http://books.google.com/books?hl=en&lr=&id=Q002_TiMJ6kC&oi=fnd&pg=PA313&dq=Porous+ceram)

211. Wittbrodt, B., and Pearce, J. M. (2015): The effects of PLA color on material properties of 3-D printed components, *Additive Manufacturing*, 8, 110–116. <https://doi.org/10.1016/j.addma.2015.09.006>
212. Wu, P., Wang, J., and Wang, X. (2016): A critical review of the use of 3-D printing in the construction industry, *Automation in Construction*, 68, 21–31. <https://doi.org/10.1016/j.autcon.2016.04.005>
213. Yamaguchi, Y. (1990): Chapter 2 Wear, in *Tribology of Plastic Materials - Their Characteristics and Applications to Sliding Components*. 1st edn. Elsevier, 93–142. [https://doi.org/10.1016/S0167-8922\(08\)70108-1](https://doi.org/10.1016/S0167-8922(08)70108-1)
214. Yang, C., Xu, J., Xing, Y., Hao, S., and Ren, Z. (2020): Covalent polymer functionalized graphene oxide/poly(ether ether ketone) composites for fused deposition modeling: improved mechanical and tribological performance, *RSC Advances*, 10(43), 25685–25695. <https://doi.org/10.1039/D0RA04418K>
215. Yang, J., Cho, J. H., and Yoo, M. J. (2017): Selective metallization on copper aluminate composite via laser direct structuring technology, *Composites Part B: Engineering*, 110, 361–367. <https://doi.org/10.1016/j.compositesb.2016.11.041>
216. Yang, L., Phua, S. L., Toh, C. L., Zhang, L., Ling, H., Chang, M., Zhou, D., Dong, Y., and Lu, X. (2013): Polydopamine-coated graphene as multifunctional nanofillers in polyurethane, *RSC Advances*, 3(18), 6377. <https://doi.org/10.1039/c3ra23307c>
217. Yang, L., Wang, D., and Guo, Y. (2018): Frictional behaviors of iron based tools-casing with sand deposition, *Tribology International*, 123, 180–190. <https://doi.org/10.1016/j.triboint.2018.03.013>
218. Yao, S.-S., Jin, F.-L., Rhee, K. Y., Hui, D., and Park, S.-J. (2018): Recent advances in carbon-fiber-reinforced thermoplastic composites: A review, *Composites Part B: Engineering*, 142, 241–250. <https://doi.org/10.1016/j.compositesb.2017.12.007>
219. Yap, C. Y., Chua, C. K., Dong, Z. L., Liu, Z. H., Zhang, D. Q., Loh, L. E., and Sing, S. L. (2015): Review of selective laser melting: Materials and applications, *Applied Physics Reviews*, 2(4), 041101. <https://doi.org/10.1063/1.4935926>
220. Yu, J., Chary, S., Das, S., Tamelier, J., Pesika, N. S., Turner, K. L., and Israelachvili, J. N. (2011): Gecko-Inspired Dry Adhesive for Robotic Applications, *Advanced Functional Materials*, 21(16), 3010–3018. <https://doi.org/10.1002/adfm.201100493>
221. Zaldivar, R. J., Witkin, D. B., McLouth, T., Patel, D. N., Schmitt, K., and Nokes, J. P. (2017): Influence of processing and orientation print effects on the mechanical and thermal behavior of 3D-Printed ULTEM® 9085 Material, *Additive Manufacturing*, 13, 71–80. <https://doi.org/10.1016/j.addma.2016.11.007>
222. Zhang, J., and Xiao, P. (2018): 3D printing of photopolymers, *Polymer Chemistry*, 9(13), 1530–1540. <https://doi.org/10.1039/C8PY00157J>
223. Zhang, W., Cotton, C., Sun, J., Heider, D., Gu, B., Sun, B., and Chou, T.-W. (2018): Interfacial bonding strength of short carbon fiber/acrylonitrile-butadiene-styrene composites fabricated by fused deposition modeling, *Composites Part B: Engineering*, 137, 51–59. <https://doi.org/10.1016/j.compositesb.2017.11.018>
224. Zhang, Y., Li, H., Yang, X., Zhang, T., Zhu, K., Si, W., Liu, Z., and Sun, H. (2018): Additive manufacturing of carbon nanotube-photopolymer composite radar absorbing materials, *Polymer Composites*, 39(S2), E671–E676. <https://doi.org/10.1002/pc.24117>



- 
225. Zhao, L., Lee, V. K., Yoo, S.-S., Dai, G., and Intes, X. (2012): The integration of 3-D cell printing and mesoscopic fluorescence molecular tomography of vascular constructs within thick hydrogel scaffolds, *Biomaterials*, 33(21), 5325–5332.  
<https://doi.org/10.1016/j.biomaterials.2012.04.004>
226. Zhao, X., Zhang, Q., Chen, D., and Lu, P. (2010): Enhanced Mechanical Properties of Graphene-Based Poly(vinyl alcohol) Composites, *Macromolecules*, 43(5), 2357–2363.  
<https://doi.org/10.1021/ma902862u>
227. Zhiani Hervan, S., Altinkaynak, A., and Parlar, Z. (2020): Hardness, friction and wear characteristics of 3D-printed PLA polymer, *Proceedings of the Institution of Mechanical Engineers, Part J: Journal of Engineering Tribology*, 135065012096640.  
<https://doi.org/10.1177/1350650120966407>
228. Zhuang, Y., Song, W., Ning, G., Sun, X., Sun, Z., Xu, G., Zhang, B., Chen, Y., and Tao, S. (2017): 3D-printing of materials with anisotropic heat distribution using conductive polylactic acid composites, *Materials & Design*, 126, 135–140.  
<https://doi.org/10.1016/j.matdes.2017.04.047>
229. Zsidai, L., De Baets, P., Samyn, P., Kalacska, G., Van Peteghem, A. P., and Van Parys, F. (2002): The tribological behaviour of engineering plastics during sliding friction investigated with small-scale specimens, *Wear*, 253(5–6), 673–688.  
[https://doi.org/10.1016/S0043-1648\(02\)00149-7](https://doi.org/10.1016/S0043-1648(02)00149-7)
230. Zsidai László (2005): *Műszaki polimerek tribológiai kutatása különböző rendszerekben (Tribology research of engineering polymers in different systems)*. PhD dissertation, Szent István University, Gödöllő, Hungary

**A2: Publications related to the dissertation***Refereed papers in foreign languages:*

1. **Hanon M. M.**, Zsidai L. (2021): Comprehending the role of process parameters and filament color on the structure and tribological performance of 3D printed PLA. *Journal of Materials Research and Technology, Elsevier*. 15, 647-660. ISSN: 2238-7854, <http://dx.doi.org/10.1016/j.jmrt.2021.08.061>, (IF: 5.039\*).
2. **Hanon M. M.**, Ghaly A., Zsidai L., Szakál Z., Szabó I., Kátai L. (2021): Investigations of the mechanical properties of DLP 3D printed graphene/resin composites. *Acta Polytechnica Hungarica, Obuda University*. 18 (8), 143–161. ISSN: 1785-8860, <http://dx.doi.org/10.12700/APH.18.8.2021.8.8>, (IF: 1.806\*).
3. Dobos J., **Hanon M. M.**, Oldal I. (2021): Effect of infill density and pattern on the specific load capacity of FDM 3D-printed PLA multi-layer sandwich. *Journal of Polymer Engineering, De Gruyter*. ISSN: 0334-6447, <https://doi.org/10.1515/polyeng-2021-0223>, (IF: 1.367\*).
4. Rudnik M., **Hanon M. M.**, Szot W., Beck K., Gogolewski D., Zmarzły P., Koziar T. (2022): Tribological properties of medical material (MED610) used in 3D printing PJM technology. *Tehnički vjesnik / Technical Gazette*. (In press). ISSN: 1848-6339, (IF: 0.783\*).
5. **Hanon M. M.**, Marczis R., Zsidai L. (2021): Influence of the 3D Printing Process Settings on Tensile Strength of PLA and HT-PLA. *Periodica Polytechnica Mechanical Engineering, Budapest University of Technology and Economics*. 65 (1), 38–46. ISSN: 1587-379X, <http://dx.doi.org/10.3311/PPme.13683>, (Scopus Q2, CiteScore: 2.9\*).
6. **Hanon M. M.**, Alshammas Y., Zsidai L. (2020): Effect of print orientation and bronze existence on tribological and mechanical properties of 3D-printed bronze/PLA composite. *The International Journal of Advanced Manufacturing Technology, Springer*. 108: 553–570. ISSN: 0268-3768, <https://link.springer.com/article/10.1007/s00170-020-05391-x>, (IF: 3.226\*).
7. **Hanon M. M.**, Marczis R., Zsidai L. (2020): Impact of 3D printing structure on the tribological properties of polymers. *Industrial Lubrication and Tribology, Emerald*. 72(6): 811–818. ISSN: 0036-8792, <http://dx.doi.org/10.1108/ILT-05-2019-0189>, (IF: 1.29\*).
8. **Hanon M. M.**, Kovács M., Zsidai L. (2019): Tribology Behaviour Investigation of 3D Printed Polymers. *International Review of Applied Sciences and Engineering, Akadémiai Kiadó*. 10 (2), 173–181. ISSN: 2063-4269, <http://dx.doi.org/10.1556/1848.2019.0021>.
9. **Hanon M. M.**, Kovács M., Zsidai L. (2019): Tribological behaviour comparison of ABS polymer manufactured using turning and 3D printing. *International Journal of Engineering and Management Sciences (IJEMS)*. 4(1): 46-57. ISSN: 2498-700X, <http://dx.doi.org/10.21791/IJEMS.2019.1.7>.
10. **Hanon M. M.**, Zsidai L. (2018): Evaluation of 3D printing process of testing samples using DLP and FDM techniques. *Mechanical Engineering Letters, Szent István University*. 17(1), 57-66. HU ISSN: 2060-3789.

*International conference proceedings:*

11. **Hanon M. M.**, Dobos J., Zsidai L. (2021): The influence of 3D printing process parameters on the mechanical performance of PLA polymer and its correlation with hardness. *10th CIRP Sponsored Conference on Digital Enterprise Technologies (DET 2020), Budapest, Hungary, October 11–13, 2021*. Published in: *Procedia Manufacturing, Elsevier*. 54, 244-249. ISSN: 2351-9789, <http://dx.doi.org/10.1016/j.promfg.2021.07.038>, (Scopus Q2, CiteScore: 2.3\*).

12. **Hanon M. M.**, Zsidai L., Ma Q. (2021): Accuracy investigation of 3D printed PLA with various process parameters and different colors. *3rd International Conference on Materials Engineering & Science 2020 (IconMEAS 2020)*, Kuala Lumpur, Malaysia (Online Meeting), December 28–30, 2020. Published in: *Materials today: Proceedings*, Elsevier, 45(5), 3089-3096. ISSN: 2214-7853, <http://dx.doi.org/10.1016/j.matpr.2020.12.1246>.
13. **Hanon M. M.**, Zsidai L. (2020): Tribological and Mechanical Properties Investigation of 3D Printed Polymers Using DLP Technique. *2nd International Conference on Materials Engineering & Science (IconMEAS 2019)*, Baghdad, Iraq, September 25-26, 2019. Published in: *AIP Conference Proceedings*, 2213, 020205. ISSN: 1551-7616, <http://dx.doi.org/10.1063/5.0000267>.
14. **Hanon M. M.**, Zsidai L. (2020): Sliding Surface Structure Comparison of 3D Printed Polymers Using FDM and DLP Technologies. *The International Conference of the Carpathian Euro-Region Specialists in Industrial Systems (CEurSIS 2019)*, Baia Mare, Romania. 12th Edition, April 11–12, 2019. Published in: *IOP Conference Series: Materials Science and Engineering*, 749, 012015. ISSN: 1757-899X, <http://dx.doi.org/10.1088/1757-899X/749/1/012015>.
15. **Hanon M. M.**, Zsidai L. (2022): Investigation on The Accuracy, Hardness, and Surface Roughness of Photopolymerization 3D Printing Technique Objects. *36th International Conference of the Polymer Processing Society (PPS-36)*, Montréal, Canada, September 26-29, 2021. Published in: *AIP Conference Proceedings*, (In press). ISSN: 1551-7616.
16. **Hanon M. M.**, Marczis R., Zsidai L. (2019): Anisotropy Evaluation of Different Raster Directions, Spatial Orientations, and Fill Percentage of 3D printed PETG tensile test specimens. *The 9th International Conference on Key Engineering Materials (ICKEM 2019)*, Oxford, United Kingdom, March 29-April 1, 2019. Published in: *Key Engineering Materials*, 821(1), 167-173. ISSN: 1662-9795, <http://dx.doi.org/10.4028/www.scientific.net/KEM.821.167>.

*International conference abstracts:*

17. **Hanon M. M.**, Kovács M., Zsidai L. (2018): Tribological behaviour comparison of ABS polymer manufactured using turning and 3D printing. *6th International Scientific Conference on Advances in Mechanical Engineering (ISCAME 2018)*, Debrecen, Hungary, October 11-13, 2018. Published in: *Conference Proceedings (Book of Extended Abstracts)*, pp. 63-64. ISBN: 978-963-490-051-1.

*Book chapter in foreign languages:*

18. Ma Q., Rejab R., **Hanon M. M.**, Sahat I. M., Siregar J. P. (2021): 3D-Printed spherical-roof contoured-core (SRCC) composite sandwich structures for aerospace applications. In: *High-Performance Composite Structures, Part of the Composites Science and Technology book series*, Springer, Singapore. pp. 75-91. ISBN: 978-981-16-7377-1, [http://dx.doi.org/10.1007/978-981-16-7377-1\\_4](http://dx.doi.org/10.1007/978-981-16-7377-1_4).

**A3: Technical specifications of the used printers**

Specifications	WANHAO duplicator 6 (FDM)	WANHAO D7 (DLP)
<b>Technology</b>	FFF (Fused Filament Fabrication)	DLP LCD printer
<b>Printing materials</b>	PLA, ABS, PVA, PEVA and HIPS	405 nm Resin
<b>Printable volume</b>	200x200x175 mm	120.96*68.5*180 mm
<b>Layer thickness</b>	50 - 400 $\mu\text{m}$	35-100 $\mu\text{m}$
<b>Material form</b>	Filament diameter of 1.75 mm	Resin
<b>Heating or curing source</b>	Extrusion nozzle (0.4 mm)	5.5 inch LCD, 405 nm UV lamp
<b>Print speed</b>	30-150 mm/s	30 mm/hour (in height)
<b>Operating temperature</b>	180-260 $^{\circ}\text{C}$	23 $^{\circ}\text{C}$
<b>Position precision</b>	X: 12.5 $\mu\text{m}$ , Y: 125 $\mu\text{m}$ and Z: 5 $\mu\text{m}$	X: 0.01 $\mu\text{m}$ , Y: 0.01 $\mu\text{m}$ , Z: 4 $\mu\text{m}$

**A4: Chemical composition of the used photopolymer resin materials**

For the Wanhao UV resin

Chemical name	Weight %
Polyurethane acrylate (PUA)	45 - 47
4-Morpholine	34 - 36
Tripropylene glycol diacrylate	15 - 17
Phenylbis (2,4,6-trimethylbenzoyl) phosphine oxide	1.6 - 2.0
Pentaerythritol triacrylate	0.8 - 1.2
4-Methoxyphenol	0.02 - 0.07

For the Esun photopolymer resin

Chemical name	Percentage by weight
Polyurethane acrylate (PUA)	30% min
Monomer	30% min
Photo initiators	5% max
Colour pigment	5% max

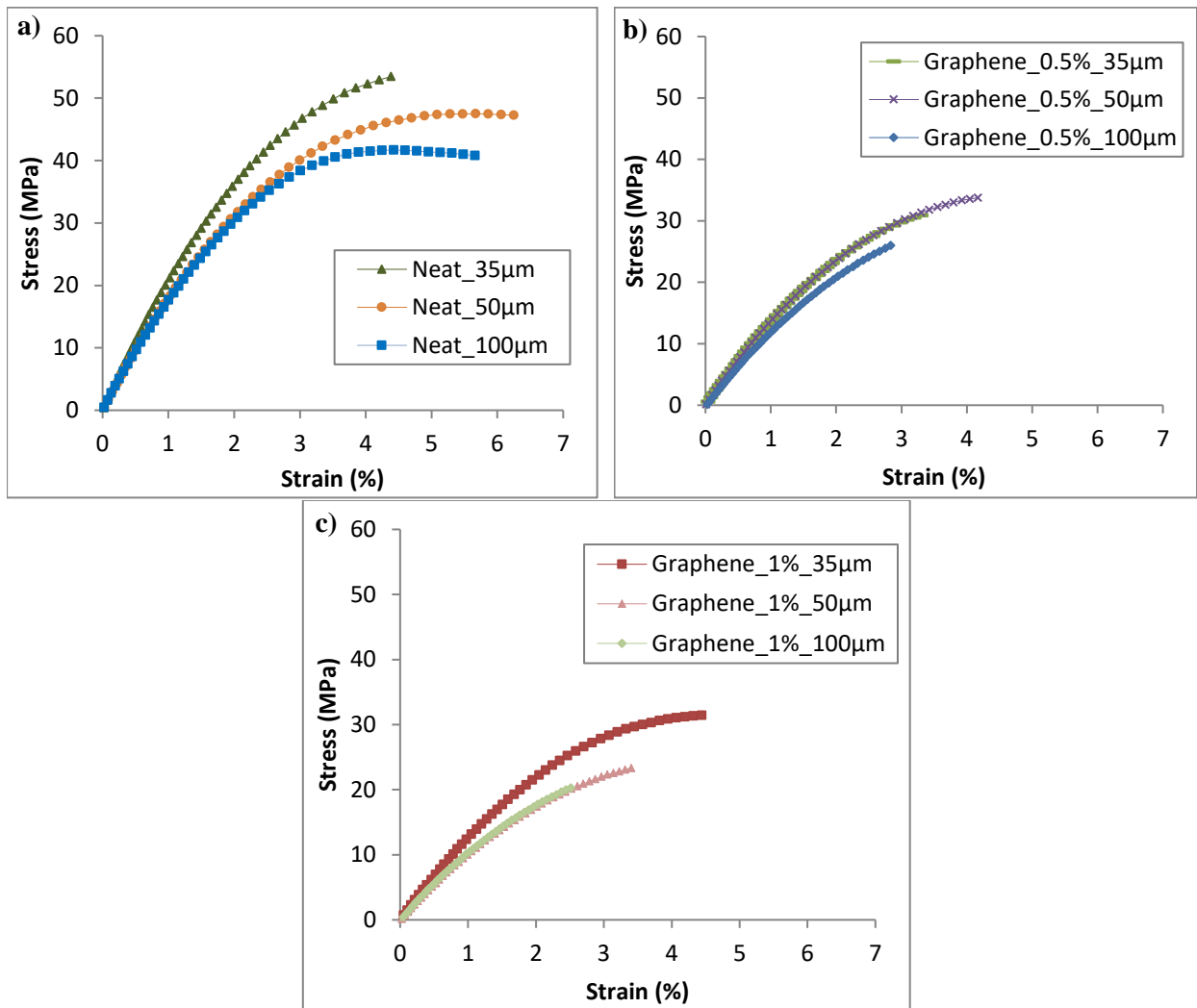
**A5: Tensile stress-strain curves of various layer thickness specimens**

Fig. 8.1. Tensile stress-strain curves of various layer thickness specimens at a) neat resin material; composite with graphene concentration of b) 0.5 wt.%, and c) 1 wt.%

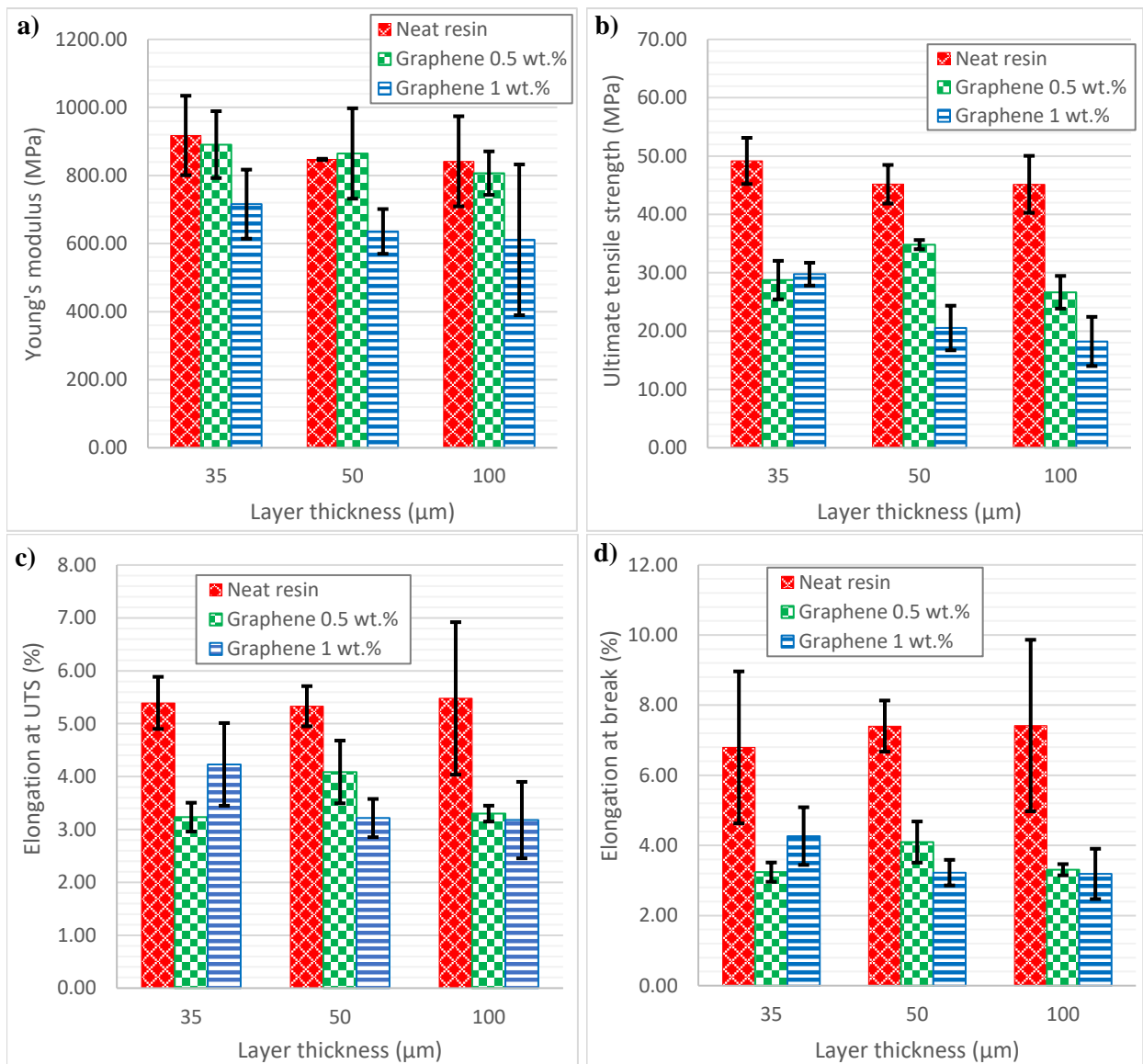
**A6: Mechanical behaviour under different graphene concentrations**

Fig. 8.2. Comparison of mechanical behaviour under different graphene concentrations and printing layer thickness in terms of a) Young's modulus, b) ultimate tensile strength (UTS), c) elongation at UTS, and d) elongation at break

**A7: Variance in values of tensile test results**

For the layer thickness effect as compared to the reference specimen (35  $\mu\text{m}$  layer thickness, highlighted with blue colour)

Printing parameter		Variance in values			
Graphene concentration (wt.%)	Layer thickness ( $\mu\text{m}$ )	Young's modulus	UTS	Elongation at UTS	Elongation at break
0	35	917.66 (MPa)	49.17 (MPa)	5.39 (%)	6.79 (%)
	50	-7.65 %	-8.14%	-1.11%	+8.98%
	100	-8.27%	-8.16%	+1.67%	+9.28%
0.5	35	890.87 (MPa)	28.74 (MPa)	3.23 (%)	3.24 (%)
	50	-2.92%	+21.15%	+26.63%	+26.23%
	100	-9.40%	-7.24%	+2.17%	+2.16%
1	35	715.85 (MPa)	29.76 (MPa)	4.23 (%)	4.27 (%)
	50	-11.18%	-31.01%	-23.88%	-24.59%
	100	-14.64%	-38.74%	-24.82%	-25.29%

For the graphene addition effect as compared to the reference specimen (neat resin material "0 graphene concentration", highlighted with blue colour)

Printing parameter		Variance in values			
Layer thickness ( $\mu\text{m}$ )	Graphene concentration (wt.%)	Young's modulus	UTS	Elongation at UTS	Elongation at break
35	0	917.66 (MPa)	49.17 (MPa)	5.39 (%)	6.79 (%)
	0.5	-2.92%	-41.55%	-40.07%	-52.28%
	1	-21.99%	-39.48%	-21.52%	-37.11%
50	0	847.46 (MPa)	45.17 (MPa)	5.33 (%)	7.40 (%)
	0.5	+2.04%	-22.91%	-23.26%	-44.73%
	1	-24.98%	-54.55%	-39.59%	-56.48%
100	0	841.78 (MPa)	45.16 (MPa)	5.48 (%)	7.42 (%)
	0.5	-4.12%	-40.97%	-39.78%	-55.39%
	1	-27.41%	-59.63%	-41.97%	-57.01%

## A8: Illustration of hardness testing along with the specimen length

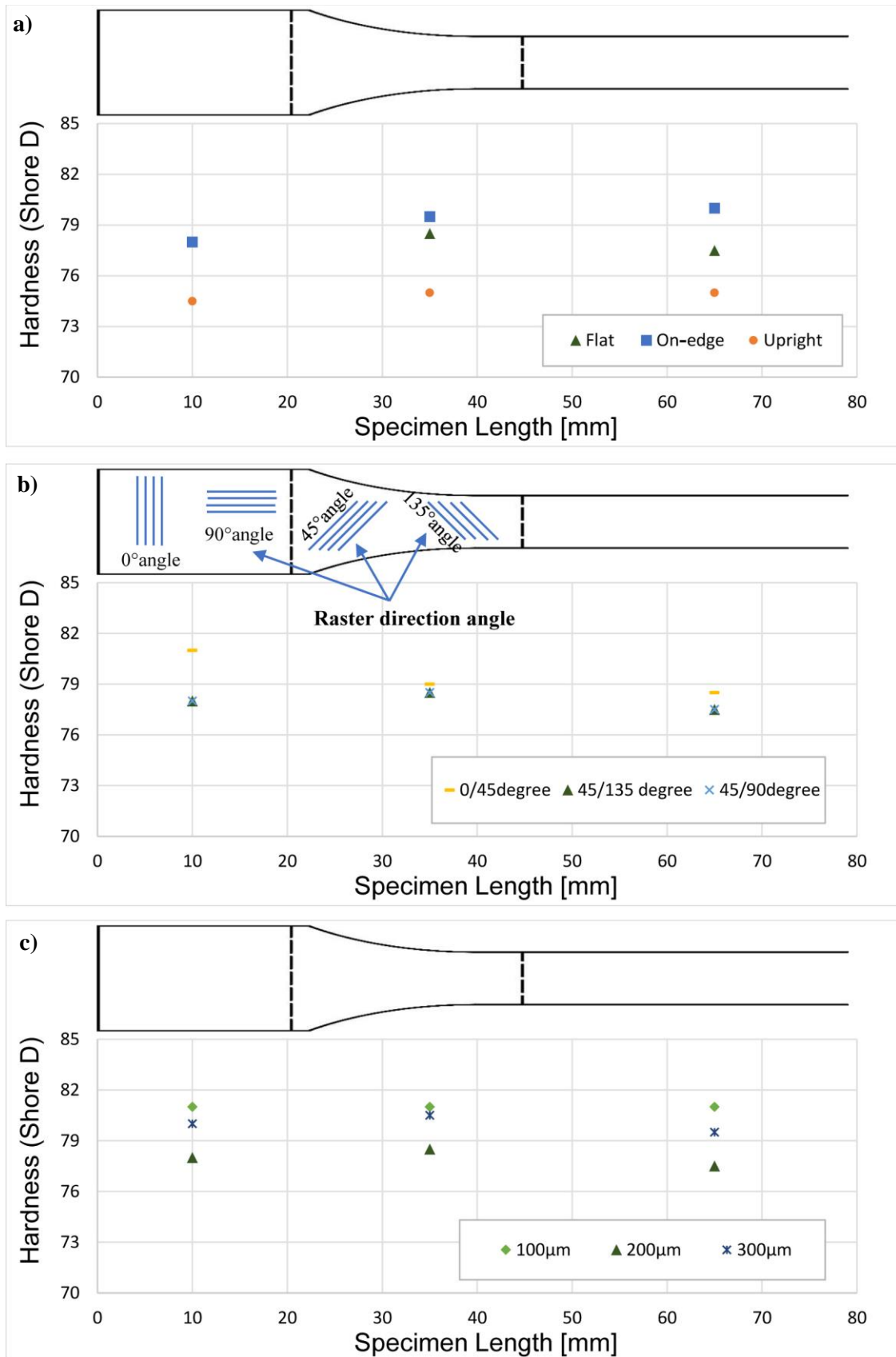


Fig. 8.3. Hardness values along with the specimen length in various print conditions a) build orientation, b) raster direction angle, and c) layer thickness



## A9: Correlation between the tribological and mechanical/physical properties

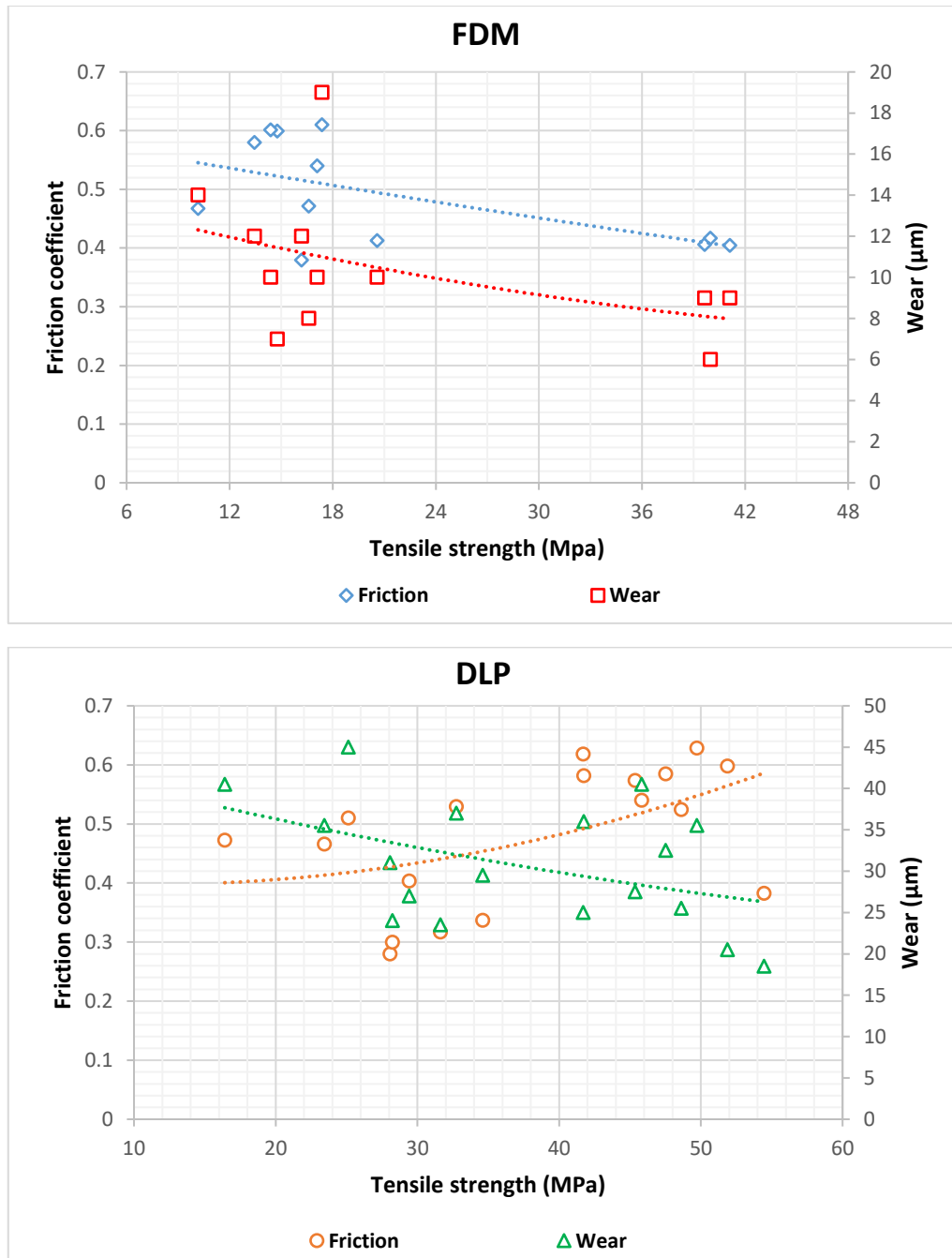


Fig. 8.4. The relation of wear depth and coefficient of friction versus tensile strength for FDM (top) and DLP (down) specimens

For FDM components, Fig. 8.4 shows that tensile strength is inversely proportional with the coefficient of friction and wear as friction coefficient and wear decreased with increasing tensile strength. However, the DLP specimens exhibited incompatible attitudes, as tensile strength was directly proportional with the coefficient of friction but with wear was in an inverse proportion. This indicates the influence of the DLP technique (and the resin material implicitly) on friction behaviour.

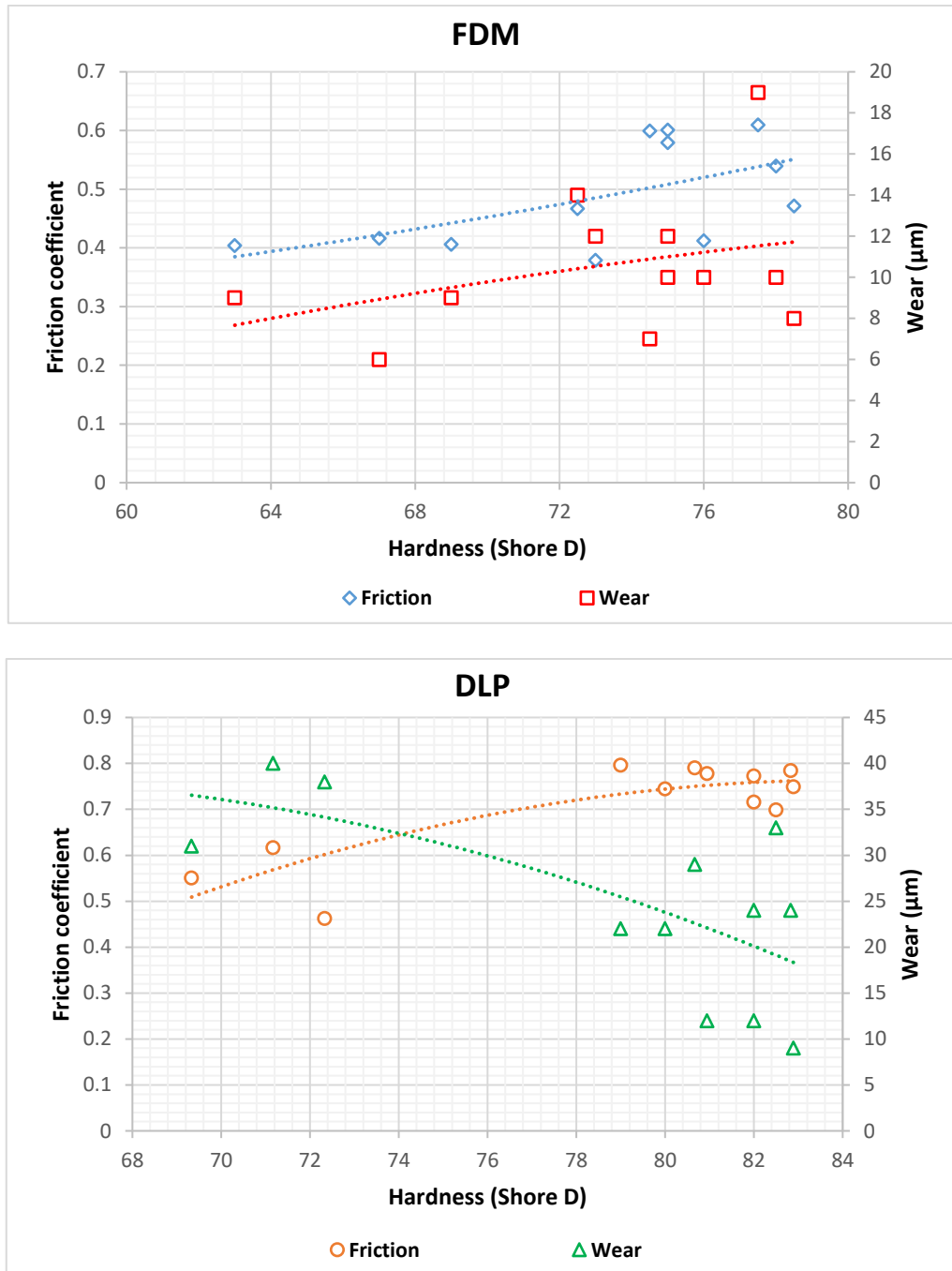


Fig. 8.5. The relation of wear depth and coefficient of friction versus hardness for FDM (top) and DLP (down) specimens

The general tendency shows that the coefficient of friction and wear were increasing as much as the hardness increased (directly proportional), as demonstrated in Fig. 8.5. However, the only exception was in the case of wear of the DLP, as the latter dropped with the growing of hardness which can be attributed to the improvement obtained by the post-processing, which makes the surfaces of DLP samples stiffer, thus resisting wear.



## 9. ACKNOWLEDGEMENT

In this long journey for my PhD, which started in Sep 2017 and ended by the middle of 2022, many people (including professors and staff members, classmates, senior and junior fellows, technical and support staff at the university, friends from local Hungarians and the internationals, and family members and relatives) have helped and supported me to attain this endeavour. Many thanks to them all. I wish I could refer to everyone, but I suppose it is not easy to do it on a single page. However, it is essential to name at least those who have primarily been engaged in it.

This work has been supported financially by the Stipendium Hungaricum Scholarship Programme and accomplished under the direction of the Mechanical Engineering Doctoral School at MATE (Szent István University formerly), Gödöllő, Hungary.

First and foremost, I am incredibly grateful to my supervisor Dr László Zsidai for his valuable advice, uninterrupted support, and patience during my PhD studies. His vast knowledge and experience have been a source of inspiration throughout my academic research. This dissertation would not have been feasible without his supervision and significant guidance.

I would like to express my gratitude and appreciation for Prof. István Farkas, the former head of the Mechanical Engineering Doctoral School, whose recommendations, suggestions, and support throughout the period of study have facilitated the fulfilment of all requirements for obtaining this PhD. In addition, I would like to extend my sincere gratitude to Prof. Gábor Kalácska, the current head of the Mechanical Engineering Doctoral School, for the invaluable recommendations and thoughtful comments on this dissertation.

Moreover, I am grateful to all members of the Institute for Mechanical Engineering Technology, Institute of Technology, for organizing the IPMP meetings, which significantly contributed to improving my work throughout the past years. Also, the assistance provided by Dr. Zoltán Szakál, Dr. Róbert Keresztes, and Mr Ádám Sarankó was greatly appreciated. They were so generous to deliver the necessary knowledge to help conduct the experiments of tribology, surface roughness, optical microscope, and mechanical testing.

I am also thankful for Mr Yazan Alshammas, Miss Csilla Agócs, and Mr Arsany Ghaly, who were under my supervision throughout their MSc studies between 2018 and 2021. Thanks for being part of my project and working hard in the lab to help achieve our aims, represented successfully by publishing many scientific articles from our research work in reputed journals.

Ms Zsuzsanna Tassy, the International PhD coordinator at the University's Doctoral and Habilitation Center, deserves special mention. Words fail to express my gratitude to this lady for the diverse support and her assistance provided to my family in several critical situations.

Further, I wish to show my enormous appreciation to Mrs Nihal D. Salman, my wife, for being the most supporter to me ever. This superhero lady has been amazing; she gave birth twice during these years and took care of our kids and me, despite being also a PhD candidate. Thanks for your patience and for acting as a sounding board whenever required. Additionally, my biggest thanks to my family (mother and sisters) for all support they have shown me through this research.

Finally, I wish to acknowledge the Ministry of Higher Education of Iraq and the Middle Technical University (MTU) - Iraq, my home university, to nominate me for this position.

Muammal M Hanon Sharba

Gödöllő, 2022